Additive Manufacturing of Smart Antennas and Frequency Selective Surfaces

A Thesis Submitted to The University of Kent

for the Degree of Doctor of Philosophy

in Electronic Engineering

By

Anshuman Shastri

Abstract

This thesis presents the development and the additive manufacturing of smart antennas and frequency selective surfaces (FSS) for microwave, millimetre wave, and low-Terahertz applications. Numerous fabrications techniques such as etching, low-cost inkjet-printing, Fused Filament Fabrication (FFF) and Aerosol Jet Printing are employed to fabricate the antennas and FSS. Firstly, frequency reconfigurable antennas with close-coupled biasing technique are developed using double-sided etching on a thin mylar substrate for smart current and voltage sensing applications. The frequency tunable antenna also acts as a novel current sensing antenna in a smart sensing system that can sense the alternating current passing through a wire. The design is followed by introducing a low-cost inkjet-printed industry ready solution for frequency reconfigurable antennas where a single antenna aperture solution is utilised to demonstrate frequency reconfigurability in both switching and tuning configurations. Development of Frequency Selective Surfaces using low-cost printing machine is demonstrated in which FSS structures are inkjet-printed as wallpaper posters for Radio Frequency (RF) shielding and signal enhancements for 4G and 5G applications. A novel approach for fully 3D printing an FSS structure is also demonstrated using a low-cost open-source printer, which was modified to print the filament and the conductive inks simultaneously. Widespread investigation of industry-grade Aerosol Jet printing is utilised for additive manufacturing of bandstop and bandpass FSS designs for RF shielding and signal filtering. The bandstop designs are developed for microwave and millimetre-wave applications. The bandpass slot FSS designs are developed for millimetre wave and low-Terahertz applications for futuristic Beyond 5G and 6G systems.

Anshuman Shastri

November 24, 2020

Acknowledgement

I would like to express my uttermost gratitude towards my supervisors Dr. Benito Sanz-Izquierdo and Prof. Mohammed Sobhy. Their persistent encouragement, valuable assistance, and priceless suggestions throughout the advancement of this research has helped me complete the work. I deem myself extremely lucky to have worked under supervisors like them. I came under Dr. Benito's guidance in 2014 as a raw, aspiring researcher who was a beginner to the field of research. Today, I feel immensely proud in admitting the fact that I have become a much better researcher under his able guidance over time. The never-ending research ideas that consistently came from him gave me motivation and vision to enhance the spectrum of my knowledge and develop the experimental background throughout my research. I would also like to thank my co-supervisor Prof. Sobhy for providing me the motivation to work harder and provide the invaluable support during the trying and testing lockdown period.

A vote of thanks must also go towards the Head of School, Prof. Jiangzou Wang for consistently motivating us researchers to keep accomplishing ground-breaking research. I would like to convey my gratitude towards the hard-working staff of School of Engineering and Digital Arts at University of Kent for providing all the necessary assistance during my time. A special vote of thanks goes towards Simon Jakes and Antonio Mendoza for their assistance with fabrications and measurements.

Finally, I can never express enough gratitude towards my parents (Prof. Aditya Shastri and Prof. Ina Shastri) and my brother (Ishan Shastri) ever for providing me with their continuous encouragement, support and understanding throughout the course of my PhD and my life. I would not have been able to finish the work without their support and belief in me. I would like to thank my colleagues Sung-Yun Jun, Peter Njogu, and all the fellow researchers who helped me throughout my journey.

Table of Contents

CHAPTER 1 18
INTRODUCTION 18
1.1 Overview and Motivations 18
1.2 Thesis Outline 20
1.3. List of Publications 25
1.4. Awards and nominations 27
1.5. List of Seminars and Webinar Lectures 27
References 28
CHAPTER 2 30
LITERATURE REVIEW AND THEORETICAL BACKGROUND 30
2.1 Introduction 30
2.2 Smart and Reconfigurable Antennas 31
2.2.1 Smart Antennas 31
2.2.2 Frequency Reconfigurable Antennas 31
2.3 Frequency Selective Surfaces 37
2.3.1 Introduction to Frequency Selective Structures and Applications 37
2.3.2 Application of FSS in Radio Frequency Shielding 40
2.3.3 Application of FSS in Mobile Communications 41
2.4 Additive Manufacturing of Electromagnetic Structures 42
2.4.1 Additive Manufacturing of Antennas 42
2.4.2 Inkjet Printing of Antennas 44
2.4.3 Additive Manufacturing of Frequency Selective Surfaces 48
2.4.4 Fused Deposition Modelling (FDM) 49
2.4.5 Aerosol Jet Printing 51
References 53
CHAPTER 3 66
FREQUENCY RECONFIGURABLE ANTENNAS FOR SMART SENSING APPLICATIONS 66
3.1 Introduction 66
3.2 Switchable Slot Antennas 68
3.2.1 Switchable slot antenna design 68
3.2.2 Close-Coupled Biasing Technique 71

3.2.3 Switching Antenna Fabrication and Measurements 74
3.3 Tunable Antenna 77
3.3.1 Tunable Antenna Design 77
3.3.2 Tunable Design Fabrication and Results 80
3.4 AC Current Sensing with Tunable Antenna 84
3.4.1 AC Current Sensing System 84
3.4.2 AC Current Sensing Measurements 87
3.4.3 Wireless Transmission at 2.5 GHz 91
3.5 Conclusion 92
References 94
CHAPTER 4 98
MANUFACTURING OF LOW-COST INKJET PRINTED FREQUENCY RECONFIGURABLE ANTENNAS 98
4.1 Introduction 98
4.2 Manufacturing Considerations 99
4.3 Switchable Antenna Design 100
4.3.1 Design dimensions 100
4.3.2 Simulation Results 102
4.3.3 Design fabrication and measurements 103
4.4 Frequency tunable antenna 110
4.4.1 Antenna design 110
4.4.2 Measurement results 113
4.5 Conclusion 117
References 119
CHAPTER 5 122
LOW-COST FABRICATION OF FREQUENCY SELECTIVE SURFACES 122
5.1 Introduction 122
5.2 Low-cost Fabrication of Wallpaper Poster FSS 123
5.2.1 Wallpaper poster designs 123
5.2.2 Fabrication and Measurements 126
5.3 Full 3D Printing of an FSS using a Low-Cost Open-Source Printer 130
5.3.1 Considerations for the Printer System 130
5.3.2 Printer Assembly and Calibration 132
5.3.3 Square Loop FSS Design 136

5.3.4 Fabrication and Measurements 142
5.4 Conclusion 146
References 148
CHAPTER 6 151
AEROSOL JET PRINTING OF BANDSTOP AND BANDPASS FREQUENCY SELECTIVE SURFACES 151
6.1 Introduction 151
6.2 Microwave bandstop FSS design 154
6.2.1 Design dimensions 154
6.2.2 Simulation responses 156
6.3 Millimetre wave bandstop FSS design 157
6.3.1 Design dimensions 157
6.3.2 Simulated transmission responses 159
6.4 Aerosol Jet printing and measurement results 160
6.4.1 Aerosol Jet printing 160
6.4.2 Measurement results 165
6.5 Millimetre wave low-THz bandpass FSS design 170
6.5.1 Design dimensions 170
6.5.2 Simulation responses 171
6.6 Aerosol Jet printing of design 172
6.7 Surface profiles and measurement results 176
6.7.1 Surface profiles 176
6.7.2 Measurement results 182
6.8 Conclusion 189
References 192
CHAPTER 7 199
CONCLUDING REMARKS 199
7.1 Conclusion 199
7.2 Future work 205
References 210

LIST OF FIGURES

Figure 1.1	3D printed battery using additive manufacturing	20
Figure 1.2	Estimated market share for additive manufacturing [14]	20
Figure 2.1	Functioning of smart antennas [4]	31
Figure 2.2	A pattern reconfigurable cubic slot antenna [27]	33
Figure 2.3	Circular polarised reconfigurable Crossed-Yagi Patch antenna (a) top view and (b) bottom view [28]	33
Figure 2.4	A typical fundamental FSS model of bandpass and bandstop FSS structures in (a), Transmission coefficient for the two FSSs in (b) and capacitive patch array and inductive mesh filters in (c) [53]	38
Figure 2.5	A variety of FSS unit cells structures with their given names [54]	39
Figure 2.6	Split ring resonator FSS array for (a) Switching and (b) tuning [70]	39
Figure 2.7	Representative figure of an anchor shaped Bandstop FSS [71]	40
Figure 2.8	RF Shielding surface for walls [78]	41
Figure 2.9	A typical IRS/metasurfaces structure and functioning [85]	42
Figure 2.10	5G MIMO Antenna with (a) proposed design, (b) printed polymer, (c) metal coated antenna with 2 feeds and (d) antenna mounted on the copper plane [95]	44
Figure 2.11	A typical household Inkjet printer in (a) and a typical piezoelectric inkjet printing mechanism in (b)	46
Figure 2.12	A typical Diamatix printer	47
Figure 2.13	Unfolded inkjet-printed patch antenna in (a) and 3D folded origami structure in (b) [92]	47

Figure 2.14	A typical Fused Deposition Modelling (FDM) system [106]	50
Figure 2.15	A typical Aerosol Jet Printer setup (a) with its functioning block diagram (b) [115]-[117]	52
Figure 3.1	Switchable antenna design with side view (a) back view (b) and front view (c)	69
Figure 3.2	Switching antenna simulated reflection coefficient results for ON-state and OFF-state	70
Figure 3.3	Simulated Surface currents of the OFF state at 1.88 GHz	71
Figure 3.4	Simulated Surface currents of the ON state at 2.32 GHz	71
Figure 3.5	Effects of increased thickness of substrate H on S_{11} in (a) and the effects of the increased gap between metallic tracks and the antenna layer on S_{11} of the ON state in (b)	73
Figure 3.6	Etched antenna design displaying the SMA connector and extension wires from (a) front, (b) back, (c) side	74
Figure 3.7	Measured reflection coefficient results for ON state and OFF State	75
Figure 3.8	Radiation patterns for OFF state at 1.7 GHz in (a) XY, (b) XZ and (c) YZ planes	76
Figure 3.9	Radiation patterns for ON state at 2.32 GHz in (a) XY, (b) XZ and (c) YZ planes	77
Figure 3.10	Simulated reflection coefficient (S_{11}) results for the capacitance range of 0.5 - 6.6 pF	78
Figure 3.11	Capacitance vs Frequency vs Bandwidth relationship from simulation results	80
Figure 3.12	Simulated Surface currents at 0.5 pF (top), 4 pF (middle) and	

	6.6 pF (bottom) respectively	81
Figure 3.13	Measured reflection coefficient (S_{11}) with the corresponding Voltages	81
Figure 3.14	Plot for DC Supply Voltage vs frequency vs bandwidth from measurements	82
Figure 3.15	Measured first mode radiation patterns at 28 V for 2.42 GHz for the antenna (a) XY-plane, (b) XZ-plane and (c) YZ-plane	82
Figure 3.16	Measured first mode radiation patterns at 6.4 V for 2.12 GHz for the antenna (a) XY-plane, (b) XZ-plane and (c) YZ-plane	83
Figure 3.17	Measured first mode radiation patterns at 1 V for 1.4 GHz for the antenna (a) XY-plane, (b) XZ-plane and (c) YZ-plane	83
Figure 3.18	Equivalent circuit schematics of the CT connected to the reconfigurable antenna	85
Figure 3.19	Reconfigurable antenna connected with split wires and CT	85
Figure 3.20	Expected AC current input and DC output voltage for CT [34]	86
Figure 3.21	Relationship between the reverse biased voltage and capacitance of BB857 diode [32]	87
Figure 3.22	AC Current sensing measurement system setup	88
Figure 3.23	Measured AC current input and DC output voltage for CT	88
Figure 3.24	Current sensing measurement results	89
Figure 3.25	Sensing reflection coefficient measurements using the current sensing setup measuring 1 A to 8 A	90
Figure 4.1	Switching antenna design	101
Figure 4.2	Simulated reflection coefficient (S_{11}) results for ON state and	

	OFF state	103
Figure 4.3	Simulated surface currents for (a) OFF-state and (b) ON-state	103
Figure 4.4	Brother inkjet printer used for printing	104
Figure 4.5	A refillable Brother printer cartridge	105
Figure 4.6	Printed antenna design for frequency switching	106
Figure 4.7	Magnified image of the affixed capacitor	106
Figure 4.8	The Keyence® 4K Microscope surface profile photos of the printed antenna surface with 30x Zoom in (a) and 150x Zoom in (b)	107
Figure 4.9	3D surface map of a section of printed patch	108
Figure 4.10	Lateral surface roughness profile of the printed aperture	108
Figure 4.11	Measured reflection coefficient (S_{11}) of the antenna	109
Figure 4.12	Radiation pattern for the OFF state at 2.25 GHz in (a) XY-plane (b) XZ-plane and (c) YZ-plane	109
Figure 4.13	Radiation pattern for the ON state at 2.68 GHz in (a) XY-plane (b) XZ-plane and (c) YZ-plane	110
Figure 4.14	Tunable antenna Simulated Reflection coefficient (S_{11})	111
Figure 4.15	Frequency vs Capacitance vs Bandwidth relationship representation	112
Figure 4.16	Simulated surface currents at (a) 0.45 pF, (b) 3 pF and (c) 6.6 pF	113
Figure 4.17	Tunable antenna measurement results	114
Figure 4.18	Frequency vs Voltage vs Bandwidth relationship representation	115
Figure 4.19	Measured and simulated Radiation pattern results at 2.5 GHz for 28 V in (a) XY, (b) XZ and (c) YZ planes respectively	115
Figure 4.20	Measured and simulated Radiation pattern results at 2.2 GHz for 12 V in (a) XY, (b) XZ and (c) YZ planes respectively	116

Figure 4.21	Measured and simulated Radiation patterns at for 1.38 GHz at 1 V in (a) XY, (b) XZ and (c) YZ planes respectively	116
Figure 5.1	Square loop unit cell layout	124
Figure 5.2	Simulated transmission response for the microwave FSS poster design operating at 2.45 GHz central frequency	125
Figure 5.3	Simulated transmission response for the sub mm-wave FSS poster design operating at 25.21 GHz central frequency	125
Figure 5.4	Printed 4x4 sample area of the microwave FSS poster	127
Figure 5.5	Printed sub mm-wave FSS poster with the full FSS in (a) and a magnified section of the poster in (b)	127
Figure 5.6	Measurement Setup	128
Figure 5.7	Measured Transmission responses for the microwave poster FSS	129
Figure 5.8	Measured Transmission responses for the sub mm-wave poster FSS	129
Figure 5.9	Proposed 3D printer setup with dual extruders for simultaneous printing	131
Figure 5.10	Assembled 3D printer setup with dual-extruder deposition heads and the extension components	134
Figure 5.11	Square-loop element FSS unit cell design	137
Figure 5.12	Simulated transmission response and angle of incidence responses	138
Figure 5.13	Effects of the thickness of the substrate on the resonant frequency	138
Figure 5.14	Simulated transmission responses for (a) $\varepsilon_r = 2$ and (b) $\varepsilon_r = 2.7$	141

Figure 5.15	Printed square loop unit element in (a) and the gap between two adjacent square loops in (b)	143
Figure 5.16	Surface profile of the printed PLA substrate	143
Figure 5.17	Measured side profile of a printed track in (a) and 3D profile in (b)	144
Figure 5.18	Measurement Setup Layout	145
Figure 5.19	FSS structure fitted inside the absorber screen	145
Figure 5.20	Measured Transmission Response of the FSS structure	146
Figure 6.1	A typical FSS reflector implemented on glass in windows [10]	153
Figure 6.2	Unit Cell of square loop element	155
Figure 6.3	Square loop element equivalent circuit	155
Figure 6.4	Simulated transmission response of the microwave Bandstop FSS on glass	157
Figure 6.5	Simulated transmission response of the microwave Bandstop FSS on Kapton	157
Figure 6.6	Millimetre wave square-loop patch FSS unit cell design	158
Figure 6.7	Simulated transmission response for bandstop FSS design on glass	159
Figure 6.8	Simulated transmission response for bandstop FSS design on Kapton	160
Figure 6.9	A typical Aerosol Jet Printer in (a) with its functioning block in (b) [48]	161
Figure 6.10	Aerosol Jet printing bed with printed Sub mm-wave Bandstop FSS on Kapton	163
Figure 6.11	Microwave bandstop FSS design on (a) Corning eagle	

	Glass and (b) Kapton	164
Figure 6.12	Measured surface profile of microwave Glass design	164
Figure 6.13	Measured surface profile of microwave Kapton design	165
Figure 6.14	Microwave design Measurement setup (a) Side view and (b) diagonal view	166
Figure 6.15	Measured transmission coefficient for microwave FSS design on Glass	166
Figure 6.16	Measured transmission coefficient for microwave FSS design on Kapton	167
Figure 6.17	Fabricated millimetre wave FSS designs on (a) Corning eagle Glass and (b) Kapton	167
Figure 6.18	Magnified view of the printed tracks on (a) Glass and (b) Kapton	168
Figure 6.19	Measurement setup for millimetre wave bandstop FSS designs	168
Figure 6.20	Transmission responses for mm-wave FSS design on Glass	169
Figure 6.21	Transmission responses for mm-wave FSS design on Kapton	169
Figure 6.22	Mm-wave Slot Bandpass FSS design unit cell layout with dimensions	170
Figure 6.23	Simulated transmission response of 125 GHz bandpass slot FSS design	172
Figure 6.24	Simulated transmission response of 280 GHz bandpass	

slot FSS design 172

Figure 6.25 A typical Aerosol jet printing toolpath designer with vertical zigzag track lines 174

Figure 6.26 The three stages of the ink dispersion onto the substrate in fabrication with (a) pre deposition, (b) post deposition and (c) after complete dispersion of ink 175

Figure 6.27 Surface profile of a failed attempt for the fabrication of bandpass FSS on Glass 176

Figure 6.28 Printed 125 GHz Slot FSS designs on Kapton (a) Full FSS design photograph and (b) Magnified photograph 177

Figure 6.29 Fabricated 125 GHz Slot FSS microscopic view of (a) Printed slot array and (b) Individual Slot height 178

Figure 6.30 Fabricated 125 GHz Slot FSS microscopic view with (a) Profile measurement of printed height, (b) slot depth and (c) 3D profile of the printed area 179

Figure 6.31 Printed 280 GHz FSS design on Kapton (a) Full FSS photo and (b) Magnified view of the FSS 180

Figure 6.32 Fabricated 280 GHz Slot FSS microscopic view (a) Printed slot array and (b) Individual Slot height 181

Figure 6.33 Fabricated 280 GHz Slot FSS microscopic view (a) Profile measurement of printed height, (b) slot depth and (c) 3D profile of the printed area 182

Figure 6.34 Measurement test setup for transmission responses at 125 GHz and 280 GHz 183

Figure 6.35	Measured responses of 125 GHz Bandpass slot FSS design on Kapton	184
Figure 6.36	Real Permittivity and loss tangents of Kapton Polymide and Cirlex Polymide for THz frequency [56]	185
Figure 6.37	Measured transmission responses of 280 GHz Bandpass slot FSS design	186
Figure 7.1	Inkjet-printed active dipole FSS with H-shaped matching stubs	208
Figure 7.2	Simulated CST Transmission Response of the proposed Active FSS design	208

List of Acronyms

3D	3-Dimensional
ABS	Acrylonitrile Butadiene Styrene
AC	Alternating Current
AJP	Aerosol Jet Printing
AM	Additive Manufacturing
CAD	Computer-Aided-Design
CNC	Computer Numeric Control
CST	Computer Software Technology
CT	Current Transformer
DC	Direct Current
EM	Electro-Magnetic
FDM	Fused Deposition Modelling
FET	Field-Effect Transistor
FFF	Fused Filament Fabrication
FIT	Finite Integration Technique
FSS	Frequency Selective Surface
GHz	Gigahertz
LCD	Liquid Crystal Display
MM-wave	Millimetre Wave
MWS	Microwave Studio
MEMS	Micro-Electro-Mechanical-Systems

MHz	Megahertz
MOD	Metallo-Organic Decomposition
OI	Optical Interfereometer
PET	Polyethylene Terephthalate
PIN	p-type Intrinsic n-type Diode
PLA	Polylactic Acid
R^2-value	Coefficient of Determination Value
RF	Radio Frequency
RFID	Radio Frequency Identification
R&S	Rhode & Schwartz
S-Parameter	Scattering Parameter
SLA	Stereolithography
SLS	Selective Laser Sintering
SLM	Selective Laser Melting
SMA	Sub-Miniature connector version A
TE	Transverse Electric
THz	Terahertz
TM	Transverse Magnetic
UHD	Ultra High-Definition
V-I Curve	Voltage and Current Curve
VNA	Vector Network Analyser
WLAN	Wireless Local Area Network
WSN	Wireless Sensor Network

CHAPTER 1

INTRODUCTION

1.1 Overview and Motivations

Frequency reconfigurable antennas are antennas that can alter their frequency of operation to resonate at a different frequency. The lucrative concept to accommodate numerous frequency bands contained by the same antenna design has been drawing considerable amount of attention from the research community for many years. The capability to encompass a wide range of spectrum helps in developing designs that find a large number of contemporary applications. Frequency reconfigurable antennas allow a single antenna to operate in a wide spectrum of frequency bands. Frequency reconfigurable antennas are particularly useful and can be deployed for a range of smart applications such as sensing, mobile and wireless communications, beam steering and satellite communications [1] - [3]. With a wide range of possibilities with antenna designs and fabrication techniques, reconfigurable antennas can provide low-cost, efficient and environment friendly designs with the option of being flexible and foldable when printed on flexible substrates.

Frequency selective surfaces are filtering screens that are typically employed to filter the incident Electromagnetic (EM) wave responses [4]. There are two types of frequency selective surfaces (FSSs): Bandstop FSS and Bandpass FSS. Bandstop FSS designs work as frequency shields that filters and reflects the resonant frequency band and transmits all the other frequency bands and signals. Bandpass FSS designs work as frequency reflectors and filters that reflect and filter all the bands neighbouring from the resonant frequency bands. FSSs find diverse applications in mobile communications, RF shielding, frequency reflectors in indoor environments, 5G communications and the imminent 6G communications.

In general, frequency reconfigurability solutions are particularly useful to obtain a wide range of frequency bands and various manufacturing techniques that provide both the alternative and the cost-efficient solutions for antennas and FSS designs [4]. Development of Frequency Selective Surfaces for the millimetre wave and low-THz bands find particular interest with the 5G communications as well as the imminent arrival of the 6G communications. Fabrication techniques for the smart designs can also be investigated and evaluated for reliable and cost-efficient results.

With the increased demand for rapid, economical and environment friendly prototyping of electronics and ever so increasing demand in the printable electronics department, additive manufacturing or AM has seen a lot of growth in the last couple of decades [5] - [8]. A number of ways exist for 3D printing is achieved using a variety of techniques such as fused deposition modelling (FDM) [9], selective laser sintering (SLS) [10], sterolithography (SLA) [11], inkjet printing [12] and Aerosol Jet printing [13] to name a few. 3D printed batteries using additive manufacturing is presented in Fig. 1.1. The designs can be printed on a variety of substrates that offer a wide range of thickness, flexibility, transparency along with providing reliable conductivity and performances across the entire printed area. Advantages and disadvantages of various additive manufacturing on different substrates and with different inks can be studied to determine their specified applications. Surface profiles and surface roughness of the printed substrates and designs also provide a good study of the results for comparison and analysis.

With the fastest growing market, 3D printing and additive manufacturing is expected to capture a large share of the global manufacturing market with the market expected to reach $9.3 billion by the year 2027, 10 years from when this study was conducted [14].

Fig. 1.1 3D printed battery using additive manufacturing

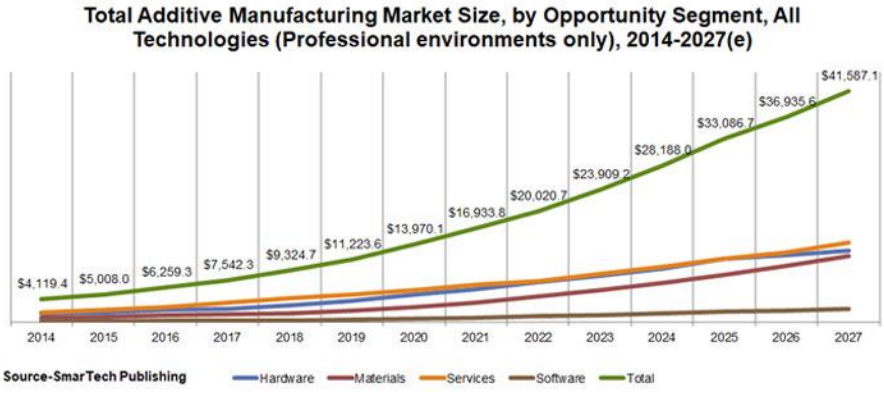

Fig. 1.2 Estimated market share for additive manufacturing [14]

1.2 Thesis Outline

The research work starts with the literature review presented in Chapter 2 that covers the developments across the field of smart antennas, FSSs and additive manufacturing of smart antennas and FSS designs over the years. The review starts with the advancements in the research and the most frequently reported frequency reconfigurable antennas and designs. A variety of bandpass and bandstop frequency selective surfaces are also reviewed. A number of traditional and modern additive manufacturing techniques are also presented within this chapter.

Chapter 3 demonstrates the development of frequency reconfigurable antennas using close-coupled biasing technique for smart Alternating Current (AC) sensing applications. This chapter presents a novel approach for sensing application for the reconfigurable antenna in a smart and novel Alternating Current Sensing system. Inexpensive PIN diodes are deployed to realise the frequency reconfigurability with the help of slot antenna designs. Close-coupled biasing technique was presented for smart antennas for the first time. The design solutions were able to switch and tune between several frequencies and covered a wide range of frequency bands of interest. The low-cost designing on flexible substrates provided a solution for the development of designs for wireless communications and sensor applications. The tunable antenna is deployed in a novel smart current sensing system that detects the currents which are passing through the wire of a typical household appliance and can transmit the data over Bluetooth.

Chapter 4 presents a reusable solution and the manufacturing considerations that went into developing frequency reconfigurable antenna aperture using low-cost inkjet printing technique. Inkjet printing finds particular interest for its simplicity and rapid prototyping and in developing electronics and antennas on foldable substrates such as photo-paper and PET. This novel solution presents a single-layer aperture of two rectangular patches that are printed using conductive ink filled in refillable cartridges on PET substrate at a small distance apart from one another, effectively creating a slot of infinite length between them. Active RF components are mounted on the proposed aperture to create a complimentary dipole antenna. Two operations of frequency-switching and frequency-tuning are described using the same antenna aperture. Low-cost Inkjet printing of the proposed aperture provides a low-cost, environment friendly commercially available solution that can produce designs at a rapid rate with reliable performances and consistent electronic attributes.

Chapter 5 presents the additive manufacturing of Bandstop FSS wallpapers using low-cost inkjet printing for microwave and sub millimetre wave frequency shielding applications. Two distinct methods are presented for the low-cost fabrication of Bandstop FSS. In the first method, two bandstop FSS wallpapers are inkjet-printed using the household Inkjet printer discussed in Chapter 4. The designs were printed on the raisin coated photo paper

to operate in the frequency bands of 2.4 GHz and 24 GHz, respectively. The wallpapers can be mounted inside an enclosed ambience to improve the signal strengths of 4G and 5G networks and decrease the signal drop due to the absorption of signals by walls, roofs, and other construction materials. The second part of this chapter demonstrates the development of a novel open-source 3D printer system that can simultaneously deposit the filament-based substrate as well as the conductive ink to develop a fully 3D printed microwave bandstop FSS structure of square-loop elements. The printer system was developed in collaboration with an on-site team of researchers at University of Kent and the development of the FSS using the low-cost open-source printer is presented for the first time. A standard Fused Filament Fabrication (FFF) printer was modified and calibrated and the extension components were 3D printed to mount the two extruders that could print the filament and the ink without a need for any additional curing methods.

Chapter 6 presents the Aerosol Jet Printing of FSS designs using Aerosol Jet printing. The industry grade expensive equipment was accessed at Centre for Process Innovation, Durham, U.K. The state-of-the-art machine was deployed to manufacture Bandstop and Bandpass FSS structures. Bandstop FSS were developed for WLAN, 4G and 5G frequency shielding applications with the help of microwave and sub-millimetre wave designs comprising of square loop elements. The designs operate at 2.5 GHz and 27.5 GHz, respectively covering the 2.4 GHz and 26-28 GHz bands. The designs were printed directly onto the substrate using Aerosol Jet Printer and fabrication was done on Corning eagle glass as well as on flexible Kapton. The designs demonstrated exemplary performances and worked perfectly well for various angle of incidence responses. The second segment of this chapter introduces the novel fabrication of mm wave and low-THz Bandpass slot FSS designs. These designs pushed and tested the precision limits of the Aerosol Jet machines. Several reiterations were completed to get the precise designs. The designs required the micrometre-level precision that an Aerosol Jet can provide, and strategic toolpaths were developed to create the required designs to form in the shape of slot arrays. Two designs of slot Bandpass FSS were presented that resonated at 125 GHz and 280 GHz, respectively. The bandpass designs operated in wideband millimetre wave regions and the measured transmission responses corresponded well with the simulated responses. The

designs find application with sensing, space communications, counter terrorism systems, and especially with the Beyond 5G and the imminent 6G systems. Using flexible Kapton substrates also allows the options to make the designs flexible and foldable in nature and they can be deployed for space systems owing to the Kapton's high temperature tolerance.

Finally, Chapter 7 concludes with a summary of the findings in chapters and provides the concluding remarks for the work conducted and the scope for further development of the work in the future.

The primary objectives of the work presented through this research are:

1. Development of frequency reconfigurable antennas for smart sensing applications
2. Development of a novel low-cost inkjet-printed frequency reconfigurable antenna solution that can be used in switching and tuning configurations
3. Additive manufacturing of FSS wallpaper reflectors using low-cost inkjet printing on paper substrate to enhance the 4G and 5G signal strength in an indoor environment
4. Additive manufacturing of a fully 3D printed bandstop FSS with the help of a novel modified low-cost open-source printer with dual extrusion feature
5. Additive manufacturing of bandstop FSS structures for microwave and sub mm-wave applications on transparent substrates using industry-grade Aerosol Jet printing technology
6. Additive manufacturing of novel bandpass FSS structures for millimetre wave and low-THz applications using industry-grade Aerosol Jet printing technology

The primary contributions that were made through the course of this research are listed below. These contributions are complemented and supplemented by the list of publications which is presented in Section 1.3. The main contributions are:

1. Developing and utilising a frequency reconfigurable antenna with close-coupled biasing technique for smart sensing and smart metering applications. The antenna can be directly integrated as a novel sensing system to detect the current passing

through the wire of a domestic appliance. The antenna is also useful in detecting the current through the first mode and transmitting through the second mode.

2. Additive manufacturing of a novel, low-cost inkjet-printed reconfigurable antenna design solution which can be modified as a switching antenna or a tuning antenna by rearranging the RF components. The manufacturing aspects and considerations are also presented which can facilitate the development of such antennas in the future.
3. Inkjet printing of wallpaper posters printed on paper using low-cost household inkjet printers are presented for RF shielding and signal strength enhancement of 4G and 5G networks. A low-cost wallpaper for 5G applications is presented for the first time that demonstrated the testing of the limits of the low-cost inkjet printers.
4. A novel full 3D printing of a microwave FSS array using a low-cost open-source printer that was modified to extrude the plastic-based PLA filament and the conductive ink simultaneously. The thickness of the PLA substrate as well as permittivity can be altered which is a useful alternative to design structures with specific requirements.
5. Additive manufacturing of FSS structures for microwave, millimetre wave and low-THz applications using the industry-grade Aerosol Jet printing is introduced for the first time. The extreme precious of Aerosol Jet machine offered the fabrication of intricate designs with reliable accuracy. Direct, single-step 3D printing Bandstop FSS designs for sub mm-wave filtering on transparent substrates was presented for the first time. Additive manufacturing of Bandpass slot FSS arrays for millimetre wave and low-THz applications are introduced which tested the fabrication capabilities of Aerosol Jet printers to their limits.

All the antennas and Frequency Selective structures presented in this thesis were simulated using CST Microwave Studio™ software. The fabrication of these designs was realised with a number of additive manufacturing machine such as the low-cost household inkjet printer, open-source Fused Filament Fabrication (FFF) based 3D printer and Optomec© Aerosol Jet Printers.

1.3. List of Publications

Publications arising from this work:

1. **A. Shastri**, B. Sanz-Izquierdo, E. Elibiary, E. A. Parker, "Manufacturing Development and Constraints in full 3D Printing of Frequency Selective Surface using Low-Cost Open-Source Printer", in *IEEE Transactions on Components, Packaging and Manufacturing Technology*, 2021 (**Accepted**)
2. **A. Shastri**, B. Sanz-Izquierdo, S. Gao, "Manufacturing Considerations for the Development of Reconfigurable Antennas using Inexpensive Inkjet Printing", in *IEEE Transactions on Components, Packaging and Manufacturing Technology*, 2021 (**Under Minor Revision**)
3. **A. Shastri**, I. Ullah and B. Sanz-Izquierdo, "Alternating Current Sensing Slot Antenna," in *IEEE Sensors Journal*, vol. 21, no. 7, pp. 9484-9491, 1 April1, 2021, doi: 10.1109/JSEN.2021.3055639.
4. **A. Shastri**, B. Sanz-Izquierdo, E. A. Parker, S. Gao, P Reynaert, Z. Chen, L. Winchester, "3D Printing of Millimetre Wave and Low-Terahertz Frequency Selective Surfaces Using Aerosol Jet Technology," in *IEEE Access*, vol. 8, pp. 177341-177350, 2020, doi: 10.1109/ACCESS.2020.3024584.
5. **A. Shastri**, P. Njogu, B. Sanz-Izquierdo, S. Gao and Z. Chen, "Low-cost Inkjet Printed Paper Poster FSS for 5G Applications," *2021 15th European Conference on Antennas and Propagation (EuCAP)*, 2021, pp. 1-4, doi: 10.23919/EuCAP51087.2021.9411448.
6. **A. Shastri**, K. Putta, B. S. Izquierdo, E. A. Parker, S. Gao, L. Winchester, A McCelland, "Evaluation of Aerosol Jet Printing of Frequency Selective Surface on Glass for Building and RF Applications," *2020 14th European Conference on Antennas and Propagation (EuCAP)*, Copenhagen, Denmark, 2020, pp. 1-5, doi: 10.23919/EuCAP48036.2020.9135346.
7. **A. Shastri**, M. Sobhy, and B. Sanz-Izquierdo, "A comparative study of the harvested wireless power using multiple antenna designs implemented in a

common domestic environment," *2019 IEEE-APS Topical Conference on Antennas and Propagation in Wireless Communications (APWC)*, Granada, Spain, 2019.

8. **A. Shastri**, B. Sanz-Izquierdo, D. Atkins, and A. McClelland, "Frequency Reconfigurable Double-sided Slot Antenna Using Close-coupled Biasing Technique," *2018 8th IEEE India International Conference on Power Electronics (IICPE)*, Jaipur, India, 2018.
9. **A. Shastri**, B. Sanz-Izquierdo, S. Gao, D. Atkins, and A. McClelland, "Switchable slot antenna using close-coupled biasing technique," *2017 International Conference on Electromagnetics in Advanced Applications (ICEAA)*, Verona, Italy, 2017.

Other Publications:

1. P. Njogu, P. Jablonski, **A. Shastri** and B. Sanz-Izquierdo, "Origami Boat Sensing Antenna," *2021 15th European Conference on Antennas and Propagation (EuCAP)*, 2021, pp. 1-5, doi: 10.23919/EuCAP51087.2021.9411024.
2. T. E. A. Alharbi, **A. Shastri**, O. A. Alzahrani and B. Sanz-Izquierdo, "Evaluation of a wideband monopole antenna with tunable stop notches," *Antennas and Propagation Conference 2019 (APC-2019)*, Birmingham, UK, 2019, pp. 1-4, doi: 10.1049/cp.2019.0732.
3. S. Y. Jun, **A. Shastri**, B. Sanz-Izquierdo, D. Bird, and A. McClelland, "Investigation of Antennas Integrated Into Disposable Unmanned Aerial Vehicles," *IEEE Transactions on Vehicular Technology*, vol. 68, no. 1, pp. 604–612, 2019.
4. S. Jun, **A. Shastri**, B. Sanz-Izquierdo and A. McClelland, "Inkjet Printed Dual-Band Origami Frog Antenna", *2017 IEEE International Symposium on Antennas and Propagation (APSURSI)*, San Diego, California, USA, 2017.

1.4. Awards and nominations

1. **WINNER**, "International Young Scientist Award" in Electronics Engineering *World Teachers' Day Awards & Appreciations Conferring Ceremony* from *Research Education Talks Daily International (REd)* on Oct 5th, 2020.
2. **NOMINATION, "**Best Young Researcher Award (Male) (Below 40 years) (Overseas)", *2nd International Academic and Research Excellence Awards (IARE) 2020 - An initiative by GISR Foundation* held on Oct 3rd, 2020.

1.5. List of Seminars and Webinar Lectures

1. "Advantages and Challenges with Additive Manufacturing of Electromagnetic Structures" Webinar for IEEE Telewebinar hosted by Universidad Politecnica Salesiana, Cuenca Ecuador on May 20th, 2020.
2. "Not so expert in Coronavirus: 5G Towers and Coronavirus" Webinar for Kent Business School hosted by *KBS Not So Expert,* University of Kent on May 15th, 2020.
3. "3D Printing and How it Can Help in Developing Modern Antenna Designs and Structures" Webinar for IEEE ComSoc hosted by Universidad Politecnica Salesiana, Cuenca, Ecuador on May 13th, 2020.
4. "Ambient Energy Harvesting and Wireless power Transfer: for Today and Tomorrow", Guest Lecture at Banasthali Vidyapith, Banasthali, India on January 8th, 2019.

References

[1] J. Bernhard, Reconfigurable antennas, 1st ed. San Rafael, Calif: Morgan & Claypool Publishers, 2007.

[2] C. G. Christodoulou, Y. Tawk, S. A. Lane and S. R. Erwin, "Reconfigurable Antennas for Wireless and Space Applications," in *Proceedings of the IEEE*, vol. 100, no. 7, pp. 2250-2261, July 2012, doi: 10.1109/JPROC.2012.2188249.

[3] M. A. Matin, Wideband, "Multiband, and smart reconfigurable antennas for modern wireless communications". *Hershey, PA: Information Science Reference*, 2016.

[4] B. A. Munk, *Frequency selective surfaces: theory and design*. New York: John Wiley, 2000.

[5] I. Gibson, D. W. Rosen, B. Stucker, Additive manufacturing technologies, Springer, 2010.

[6] H. Lipson and M. Kurman, *Fabricated: The new world of 3D printing*, Indianapolis: John Wiley & Sons, Inc., 2013

[7] E. Macdonald *et al*., "3D Printing for the Rapid Prototyping of Structural Electronics," in *IEEE Access*, vol. 2, pp. 234-242, Dec. 2014, doi: 10.1109/ACCESS.2014.2311810.

[8] F. Calignano *et al*., "Overview on Additive Manufacturing Technologies," in *Proceedings of the IEEE*, vol. 105, no. 4, pp. 593-612, April 2017, doi: 10.1109/JPROC.2016.2625098.

[9] N. S. A. Bakar, M. R. Alkahari and H. Boejang, "Analysis on fused deposition modelling performance", *J. Zhejiang Univ.-Sci. A*, vol. 11, no. 12, pp. 972-977, Dec. 2010.

[10] B. Zhang *et al*., "Metallic 3-D Printed Antennas for Millimeter- and Submillimeter Wave Applications," in *IEEE Transactions on Terahertz Science and Technology*, vol. 6, no. 4, pp. 592-600, July 2016, doi: 10.1109/TTHZ.2016.2562508.

[11] R. B. Wicker and E. W. MacDonald, "Multi-material multi-technology stereo-lithography", *Virtual Phys. Prototyping*, vol. 7, no. 3, pp. 181-194, 2012.

[12] B. S. Cook and A. Shamim, "Inkjet Printing of Novel Wideband and High Gain Antennas on Low-Cost Paper Substrate," in *IEEE Transactions on Antennas and Propagation*, vol. 60, no. 9, pp. 4148-4156, Sept. 2012, doi: 10.1109/TAP.2012.2207079.

[13] J. A. Paulsen, M. Renn, K. Christenson and R. Plourde, "Printing conformal electronics on 3D structures with Aerosol Jet technology," *2012 Future of Instrumentation International Workshop (FIIW) Proceedings*, Gatlinburg, TN, 2012, pp. 1-4, doi: 10.1109/FIIW.2012.6378343.

[14] "The global additive manufacturing market accounts for $ 9.3 billion in 2018 - 3Dnatives", *3Dnatives*, 2018. [Online]. Available: https://www.3dnatives.com/en/additive-manufacturing-market-billions-2018-201220185/. [Accessed: 16- May- 2020].

CHAPTER 2

LITERATURE REVIEW AND THEORETICAL BACKGROUND

2.1 Introduction

This chapter reviews the existing literature on the advancements over the years to provide a background and basis for this research. The literature background primarily focuses on frequency reconfigurable antennas, frequency selective surfaces, traditional fabrications methods and additive manufacturing (AM) or 3D printing and their implementations using various machines. A variety of antenna designs are reviewed which are implemented to realise frequency reconfigurability [1]. Developing designs using traditional subtractive manufacturing methods such as etching provides a standard, cost-efficient fabrication method on substrates that are readily available in the market. With their durability, consistency and variety in thicknesses, substrates suitable for etching provide the liberty to develop design that may be both single sides as well as double sided in nature. Flexible and foldable designs can also be created using significantly thinner substrates.

Traditional methods have been in use for decades but with the recent expansions and advancements of additive manufacturing machines and 3D printers with extreme precisions, manufacturing prototypes of various designs at a rapid rate has become substantially simpler [2]. Complex and precise 3D models, antennas and circuitries can be printed in a fast, cost-economical way whilst providing a significantly greater degree of freedom in designing in comparison to the traditional techniques. 3D printing breaks a design down into several layers and deposits the conductive material layer-by-layer. Several technologies are discussed such as inkjet printing, Fused Deposition Modelling (FDM), Aerosol Jet Printing etc.

An introduction to smart and frequency reconfigurable antennas are presented in Section 2.2. Frequency selective surfaces and the advancements with their applications for various applications are reviewed in Section 2.3. Section 2.4 puts light on the recent advancements in the additive manufacturing of electromagnetic structures where the additive manufacturing of antennas and frequency selective surfaces is reviewed. Section 2.5 covers the theoretical background which acts as the essential prelude to the subsequent chapters of this thesis.

2.2 Smart and Reconfigurable Antennas

2.2.1 Smart Antennas

Smart Antennas are antenna arrays, also referred to as multiple antennas or adaptive-array antennas and are beneficial in increasing the system efficiency of wireless networks. These antenna arrays are used in combination with Digital-Signal-Processing (DSP) algorithms that ease the tracking and location of wireless devices such as mobiles [3].

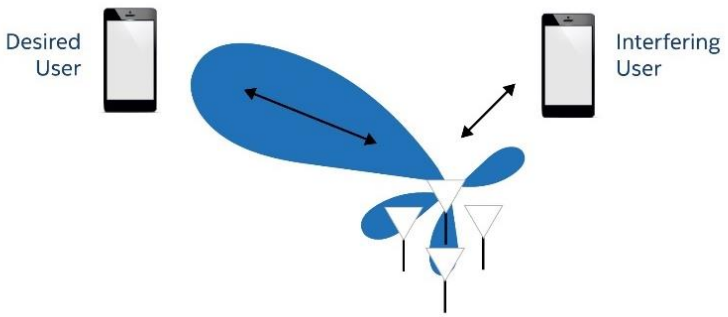

Fig. 2.1 Functioning of smart antennas [4]

2.2.2 Frequency Reconfigurable Antennas

Frequency reconfigurable antennas are antennas that can actively alter their frequency of operation and radiation patterns in a controllable and adjustable way [1], [5].

Reconfigurable antennas differ from smart antennas because of their reconfiguration mechanism. The reconfiguration mechanism is typically incorporated within the reconfigurable antenna design while smart antenna relies on beamforming networks that are supplied externally [1], [3]. Over the past five decades, wireless transmission and sensing structures have undergone unimaginable growth and development. A number of antenna design variants have been conceptualised, realised and deployed in the wireless transmission and radar structures. Reconfigurable antennas do not just change their frequency of operation but their impedance, transmission bandwidths, polarities and radiation pattern responses change individually to have a capability for shifting operational conditions [5]. One of the earliest recorded available account of reconfigurable antenna dates to 1981 [6] where a reconfigurable microstrip patch antenna design was proposed.

Patch antennas are an attractive alternative for the designing of frequency reconfigurable antennas. The prospect of being able to make patch antenna designs smaller in size make them an alluring option for several applications. The miniaturization of a patch is typically realised by optimising the geometry of the metallic patch. Microstrip patch-based frequency reconfigurable antennas have since been widely reported over the years [6] – [28]. Microstrip patch antenna using switchable slots was proposed in [7] for circular polarization diversity. A wideband bow-tie patch antenna was proposed in [8] while a circular microstrip reconfigurable antenna was proposed in [9]. 3D cubic antenna is proposed in [10] which can be seen in Fig. 2.2. A circular-polarized crossed-Yagi reconfigurable patch antenna is reported in [11]. The structure of the proposed antenna can be seen in Fig. 2.3. The Miniaturized antenna for reconfigurability was reported in [12] where miniaturization was typically realised by optimising the geometry of the pixelated metallic patch. The bands of operation were 2.2 GHz - 2.6 GHz and 3 GHz - 4.2 GHz, respectively. Aeroflex MGV-100-25 hyper abrupt varactor diode was deployed, and the affective capacitance value was varied was varied from 0.2 pF to 5 pF to achieve the tuning operation.

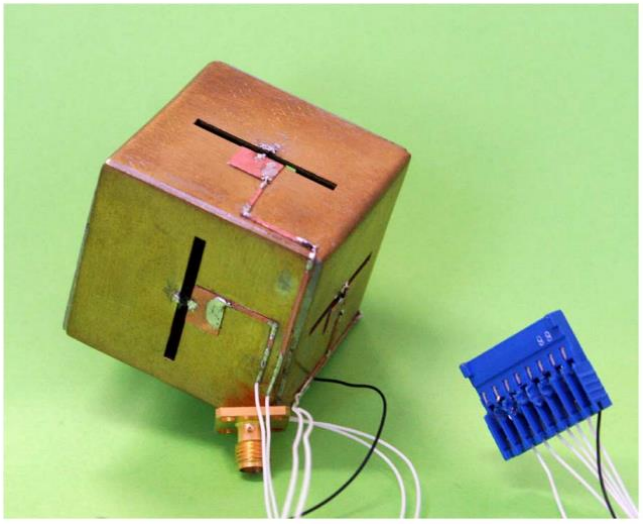

Fig. 2.2 A pattern reconfigurable cubic slot antenna [10]

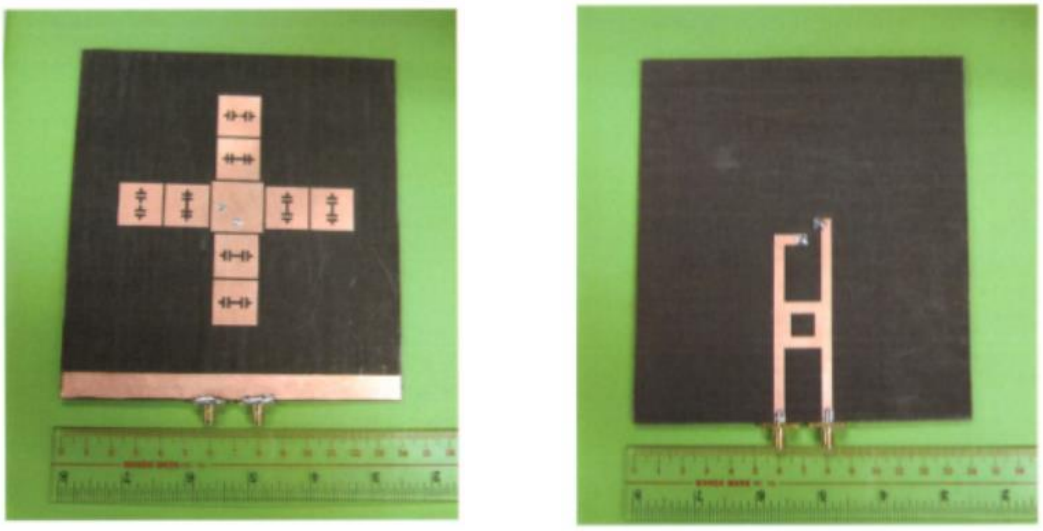

(a) (b)

Fig. 2.3 Circular polarised reconfigurable Crossed-Yagi Patch antenna (a) top view and (b) bottom view [11]

Radio Frequency Micro Electro-Mechanical Systems (MEMS) based designs have also become popular recently with a wide range of frequency reconfigurability prospects being explored in [13] – [17] using MEMS over the past two decades. MEMS have been deployed as frequency switches [13], [14] to MEMS based tunable patch antennas [15], antenna for MIMO communication [16] and slot antennas [17]. Frequency

reconfigurability can also be realised by mechanical means with reconfigurable rolled antenna and rotatable antennas reported in [18] and [19] respectively. Changing the characteristics is another way using which frequency reconfigurable antennas can be produced. Two such methods are reported in [20] and [21] where reconfigurable resonator antenna on colloidal dispersions is reported in [20] and microstrip antenna on ferrite substrate is proposed in [21]. Field-programmable gate array (FPGA) IC controlled frequency switching antenna is proposed in [22]. Mechanical means of reconfigurability are not particularly popular among researchers due to their lack of repeatability and reliability.

Numerous designs mentioned above have successfully implemented RF MEMS to reconfigure their frequency performances which depend upon the mechanical movement of their little switches as an alternative to electronically varying the input voltage to accomplish the desired frequency reconfiguration. However, PIN diodes are characteristically swifter and are a significantly more efficient alternative to RF-MEMS. PIN diodes also tend to be among the lower cost solutions and can be implemented in combination with conventional etching techniques as well as with the present-day additive manufacturing fabrication techniques. Diodes can facilitate both switching and tuning operations of frequency in reconfigurable antennas with the help of changing the frequency of operation caused by the variations in the input voltage [23] – [35].

Frequency switchable slot antennas have been widely reported in the literature [23] – [29]. One of the earliest descriptions of switchable antennas can be observed in [24], where varactor diodes are combined with transverse microstrip fed slot antenna to switch between frequencies. Further frequency switching is reported to be achieved by shorting the effective length of the slot with the help of PIN diodes. The base designs for the designs vary from being straight lines [25] to bent lines [26] to consisting of slot rings [27] and annular slot shapes [28], [29].

Tuning slot antennas can be realised by changing of the reactance of the slots by implementing active components within the design. One of the initial accounts in this area is described in [30] where a slot antenna of λ wavelength in length is electronically tuned with the use of reactive Field-Effect Transistors (FET). By changing the bias voltage, the

reactance of FETs is varied which in turn changed the effective length of the slot and its operational frequency. A novel PIFA-type tuning U-slot antenna was proposed in [31]. Similar procedure can be realised by using varactor diodes [32] – [35]. In [32], a dual-band design that is able to tune from 1.8 GHz to 1.95 GHz in the first band and from 2.15 GHz to 3.22 GHz in the second band with A frequency ratio between 1.08 – 1.49 with the help of varactor diodes with effective capacitance range of 0.5 pF – 2.2 pF. In [33], a similar implementation tunes from 1.36 GHz -1.52 GHz in the first resonant and 2.12 GHz– 2.63 GHz in the second resonant with a frequency ratio of 1.56 – 1.73. In [34], a singular and dual-polarised slot-ring antennas are reported that cover a frequency ratio between 1.73 – 1.89 where the single-polarized antenna deploys two varactor diodes whereas the dual-polarized antenna uses four varactors. A substrate integrated varactor-tuned dumbbell shaped slot antenna is presented in [35] which had a tuning frequency ratio of 1.38.

Most reconfigurable slot antennas make use of a combination of bias circuit and vias connecting the top layer containing and bottom layer for double layer structures [24], [25], [27], [28], [32], [33]. Some designs require the development of additional circuitry such as matching stubs [28] or an additional filter [32]. In other cases, such as [27], wires are connected to the components directly which can cause interference with the radiation pattern and are not practical for real life applications.

The slot antenna consists of a radiator formed by cutting a narrow slot in a large metal surface [1], [5]. The slot length is a $\frac{\lambda}{2}$ wavelength at the desired frequency and the width is a small fraction of a wavelength. The antenna is frequently compared to a conventional half-wave dipole consisting of two flat metal strips. The slot antenna is compared to its complementary dipole to illustrate that the radiation patterns produced by a slot antenna cut into an infinitely large metal sheet and that of the complementary dipole antenna are the same. If the slot antenna is superimposed onto its complementary dipole antenna structure, one would obtain an infinite conducting plane. Several important differences exist between the slot antenna and its complementary antenna. First, the electric and magnetic fields are interchanged. In the case of the dipole antenna, the electric lines are horizontal while the magnetic lines form loops in the vertical plane. With the slot antenna, the magnetic lines are horizontal, and the electric lines are vertical. The electric

lines are built up across the narrow dimensions of the slot. As a result, the polarization of the radiation produced by a horizontal slot is vertical. If a vertical slot is used, the polarization is horizontal. A second difference between the slot antenna and its complementary dipole is that the direction of the lines of electric and magnetic force abruptly reverse from one side of the metal sheet to the other. In the case of the dipole, the electric lines have the same general direction while the magnetic lines form continuous closed loops. When energy is applied to the slot antenna, currents flow in the metal sheet. These currents are not confined to the edges of the slot but rather spread out over the sheet. Radiation then takes place from both sides of the sheet. In the case of the complementary dipole, however, the currents are more confined; so, a much greater magnitude of current is required to produce a given power output using the dipole antenna. The theory called Babinet's principle [5] states that employing certain symmetry in Maxwell's equations and realizing the complementary nature of the two complimentary structures, it can be shown that the fields of a slot antenna and that of a complementary dipole antenna are related to each other in a simple manner. the various transmit/receive characteristics, such as the pattern, gain, and input impedance of the two complementary antennas. According to Babinet's principle, the fields produced by a slot antenna can be obtained directly from the corresponding complementary strip dipole antenna.

Slot antennas are employed usually at the frequency range of 300 MHz and 24 GHz. The slot antennas are in demand because they can be etched or fabricated out of whatever surface they are to be mounted on and have radiation patterns that are roughly omnidirectional for most of its designs. It needs to be noted that a voltage source is applied across the short end of the slot antenna which induces an E-field within the slot, and currents that move around the length and the breath of the slot, both contributed to radiation. The dual antenna has a number of similarities with a dipole antenna. The voltage source is applied at the centre of the dipole, so that the voltage source is rotated.

Rather than a $\frac{\lambda}{2}$ wavelength of centre-fed wire in free space making up a dipole antenna, a dipole slot antenna is usually $\frac{\lambda}{2}$ wavelength long slot in a large ground plane. It can be fed

in a number of ways. One frequently used method is to place slots in a waveguide. With the correct placement and gaps in between slots, an array of slots can act as a directional and effective antenna. Or it may be a slot in the ground plane on a PCB with the signal fed to the centre edges, often a bit off centre to match impedances.

These antennas can be suitable because they can all be designed in significantly smaller sizes using substrate having thickness in microns and can still obtain very good output matching at the desired frequency.

2.3 Frequency Selective Surfaces

2.3.1 Introduction to Frequency Selective Structures and Applications

Frequency Selective Surfaces or FSSs are electromagnetic filtering screens that demonstrate a variety of transmission or reflection characteristics as a function of the frequency. Typically, any surface which cannot be deemed to be completely flat and not a thoroughly conductive surface can play a role of an FSS. There are two rudimentary types of FSS arrays: arrays that are made of slots and arrays comprising of dipoles [36], [37]. Resonant dipole array performs a Bandstop filtering response which allows the electromagnetic waves above and below the resonant frequency of the dipole to pass but blocks the waves at the resonant frequency. Complementary slot arrays perform what is commonly known as Bandpass filtering response that allows the Electromagnetic waves at the resonant frequency to pass but reflect or block them at the frequency bands lower and higher to the resonant frequency band. In terms of equivalent circuit models, the dipoles in bandstop filter FSSs act as a series equivalent circuit model whereas the slots in bandpass FSSs operate as a parallel equivalent circuit model. A typical layout of the standard FSS designs and their equivalent circuit models can be seen in Fig. 2.4.

FSSs find a wide range of applications in various fields [37]. FSSs can be installed in and as radome designs with the help of simplistic designing equations [38], thin-layer microwave frequency absorbers [39] which was reported three decades ago dating back to 1989 where they have also referred to the works that were publish in 1970s with recent

developments in frequency scanned antennas for beam switching and steering applications in [40] – [43].

Single-layered cylindrical FSS structure made up of strip dipoles are presented with PIN diodes to switch the beams in [40] where the steering is realized by altering the characteristics of GMP-4201 PIN diode. A complementary structure of cylindrical FSS made up of slot arrays is reported in [41] where a monopole antenna along with the active cylindrical slot FSS structure create a system that can switch between opaque and transparent states of the FSS. A standard BAR64-02 diode was deployed to switch between the states. A planar collinear array with cylindrical FSS array is also reported in [42]. Electromagnetic-bandgap (EBG) sub-array design for base station application is proposed in [43]. Figure 2.5 depicts some reported FSS unit cells. Their names are also given.

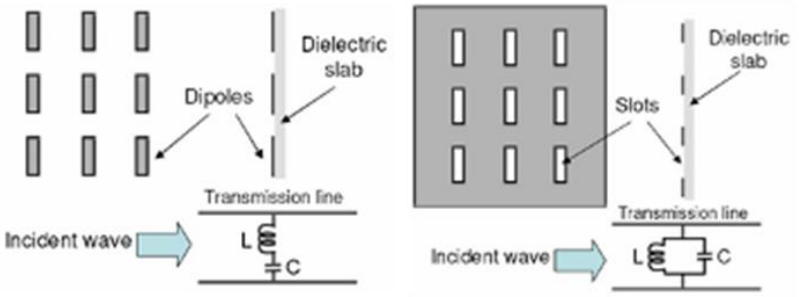

(a)

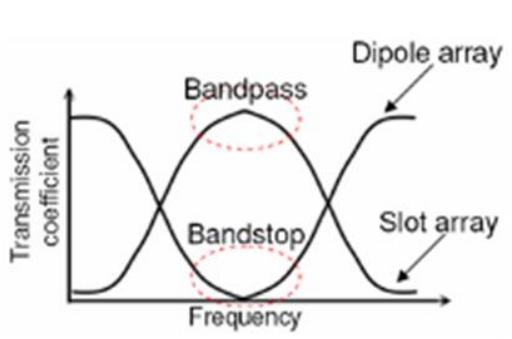

(b)

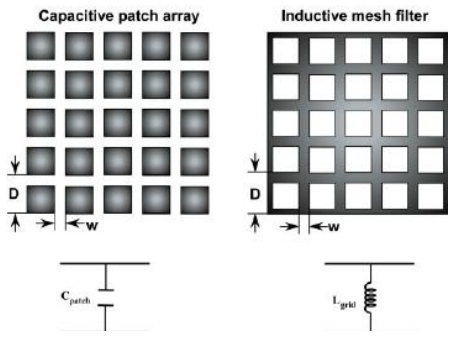

(c)

Fig. 2.4 A typical fundamental FSS model of bandpass and bandstop FSS structures in (a), Transmission coefficient for the two FSSs in (b) and capacitive patch array and inductive mesh filters in (c) [36]

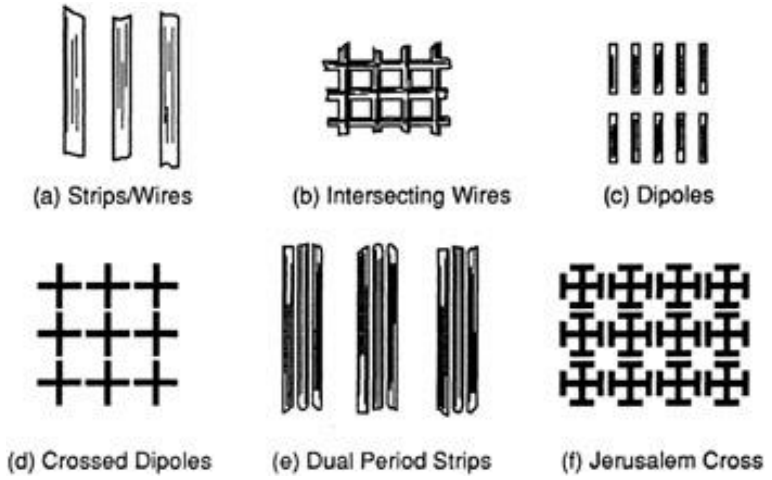

Fig. 2.5 A variety of FSS unit cells structures with their given names [37]

A number of contemporary, cutting-edge applications such as efficient wireless communications [44], THz remote sensing for earth observations [45], defence communication systems [46], smart satellite communications [47], terrestrial networks [48], gyromultipliers [49] and 5G technologies [50]. Use of active Frequency Selective Surfaces (AFSS) depicted for reconfigurability with tuning applications widely reported in [51] – [53]. Tunable FSS using arrays of slots [51] and split ring resonators [53] can tune the FSS structure to operate at different frequencies in various states. Split ring resonator design can be seen in Fig. 2.6. All the applications mentioned above make use of a selection of FSS designs and configurations to execute their expected implementations.

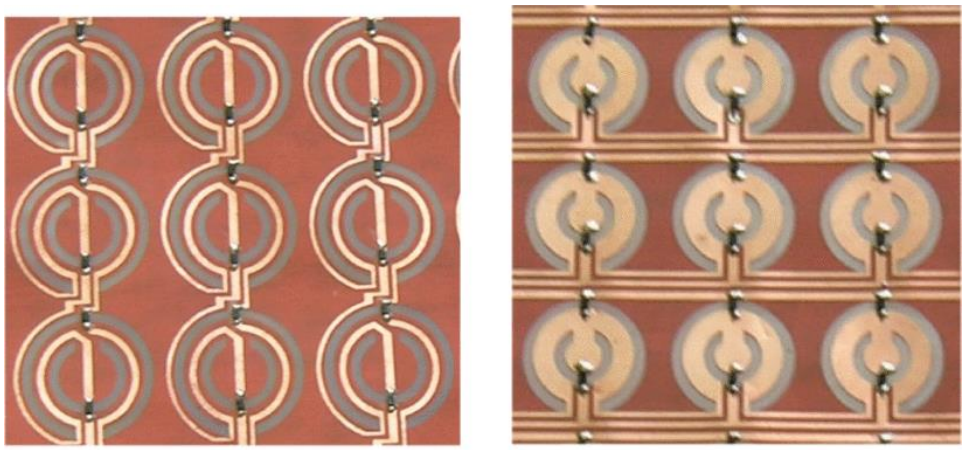

Fig. 2.6 Split ring resonator FSS array for (a) Switching and (b) tuning [53]

2.3.2 Application of FSS in Radio Frequency Shielding

Ambient RF and microwave signals constantly witness a drop in signal within a typical indoor environment or a sudden loss of signal as the receiver moves to an indoor or underground location. The signal loss happens owing to the reflections and transmission of the incident signals through the rigid materials used in buildings and structures. The magnitude of signal dispersion and losses hinges upon the dielectric properties, conductivity, composition, and the periodicity of the raw materials used. These parameters are now becoming an integral part of the electromagnetic architecture of a building. FSS can act as frequency shields and frequency reflectors to significantly improve the coverage within a defined area by reflecting certain signals back within the given areas in the house or building while allowing for some necessary mobile signals to pass through for elementary communications for mobile and emergency situations. An example of an anchor shaped Bandstop FSS design can be seen in Fig. 2.7 [54].

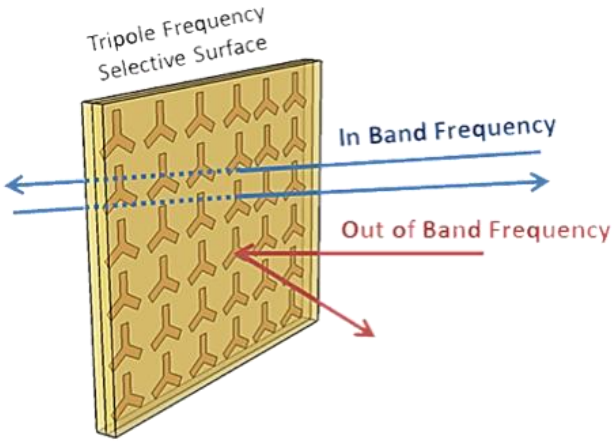

Fig. 2.7 Representative figure of an anchor shaped Bandstop FSS [54]

Passive FSS structures or bandstop FSS structures have often been proposed as a solution to minimize and reduce the drop in signals. Installation of FSS structures within windows and walls of an indoor environment have been repeatedly proposed in [55] – [63] where FSS structures are deployed within windows [55] – [58] and walls [59] – [63] to diminish

the loss of signals. In [61], a layer of transparent material is used as the shielding FSS that can be seen in Fig. 2.8.

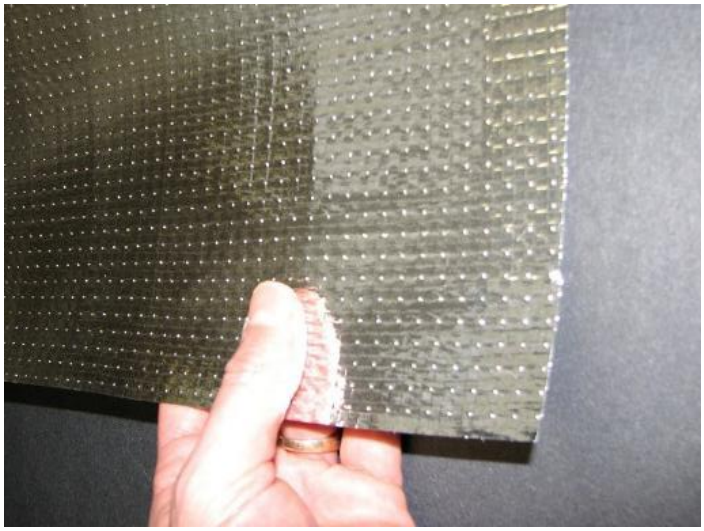

Fig. 2.8 RF Shielding surface for walls [61]

The FSS shield is created by directly grinding on top of the coating layer of an energy saving glass in [62]. A convoluted square-loop FSS array structure is screen printed on polyethylene terephthalate (PET) substrate and is then affixed to glass for shielding in [63]. The FSS structures are fabricated using a variety of techniques which will be discussed separately in the coming section.

2.3.3 Application of FSS in Mobile Communications

Active FSS designs operate as FSS antenna arrays and can be used for beam switching and steering applications along with improving the directivity of the transmitted signals. Some FSS used in mobile communication have already been discussed from [40] – [43] and [51] – [54]. The active FSS designs can be deployed to create Intelligent Reflective Surfaces (IRS), which can also be referred to as metasurfaces. IRS as the name implies, are controllable smart surfaces that can control and adjust the way an incident signal is reflected. They are also referred to as software-controlled metasurfaces [64] and reconfigurable intelligent surfaces [65]. Wireless communication using IRS has garnered

significant interest since the rollout of the white paper on Beyond 5G [66] and 6G technologies [67] by companies such as Samsung. These papers highlight the need to develop surfaces to improve the signal quality along with developing reflective surfaces that can minimise the signal drop since the white papers refer to the use of terahertz technologies to bring the technologies to reality. The use of terahertz technologies implies the use of millimetre wavelength frequencies. The frequencies have the potential to penetrate through surfaces and therefore, the need for IRS and millimetre-wave reflective structures will be at the core of the development of Beyond 5G and 6G communication technologies [68]. A typical IRS or metasurfaces architecture and functioning is depicted in Fig. 2.9. The designing, fabrication, installation, and measurements pose a challenge within themselves.

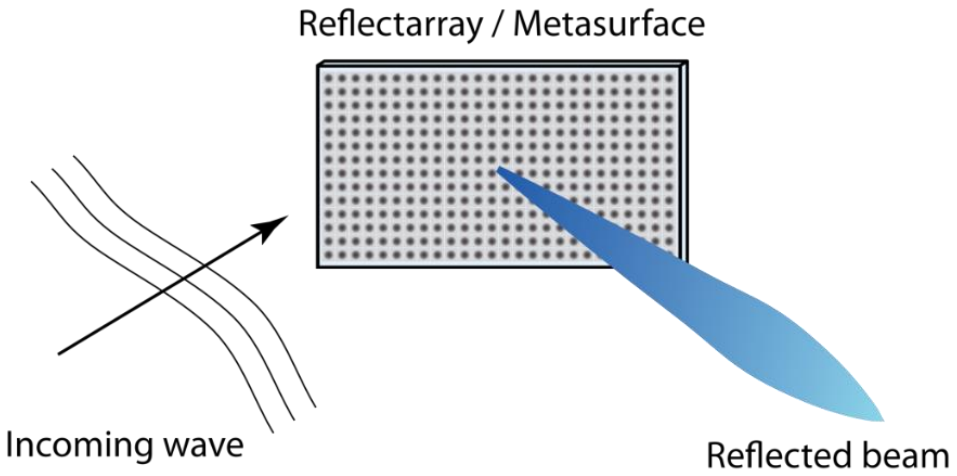

Fig. 2.9 A typical IRS/metasurfaces structure and functioning [68]

2.4 Additive Manufacturing of Electromagnetic Structures

2.4.1 Additive Manufacturing of Antennas

Printable electronics has progressively become one of the fastest emerging field of interest of modern-day electronics manufacturing with its salient features of rapid prototyping and custom-made designs [69]. With the enhanced requirements in the applications of electronic devices and structures, a rapid growth is witnessed in the field of printable electromagnetic structures. Additive manufacturing (AM) which is generally referred to as 3D printing, is a method of producing electronics and other 3D digital designs by adding

them onto substrate layer-by-layer [70]. Additive manufacturing presents numerous environmental, economic, as well as technical benefits to the traditional fabrication techniques such as etching and electroplating. The reduction in the wastage of material remains the first and the foremost among the benefits. The ability to develop rapid prototypes, fabrication of a variety of substrates, cost efficiency, designing and printing without the use of any masks and repeatability of the process make them highly desirable. Printed antennas and electromagnetic structures can be fabricated using a variety of additive manufacturing techniques.

Antennas and conductive structures are key elements of electronics and numerous AM methods have been considered for the fabrication and development of antennas and radio frequency devices. Antennas have been fabricated using a combination of popular AM techniques. Techniques such as inkjet printing [71], Fused Deposition Modelling (FDM) [72], Fused Filament Fabrication (FFF) [73], stereolithography (SLA) [74] and Selective Laser Melting (SLM) [75] have been reported for the development of antennas.

A variety of antenna designs have been realised using the existing techniques. Designs ranging from patch antenna fabricated using a combination of SLA and Inkjet-printing [76], fractal antennas using binder jet AM technique in [77], MIMO antennas with [78] (shown in Fig. 2.10), mm-wave Fabry-Perot resonator antennas (FPRAs) using binder jetting in [79], 3D WLAN antennas using Aerosol Jet printing and electroplating in [80], and inkjet-printed foldable monopole antennas [81] have been reported. Application of AM on fabric is illustrated in [82]. where a tracking system antenna is screen printed on textile as the substrate. Inkjet printing has presented itself as the go to option for most researchers as numerous reported developments in antennas have used inkjet printing as an alternative to etching and modern expensive fabrication procedures. The dual alternatives of industry grade inkjet printing and low-cost inkjet-printed simply add to the value of this technique.

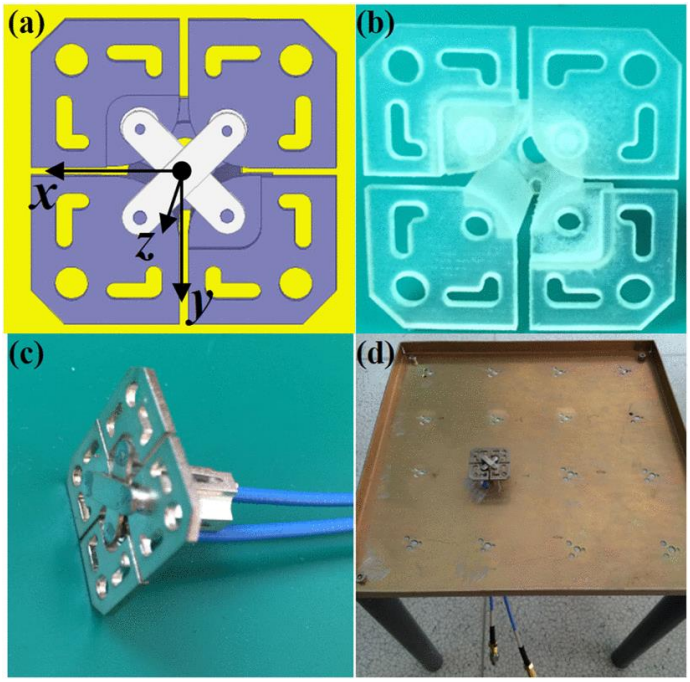

Fig. 2.10 5G MIMO Antenna with (a) proposed design, (b) printed polymer, (c) metal coated antenna with 2 feeds and (d) antenna mounted on the copper plane [78]

2.4.2 Inkjet Printing of Antennas

Inkjet-printing is a direct-printing fabrication technique that can print on a range of substrates by direct deposition of the conductive inks. Inkjet printing is normally a single-step procedure where the ink, in the shape of the design layout is precisely deposited onto the substrate. The process is repeated when a thicker layer of deposited ink is required.

Inkjet printing is significantly more environment friendly in comparison with the traditional fabrication techniques [83] – [88]. Inkjet printing substantially reduces the wastage of materials by only deploying the amount of conductive ink which is essential. The substrates most frequently used for inkjet printing are raisin coated photo paper, polyethylene terephthalate (PET) and polymide [88]. Polymide and PET are exceedingly popular because they both have extremely high levels of thermal stability as well as uniform flexibility across the printed surface area. The metallic, conductive inks used for

3D printing can be divided into two categories namely the nanoparticle inks and Metallo-organic decomposition (MOD) inks [86]. MOD inks consist of MOD compounds which can be deposited into metallic layers onto the printing substrate whereas the nanoparticle inks are made up of metal nanoparticles packed by organic covering [87].

Inkjet printing method makes use of a printing nozzle which consists of hundreds of tiny guns that discharge a number of tiny droplets of silver nanoparticle ink onto the substrate. The dots are extremely miniscule and can only be investigated under a high-precision microscope. There are a number of ways using which an inkjet printer can release ink onto the substrate which includes bubble jets [88] and inkjets [84] that work on piezoelectricity. Inkjet Printers manufactured by Cannon® use the terminology of "Bubble Jets". This method heats up the ink that results in the formation of an ink bubble that bursts and passes through several nozzles creating the design layout which then deposits the ink onto the substrate. Epson® printers make use of piezoelectricity. In this technique, a small amount of current charges and prompts the ink crystals to relocate and accumulate ink in the process. The finest available inkjet printers have the print quality as good as 10000 dpi. The most used household printers have a quality that ranges somewhere between 1200 dpi and 2000 dpi. Silver nanoparticle inks are consistently used in printers as they provide uniform conductivity across the printed area. The outcomes obtained using inkjet printing are almost always comparable albeit not better in comparison to the traditional fabrication methods such as etching.

Mitsubishi® silver nano ink is one of the conductive inks which is available in the market that offers the ease to print electronic circuits using standard household printers [89]. Electronic circuits, antenna designs and nominally 3D patterns can be readily printed as simply as the ordinary documents are printed using a printer. The uniform conductivity also delivers dependable outcomes which facilitates the inkjet printing to manufacture solutions that are analogous to that of the traditional methods such as etching. A typical household inkjet printer and the inkjet printing mechanism as seen in Fig. 2.11 (a) and Fig. 2.11 (b) are widely used with Mitsubishi silver nano ink to print the antenna surface.

Implementation of nanoparticle inks and MOD for additive manufacturing of antennas is preferred in antennas, electronics, microwave, and mm-wave manufacturing. Numerous

designs have exhibited the applicability of 3D printing and inkjet printing in the areas stated.

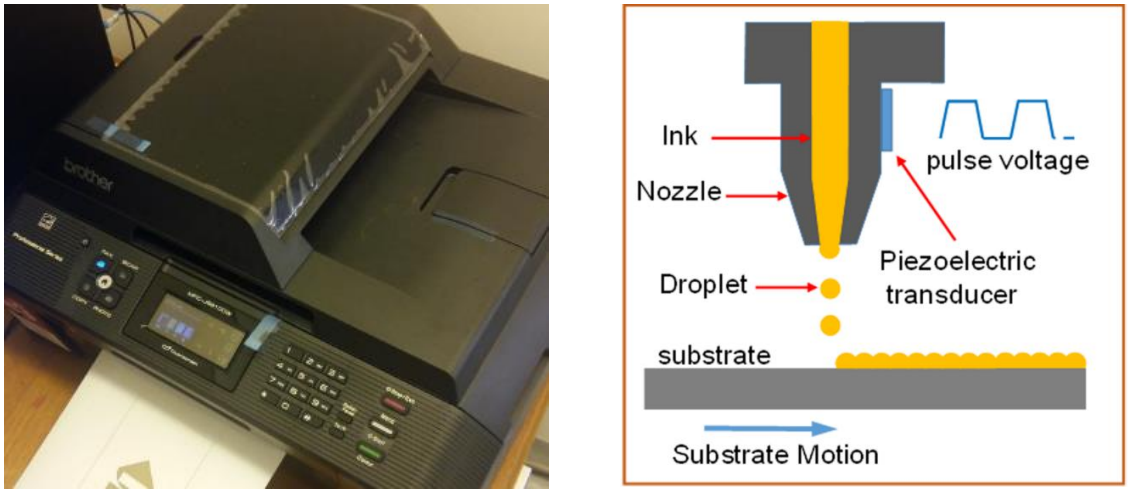

(a) (b)

Fig. 2.11 A typical household Inkjet printer in (a) and a typical piezoelectric inkjet printing mechanism in (b)

Reasonably costly inkjet printing systems such as the Diamatix platform have also been employed to fabricate inkjet-printed antennas [90] – [95]. A typical Diamatix printer can be seen in Fig. 2.12. Initial work on precise inkjet printing of antennas was focused on deploying costly industrial printers. Multilayer inkjet printing of Yagi-Uda antenna operating at 24.5 GHz is reported in [90]. A layer-by-layer fabricated patch antenna inspired by the shape of 3D honeycomb is described in [91]. AM of emitting structures using Inkjet printers have also been described along with inkjet-printed RF sensors antennas fabricated of a 3D origami structure of a foldable substrate in [92] that can be seen in Fig. 2.13 and inkjet printing of 3D helical antenna with an integrated lens is reported in [93]. Printing of a multi-layer array comprising of patch antennas using Diamatix printer is described in [94] whereas fabricating 2D phased-array antenna on malleable, heat resistant polymide, also known as Kapton substrate is reported in [95]. Contemporaneously, passive antenna configuration is proposed by fabrication using lower

cost equipment in [96], [97] where monopole EBG array antenna on a paper substrate is reported in [96] whereas an array of microstrips printed on PET is presented in [97].

For smart, reconfigurable applications, only a handful of designs are proposed that deploy inkjet printing. The two antennas presented in [98] and [99] deploy inkjet printing to develop reconfigurable antennas for WLAN applications.

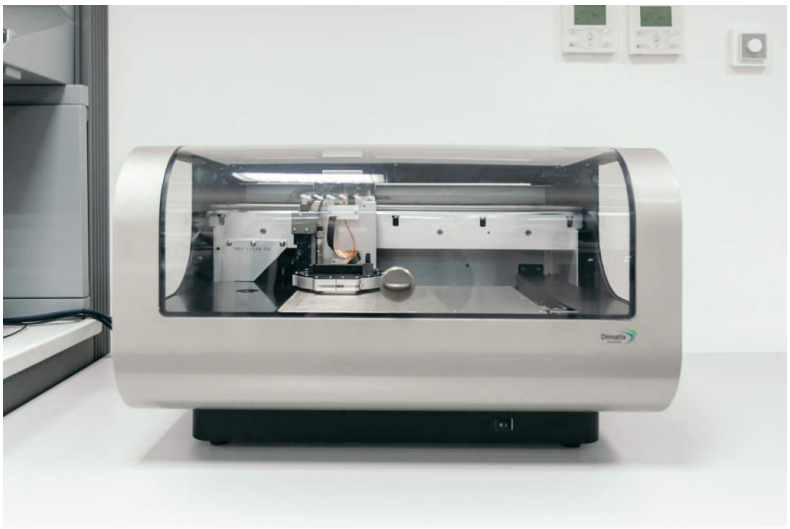

Fig. 2.12 A typical Diamatix printer

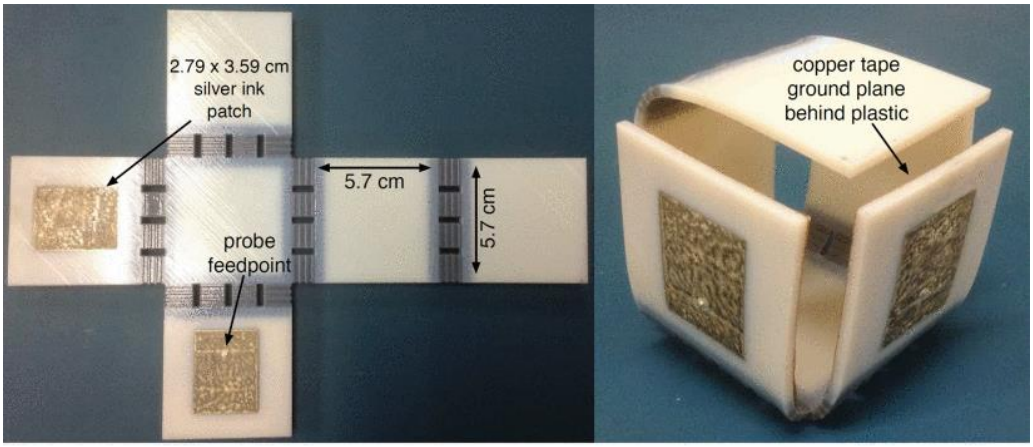

Fig. 2.13 Unfolded inkjet-printed patch antenna in (a) and 3D folded origami structure in (b) [92]

2.4.3 Additive Manufacturing of Frequency Selective Surfaces

Frequency Selective Surfaces, as discussed in Section 2.3.1 are filtering structures for electromagnetic waves that exhibit transmission or reflection characteristics as a function of their resonant frequencies. Over the time, periodic structures that are used for filtering have been proposed using traditional techniques [36] – [53] that were discussed earlier and with the advancements in additive manufacturing, the structures are also repeatedly and readily being developed with reliable performances, reduced wastage of material and direct printing on 2D and 3D surfaces.

An intricate square-loop structure of convoluted FSS array is screen printed on polyethylene terephthalate (PET) substrate and then attached to glass in [100]. Screen printing process, although demonstrated successfully here, generally does not merit consistency and reliability specially for the intricate designs and details. AM of FSS directly onto the substrate and surface has been projected in past in [101] – [104]. Inkjet printing of FSS using Nano-particle silver ink is presented to Fabricate an FSS design by printing on polyester cotton [101]. Various 3D FSS structures are created and fabricated making use of 3D printing techniques in [102] - [104]. Novel 3D FSS have also been demonstrated by inkjet printing and Origami folding paper in [105] The Origami FSS remains one interesting prospect.

Novel advancements in 3D FSS structures are described in [85] which deploy 3D printing of plastered structures coated with another supplementary layer consisting of conductive ink material. This work was developed beyond with the help of Fused Deposition modelling (FDM), that decreased the resonant frequency by partly metalizing the polymer based conductive unit cell elements of the array [86]. Carbon reinforced plastic material was used as a substrate to develop an FSS and was presented for the first time in [106] where plastic polymer FDM was fused with the Composite Filament Fabrication (CFF). An interesting bandstop FSS structure was reported in [107] where the unit cell elements were disposable and can be replaced where Fused Filament Fabrication (FFF) was deployed to print the elements. AM of metamaterial absorbers are reported in [109] where a concoction of AM methods was deployed. Broadband absorbers that cover the X and K_u

bands respectively were fabricated using Selective Laser Sintering (SLS) consisting of Nylon and Iron dust in [108]. A metamaterial absorber was fabricated using Ultimaker® with PLA as substrate in [109].

Inkjet printing with the help of conductive silver nanoparticle ink is yet another advantageous method which has been examined for creating FSS. Inkjet printing of a frame dipole FSS was reported in [110] in which a Diamatix inkjet-printer was employed to print the dipoles. This paper also discussed the various fabrications aspects of inkjet printing of FSS. Additional to those, FSS filters operating at mm-wave frequencies have also been proposed in [111], [112] where FSS designs that were operational at several mm-wave frequencies were reported. A comparative study between inkjet printing, pattern printing and other fabrication methods was also proposed in [112]. An attempt to develop FSS structures on curved lens surface was attempted in [113] using Aerosol Jet precision printing technique but no substantial results could be obtained using the technique and the design required further steps such as electroplating to provide reliable results.

2.4.4 Fused Deposition Modelling (FDM)

One of the most renowned AM technologies available in the existing marketplace is known as Fused Deposition Modelling (FDM) which is also known as Fused Filament Fabrication (FFF). FDM can be used in combination with existing technologies to print the desired plastic filament or ABS filament-based substrates and add the conductive structures on top of them by other means. FDM printers are the most popular printers among all. FDM is a procedure which makes use of a long wire-like filament of the thermoplastic raw material, that is melted and deposited layer-by-layer on top of each other forming strong operational printed parts [114]. A typical FDM printer can be seen in Fig. 2.14. The plastic is pressed through to a heated chamber block with an inner diameter that is around the same size as the filament which melts the filament to a useable temperature, the heated filament is then forced out through a heated nozzle with a small diameter. The material is squeeze out to a heated platform or a normal temperature one while moving to the defined coordinate position. The print resolution and surface of the finished area are a compromise when

equated with other methods such as Stereolithography (SLA). With a majority of open-source printers available, it permits the makers and designers to alter, scale-up, scale-down, test and improvise the whole mechanical design and system performance of the machine. The process starts with a 3D computer or CAD model which is exported to the popular, industrial Standard Tessellation Language (STL) file format, which comprises of triangular shapes defining the surface of the solid. The STL file is then uploaded into a slicing software, which breaks down the solid 3D model into several horizontal deposits. Inside each one of those sliced layers, there is an assortment of co-ordinates or toolpath that the deposition head of the printer will follow. The slicing software commands numerous variables within the design's properties. Firstly, the slicer produces a layer-by-layer contours of the design model, which controls the surface roughness. Substantial quantities material and time can be saved if the design outline height is increased. Then, secondly, the infill patterns control the dielectric constant and loss tangent of the printed area. A new and novel application of the FFF technique is presented later in Chapter 5.

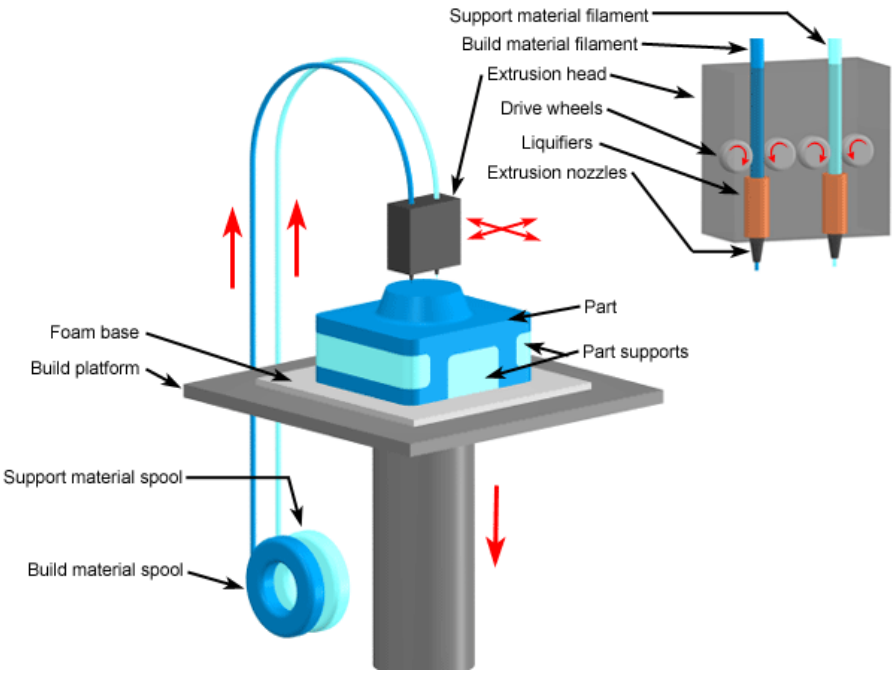

Figure 2.14 A typical Fused Deposition Modelling (FDM) system [106]

2.4.5 Aerosol Jet Printing

Aerosol Jet Printer systems are developed to facilitate, develop, repair, enhance and fabricate designs with high precision [115], [116]. The fabrication technique is expanded in detail in Chapter 6 where the development of FSS using Aerosol Jet printing is presented. An example of antenna fabrication using Aerosol Jet printing technology was demonstrated in [98]. A typical Aerosol Jet Printer and setup can be viewed in Fig. 2.15. The Aerosol jet printing method requires the usage of aerodynamic aiming to deposit the conductive silver ink onto the substrates in exceedingly detailed and precise fashion. The ink is stored within the atomizer vessel. With the help of a sheath gas, the liquid ink is transformed into a spray inside the atomizer. The spray mist is passed across the virtual impactor to the deposition head. In the deposition head, the mist is further compressed with the help of sheath gas. Nitrogen gas or compressed air are habitually used in designs as the sheath gasses. As the sheath gas and conductive ink aerosol are tossed through the tiny deposition nozzle, the aerosol is converted into an augmented flow of droplets. The accelerated ink and gasses escape the nozzle to move across the gap between nozzle and substrate to get deposited onto the substrate. The height gap between the nozzle and substrate varies between 2 to 5 mm, that allows a direct fabrication onto non-uniform and 3D surfaces that fall within the tolerance range. Tracks as narrow as <50 µm can also be printed using extremely precise nozzles. The nozzles come in a hole size range of 10 µm to 200 µm. Smaller nozzle size can help in printing smaller tracks but there is a great chance of clogging within the nozzles. Thickness of printed tracks can range from 50 µm to 250 µm depending upon the number of printed layers.

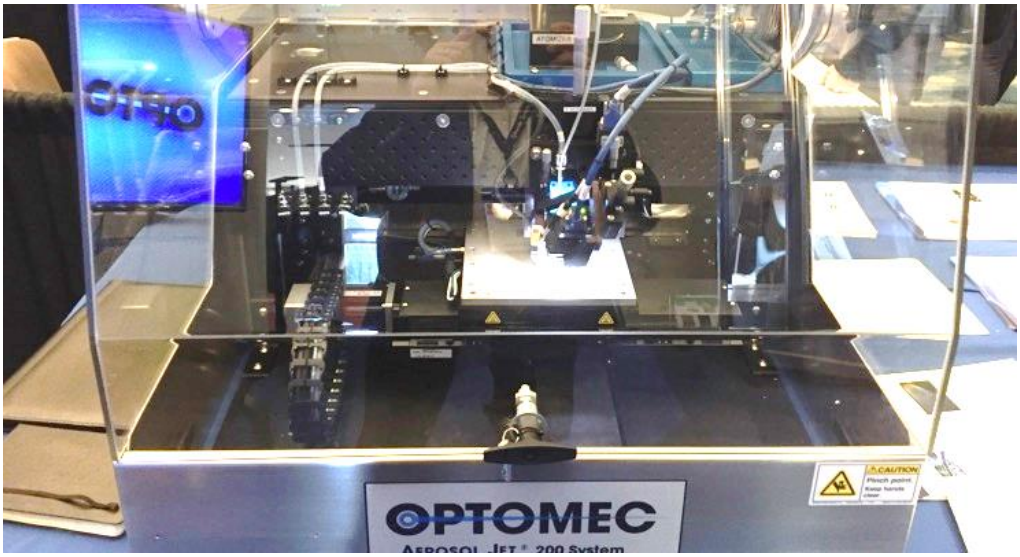

(a)

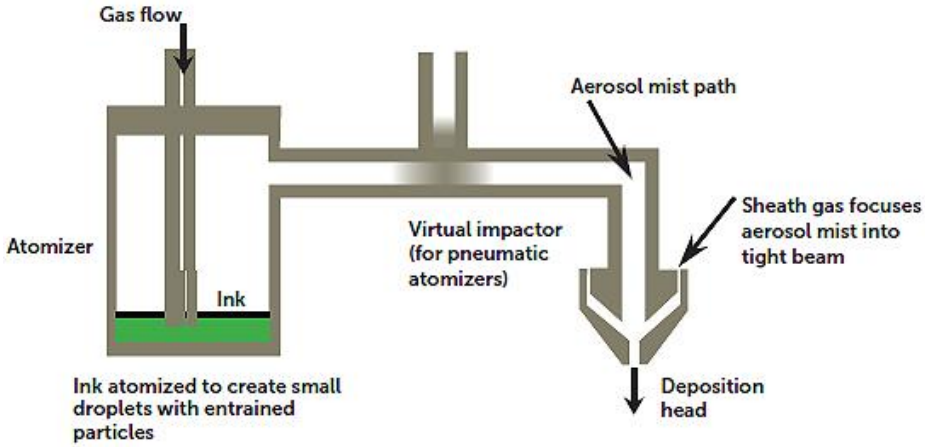

(b)

Figure 2.15 A typical Aerosol Jet Printer setup (a) with its functioning block diagram (b) [115]-[117]

References

[1] J. T. Bernhard, *Reconfigurable antennas*, 1st ed. San Rafael, Calif: Morgan & Claypool Publishers, 2007. pp. 1-66.

[2] M. Chryssomallis, "*Smart antennas*," IEEE Antennas Propag. Mag., vol. 42, pp. 129–136, 2000.

[3] Q. Luo, S. Gao, W. Liu and C. Gu, *Low-cost smart antennas*, 1st ed. John Wiley & Sons Ltd, 2019, pp. 1-23.

[4] M. Technology, "FPGA Multiple Antenna System Technologies - Intel® FPGA", *Intel*, 2020. [Online]. Available: https://www.intel.com/content/www/us/en/communications/products/programmable/applications/multiple-antenna-technology.html. [Accessed: 27- May- 2020].

[5] C. A. Balanis, *Modern Antenna Handbook*. John Wiley & Sons, Inc., 2008, DOI:10.1002/9780470294154, pp. 369-398.

[6] D. Schaubert, F. Farrar, A. Sindoris and S. Hayes, "Microstrip antennas with frequency agility and polarization diversity", *IEEE Transactions on Antennas and Propagation*, vol. 29, no. 1, pp. 118-123, 1981. Available: 10.1109/tap.1981.1142546.

[7] Fan Yang and Y. Rahmat-Samii, "A reconfigurable patch antenna using switchable slots for circular polarization diversity," in *IEEE Microwave and Wireless Components Letters*, vol. 12, no. 3, pp. 96-98, March 2002, doi: 10.1109/7260.989863.

[8] S.-J. Wu and T.-G. Ma, ''A wideband slotted bow-tie antenna with reconfigurable CPW-to slotline transition for pattern diversity,'' IEEE Trans. Antennas Propag., vol. 56, no. 2, pp. 327–334, Feb. 2008.

[9] B. Kim et al., ''A novel single-feed circular microstrip antenna with reconfigurable polarization capability,'' IEEE Trans. Antennas Propag., vol. 56, no. 3, pp. 630–638, Mar. 2008.

[10] J. Sarrazin, Y. Mahe, S. Avrillon, and S. Toutain, ''Pattern reconfigurable cubic antenna,'' IEEE Trans. Antennas Propag., vol. 57, no. 2, pp. 310–317, Feb. 2009.

[11] X.-S. Yang, B.-Z. Wang, S. H. Yeung, Q. Xue, and K. F. Man, ‘‘Circularly polarized reconfigurable crossed-yagi patch antenna,’’ IEEE Antennas Propag. Mag., vol. 53, no. 5, pp. 65–80, 2011.

[12] R. O. Ouedraogo, J. Tang, K. Fuchi, E. J. Rothwell, A. R. Diaz, and P. Chahal, “A Tunable Dual-Band Miniaturized Monopole Antenna for Compact Wireless Devices,” *IEEE Antennas and Wireless Propagation Papers*, vol. 13, pp. 1247–1250, 2014.

[13] G. H. Huff and J. T. Bernhard, "Integration of packaged RF-MEMS switches with radiation pattern reconfigurable square spiral microstrip antennas", *IEEE Trans. Antennas Propag.*, vol. 54, no. 2, pp. 464-469, Feb. 2006.

[14] Jae-Hyoung Park *et al*., "Tunable planar inverted-F antenna using rf MEMS switch for the reduction of human hand effect," *2007 IEEE 20th International Conference on Micro Electro Mechanical Systems (MEMS)*, Hyogo, 2007, pp. 163-166, doi: 10.1109/MEMSYS.2007.4433042.

[15] E. Erdil, K. Topalli, M. Unlu, O. A. Civi and T. Akin, "Frequency Tunable Microstrip Patch Antenna Using RF MEMS Technology," in *IEEE Transactions on Antennas and Propagation*, vol. 55, no. 4, pp. 1193-1196, April 2007, doi: 10.1109/TAP.2007.893426.

[16] A. Grau, J. Romeu, M. Lee, S. Blanch, L. Jofre and F. De Flaviis, "A dual linearly polarized MEMS-reconfigurable antenna for narrowband MIMO communication systems", *IEEE Trans. Antennas Propag.*, vol. 58, no. 1, pp. 4-16, Jan. 2010.

[17] B. A. Cetiner, G. R. Crusats, L. Jofre, and N. Biyikli, ‘‘RF MEMS integrated frequency reconfigurable annular slot antenna,’’ *IEEE Trans. Antennas Propag.*, vol. 58, no. 3, pp. 626–632, Mar. 2010.

[18] G. Ruvio, M. J. Ammann, and C. N. Zhi, “Wideband reconfigurable rolled planar monopole antenna”, *IEEE Trans, Antennas and Propag* on vol. 55, June 2007, pp. 1760-1767.

[19] Y. Tawk, J. Costantine, and C. G. Christodoulou, “A rotatable reconfigurable antenna for cognitive radio applications”, Radio and Wireless Symposium (RWS), 2011 IEEE, pp. 158-161.

[20] G. H. Huff, D. L. Rolando, P. Walters, and J. McDonald, “A frequency reconfigurable dielectric resonator antenna using colloidal dispersions”, *IEEE Antennas and Wireless Propagation Letters*, Vol. 9, 2010, pp. 288-290.

[21] D. M. Pozar, and V. Sanchez, “Magnetic tuning of a microstrip antenna on a ferrite substrate”, *Electronics Letters*, Vol. 24, Issue 12, 9th June 1988, pp.

[22] S. Shelley, J. Costantine, C. G. Christodoulou, D. E. Anagnostou and J. C. Lyke, "FPGA-Controlled Switch-Reconfigured Antenna," in *IEEE Antennas and Wireless Propagation Letters*, vol. 9, pp. 355-358, 2010, doi: 10.1109/LAWP.2010.2048550.

[23] H. A. Majid, M. K. A. Rahim, M. R. Hamid, N. A. Murad, M. F. Ismail, "Frequency reconfigurable microstrip patch-slot antenna", *IEEE Antennas Wireless Propag. Lett.,* vol. 12, pp. 218-220, 2013.

[24] A. Kolsrud, M.-Y. Li, and K. Chang, “Electronically switchable slot antenna fed by microstrip line”, 1998 IEEE Antennas and Propagation. Society Symp., 21-26 June 1998.

[25] L. Pazin and Y. Leviatan, “Reconfigurable Slot Antenna for Switchable Multiband Operation in a Wide Frequency Range”, *EEE Antennas Wireless Propag. Lett.*, vol. 12, pp. 329–332, 2013.

[26] D. Peroulis, K. Sarabandi, and L. P. B. Katehi, “Design of reconfigurable slot antennas”, *IEEE Trans. Antennas and Propag*, vol. 53, Feb. 2005, pp. 645-654.

[27] N. Kou and L. Li, “Frequency and pattern reconfigurable annular slot antenna with two feeding ports,” 2014 IEEE International Wireless Symposium (IWS 2014), 2014.

[28] M. Shirazi, J. Huang, T. Li, and X. Gong, “A Switchable-Frequency Slot-Ring Antenna Element for Designing a Reconfigurable Array,” *EEE Antennas Wireless Propag. Lett.*, vol. 17, no. 2, pp. 229–233, 2018.

[29] N. Symeon, R. Bairavasubramanian, C. Jr. Lugo, I. Carrasquillo, D. C. Thompson, G. E. Ponchak, J. Papapolymerou, and M. M. Tentzeris, “Pattern and frequency reconfigurable annular slot antenna using PIN diodes”, *IEEE Trans. Antennas and Propag.*, vol. 54, Feb. 2006, pp. 439-448.

[30] S. Kawasaki and T. Itoh, “A slot antenna with electronically tunable length”, 1991 Antennas and Propagation Society Symp., 24-28 June 1991.

[31] S.-K. Oh, Y.-S. Shin, and S.-O. Park, “A novel PIFA type varactor tunable antenna with U-shaped slot,” *2006 7th International Symposium on Antennas, Propagation & EM Theory*, 2006.

[32] N. Behdad and K. Sarabandi, “A Varactor-Tuned Dual-Band Slot Antenna”, *IEEE Trans. Antennas and Propag*, vol. 54, no. 2, pp. 401–408, 2006.

[33] J. Yang, W.-W. Choi, and K.-W. Tam, “A novel dual-band frequency tunable slot antenna with constant frequency ratio,” 2015 Asia-Pacific Microwave Conference (APMC), 2015.

[34] C. R. White and G. M. Rebeiz, “Single- and Dual-Polarized Tunable Slot-Ring Antennas”, *IEEE Trans. Antennas and Propag*, vol. 57, no. 1, pp. 19–26, 2009.

[35] A. H. Mohammadi and K. Fororaghi, “A varactor-tuned substrate-integrated cavity-backed dumbbell slot antenna,” *2012 15 International Symposium on Antenna Technology and Applied Electromagnetics*, 2012.

[36] B. A. Munk, *Frequency selective surfaces: Theory and design*, New York: Wiley, 2000, pp 636-659, doi: 10.1002/0471723770.

[37] G. Matthaei, E. Jones and L. Young, *Microwave filters, impedance-matching networks and coupling structures*. Dedham, Mass.: Artech House, 1980, pp. 34-887.

[38] K.-W. Lee, Y.-R. Jeong, J.-G. Yook, and I.-P. Hong, “Prediction of FSS radome performane using simple design equation,” *2012 6th European Conference on Antennas and Propagation (EUCAP)*, 2012.

[39] H. M. Musal and H. T. Hahn, "Thin-layer electromagnetic absorber design," in *IEEE Transactions on Magnetics*, vol. 25, no. 5, pp. 3851-3853, Sept. 1989, doi: 10.1109/20.42454.

[40] A. Edalati and T. A. Denidni, "Frequency Selective Surfaces for Beam-Switching Applications," in *IEEE Transactions on Antennas and Propagation*, vol. 61, no. 1, pp. 195-200, Jan. 2013, doi: 10.1109/TAP.2012.2219842.

[41] B. Liang, B. Sanz-Izquierdo, E. A. Parker and J. C. Batchelor, "Cylindrical Slot FSS Configuration for Beam-Switching Applications," in IEEE Transactions on Antennas and Propagation, vol. 63, no. 1, pp. 166-173, Jan. 2015, doi: 10.1109/TAP.2014.2367534.

[42] I. Kim and Y. Rahmat-Samii, "Electromagnetic band gap-dipole sub-array antennas creating an enhanced tilted beams for future base station," in IET Microwaves, Antennas & Propagation, vol. 9, no. 4, pp. 319-327, 19 3 2015, doi: 10.1049/iet-map.2014.0104.

[43] C. Gu, S. Gao, B. Sanz-Izquierdo, E. A. Parker, F. Qin, H. Xu, J. C. Batchelor, X. Yang, Z. Cheng , "3-D Coverage Beam-Scanning Antenna Using Feed Array and Active Frequency-Selective Surface," in *IEEE Transactions on Antennas and Propagation*, vol. 65, no. 11, pp. 5862-5870, Nov. 2017, doi: 10.1109/TAP.2017.2754400.

[44] G. I. Kiani, A. R. Weily and K. P. Esselle, "A novel absorb/transmit FSS for secure indoor wireless networks with reduced multipath fading," in *IEEE Microwave and Wireless Components Letters*, vol. 16, no. 6, pp. 378-380, June 2006, doi: 10.1109/LMWC.2006.875589.

[45] R. Dickie, R. Cahill, V. Fusco, H. S. Gamble and N. Mitchell, "THz Frequency Selective Surface Filters for Earth Observation Remote Sensing Instruments," in *IEEE Transactions on Terahertz Science and Technology*, vol. 1, no. 2, pp. 450-461, Nov. 2011.

[46] K. An, T. Liang, G. Zheng, X. Yan, Y. Li and S. Chatzinotas, "Performance Limits of Cognitive-Uplink FSS and Terrestrial FS for Ka-Band," in IEEE Transactions on Aerospace and Electronic Systems, vol. 55, no. 5, pp. 2604-2611, Oct. 2019, doi: 10.1109/TAES.2018.2886611.

[47] A. Chatterjee and Susanta Kumar Parui, "A multi-layered band-pass frequency selective surface designed for Ku band applications," *2013 IEEE Applied Electromagnetics Conference (AEMC)*, Bhubaneswar, 2013, pp. 1-2.

[48] T. Rossi *et al*., "Experimental assessment of optimal ACM parameters in Q/V-band satellite communication," *2016 IEEE Aerospace Conference*, Big Sky, MT, 2016, pp. 1-10.

[49] X. Li *et al*., "Investigation of Frequency-Selective Surfaces for a THz Gyromultiplier Output System," in *IEEE Transactions on Electron Devices*, vol. 64, no. 11, pp. 4678-4685, Nov. 2017.

[50] D. Li et al., "A Low-Profile Broadband Bandpass Frequency Selective Surface With Two Rapid Band Edges for 5G Near-Field Applications," in IEEE Transactions on Electromagnetic Compatibility, vol. 59, no. 2, pp. 670-676, April 2017, doi: 10.1109/TEMC.2016.2634279.

[51] B. Sanz-Izquierdo, E. Parker, J.-B. Robertson, and J. Batchelor, “Tuning technique for active FSS arrays,” *Electronics Letters*, vol. 45, no. 22, p. 1107, 2009.

[52] B. Sanz-Izquierdo and E. A. Parker, “Dual Polarized Reconfigurable Frequency Selective Surfaces,” *IEEE Transactions on Antennas and Propagation*, vol. 62, no. 2, pp. 764–771, 2014.

[53] B. Sanz-Izquierdo, E. A. Parker, and J. C. Batchelor, “Dual-Band Tunable Screen Using Complementary Split Ring Resonators,” *IEEE Transactions on Antennas and Propagation*, vol. 58, no. 11, pp. 3761–3765, 2010.

[54] M. Yan *et al.*, "A Miniaturized Dual-Band FSS With Stable Resonance Frequencies of 2.4 GHz/5 GHz for WLAN Applications," in *IEEE Antennas and Wireless Propagation Letters*, vol. 13, pp. 895-898, 2014.

[55] G. Sung, K. Sowerby, M. Neve, and A. Williamson, “A Frequency-Selective Wall for Interference Reduction in Wireless Indoor Environments,” IEEE Antennas and Propagation Magazine, vol. 48, no. 5, pp. 29–37, 2006.

[56] G. Sung, K. Sowerby, and A. Williamson, “The impact of frequency selective surfaces applied to standard wall construction materials,” IEEE Antennas and Propagation Society Symposium, 2004., 2004.

[57] T. Parker, J. Batchelor, J.-B. Robertson, B. Sanz-Izquierdo, and I. Ekpo, “Frequency selective surfaces for long wavelength use in buildings,” IET Seminar Digests, 2008.

[58] A. A. Dewani, M. Kanesan, D. V. Thiel, S. G. Okeefe, and M. V. Varnoosfaderani, “Screen printed frequency selective surfaces for room isolation in buildings,” 2014 International Workshop on Antenna Technology: Small Antennas, Novel EM Structures and Materials, and Applications (iWAT), 2014.

[59] S. I. Sohail, K. P. Esselle, and G. Kiani, “Design of a bandpass FSS on dual layer energy saving glass for improved RF communication in modern buildings,” Proceedings of the 2012 IEEE International Symposium on Antennas and Propagation, 2012.

[60] C. Mias, C. Tsokonas, and C. Oswald, “An investigation into the feasibility of designing frequency selective windows employing periodic structures” 2002, Nottingham Trent University, Nottingham, U.K., Tech. Rep. AY3922.

[61] E. A. Parker, C. Antonopoulos, and N. E. Simpson, “Microwave band FSS in optically transparent conducting layers: Performance of ring element arrays,” Microwave and Optical Technology Letters, vol. 16, no. 2, pp. 61–63, May 1997.

[62] M. Gustafsson, A. Karlsson, A. Rebelo, and B. Widenberg, “Design of Frequency Selective Windows for Improved Indoor-Outdoor Communication,” IEEE Transactions on Antennas and Propagation, vol. 54, no. 6, pp. 1897–1900, 2006.

[63] A. A. Dewani, S. G. Okeefe, D. V. Thiel, and A. Galehdar, “Window RF Shielding Film Using Printed FSS,” IEEE Transactions on Antennas and Propagation, vol. 66, no. 2, pp. 790–796, 2018.

[64] E. Björnson, L. Sanguinetti, H. Wymeersch, J. Hoydis, and T. L. Marzetta, “Massive MIMO is a reality—What is next? Five promising research directions for antenna arrays,” Digit. Signal Process., vol. 94, pp. 3–20, Nov. 2019.

[65] E. Basar, M. Di Renzo, J. De Rosny, M. Debbah, M.-S. Alouini, and R. Zhang, “Wireless communications through reconfigurable intelligent surfaces,” IEEE Access, vol. 7, pp. 116753–116773, 2019.

[66] Gsma.com, 2020. [Online]. Available: https://www.gsma.com/spectrum/wp-content/uploads/2020/03/5G-Spectrum-Positions.pdf. [Accessed: 21- Jun- 2020].

[67] "Samsung’s 6G White Paper Lays Out the Company’s Vision for the Next Generation of Communications Technology", News.samsung.com, 2020. [Online]. Available: https://news.samsung.com/global/samsungs-6g-white-paper-lays-out-the-companys-vision-for-the-next-generation-of-communications-technology . [Accessed: 22- Jun- 2020].

[68] E. Larsson, "Intelligent Reflecting Surfaces: On Use Cases and Path Loss Model | Massive MIMO", Ma-mimo.ellintech.se, 2020. [Online]. Available: http://ma-mimo.ellintech.se/2020/01/09/intelligent-reflecting-surfaces-on-use-cases-and-path-loss-models/. [Accessed: 31- May- 2020].

[69] D. Espalin, D. W. Muse, F. Medina, E. MacDonald, and R. B. Wicker, ‘‘3D Printing multi-functionality: Structures with electronics,’’ Int. J. Adv. Manuf. Technol., Mar. 2014.

[70] E. Macdonald et al., "3D Printing for the Rapid Prototyping of Structural Electronics," in IEEE Access, vol. 2, pp. 234-242, Dec. 2014, doi: 10.1109/ACCESS.2014.2311810.

[71] G. Shaker, S. Safavi-Naeini, N. Sangary and M. M. Tentzeris, "Inkjet Printing of Ultrawideband (UWB) Antennas on Paper-Based Substrates," in IEEE Antennas and Wireless Propagation Letters, vol. 10, pp. 111-114, 2011, doi: 10.1109/LAWP.2011.2106754.

[72] B. T. Malik, V. Doychinov, S. A. R. Zaidi, I. D. Robertson and N. Somjit, "Antenna Gain Enhancement by Using Low-Infill 3D-Printed Dielectric Lens Antennas," in IEEE Access, vol. 7, pp. 102467-102476, 2019, doi: 10.1109/ACCESS.2019.2931772.

[73] Z. Larimore, S. Jensen, A. Good, A. Lu, J. Suarez and M. Mirotznik, "Additive Manufacturing of Luneburg Lens Antennas Using Space-Filling Curves and Fused Filament Fabrication," in *IEEE Transactions on Antennas and Propagation*, vol. 66, no. 6, pp. 2818-2827, June 2018, doi: 10.1109/TAP.2018.2823819.

[74] A. Buerkle, K. Brakora and K. Sarabandi, "Fabrication of a DRA Array Using Ceramic Stereolithography", *IEEE Antennas and Wireless Propagation Letters*, vol. 5, pp. 479-482, 2006. Available: 10.1109/lawp.2006.885167.

[75] B. Zhang et al., "Metallic 3-D Printed Antennas for Millimeter- and Submillimeter Wave Applications," in IEEE Transactions on Terahertz Science and Technology, vol. 6, no. 4, pp. 592-600, July 2016, doi: 10.1109/TTHZ.2016.2562508.

[76] J. Heirons, S. Jun, A. Shastri, B. Sanz-Izquierdo, D. Bird, L. Winchester, L. Evans, and A. McClelland, "Inkjet-printed GPS antenna on a 3D printed substrate using low-cost machines," *2016 Loughborough Antennas & Propagation Conference (LAPC)*, Loughborough, 2016, pp. 1-4, doi: 10.1109/LAPC.2016.7807590.

[77] S. Y. Jun, B. Sanz-Izquierdo, E. A. Parker, D. Bird and A. McClelland, "Manufacturing Considerations in the 3-D Printing of Fractal Antennas," IEEE Transactions on Components, Packaging and Manufacturing Technology, vol. 7, no. 11, pp. 1891 - 1898, 2017.

[78] Y. Li, C. Wang, H. Yuan, N. Liu, H. Zhao and X. Li, "A 5G MIMO Antenna Manufactured by 3-D Printing Method," in IEEE Antennas and Wireless Propagation Letters, vol. 16, pp. 657-660, 2017, doi: 10.1109/LAWP.2016.2596297.

[79] R. Xu et al., "140 GHz Additive Manufacturing Low-Cost and High-Gain Fabry-Perot Resonator Antenna," 2020 International Workshop on Antenna Technology (iWAT), Bucharest, Romania, 2020, pp. 1-4, doi: 10.1109/iWAT48004.2020.1570598322.

[80] S. Y. Jun, A. Shastri, B. Sanz-Izquierdo, D. Bird and A. McClelland, "Investigation of Antennas Integrated into Disposable Unmanned Aerial Vehicles," in IEEE Transactions on Vehicular Technology, vol. 68, no. 1, pp. 604 - 612, 2019.

[81] S. Y. Jun, A. Elibiary, B. Sanz-Izquierdo, L. Winchester, D. Bird and A. McCleland, "3-D Printing of Conformal Antennas for Diversity Wrist Worn Applications," in *IEEE Transactions on Components, Packaging and Manufacturing Technology*, vol. 8, no. 12, pp. 2227-2235, Dec. 2018, doi: 10.1109/TCPMT.2018.2874424.

[82] B. Krykpayev, M. F. Farooqui, R. M. Bilal, M. Vaseem, A. Shamim, "A wearable tracking device inkjet-printed on textile," Microelectronics Journal, Volume 65, Pages 40-48, 2017.

[83] S. D. Hoath, "Index," *Fundamentals of Inkjet Printing*, pp. 7–79, 2015.

[84] F. J. Romano, Inkjet! Everything You Need to Know About Inkjet History, Technology, Markets, and Applications. Printing Industries Pr, 2012.

[85] B. Sanz-Izquierdo and E. A. Parker, "3-D Printing of Elements in Frequency Selective Arrays," IEEE Trans. Antennas Propagat., vol. 62, pp. 6060-6066, Dec 2014.

[86] B. Sanz-Izquierdo and E. Parker, "Frequency selective surfaces formed by partially metalising 3D printed shapes", 2015 9th European Conference on Antennas and Propagation (EuCAP), pp. 1-4, 2015.

[87] S. Jun, B. Sanz-Izquierdo and M. Summerfield, "UWB antenna on 3D printed flexible substrate and foot phantom", 2015 Loughborough Antennas & Propagation Conference (LAPC), pp. 1-5, 2015.

[88] T. Lindemann, H. Ashauer, Y. Yu, D. S. Sassano, R. Zengerle, and P. Koltay, "One Inch Thermal Bubble Jet Printhead With Laser Structured Integrated Polyimide Nozzle Plate," Journal of Microelectromechanical Systems, vol. 16, no. 2, pp. 420–428, 2007.

[89] Mitsubishi Silver Nanoparticle Ink, K-mpm.com, 2020. [Online]. Available: http://www.k-mpm.com/agnanoen/pdf/msds_nbsij-mu01.pdf. [Accessed: 21-May- 2020].

[90] B. K. Tehrani, B. S. Cook, and M. M. Tentzeris, "Inkjet Printing of Multilayer Millimeter-Wave Yagi-Uda Antennas on Flexible Substrates," *IEEE Antennas and Wireless Propagation Letters*, vol. 15, pp. 143–146, 2016.

[91] G. Mckerricher, D. Titterington, and A. Shamim, “A Fully Inkjet-Printed 3-D Honeycomb-Inspired Patch Antenna,” IEEE Antennas and Wireless Propagation Letters, vol. 15, pp. 544–547, 2016.

[92] J. Kimionis, M. Isakov, B. S. Koh, A. Georgiadis and M. M. Tentzeris, "3D-Printed Origami Packaging With Inkjet-Printed Antennas for RF Harvesting Sensors," in IEEE Transactions on Microwave Theory and Techniques, vol. 63, no. 12, pp. 4521-4532, Dec. 2015, doi: 10.1109/TMTT.2015.2494580

[93] M. F. Farooqui and A. Shamim, "3-D Inkjet-Printed Helical Antenna with Integrated Lens," in IEEE Antennas and Wireless Propagation Letters, vol. 16, pp. 800-803, 2017, doi: 10.1109/LAWP.2016.2604497.

[94] B. S. Cook, B. Tehrani, J. R. Cooper and M. M. Tentzeris, "Multilayer Inkjet Printing of Millimeter-Wave Proximity-Fed Patch Arrays on Flexible Substrates," in IEEE Antennas and Wireless Propagation Letters, vol. 12, pp. 1351-1354, 2013, doi: 10.1109/LAWP.2013.2286003.

[95] H. Subbaraman et al., "Inkjet-Printed Two-Dimensional Phased-Array Antenna on a Flexible Substrate," in IEEE Antennas and Wireless Propagation Letters, vol. 12, pp. 170-173, 2013, doi: 10.1109/LAWP.2013.2245292.

[96] S. Kim, Y. Ren, H. Lee, A. Rida, S. Nikolaou and M. M. Tentzeris, "Monopole Antenna With Inkjet-Printed EBG Array on Paper Substrate for Wearable Applications," in IEEE Antennas and Wireless Propagation Letters, vol. 11, pp. 663-666, 2012, doi: 10.1109/LAWP.2012.2203291.

[97] A. T. Castro and S. K. Sharma, "Inkjet-Printed Wideband Circularly Polarized Microstrip Patch Array Antenna on a PET Film Flexible Substrate Material," in IEEE Antennas and Wireless Propagation Letters, vol. 17, no. 1, pp. 176-179, Jan. 2018, doi: 10.1109/LAWP.2017.2779440.

[98] S. M. Saeed, C. A. Balanis and C. R. Birtcher, "Inkjet-Printed Flexible Reconfigurable Antenna for Conformal WLAN/WiMAX Wireless Devices," in IEEE Antennas and Wireless Propagation Letters, vol. 15, pp. 1979-1982, 2016, doi: 10.1109/LAWP.2016.2547338.

[99] H. F. Abutarboush and A. Shamim, "A Reconfigurable Inkjet-Printed Antenna on Paper Substrate for Wireless Applications," in IEEE Antennas and Wireless Propagation Letters, vol. 17, no. 9, pp. 1648-1651, Sept. 2018, doi: 10.1109/LAWP.2018.2861386.

[100] A. A. Dewani, S. G. Okeefe, D. V. Thiel, and A. Galehdar, "Window RF Shielding Film Using Printed FSS," IEEE Transactions on Antennas and Propagation, vol. 66, no. 2, pp. 790–796, 2018

[101] W. Whittow, K. Yang, Y. Li, R. Torah, J. Tudor, and S. Beeby, "Printed frequency selective surfaces on textiles," Electronics Letters, vol. 50, no. 13, pp. 916–917, 2014.

[102] J. C. Batchelor, E. A. Parker, J. A. Miller, V. Sanchez-Romaguera, and S. G. Yeates, "Inkjet printing of frequency selective surfaces," Electronics Letters, vol. 45, no. 1, p. 7, 2009.

[103] B. Sanz-Izquierdo and E. A. Parker, "3D printed FSS arrays for long wavelength applications," The 8th European Conference on Antennas and Propagation (EuCAP 2014), 2014.

[104] B. Sanz-Izquierdo and E.A. Parker, "3D Printing of Elements in Frequency Selective Arrays", IEEE Trans. Antennas Propag, Vol. 62, No.12, pp. 6060 - 6066, 2014

[105] Y. Cui, S. A. Nauroze, and M. M. Tentzeris, "Novel 3D-Printed Reconfigurable Origami Frequency Selective Surfaces With Flexible Inkjet-Printed Conductor Traces," 2019 IEEE MTT-S International Microwave Symposium (IMS), 2019.

[106] R. Mirzavand, M. M. Honari, S. Aslanzadeh, H. Saghlatoon and P. Mousavi, "Evaluation of One-Staged 3-D Printed Frequency Selective Surface Using Carbon-Fiber-Reinforced Thermoplastic Composite," in IEEE Transactions on Components, Packaging and Manufacturing Technology, vol. 9, no. 11, pp. 2298-2304, Nov. 2019, doi: 10.1109/TCPMT.2019.2917197.

[107] S. Cho, S. Yoon and I. Hong, "Design of Three-Dimensional Frequency Selective Structure With Replaceable Unit Structures Using a 3-D Printing Technique," in IEEE Antennas and Wireless Propagation Letters, vol. 17, no. 11, pp. 2041-2045, Nov. 2018, doi: 10.1109/LAWP.2018.2871175.

[108] D. Zhou, X. Huang and Z. Du, "Analysis and Design of Multilayered Broadband Radar Absorbing Metamaterial Using the 3-D Printing Technology-Based Method," in

IEEE Antennas and Wireless Propagation Letters, vol. 16, pp. 133-136, 2017, doi: 10.1109/LAWP.2016.2560904.

[109] D. Lim, S. Yu and S. Lim, "Miniaturized Metamaterial Absorber Using Three-Dimensional Printed Stair-Like Jerusalem Cross," in IEEE Access, vol. 6, pp. 43654-43659, 2018, doi: 10.1109/ACCESS.2018.2862160.

[110] B. M. Turki et al., "Significant Factors in the Inkjet Manufacture of Frequency-Selective Surfaces," in IEEE Transactions on Components, Packaging and Manufacturing Technology, vol. 6, no. 6, pp. 933-940, June 2016, doi: 10.1109/TCPMT.2016.2561972.

[111] O. Sushko, M. Pigeon, T. Kreouzis, C. Parini, R. Donnan and R. Dubrovka, "Low-cost inkjet-printed FSS band-pass filters for 100 and 300 GHz," 2016 10th European Conference on Antennas and Propagation (EuCAP), Davos, 2016, pp. 1-3, doi: 10.1109/EuCAP.2016.7481780.

[112] O. Sushko, M. Pigeon, R. S. Donnan, T. Kreouzis, C. G. Parini and R. Dubrovka, "Comparative Study of Sub-THz FSS Filters Fabricated by Inkjet Printing, Microprecision Material Printing, and Photolithography," in IEEE Transactions on Terahertz Science and Technology, vol. 7, no. 2, pp. 184-190, March 2017, doi: 10.1109/TTHZ.2017.2662582.

[113] J. A. Byford, C. Oakley and P. Chahal, "Additively Manufactured Frequency Selective Structures on Curved Surfaces," 2018 48th European Microwave Conference (EuMC), Madrid, 2018, pp. 671-674, doi: 10.23919/EuMC.2018.8541568.

[114] K. Church, H. Tsang, R. Rodriguez, P. Defembaugh, and R. Rumpf, (2013). Printed Circuit Structures: The Evolution of Printed Circuit Boards. The PCB Magazine, pp.12-26, 2013

[115] "Optomec Showcases Aerosol Jet 3D Printing Systems At 2018FLEX", *The Independent Global Source for the Flexible and Printed Electronics Industry.*, 2018. [Online]. Available: https://www.printedelectronicsnow.com/contents/view_breaking-news/2018-02-13/optomec-showcases-aerosol-jet-3d-printing-systems-2018flex/46369. [Accessed: 23- May- 2020].

[116] A. Delage et al., "Aerosol jet printing of millimeter wave transmission lines on 3D ceramic substrates made by additive manufacturing," 2018 IEEE/MTT-S International Microwave Symposium - IMS, Philadelphia, PA, 2018, pp. 1557-1560, doi: 10.1109/MWSYM.2018.8439498.

[117] L. Teschler, "Your next circuit design could be fabricated on a printer", Design World, 2015. [Online]. Available: https://www.designworldonline.com/your-next-circuit-design-could-be-fabricated-on-a-printer/. [Accessed: 22- May- 2020].

CHAPTER 3

FREQUENCY RECONFIGURABLE ANTENNAS FOR SMART SENSING APPLICATIONS

3.1 Introduction

This chapter discusses the designing and fabrication of frequency reconfigurable antennas using the close-coupled biasing and their potential application in smart AC current and voltage sensing. Two major solutions to demonstrate the reconfigurability in antennas are proposed namely Switching antenna and tuning antenna. Switching antenna switch their frequency of operation between two adjacent bands and tuning antenna tunes dynamically between a wide spectrum of frequency bands. The antennas are developed using traditional etching method on an extremely thin, flexible substrate. Capacitive-coupled biasing technique is presented for the first time here incorporated within the designing of slot antennas. The capacitive coupling is a well-known procedure which is able to isolate the circuit layers at direct current (DC) while providing connectivity at alternate current (AC). At radio frequency (RF) applications, it can be realised through adding physical components to the design or creating conductive tracks that behave as capacitors. Similar techniques have previously been applied for RF circuits and more recently to frequency selective surfaces. This chapter focuses on the applicability of capacitive coupling to frequency agile slot antennas and their etching on flexible substrates. The switchable antenna is designed to be able to switch between two adjacent bands. The tuning antenna design solution provides a dynamic selection of the frequency of operation and tunes between several neighbouring frequencies. Double-sided copper clad Mylar substrate is

etched to produce the slot antenna on one side and the capacitive coupling tracks with the components on the other side. Inexpensive switching and varactor diodes are employed. The antennas operate in the UHF band and are intended for existing technologies for existing wireless and mobile phone communications systems. Finally, the application of the tuning design as a novel smart AC current sensing antenna for smart domestic appliance is presented. The novel system to use that as a sensing antenna is described there. The solution investigated is low-cost and suitable for flexible and conformal smart antenna applications.

Antenna designs which possess capacity to accommodate multiple neighbouring frequency bands are of significant interest for existing and forthcoming enclosed and outdoor settings. There are several methods by which antennas have capacity for several frequency bands such as multiband antennas and reconfigurable antennas. A range of such methods are presented in [1] – [26] and discussed in Chapter 2.

PIN diodes also possess a tendency to be the lower-cost solution which can be employed in a combination with traditional wet etching methods along with the contemporary additive manufacturing processes. Diodes can provide both switching and tuning for reconfigurable antennas by modifying the frequency of operation when alterations are made with the input voltages [14] – [25]. Frequency switching slot antennas have been extensively described in the literature [13] – [18] where switching is accomplished by shortening the effective length of the slot by means of using PIN diodes [14] – [19].

Tunable slot antennas can be accomplished by adjusting of the reactance of the slots by the means of active RF components. Tunable antennas using varactor diodes are presented in [22] – [25]. Most reconfigurable slot antennas make use of a combination of bias circuit and vias connecting the top layer containing and bottom layer for double layer structures.

Tunable antennas can also be deployed as a part of current sensors mechanisms. Current sensing is primarily done using RFID chips [26] – [29] but an additional option of using antennas as a part of the sensing mechanism is also a potential option that have also been proposed for sensing applications.

This chapter presents two frequency reconfigurable slot antennas designed using close-coupled biasing technique. Switching and tuning antennas are presented. The tuning antenna is also proposed as a part of a novel AC current sensing antenna system that can sense the current passing through the wire of a smart domestic appliance and can also transmit the data over Bluetooth through the second mode which can be useful for smart metering.

The chapter is arranged with section 3.2 presents the frequency switchable slot antenna and section 3.3 presents the frequency tunable slot antenna. Section 3.4 presents the novel application of the tuning antenna within an AC current sensing system. The whole proposed sensing system setup is also described in this section.

3.2 Switchable Slot Antennas

3.2.1 Switchable slot antenna design

A slot antenna design is developed to demonstrate frequency switching antennas using a capacitive-coupling biasing technique. The initial design for the switching antenna can be seen from Fig. 3.1. An extensive study of this antenna and the implementation of the biasing technique for switching antennas along with the parametric analysis of the critical dimensions for biasing is described here. Fig 3.1 (a) denotes the cross-segment viewpoint, Fig. 3.1 (b) the backside and Fig. 3.1 (c) represents the front side of the antenna with the dimensions shown in Table I. On top of the front layer, the slot is etched whilst on the back layer, rectangular shaped square patches (in black) are etched to add the coaxial port (in orange) on one side, and the biasing tracks (in grey) comprising of the switching diode (in purple).

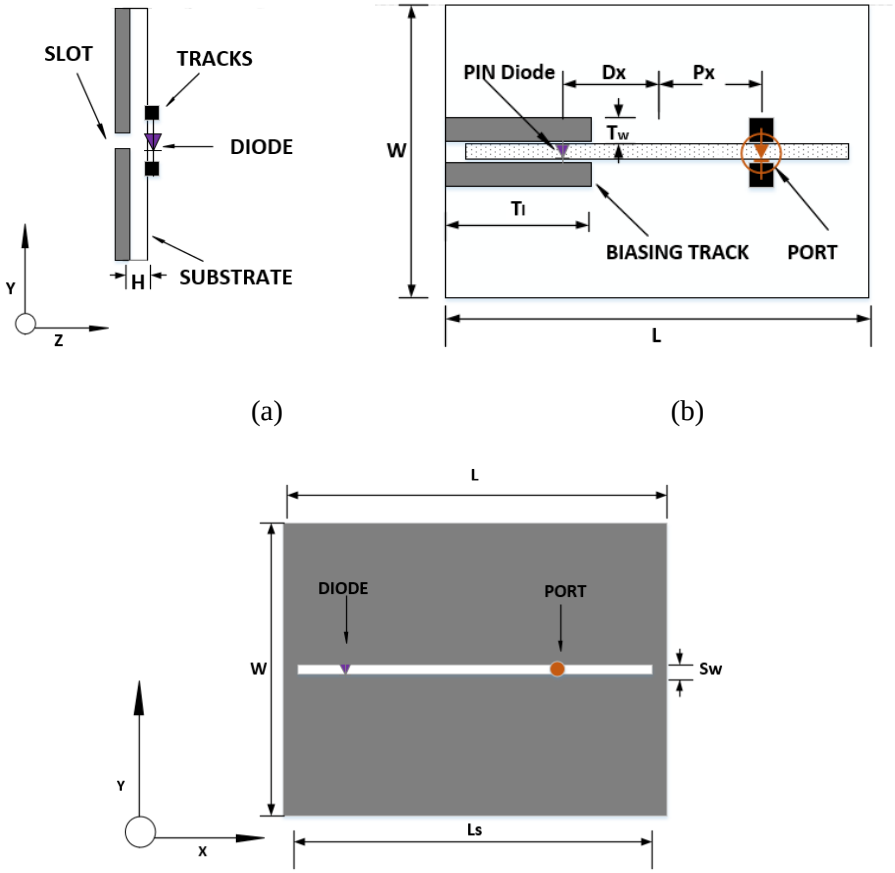

Fig 3.1. Switchable antenna design with side view (a) back view (b) and front view (c)

TABLE I

Switchable antenna dimensions (mm)

Length	L_s	S_w	L	W	P_x	D_x	T_l	T_w
Dimensions (mm)	75	0.5	83	50	28.75	28.75	15	3.5

Total dimension of antenna, as seen in Table I, are 83 mm in length and 50 mm in width and the rectangular slot is 75 mm long and 0.5 mm wide which was slightly larger than the typical $\frac{\lambda}{2}$ wavelength of the slots. The antenna design was simulated using the time domain solver in CST microwave studio^{TM}. The diode was computed as a lumped element using a

simplified equivalent circuit model for the BAR64 diode [31]. RF equivalent circuit diode models for switching diodes consist of two different circuit representing the two states. The OFF-state is represented with a parallel R-C circuit whereas the ON-state is represented by a serial R-C circuit. As per the manufacturer's datasheet [31], A resistance of 2.1 Ω in the ON-state and capacitance of 0.17 pF in the OFF-state were used. The simulation reflection coefficient (S_{11}) can be seen in Fig. 3.2.

The continuous black line denoted the simulation patterns for the OFF-state whereas the dashed red line denoted the simulation results for the ON-state. Switching from one frequency to the other can be clearly observed through the plot. The antenna resonated at a central frequency of 2.32 GHz in the ON-state with -10 dB bandwidth of about 16%. In the OFF state, it resonated at a central frequency of 1.88 GHz with a bandwidth of 12%. The combined -10 dB bandwidth increased by approximately 20% from the OFF state.

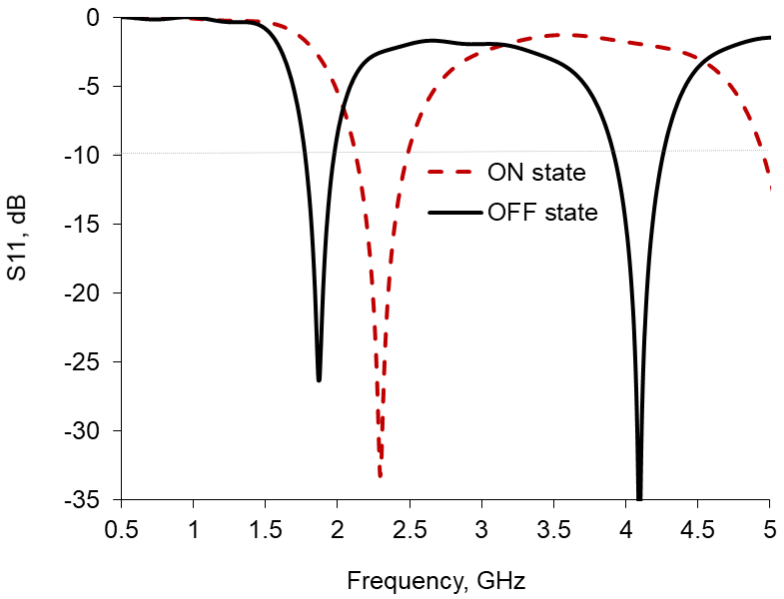

Fig. 3.2 Switching antenna simulated reflection coefficient results for ON-state and OFF-state.

The surface currents of the antenna in the OFF and ON state is shown in Fig. 3.3 and Fig. 3.4, respectively. It can clearly be observed that the diode reduces the effective length

of the slots when it is in the ON state and currents are concentrated around the slot of the remaining size.

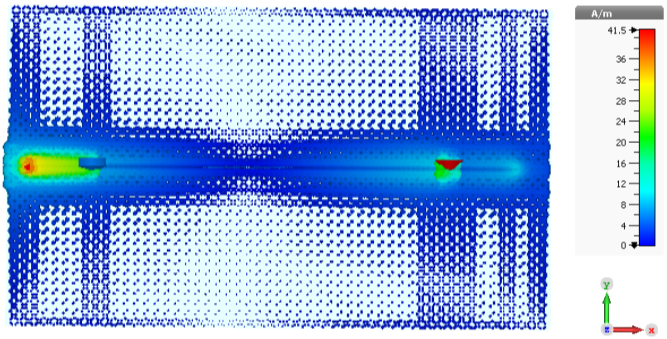

Fig. 3.3 Simulated Surface currents of the OFF state at 1.88 GHz

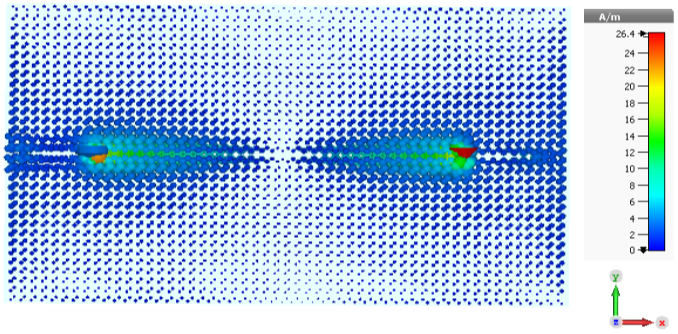

Fig. 3.4 Simulated Surface currents of the ON state at 2.32 GHz

3.2.2 Close-Coupled Biasing Technique

The capacitive-coupled biasing technique is accomplished by means of two tracks stretching along the slot at the backside. A substrate of 0.05 mm thickness, which is extremely thin in comparison to the wavelength of operation facilitates the tracks to be considered as connected to the metallic layer on the front side at RF. That effect is exhibited owing to the low impedance of the capacitive components at high frequency. At DC, nevertheless, the biasing circuit remains entirely isolated from the circuitry on the front layer which avoids any form of connection amongst the two layers which simplifies the biasing circuit.

The capacitance between each track and the ground plane containing the slot can be calculated using the Faraday's equation for the capacitance for two parallel plates:

$$C = (\varepsilon_0 \varepsilon_r A) / d \quad (1)$$

Where *A* stood for the cross-section area of the biasing tracks and *d* referred to the distance between the tracks and the front layer. ε_0 and ε_r denoted the dielectric permittivity of the free space as well as the relative permittivity of the material, respectively. Value for ε_0 is 8.854×10^{-12} F. m^{-1} whereas the ε_r value for the Mylar substrate is 3.1. The Mylar substrate had a thickness of 0.05 mm. Although the equation is a Quasi-Static equation, it is valid for use here because, due to close-coupled biasing, the two layers of the antenna function at RF and they act as separated at DC, where these equations are valid. This equation gave a capacitance of approximately 10.3 pF for a track of dimensions of 15 mm by 3.5 mm and the subsequently calculated value of impedance was 8.48 Ω at the OFF-state frequency of operation of 1.88 GHz.

Fig. 3.5 (a) shows a simulation based parametric study analysing the effects of increasing substrate thickness on frequency response in two ways. The two novel studies analyse the effects of the increase in thickness of the substrate and the hypothetical increase in gap between the metallic layers. As the thickness of substrate is increased from original 0.05 mm thickness of the Mylar, the matching between two states is gradually lost. A shift in the ON-state and OFF-state is observed when the thickness of substrate is increased by 0.09 mm. The OFF state is observed to be operational at a much lower band. When the thickness is increased by 0.1 mm, the OFF-state shifts towards a higher frequency of operation which is much closer to the corresponding ON-state, thus removing the switching capability of the antenna. As the thickness is increased further, the same trend can be observed, and the effectiveness of the biasing is entirely lost. That is the main reason why previously reported works [22]-[25] on the frequency switchable antennas required the use of additional vias and components incorporated within their designs which is simplified in the design presented here. The dimension at which the effectiveness seems to be lost is about 0.001 λ.

Fig. 3.5 (b) shows the novel study of the antenna reflection coefficient response when the distance between the biasing circuit and the ground is varied. This study demonstrates the impact of varying the distance between the metallic layers on the coupling. It can be observed that when the distance between the substrate and the metallic tracks was increased from the original position of the proposed design, the capacitive coupling between the antenna layer and the tracks on the bottom layer started weakening. The coupling between the top and the bottom layer diminishes completely when the separation between the Mylar layer and the tracks is increase to a distance of 0.13 mm. At that point, the tracks disconnect completely from the slot. The antenna then tunes towards the OFF-state frequency of the antenna. The effective wavelength at the given frequency is 17.4 cm. The bandwidth too gets narrower as the distance is increased and the bandwidth is reduced by about 12%. As the distance of the tracks and the diode is further increased, the antenna starts tuning closer to the OFF state but at a slightly lower frequency. That is because the OFF state works as a capacitive state and with the increase in distance between the slot and the bottom layer, the capacitance value is reduced almost to a zero level. The two simulation-based analytical studies show the requirements for the minimum distance for the coupling to work between the biasing circuit and the top layer. For the antenna design to work at the optimum level, the distance must be at its minimum with the due considerations for the size of the substrate.

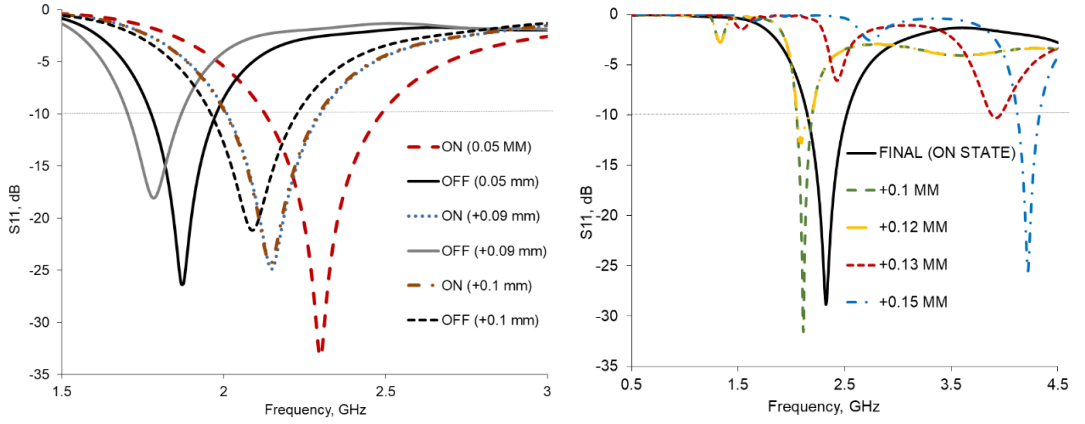

(a) (b)

Fig. 3.5. Effects of increased thickness of substrate H on S_{11} in (a) and the effects of the increased gap between metallic tracks and the antenna layer on S_{11} of the ON state in (b)

Therefore, using a Mylar substrate which had a thickness of 0.05 mm (0.0004 λ) was a perfect solution for the choice of substrate to demonstrate close-coupled biasing technique.

3.2.3 Switching Antenna Fabrication and Measurements

The design was fabricated making use of the traditional copper wet etching technique on a double-sided copper clad Mylar substrate of 0.05 mm thickness. This kind of substrate is flexible and can be moulded and mounted around surfaces if required. The double-sided Mylar was etched and the coaxial cable as well as the BAR64 diode were soldered at the backside. The antenna design can be seen in Fig. 3.6.

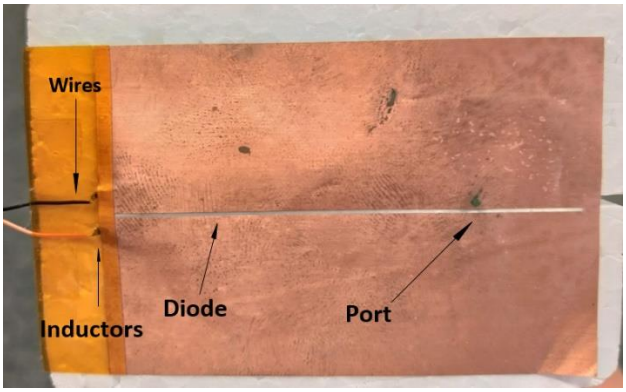

(a)

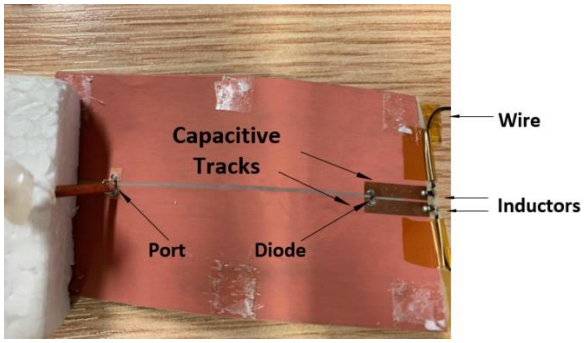

(b)

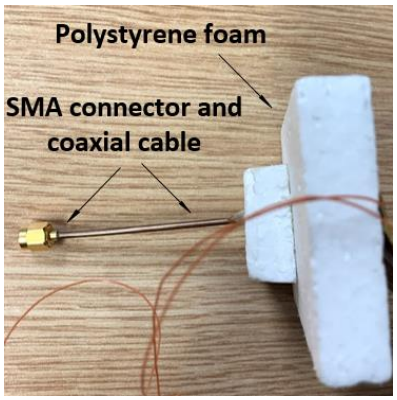

(c)

Fig 3.6. Etched antenna design displaying the SMA connector and extension wires from (a) front, (b) back, (c) side

The etched antenna design was mounted over a piece of Polystyrene foam for strength. At the ending of the biasing circuit tracks at the backside, two 47 nH inductors were soldered. The two inductors were used for RF separation. At the end of the inductors, two thin wires were expanded up to a distance of 100 cm to supply the input voltage and a 1 kΩ resistor was added to protect the biasing circuit from burning out and to stem the flow of current going into the diode.

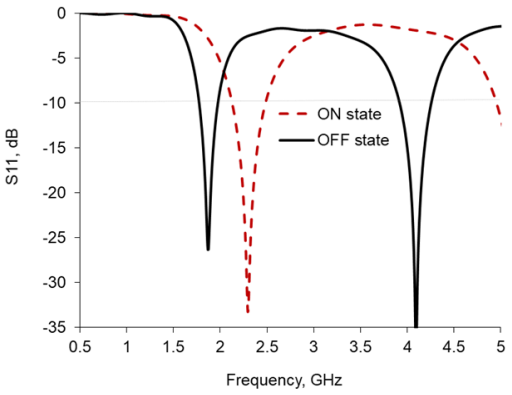

(a)

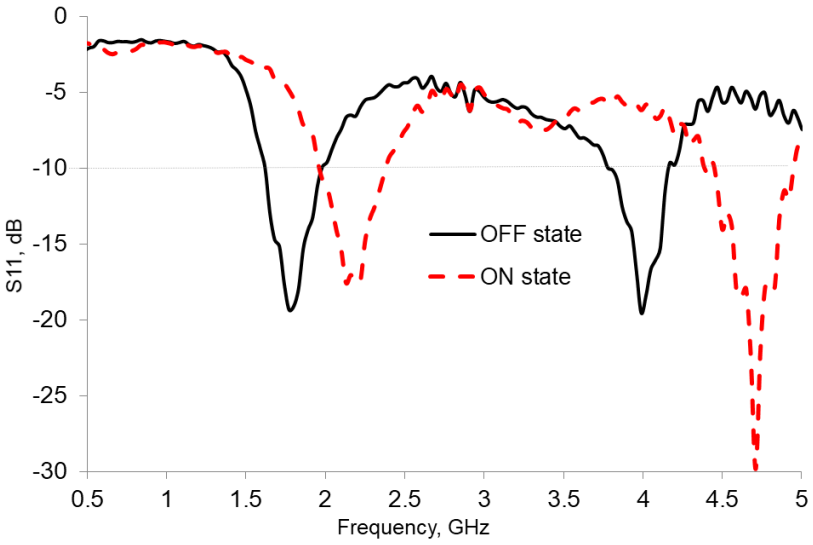

(b)

Fig. 3.7. Reflection coefficient results for ON state and OFF state with (a) Simulation results and (b) Measurement results.

Reflection coefficient (S_{11}) measurements of this antenna were conducted using an R&S® ZVL135 Vector Network Analyzer while supplying the diode with a DC power supply. The effect of the ON and the OFF states on S_{11} can be seen in Fig. 3.7. The measured -10 dB band ranged from 1.56 GHz to 2.5 GHz. The central frequency of operation increased from 1.7 GHz in the OFF state to 2.32 GHz in the ON state. The differences from the simulations were probably caused by the physical characteristics and the encapsulate effect at RF of the diode which could not entirely be included in the simulations due to the extreme disparities in the effects of various diodes. The radiation patterns for the two states can be seen in Fig. 3.8 and Fig. 3.9. The radiation patterns were in agreement with the expected radiation pattens of a complementary dipole. The radiation patterns in the XZ-plane were omnidirectional with higher directivity observed towards the front and the backside of the antenna than to the sides. Patterns obtained were akin to the simulations. The long and rigid coaxial cable at the back was probably the primary cause for the differences between simulations and measurements along the YZ-plane. As the cable was not affixed and was free to move, modelling and considering the cable in the simulations was not feasible. The gain of the antenna was measured in the anechoic chamber with the help of the standard horn antenna that was available. The computed gains of the antenna were 5.0 dBi at 1.87 GHz in the OFF-state and about 5.2 dBi at 2.32 GHz in the ON-state. The measured gain was 4.2 dBi for the OFF state at 1.7 GHz and 4.4 dBi for ON state at 2.32 GHz which was approximately 0.7 dBi lower than the simulated and computed gains.

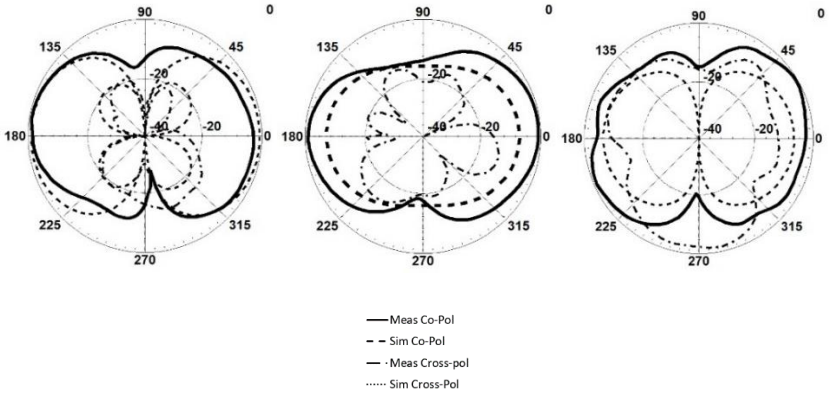

(a) (b) (c)

Fig 3.8. Radiation patterns for OFF state at 1.7 GHz in (a) XY, (b) XZ and (c) YZ planes

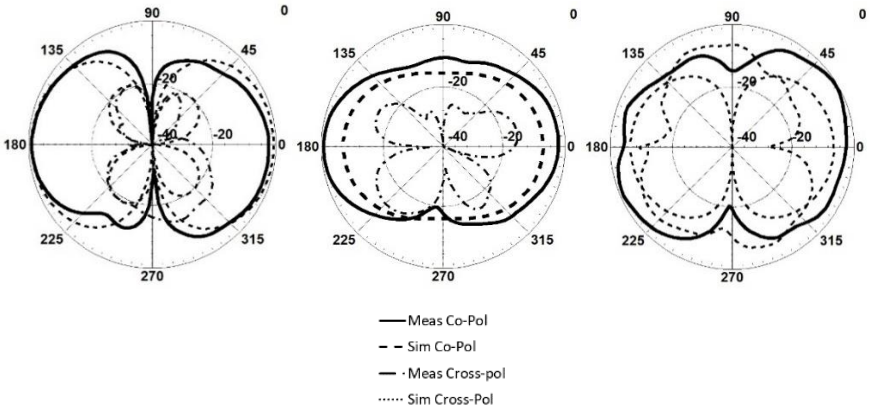

(a) (b) (c)

Fig 3.9. Radiation patterns for ON state at 2.32 GHz in (a) XY, (b) XZ and (c) YZ planes

3.3 Tunable Antenna

3.3.1 Tunable Antenna Design

The design of a tunable antenna was realised using the same design as the one illustrated in Fig. 3.2. The switching diode was replaced with a varactor (varicap) diode and the dimensions of the slot and the antenna aperture were adjusted. The tunable antenna was smaller in dimensions as compared to switching antenna. The positioning of the diode on the tracks and the positioning of the port were also changed for the tunable antenna. In addition to these changes, the orientation of the DC source had to be reversed in order to operate in the variable capacitance region of the varactor. The new dimensions of the tunable antenna design are given in Table II. The design consisted of a square patch of 69.4 mm by 47.1 mm dimensions comprising of a slot with 65.4 mm length and 0.5 mm height. A BB857 varactor diode [32] was soldered between the two biasing tracks, which were of 15 mm by 3.5 mm dimensions at the backside. Two 47 nH inductors were soldered on the left side at the rear end of the antenna within the biasing tracks along with the connecting wires that followed the inductors for DC isolation as well as the wired connection which was essential to tune the antenna by varying the supply voltage.

TABLE II

Tunable antenna dimensions (mm)

Length	L_s	S_w	L	W	P_x	D_x	T_l	T_w
Dimensions (mm)	65.4	0.5	69.4	47	15.8	30.7	15	3.5

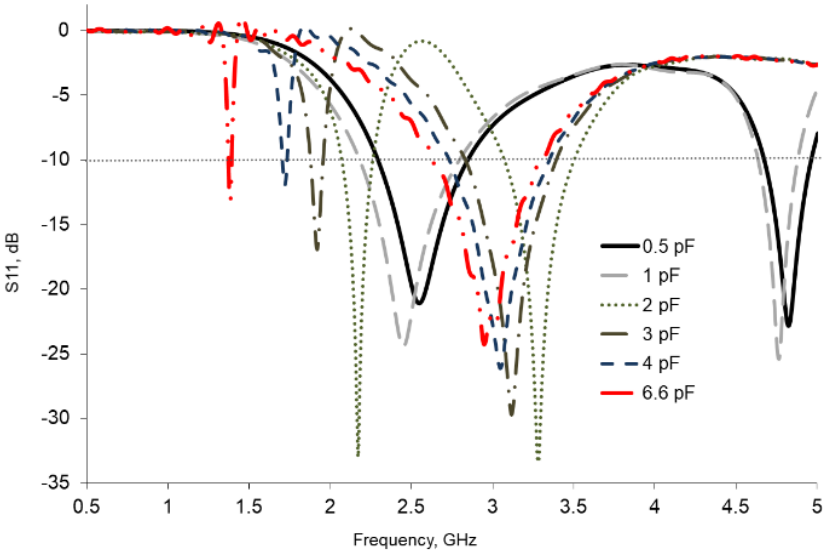

Fig. 3.10 Simulated reflection coefficient (S_{11}) results for the capacitance range of 0.5 - 6.6 pF

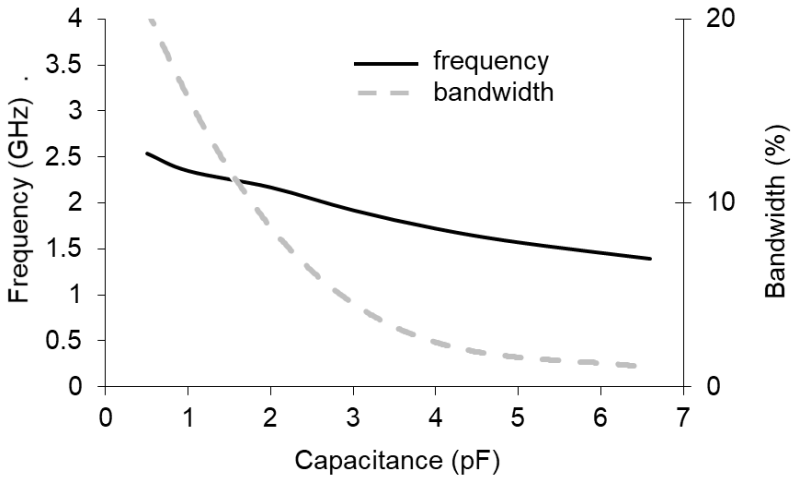

Fig. 3.11 Capacitance vs Frequency vs Bandwidth relationship from simulation results

The simulated S_{11} results can be observed from Fig. 3.10. The resonant central frequency fluctuated from 2.53 GHz at a capacitance value of 0.5 pF to 1.4 GHz for a capacitance value of 6.6 pF of the varactor diode. A correlation between capacitance values and frequency along with the bandwidth can be observed in Fig. 3.11.

The value of the frequency progressively decreased with an increase in capacitance. This led to a liner correlation that can be tracked with the help of the following fitted equation:

$$f_o = -0.1895C + 2.5497 \quad (2)$$

Where f_o stood for the frequency of operation whereas C represented the capacitance. This fitting curve contained the coefficient of determinant, also known as the R^2 value of 97%. As per bandwidth, higher capacitance values produced a lower -10 dB bandwidth up to a capacitance value of 4 pF mark beyond which the curve stabilized and the bandwidth gradually increased from 4 pF to 0.5 pF.

The simulated value of the surface currents for the three capacitance values of 0.5 pF, 4 pF and 6.6 pF and their respective resonant frequencies can be seen in Fig. 3.12. The representation was different from the switchable antenna to segregate between the two surface currents. The surface current density was highest along the area around the varactor diode and the positioning of the port. The current density decreased gradually as the capacitance value was increased. The density of the surface currents was highest at 0.5 pF and at its lowest when the capacitance value was increased to 6.6 pF. The distribution of the surface current too was critical, as it can be seen through this study. The surface current density was highest at 0.5 pF and the current were distributed throughout the top layer. The surface currents were distributed non-uniformly around the surface area. At 4 pF, the density and the distribution of the surface currents reduced significantly and at 6.6 pF, the surface currents were only distributed around the slot and the effective length of the slot.

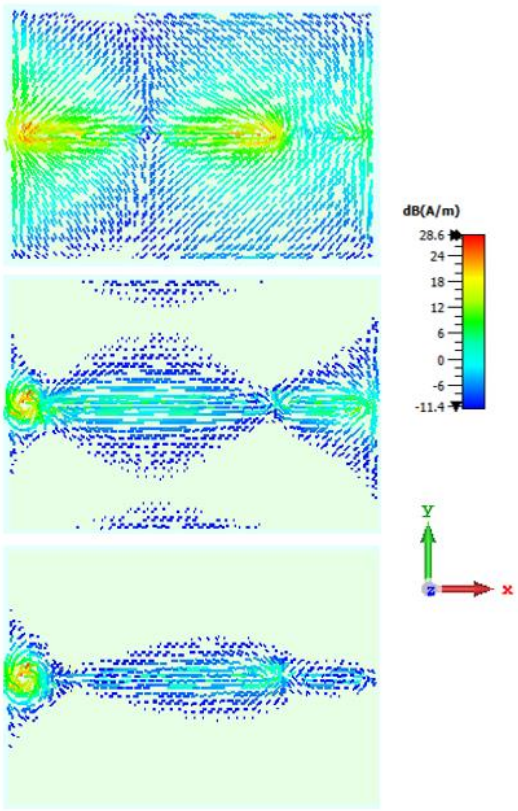

Fig. 3.12. Simulated Surface currents at 0.5 pF at 2.53 GHz (top), 4 pF at 1.72 GHz (middle) and 6.6 pF at 1.4 GHz (bottom) respectively

3.3.2 Tunable Design Fabrication and Results

As illustrated for the previous switchable design, the antenna and biasing tracks were etched on a double-sided copper clad Mylar substrate and the varactor and the SMA port along were soldered to it.

The S_{11} was measured as the DC voltage supply was varied from 28 V to 1 V. The corresponding S_{11} is seen in Fig. 3.13. The resonant frequencies increased from 1.38 GHz to 2.48 GHz as the specified range of supply voltages were varied from 1 V to 28 V. All measured results observed a shift to a slightly lower resonant central frequency and showed to have encompassed a relatively larger bandwidth compared to the simulated results. The differences could be due to effect of the physical characteristics such as the encapsulation of the diode at Radio Frequencies.

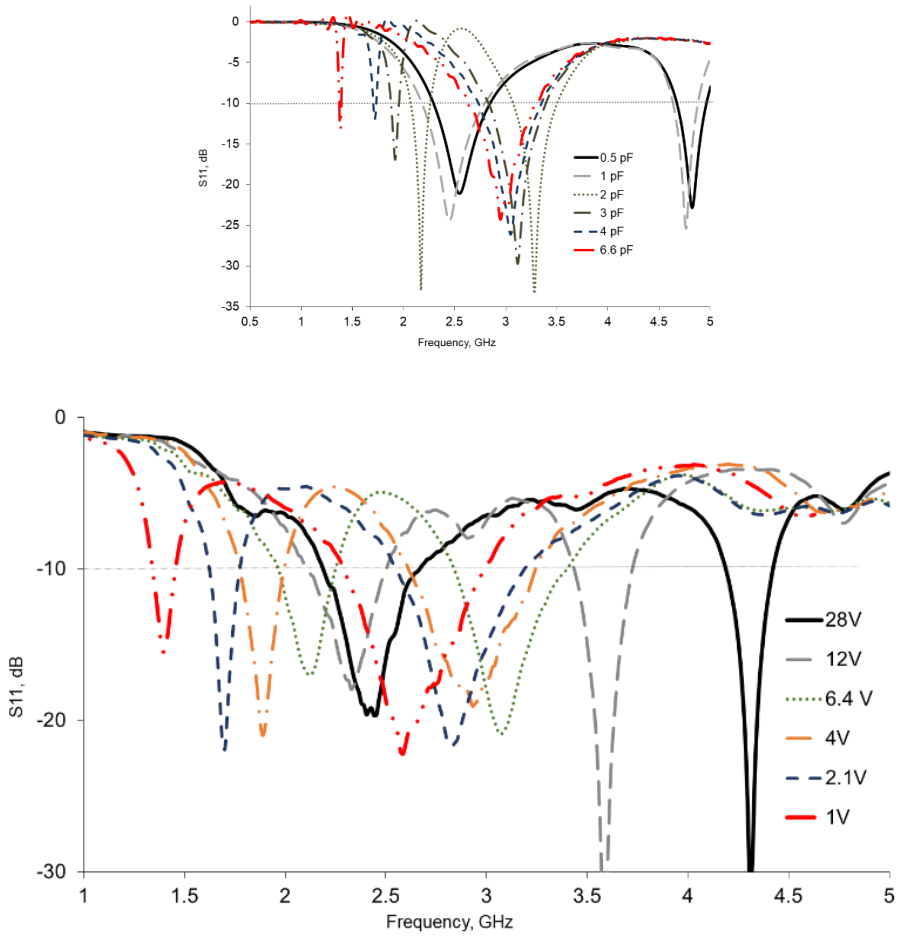

Fig 3.13. Measured reflection coefficient (S_{11}) with the corresponding voltages

A relationship between the DC supply voltage vs frequency vs bandwidth can be observed in Fig. 3.14. The frequency progressively escalated with the increase in voltage (drop in capacitance) which led to a liner relationship that followed the fitted equation:

$$f_o = 0.0378V + 1.6658 \quad (3)$$

Where f_o represented the frequency of operation whereas V represented the supply input voltage. The fitting curve had a high R^2 value of 99%. In Fig. 3.13, the frequency could be seen to be increasing with an increase in voltage from 1 V all the way up to 28 V. The bandwidth did not display a linear relationship but showed a consistent curve which gradually increased with increase in voltage. This was probably due to the losses and the internal resistance of the diode and their effects at RF levels.

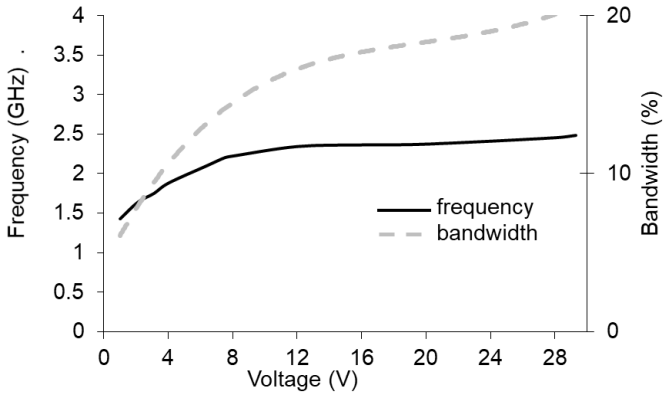

Fig. 3.14 Plot for DC Supply Voltage vs frequency vs bandwidth from measurements

The radiation patterns are presented in Fig. 3.15 to Fig. 3.17 for the supply DC voltage levels of 28 V, 12 V and 0 V, respectively. The three planes namely the XY-plane, the XZ-plane and the YZ-plane are shown in (a), (b) and (c) sub-sections of Fig. 3.16 to Fig. 3.18, respectively. The patterns are those anticipated for a complementary dipole which is fed through a coaxial cable which is mounted at the rear side of the antenna. The patterns were predominantly omnidirectional along the XZ-plane.

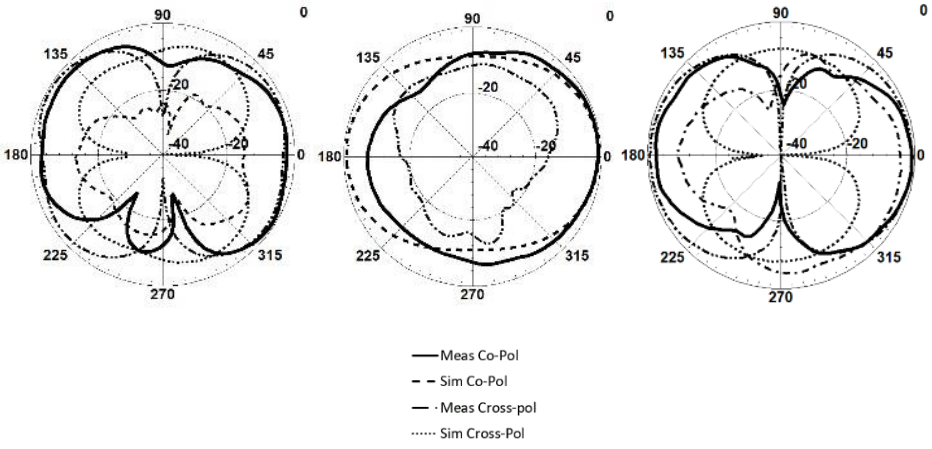

(a) (b) (c)

Fig. 3.15. Measured first mode radiation patterns at 28 V for 2.42 GHz for the antenna (a) XY-plane, (b) XZ-plane and (c) YZ-plane

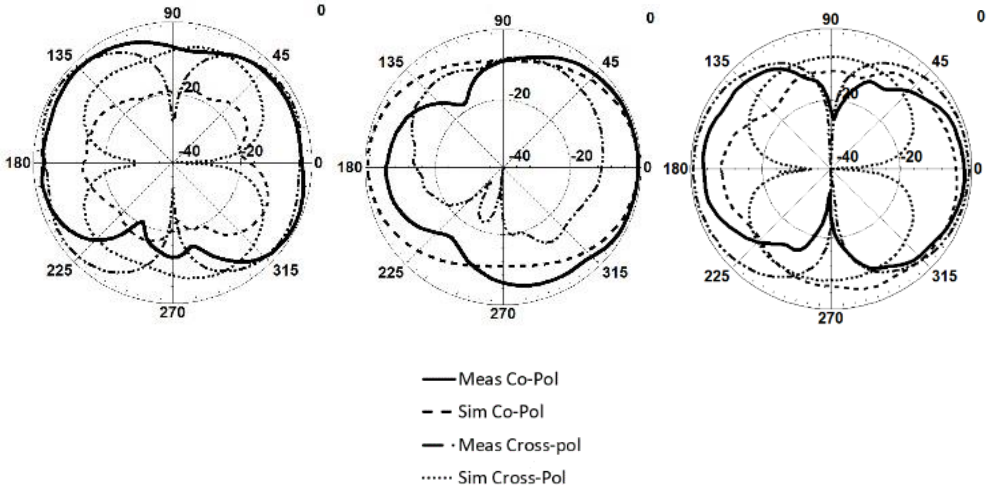

(a) (b) (c)

Fig. 3.16. Measured first mode radiation patterns at 6.4 V for 2.12 GHz for the antenna (a) XY-plane, (b) XZ-plane and (c) YZ-plane

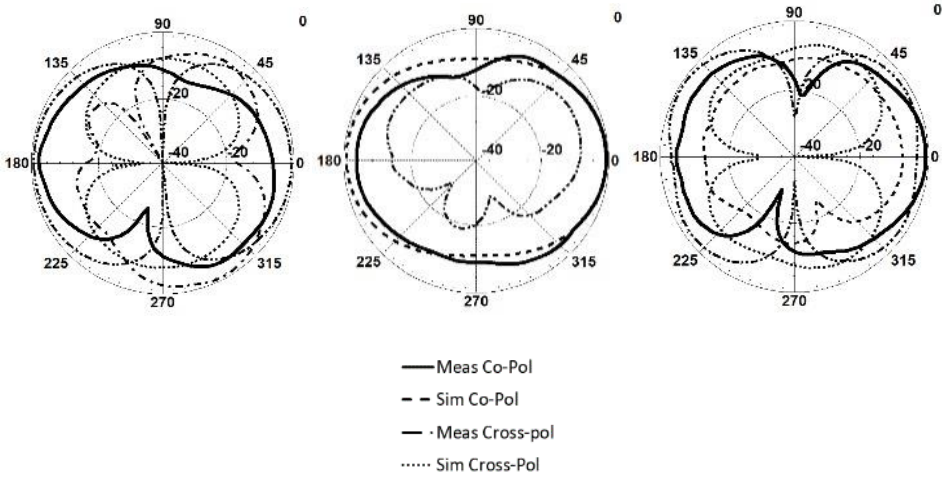

(a) (b) (c)

Fig. 3.17. Measured first mode radiation patterns at 1 V for 1.4 GHz for the antenna (a) XY-plane, (b) XZ-plane and (c) YZ-plane

The gains were calculated using the varactor models at the two end capacitances and the gains were 5.09 dBi for the 0.5 pF capacitance and 2.6 dBi for 6.6 pF. The measured gains were 4.7 dBi at 28 V and -1.7 dBi at 1 V which contained approximately 0.4 dBi drop in the gain from simulations at 0.5 pF and about 4 dBi drop at 6.6 pF in simulations.

3.4 AC Current Sensing with Tunable Antenna

An application for the tunable antenna is proposed in this section where the antenna can be deployed as a key component within a current sensing setup. The system can be deployed in domestic appliances as a sensing system that can detect the current passing through a wire of an appliance. The AC current passing through a wire can be converted into DC using an AC/DC converter. The converted DC voltage can be supplied to alter the frequency response of the tunable antenna. By detecting the altered frequency response of the antenna, the dual-operation sensing system can not only sense the AC variations in the wire but also potentially transmit the data over Bluetooth band.

3.4.1 AC Current Sensing System

The current sensing setup comprises of the tunable antenna connected to a current transformer and an AC/DC convertor to create a smart AC current sensing mechanism. The tunable antenna discussed in the previous section is deployed here. The proposed current sensing setup incorporates the tuning antenna with a current transformer (CT). The prominence and the novelty of the concept here lies in the implementation of the sensing mechanism by deploying the reconfigurable antenna as a part of a sensing system that can detect the variations in the current through the first band and transmit the signals using the Bluetooth band for smartphone networks. The representation outline of the proposed current sensing mechanism is depicted in Fig. 3.18 which circumscribed three essential aspects: (I) Sensor transformer coil, (II) rectifier and filtering circuit, and (III) Reconfigurable tunable antenna. Current transformer already contains the first two aspects. The mechanism is utilized to sense the AC current passing through a wire and convert it into DC voltage [33]. This converted DC voltage is then utilized to monitor and alter the reactance of the varactor diode used within the tuning circuit of the antenna. The physical application of Fig. 3.18 is realised in Fig. 3.19.

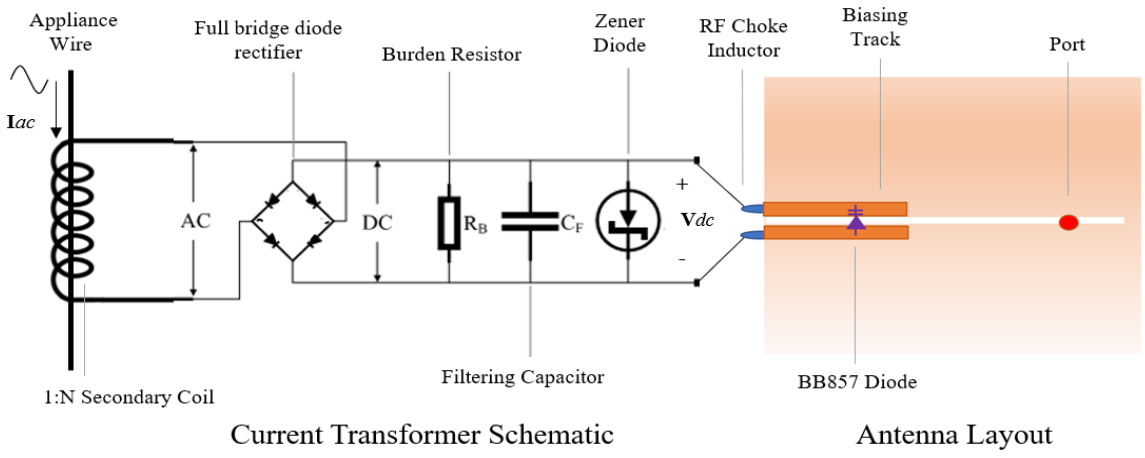

Fig. 3.18. Equivalent circuit schematics of the CT connected to the reconfigurable antenna.

The CT is attached to the tunable antenna as well as an AC current wire. The biasing tracks of the antenna are not visible in this photograph but were introduced earlier in Fig. 3.6 (b). The CT provided a linear correlation among the input current and DC output voltage under ideal conditions that can be seen in Fig. 3.20. By using results from Fig. 3.20, a novel sensing system is proposed for AC current sensing applications which senses AC current and transmits the recorded data over Bluetooth channel by deploying voltage switch.

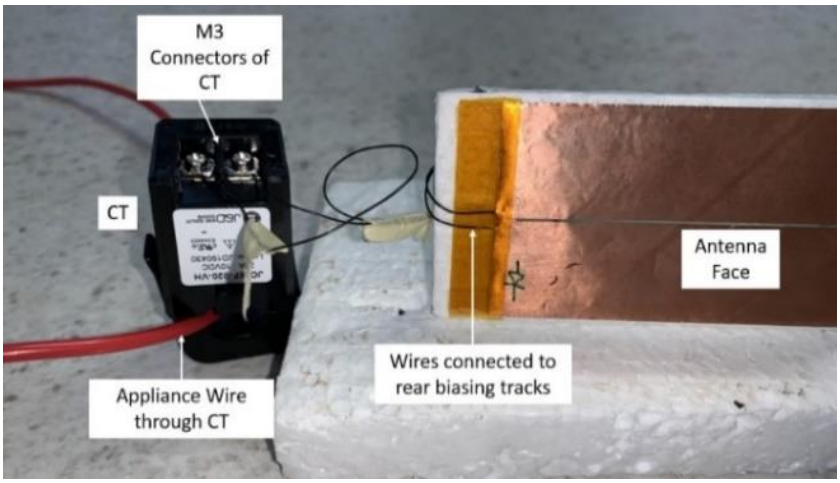

Fig. 3.19. Reconfigurable antenna connected with split wires and CT

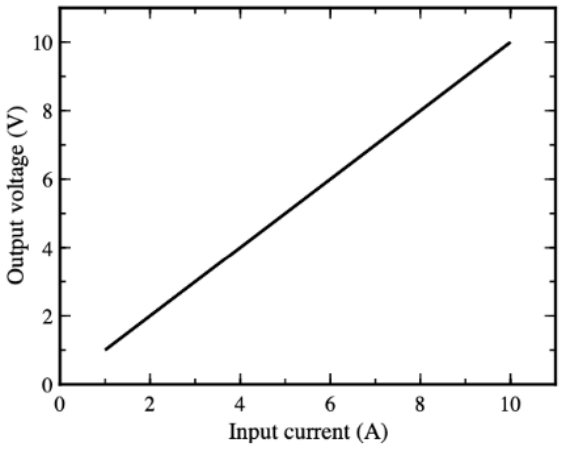

Fig. 3.20. Expected AC current input and DC output voltage for CT [34]

The reconfigurable antenna operated as a part of the current sensing mechanism while using the supply DC voltage that was transformed from the AC current coming off the electronic appliance wire by using CT or as a standalone sensing antenna with the help of an external DC voltage supply. A typical split-core CT fitted with full bridge rectifiers detects the input current which is usually passing across an electrical appliance wire and transforms the AC current value into a DC voltage output [34], [35]. This commonly available CT detects the input currents over a span of 0 A to 10 A and transforms that into a 0 V to 10 V DC output. The CT packaging also contains a burden resistor, a Zener diode, and a low-pass filter as shown in Fig. 3.18. The Zener diode restrictions the DC voltage output to a secure limit of 15 V to avoid the abrupt spikes of voltages across the output. Two M3 screw stations are mounted in CT over the removable cover that act that as the voltage output points.

BB857 Varactor diodes [32] offers a wide range of variable capacitance across the voltage. Reverse biased voltage with diode capacitance is predominantly linear from 1 V to 7 V as per the datasheet provided by the manufacturers [32] and as seen in Fig. 3.21. The voltage curve provided by the manufacturer is at 1 MHz [32]. Due to the linear characteristics of the varactor diode, the diode could provide reliable results for sensing applications.

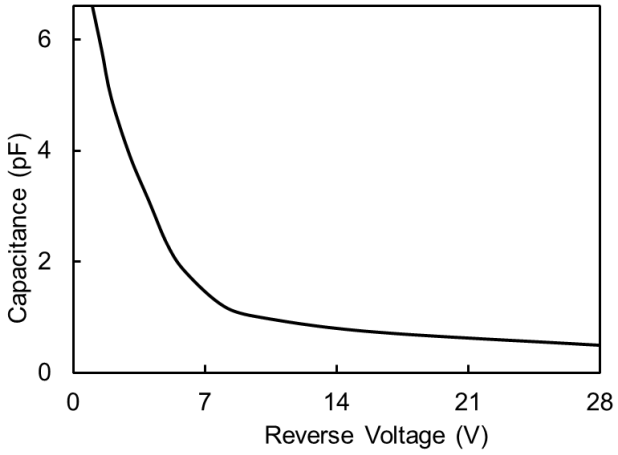

Fig. 3.21. Relationship between the reverse biased voltage and capacitance of BB857 diode [32]

3.4.2 AC Current Sensing Measurements

The AC current sensing measurement setup is shown in Fig. 3.22. The sensing mechanism comprised of a switchable standard electric heater load, a variac to change the supply AC current, an ABS box [36] that contained the CT as well as the tunable antenna. The CT was covered within the ABS box for health and safety reasons. The two output wires from the CT were expanded out of the box through the M3 screws to link up to the antenna. The antenna was attached to a VNA to observe the reflection coefficient (S_{11}).

Because of the type of switchable electric load that was available within the permissible health and safety concerns, only the sensing measurements ranging from 1-8 A were feasible. A range of up to 10 A can be accomplished if higher powered loads can be utilized. A commercial Brennenstuhl PM 231 E current meter [37] was used at the input mains power supply to supervise the AC current passing through in the system. The measured input current and output voltage characteristics of the system through CT can be seen in Fig. 3.23.

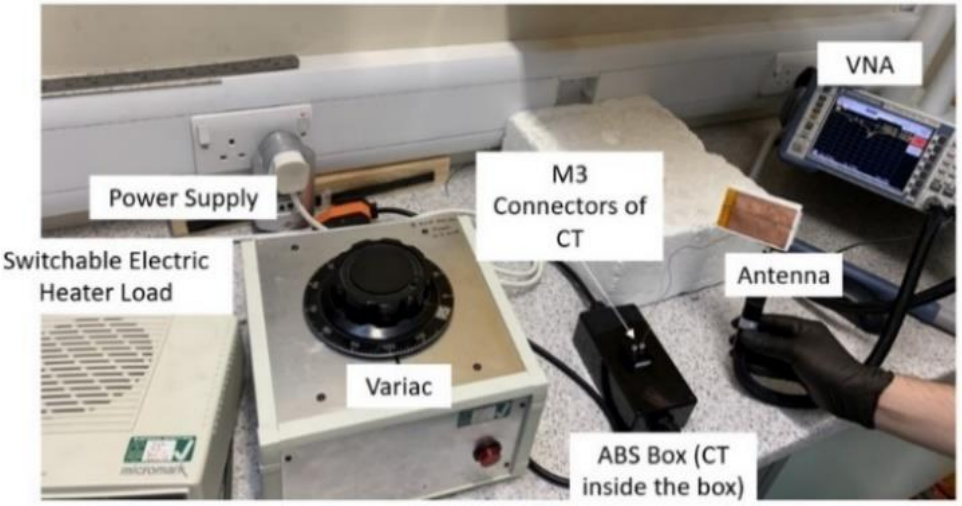

Fig. 3.22. AC Current sensing measurement system setup

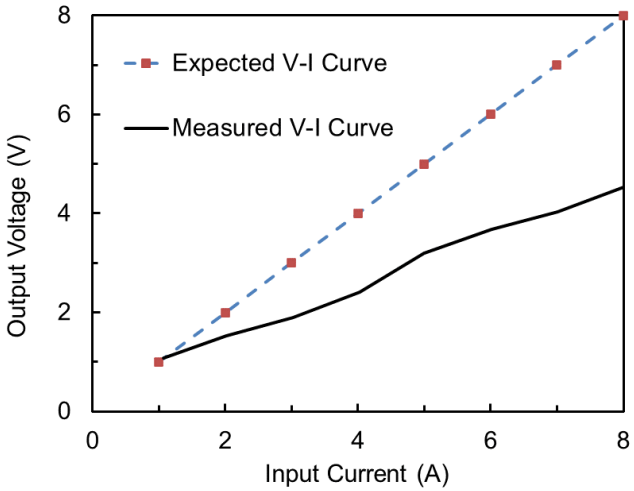

Fig. 3.23. Measured AC current input and DC output voltage for CT

As it is evident from Fig 3.23, the real DC voltage output from the AC current input did not follow a linear response and the output DC voltage was significantly lower in comparison to the expected voltage. Lower levels of DC voltage are measured due to the losses that were experienced across the switchable electric heater and owing to the coupling with the antenna components. The relation between AC current versus the resonant frequency of the antenna is demonstrated in Fig. 3.24. The resonant frequency of the antenna was measured using the VNA which was used for previous reflection coefficient measurements. Frequency of operation and the AC current values established a linear

relationship by showing a steady increase in the frequency of operation with an increase in the AC current supply. The corresponding measured reflection coefficient responses using the AC current sensing mechanism is presented in Fig. 3.25. The results are in sync with the measured results obtained in Fig. 3.24. A significant shift towards the lower band was detected beyond 1 A due to the actual received DC voltage at the antenna being different to the expected voltage as shown using Fig. 3.23. The relationship between the shift in voltage was determined through the measured voltage at the precise current values. Although the frequency of the first mode varied as the supply current changed, the second mode responses were mostly stable and covered the below -10 dB bandwidth at or around 2.5 GHz frequency band for currents up to 6 A.

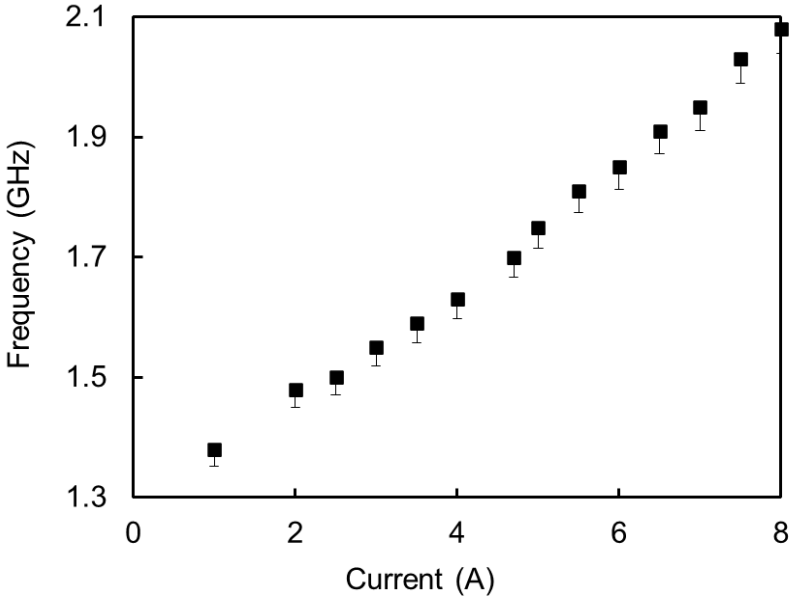

Fig. 3.24. Current sensing measurement results

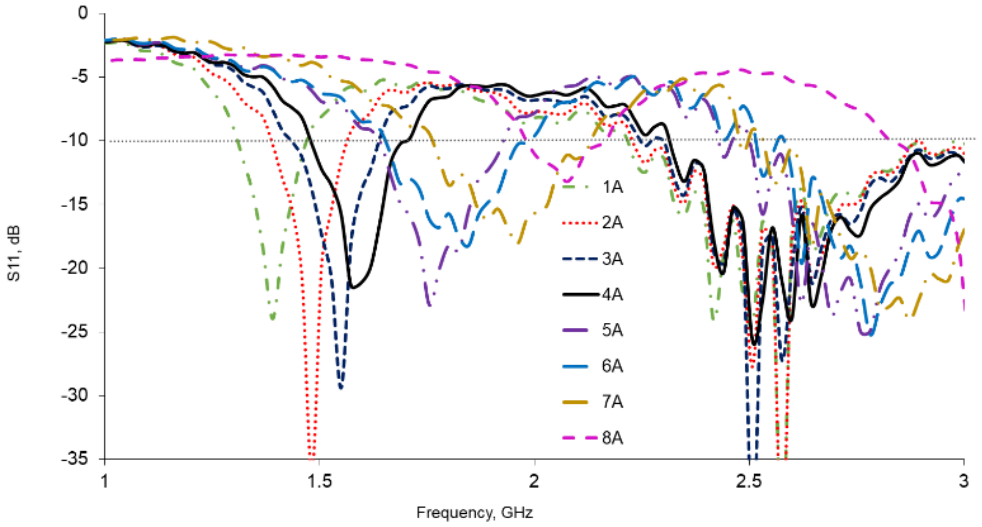

Fig. 3.25. Sensing reflection coefficient measurements using the current sensing setup measuring 1 A to 8 A

The measurements were repeated multiple times with the help of the same setting of all equipment and predominantly same conditions to demonstrate the repeatability of these results. The results were predominantly consistent and repeatable. Only some minor variations were observed that were caused due to the movement of the position of the system or the ones that were caused due to the fluctuations caused by the standard equipment. The variations remained within the tolerance range of the equipment. For the AC sensing system, the least count of the system or the lowest variation in the current that can be detected is called Sensitivity. From Fig. 3.24, the linear correlation between the frequency and the current can be described using the equation:

$$f_o = 0.1032I + 1.2438 \quad (4)$$

Where, f_o represents the frequency and I represent the current. The sensitivity of the current sensor can be determined as the slope of the curve [38]. The slope or the sensitivity of the measurements, as per equation (4) was 0.1032 GHz A^{-1}. The range of the sensitivity was from 0.075 GHz A^{-1} to 0.115 GHz A^{-1}.

3.4.3 Wireless Transmission at 2.5 GHz

Transmission at the Bluetooth band of 2.4 GHz to 2.5 GHz range can potentially take place by switching from the current sensing system mode to the signal transmission mode with an external supply of 28 V. This 28 V input can also be delivered with the help of a separate transformer that could potentially be connected to the mains AC voltage. By adding a transformer, detection of voltage fluctuations to measure power levels can also be feasible within this same system. Extremely small amount of 10 nA current is necessary for the varactor diode to operate and consequently, the external supply requires very low power and the power source can be incorporated within the proposed system in the form of a standard battery for example. For further enhancements, the antenna can use both the modes of operation where the first mode is used to sense and detect the AC current levels in the wire while the second mode can be utilized to transmit the recorded data wirelessly through Bluetooth networks. This concept can be an exciting prospect to discover in the coming future. The antenna can then be a part of a smart sensing metering system for domestic appliances. Lastly, a table comprising of a comparison between a number of smart sensing systems with this proposed AC sensing antenna system is given as Table III. A selection of smart sensing systems are compared in terms of the type of sensing, frequency range of operation, capability of direct tuning, antenna sensing, and the requirements of each system for powering, referred to as powering type. This proposed sensing system combined transmission and sensing inside the same design and offered broadband sensing that presented superior range of operation. Proposed system was the only one that offered a direct tuning throughout its entire frequency range while providing foldability and the highest degree of flexibility.

TABLE III

Comparison of Smart Power Sensing Systems and Proposed Sensing Antenna System

Ref.	Sensing Style	Frequency range of Operation	Direct Tuning Ratio	Sensing with Antenna	Powering Style
[41]	Energy-Harvesting Metering	868 MHz	No	No	Passive
[39]	Wireless, powerless RFID	850 MHz – 950 MHz	No	No	Passive
[42]	Clamp-on Inductive current	(LoRa Based)	No	No	Passive
[40]	ZigBee controller	2.4 GHz	No	No	Active
[33]	Sensor code-based RFID	768 MHz – 868 MHz	1.1:1 Sensor code	Possible	Passive
This Work	Proposed system	1.38 GHz – 2 GHz. 2.45 GHz Transmitting	2:1	Possible	Active or Passive

3.5 Conclusion

The implementation of a capacitive coupling technique to slot antennas on thin flexible substrates has been demonstrated in this chapter. The designs employ low-cost fabrication techniques as well as low-cost components and substrates. Switching and tuning antennas

can be developed using the same basic design structure. The initial design switches frequency electronically between adjacent frequency bands for the OFF and the ON state, between 1.87 GHz and 2.32 GHz. The tuning antenna can dynamically alter frequencies in the range from about 1.4 GHz to 2.6 GHz. A linear relationship between capacitance and resonant frequency can be found in the simulations, while similar linear trend between voltage and frequency is found in the measurements.

There were slender variances between simulations and measurements, both in reflection coefficient as well as radiation patterns. This was mainly due to the use of low-cost components and unavoidable fabrication errors. The complete encapsulation aspects of the diodes were not included in the simulations in the case of both the designs. The measured radiation patterns were partly affected by the coaxial cable and the wires added to connect to the biasing circuit.

It has been demonstrated that capacitive coupling provides a simple and efficient technique to create a biasing network for reconfigurable antennas where the two layers of the design remain isolated at DC but form a capacitive coupling at RF. The thin Mylar substrate also provides the option of creating the designs flexible and foldable.

A dual-function conceptual application for smart AC current sensing and transmission for smart metering by deploying the tunable slot antenna as a part of the sensing system has also been introduced and demonstrated. The smart sensing antenna system can sense AC currents passing through an electric wire of a smart domestic appliance or any other typical household electrical device. The tunable antenna provides a wide frequency response as a function of its voltage. The AC current passing through the wire is converted into its DC voltage equivalent and is directly connected to the active circuit of the antenna. The wide frequency range as a function of voltage can be sub-divided so that the lower frequencies can be used for sensing while the higher frequencies can be used for transmission wirelessly using the 2.4 GHz Bluetooth band.

References

[1] J. Barnhard, *Reconfigurable Antennas*, vol. 1. San Rafael, CA: Morgan & Claypool Publishers, 2007.

[2] M. A. Matin, "Recent Trends in Antennas for Modern Wireless Communications," *Wideband, Multiband, and Smart Reconfigurable Antennas for Modern Wireless Communications*, pp. 1–26, 2016.

[3] J. Kiriazi, H. Ghali, H. Ragaie, *et al*., "Reconfigurable dual-band dipole antenna on silicon using series MEMS switches," *IEEE Antennas and Propagation Society International Symposium. Digest. Held in conjunction with: USNC/CNC/URSI North American Radio Sci. Meeting* (Cat. No.03CH37450), 2003.

[4] B. Cetiner, G. Crusats, L. Jofre, *et al*., "RF MEMS Integrated Frequency Reconfigurable Annular Slot Antenna," *IEEE Transactions on Antennas and Propagation*, vol. 58, no. 3, pp. 626–632, 2010.

[5] E. Erdil, K. Topalli, M. Unlu, *et al*., "Frequency Tunable Microstrip Patch Antenna Using RF MEMS Technology," *IEEE Transactions on Antennas and Propagation*, vol. 55, no. 4, pp. 1193–1196, 2007.

[6] R. Bose and A. Sinha, "Tunable patch antenna using a liquid crystal substrate," 2008 *IEEE Radar Conference*, 2008.

[7] G. Ruvio, M. J. Ammann, and Z. N. Chen, "Wideband Reconfigurable Rolled Planar Monopole Antenna," *IEEE Transactions on Antennas and Propagation*, vol. 55, no. 6, pp. 1760–1767, 2007.

[8] Y. Tawk, J. Costantine, and C. G. Christodoulou, "A rotatable reconfigurable antenna for cognitive radio applications," *2011 IEEE Radio and Wireless Symposium*, 2011.

[9] G. H. Huff, D. L. Rolando, P. Walters, *et al*., "A Frequency Reconfigurable Dielectric Resonator Antenna Using Colloidal Dispersions," *IEEE Antennas and Wireless Propagation Letters*, vol. 9, pp. 288–290, 2010.

[10] D. Pozar and V. Sanchez, "Magnetic tuning of a microstrip antenna on a ferrite substrate," *Electronics Letters*, vol. 24, no. 12, p. 729, 1988.

[11] F. Yang and Y. Rahmat-Samii, "A reconfigurable patch antenna using switchable slots for circular polarization diversity," *IEEE Microwave and Wireless Components Letters*, vol. 12, no. 3, pp. 96–98, 2002.

[12] H. A. Majid, M. K. A. Rahim, M. R. Hamid, *et al*., "Frequency reconfigurable microstrip patch-slot antenna", *IEEE Antennas Wireless Propag. Lett*., vol. 12, pp. 218-220, 2013.

[13] A. Kolsrud, M.-Y. Li, and K. Chang, "Electronically switchable slot antenna fed by microstrip line," *IEEE Antennas and Propagation Society International Symposium. 1998 Digest. Antennas: Gateways to the Global Network. Held in conjunction with: USNC/URSI National Radio Science Meeting (Cat. No.98CH36194)*, pp. 21–26, Jun. 1998.

[14] L. Pazin and Y. Leviatan, "Reconfigurable Slot Antenna for Switchable Multiband Operation in a Wide Frequency Range," *IEEE Antennas and Wireless Propagation Letters*, vol. 12, pp. 329–332, 2013.

[15] D. Peroulis, K. Sarabandi, and L. Katehi, "Design of reconfigurable slot antennas," *IEEE Transactions on Antennas and Propagation*, vol. 53, no. 2, pp. 645–654, 2005.

[16] N. Kou and L. Li, "Frequency and pattern reconfigurable annular slot antenna with two feeding ports," *2014 IEEE International Wireless Symposium (IWS 2014)*, 2014.

[17] M. Shirazi, J. Huang, T. Li, *et al*., "A Switchable-Frequency Slot-Ring Antenna Element for Designing a Reconfigurable Array*," IEEE Antennas and Wireless Propagation Letters*, vol. 17, no. 2, pp. 229–233, 2018.

[18] N. Symeon, R. Bairavasubramanian, C. Jr. Lugo, *et al*., "Pattern and frequency reconfigurable annular slot antenna using PIN diodes", *IEEE Trans. Antennas and Propag.*, vol. 54, Feb. 2006, pp. 439-448.

[19] J. Kelly and P. Hall, "Reconfigurable slot antenna for Cognitive Radio applications," *2009 IEEE Antennas and Propagation Society International Symposium*, 2009.

[20] S.-K. Oh, Y.-S. Shin, and S.-O. Park, "A novel PIFA type varactor tunable antenna with U-shaped slot," *2006 7th International Symposium on Antennas, Propagation & EM Theory*, 2006.

[21] S. Kawasaki and T. Itoh, “A slot antenna with electronically tunable length,” *Antennas and Propagation Society Symposium 1991*, Digest, 1991.

[22] N. Behdad and K. Sarabandi, “A Varactor-Tuned Dual-Band Slot Antenna,” *IEEE Transactions on Antennas and Propagation*, vol. 54, no. 2, pp. 401–408, 2006.

[23] J. Yang, W.-W. Choi, and K.-W. Tam, “A novel dual-band frequency tunable slot antenna with constant frequency ratio,” *2015 Asia-Pacific Microwave Conference (APMC)*, 2015.

[24] C. R. White and G. M. Rebeiz, “Single- and Dual-Polarized Tunable Slot-Ring Antennas,” *IEEE Transactions on Antennas and Propagation*, vol. 57, no. 1, pp. 19–26, 2009.

[25] A. H. Mohammadi and K. Fororaghi, “A varactor-tuned substrate-integrated cavity-backed dumbbell slot antenna*,” 2012 15 International Symposium on Antenna Technology and Applied Electromagnetics*, 2012.

[26] M. Kuzlu, M. Pipattanasomporn and S. Rahman, "Hardware demonstration of a home energy management system for demand response applications", IEEE Trans. Smart Grid, vol. 3, no. 4, pp. 1704-1711, Dec. 2012.

[27] X. L. Bao and M. J. Ammann, "Monofilar Spiral Slot Antenna for Dual-Frequency Dual-Sense Circular Polarization," in IEEE Transactions on Antennas and Propagation, vol. 59, no. 8, pp. 3061-3065, Aug. 2011, doi: 10.1109/TAP.2011.2158964.

[28] A. Vamseekrishna, B. T. P. Madhav, T. Anilkumar and L. S. S. Reddy, "An IoT Controlled Octahedron Frequency Reconfigurable Multiband Antenna for Microwave Sensing Applications," in IEEE Sensors Letters, vol. 3, no. 10, pp. 1-4, Oct. 2019, Art no. 3502204, doi: 10.1109/LSENS.2019.2943772.

[29] B. P. Chacko, G. Augustin and T. A. Denidni, "Electronically Reconfigurable Uniplanar Antenna With Polarization Diversity for Cognitive Radio Applications," in IEEE Antennas and Wireless Propagation Letters, vol. 14, pp. 213-216, 2015, doi: 10.1109/LAWP.2014.2360353.

[30] C. Balanis, *Antenna theory*, 4th ed. Hoboken, New Jersey: Wiley, 2016, pp. 653-739.

[31] “Infineon BAR64-03W datasheet.” [Online]. Available: https://www.infineon.com/dgdl/Infineon-BAR64-03W-DS-v01_01-EN.pdf?fileId=5546d462689a790c01690f0250e138fe . [Accessed: 20-Jun-2020].

[32] “Infineon BB857 Datasheet.” [Online]. Available: https://www.infineon.com/dgdl/Infineon-BB837_BB857SERIES-DS-v01_01-en.pdf?fileId=db3a304313d846880113d97339a9011a . [Accessed: 21-Jun-2020].

[33] I. Ullah, R. Horne, B. Sanz-Izquierdo and J. C. Batchelor, "RFID AC Current Sensing Technique," *in IEEE Sensors Journal*, vol. 20, no. 4, pp. 2197-2204, 15 Feb.15, 2020, doi: 10.1109/JSEN.2019.2949856.

[34] Magnelab. (Jul 27, 2020). *DCT-0016-10/10Vdc Split-Core Current Sensor*. [Online]. Available: http://www.magnelab.com/products/acsplitcore-current-sensor-dct-0016-100/

[35] Dd Magnelab. (Jul. 27, 2020). *SCT-125w-100 by Magnelab*. [Online]. Available: https://www.magnelab.com/products/wireless-ac-currentsensor-system-sct-125w/

[36] Hammond 1591, "1591DSBK | Hammond 1591, Black Polystyrene Enclosure, IP54, 150 x 80 x 46mm | RS Components", *Uk.rs-online.com*, 2020. [Online]. [Accessed: 25- Jul- 2020].

[37] Brennenstuhl Smart Technology. (Jul. 19, 2020). *Primera-Line Wattage and Current Meter PM 231 E*. [Online]. Available: https://www.brennenstuhl.co.uk/en-GB/products/adapter-plugs/primera-linewattage-and-current-meter-pm-231-e-gb

[38] W. Wang, Y. Jia, X. Liu, Y. Liang, X. Xue, and Z. Du, “Enhanced sensitivity of temperature-compensated SAW-based current sensor using the magnetostrictive effect,” Smart Materials and Structures, vol. 26, no. 2, p. 025008, 2016.

[39] B. S. Cook *et al*., "RFID-Based Sensors for Zero-Power Autonomous Wireless Sensor Networks," in *IEEE Sensors Journal*, vol. 14, no. 8, pp. 2419-2431, Aug. 2014, doi: 10.1109/JSEN.2013.2297436.

[40] J. Han, H. Lee and K.-R. Park, "Remote-controllable and energy-saving room architecture based on ZigBee communication," *2009 Digest of Technical Papers International Conference on Consumer Electronics*, Las Vegas, NV, 2009, pp. 1-2, doi: 10.1109/ICCE.2009.5012332.

[41] S. DeBruin, B. Campbell, and P. Dutta, “Monjolo: An energy-harvesting energy meter architecture,” in *Proc. SenSys*, Roma, Italy, Nov. 2013, pp. 18:1–18:14.

[42] G. Dalpiaz, A. Longo, M. Nardello, R. Passerone and D. Brunello, "A battery-free non-intrusive power meter for low-cost energy monitoring," *2018 IEEE Industrial Cyber-Physical Systems (ICPS)*, St. Petersburg, 2018, pp. 653-658, doi: 10.1109/ICPHYS.2018.8390784.

CHAPTER 4

MANUFACTURING OF LOW-COST INKJET PRINTED FREQUENCY RECONFIGURABLE ANTENNAS

4.1 Introduction

This chapter describes the manufacturing aspects and considerations of developing frequency reconfigurable antennas using low-cost inkjet-printing technology. Inkjet printing using silver nanoparticle ink on a variety of substrates is a well acknowledged method that provides the choice to print designs in an uncomplicated, inexpensive way directly from the design models without the need for a mask. Use of inkjet printing to create novel, single-layer, two conductive-patch aperture antenna solution for frequency reconfigurable antennas is presented in this chapter. The solution makes use of a typical household inkjet printer, refillable ink cartridges or cassettes filled with nanoparticle silver ink and inexpensive switching and tuning diodes and RF components. Two design solutions are presented where the same single-layered antenna aperture printed on Polyethylene Terephthalate (PET) substrate is employed for frequency switching and tuning antennas. The switching and tuning antennas switch and tune between neighbouring frequency bands. The designs made use of two printed conductive patch aperture of equal size which were a short distance apart from one another. RF components are glued to produce an orifice that can be utilized for switching and tuning by mounting capacitors with the help of conductive adhesives towards the two ends of the aperture to create a complimentary dipole. Low-cost capacitors, switching and varactor diodes and inductors are mounted on the printed design by using conductive glue. Switching diodes are used for frequency switching whereas varactor diode is deployed for tunable configurations. Single-band frequency switchable antenna switched between two adjoining frequency bands when the supply voltage was varied between ON and OFF states while dual-band tuning antenna design demonstrated active and dynamic tuning between the neighbouring frequencies of operation. Highly conductive Mitsubishi ink filled in refillable cartridges was used for printing the conductive

aperture solution for antennas. The conductive silver ink creates a uniform layer with reliably uniform conductivity. The bands of operation for the solutions allow the antennas to be suitable for mobile communication, Bluetooth, and wireless technologies. Dual-band nature of the tunable antenna makes it an ideal solution to link between 3G, 4G and 5G networks. The objective of this chapter is to demonstrate the manufacturing considerations of using low-cost inkjet-printing to provide an inexpensive, efficient, and straightforward solution for smart frequency reconfigurable antennas with rapid prototyping and reliable performance. The central resonant frequencies of operation for both antenna solutions cover the 2.4 GHz band which finds its applications in the wireless communications range. The second band of the tunable solution provides coverage in 4G as well as 5G frequency spectrum thereby being an ideal link for two technologies.

Traditional etching and subtractive manufacturing have traditionally been the most common methods used in fabrications of antennas and various electronic devices. In recent times, printing electronics using additive manufacturing (AM) has become apparent as a rapidly evolving field of interest [1]. A range of electronic devices manufactured with the help of AM are presented in [2]-[9]. Techniques such as inkjet printing, SLA, FFF and FDM have been popular in AM [11]-[13]. Inkjet printing using Metallo-Organic decomposition (MOD) inks on various substrates has been reported in [7], [14]-[20]. This chapter deals with the accessibility and cost efficiency of the printers for domestic usage by presenting a frequency reconfigurable antenna solution using inkjet printing technique. The solution offers the possibility of printing the basic antenna aperture in volume and use the same antenna aperture for frequency switching as well as frequency tuning.

The chapter is arranged as follows: Section 4.2 discusses the manufacturing considerations which were contemplated before the designing of the antenna. Section 4.3 discusses the antenna design and simulation results. Section 4.4 introduces inkjet printing of the design and surface pictures and profiles. The antenna performance is verified with the experimental results. Conclusion is presented in section 4.5.

4.2 Manufacturing Considerations

A significant number of manufacturing considerations had to be taken into account before developing the reconfigurable antenna design. The manufacturing considerations were required

to design a solution that could be manufactured with reliable performances. The considerations were made keeping the broader goal of keeping the low-cost development of the design in mind.

Firstly, inkjet printing technology making use of low-cost equipment primarily allowed as a fabrication of single-sided layer as most PET and paper-based substrates are only manufactured for single-sided fabrication. Due to the characteristics of the low-cost substrates, the inkjet-printed design had to be a single-layer solution. Secondly, producing vias through flexible substrates was proven to be a cost-inefficient alternative. To overcome that hurdle, design had to be developed which did not require any vias or holes through the substrates. Thirdly, due to their small temperature tolerances, soldering active components directly onto the printed design was not a sustainable option as the soldering resulted in the substrates to burn or melt. Conductive adhesives were a potential dependable alternative to soldering. Using conductive inks could also be a potential solution that supported dismounting and reattaching the RF components.

4.3 Switchable Antenna Design

Complimentary dipoles can be developed and designed as a possible option to create frequency reconfigurable antennas by adding an active circuitry to the radiating structure as it was demonstrated in the previous chapter. The frequency switchable antennas are typically double layered structures in which the components are likely to be mounted using some form of biasing circuitry at the backside of the main design. Due to the manufacturing constraints presented by inkjet printing, an antenna was designed keeping the manufacturing limitations in focus. The design was needed to be a single sided design and a single-polarised slot antenna design, that was discussed earlier was taken as the base design. A base solution was designed that could accommodate both switching and tuning antenna within the same aperture.

4.3.1 Design dimensions

Switchable antenna solution is proposed for frequency reconfigurable antennas on PET substrate using inkjet printing technique here. Initial design for frequency switching can be seen in Fig. 4.1. The design consisted of an aperture of two conductive patches separated by a short distance. Studies of this antenna aperture and the implementation of this technique for

frequency switchable antenna is described here. Switchable antenna is realised by adding two 100pF capacitors to create an effective complimentary dipole which is finite in length. Inexpensive BAR64 PIN diode was used [23]. The positioning of the capacitors to determine the correct frequency matching was achieved using extensive parametric studies of their positioning. Fig 4.1 presents the front viewpoint of the single-layer design. Dimensions for the design are shown in Table 1. An infinite length slot was designed on the top layer on the printable side while on the backside, two tiny rectangular square patches were glued manually for the coaxial port for the feed.

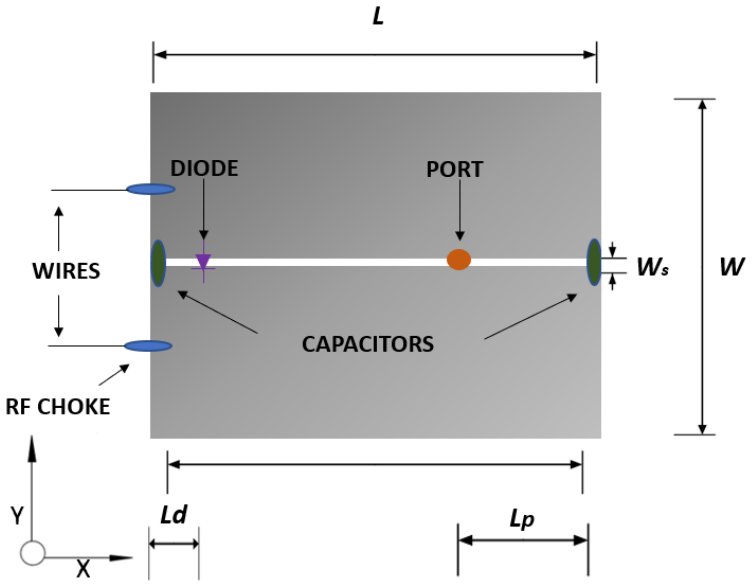

Figure 4.1 Switching antenna design.

TABLE I

Switchable antenna dimensions (mm)

Length	L_d	L_p	L	W	W_s
Dimensions (mm)	5.7	12.2	61.9	44.7	0.7

Two 100 pF capacitors were mounted at 0.6 mm from the edges across the slot that made the slot design finite in length. The diode (in purple) was mounted on one side and the port (in orange) was mounted at the rear end from the other side. The main dimensions of antenna aperture were L = 61.9 mm, W = 44.7 mm, and W_s = 0.7 mm where L and W represents the

length and the width of the design while W_s denoted the width of the created slot. Positions of the diode and the port were L_d = 5.7 mm and L_p = 12.2 mm. The desired resonant frequency was achieved by adjusting the position of the diode along the slot with parametric analysis. The thickness of the PET substrate was 0.123 mm, and the dielectric permittivity was 3.1 with a loss tangent of 0.02 and with the resistivity of 16 x 10^{15} Ω.cm.

An exceedingly thin PET substrate (0.123 mm) in comparison to the wavelength facilitated the pads at the back to be regarded as connected to the printed design layer on the front at RF. That is owing to the low impedance of the capacitive components at high frequency. At DC, the two layers act entirely detached from one another.

4.3.2 Simulation Results

The antenna was simulated with the help of CST Microwave studio™ using finite integration technique (FIT) time domain solver and simulated reflection coefficient (S_{11}) can be seen in Fig. 4.2. To switch between the two states, the effective resistance and capacitance values were altered for the diode to observe the ON-state and OFF-state respectively. The effective equivalent value of the diode was 0.17 pF for the OFF-state and 2.1 Ω for ON-state. In Fig. 4.2, the continuous black line denotes the OFF-state and the dashed violet line donates the ON-state. As it can be observed from the figure, the OFF-state resonated at 2.2 GHz with bandwidth of 17% below -10 dB whereas the ON-state resonated at 2.6 GHz with a bandwidth of 21% below -10 dB. The total resultant increase in the bandwidth was about 23%. The simulated surface current distribution can be seen in Fig. 4.3 where Fig. 4.3 (a) represents the OFF state and Fig. 4.3(b) represents the ON state. It can evidently be noticed that the addition or the active state of the diode decreases the effective length of the slot once it is in the ON state and surface currents are generally clustered around the effective slot area. A detailed comparison of the measured and simulated radiation patterns and the cross-polarizations is presented later in Section 4.3.3.

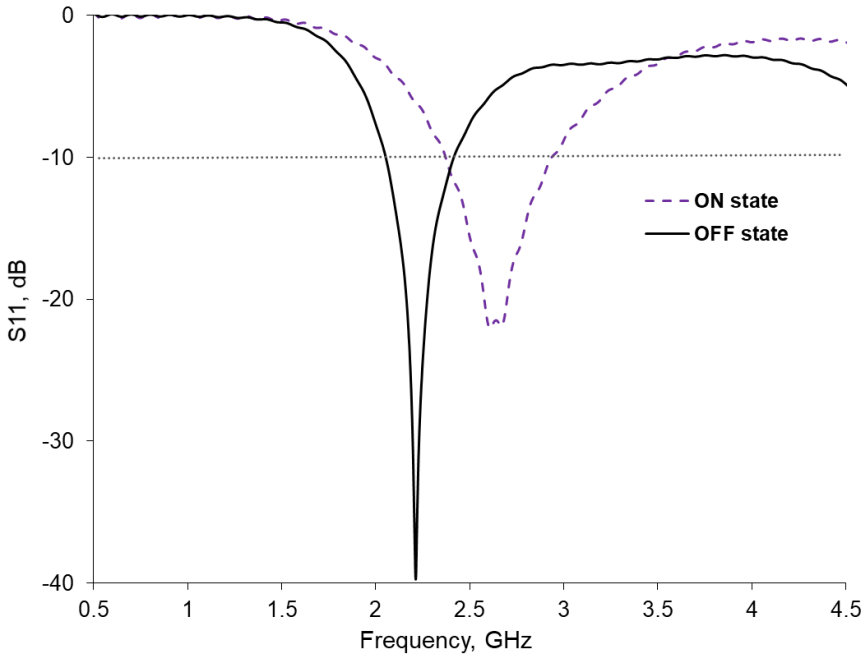

Figure 4.2 Simulated reflection coefficient (S_{11}) results for ON state and OFF state

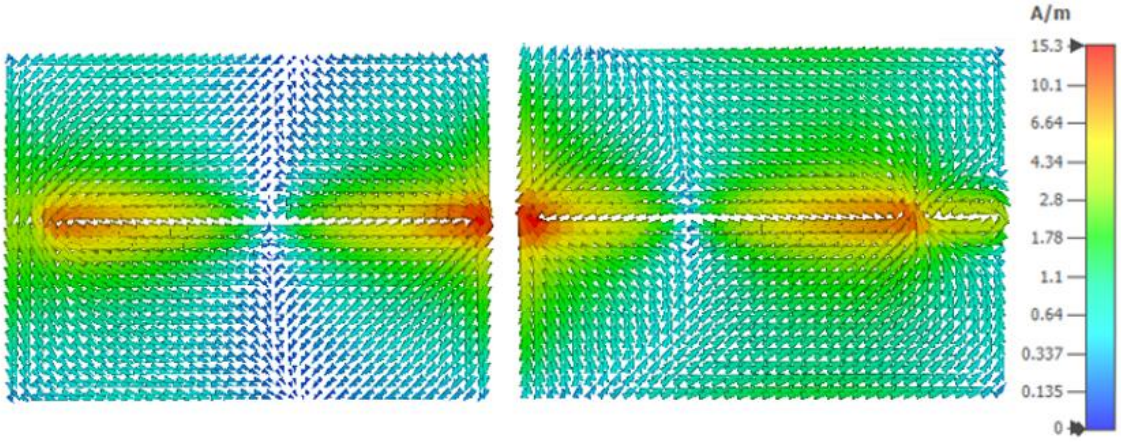

(a) (b)

Fig 4.3 Simulated surface currents for (a) OFF-state and (b) ON-state

4.3.3 Design fabrication and measurements

The conductive metallic patches for the antenna were printed using the inkjet printer. The inkjet printing techniques uses a printing nozzle which constitutes of a combination of hundreds of tiny deposition guns that fire several tiny droplets of ink directly onto the substrate. The

droplets or dots are extremely tiny in diameter and can only be examined under a high-quality microscope. The finest available inkjet printers available in the market can print as good a quality as 5000 dpi but they are industry grade and therefore, costly. The most used typical inkjet printers can print with a quality that varies from 1200 dpi to 2000 dpi. Silver nano inks are extensively used with these printers as they provide consistent conductivity throughout the printed area. The results which are acquired with the help of inkjet printing are appreciably analogous to those obtained using traditional fabrication practices such as etching.

Mitsubishi® silver nano ink is one of the commercially available conductive ink which extends the ease to print electronic circuits using typical industrial and household printers [21]. Electronic circuit designs and patterns can be printed with the same simplicity as the ordinary documents are printed using a printer. This ink is developed using a blend of silver, water, ethanol and ethylene glycol. This composition of conductive silver and chemicals lets the ink spread across the printed areas as per the design model while providing a uniform conductivity of 0.2 Ω/sq or 20 μΩ·cm at 120°C as a standard value provided by the manufacturer [21].

The design aperture structure was exported to a Single layer Gerber (gbr) file using CST Microwave Studio™. That gerber file was then introduced in Viewmate® software and a masking file was created for the desired antenna aperture. A household Brother MFC-J5910DW inkjet printer as seen in Fig. 4.4 was used for printing the design. The nanoparticle silver ink was filled in reusable cassettes as seen in Fig. 4.5 which worked as an alternate solution to using the pre-packaged nanoparticle silver ink cartridges such as AgIC. Using refillable cassettes reduced the fabrication costs even further.

Figure 4.4 Brother inkjet printer used for printing.

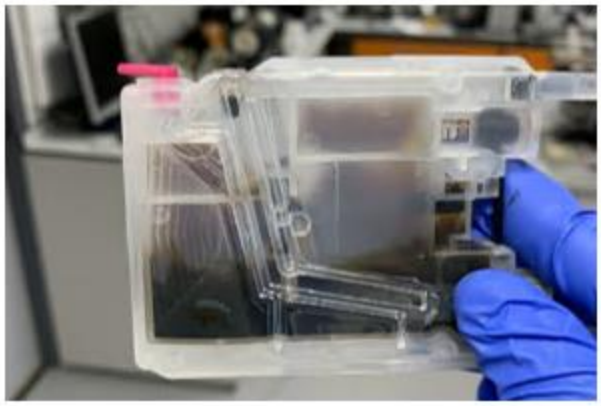

Figure 4.5 A refillable Brother printer cartridge

The aperture was printed using the printer at 1200 dpi quality. The printer creates the design pattern obtained from the mask which was creating using Gerber file. The printer reads the mask file and converts it into an electromagnetic pulse that determines the deposition of droplets of silver ink via numerous nozzles of the printer. The entire design gets printed as one single stretch of print generating using one sequential pulse with the printer internally selecting the printing of the design from the top to the bottom of the structure. This printing can be classified as a single-layer fabrication that printed design at a uniform print height of 0.05 mm. The resistivity of the thus printed area was obtained by the four-point-probe method [22] using the Jandel Multiheight-microposition probe and the measured resistivity of 4.53 x 10^{-7} Ω-m was obtained which was coherent with the expected results for the ink.

The BAR64 switching diode [23] was attached at a gap of 5.7 mm from the side using conductive ink and glue. The two 100 pF capacitors were also attached with the same method at 0.6 mm from the edges. The port was affixed at the backside of the antenna at the end of a straight coaxial cable which was attached on top of the two tiny square pads. Foam was inserted behind the antenna structure to provide durability to the design. The complete design can be seen in Fig. 4.6. Two 47 nH inductors were also mounted on edges from the diode's side and one of them can be seen in Fig. 4.7. Two wires were expanded from those two inductors which were used for DC input voltage. The antenna was then tested.

Fig. 4.8 denotes the surface profile of the designed acquired with the help of Keyence® 4K microscope. This ultra-high definition microscope aided in acquiring the picture profiles of the design with 30x zoom in Fig. 4.10 (a) and 150x zoom in fig. 4.10 (b). The figures show the

absolute precision of the printed design up to the microscopic level which further substantiates the point of the development of designs with reliable accuracy using this technique. The many tiny droplets of the deposited ink can also be seen in Fig. 4.10 (b).

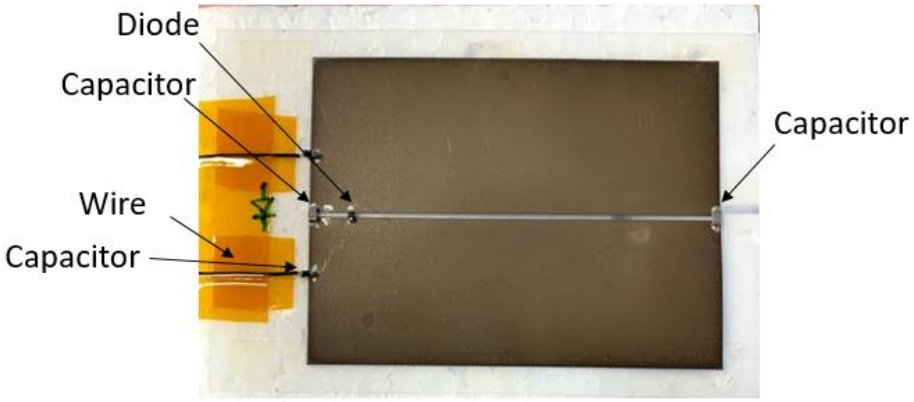

Figure 4.6 Printed antenna design for frequency switching

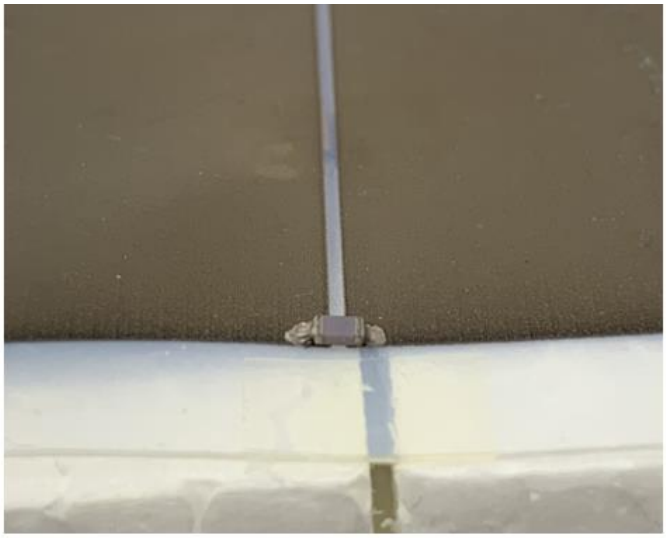

Figure 4.7 Magnified image of the affixed capacitor

3-Dimensional Surface mapping of one of the printed silver ink patches is presented in Fig. 4.9. This surface profile map was acquired with the help of Talysurf CCI L10xZ1B1S1F0Hps interferometer. The roughness of the printed surface around the slot is demonstrated in Fig. 4.10. Fig. 4.9 and 4.10 both validate that the variation in the height of the printed area was predominantly uniform with little deviation due to the fabrication constraints.

(a)

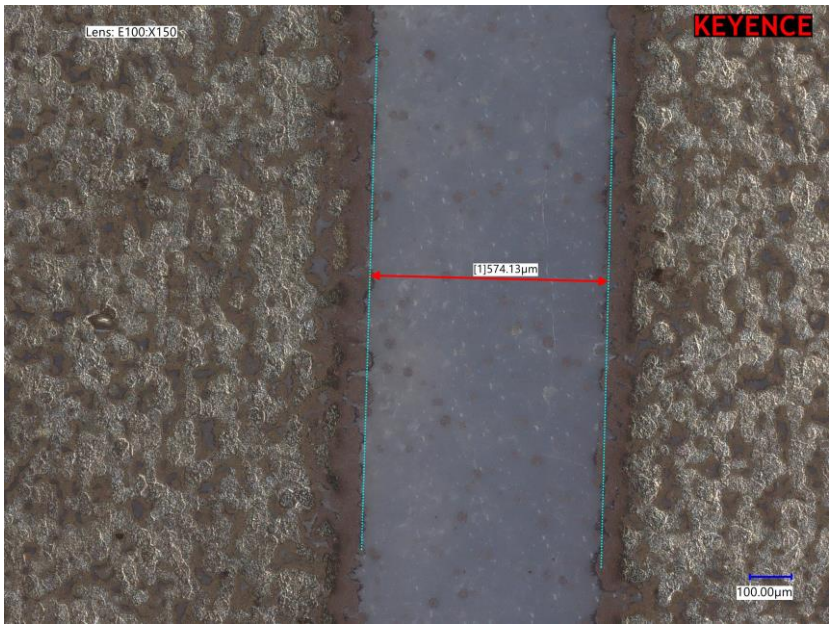

(b)

Fig. 4.8 The Keyence® 4K Microscope surface profile photos of the printed antenna surface with 30x Zoom in (a) and 150x Zoom in (b)

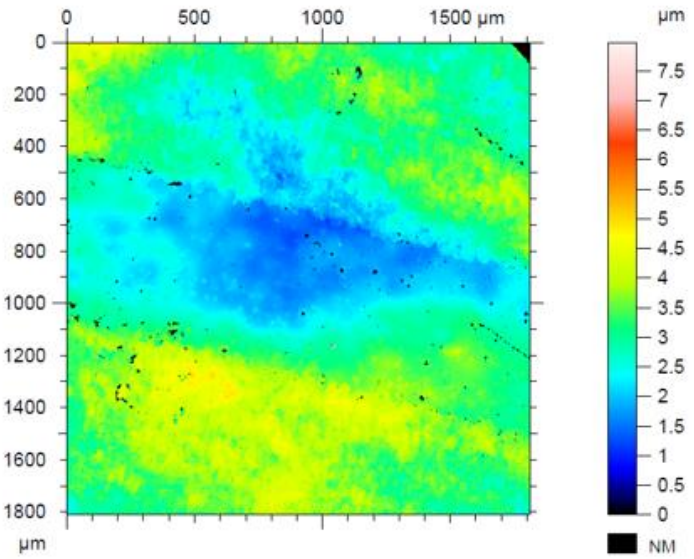

Fig. 4.9. 3D surface map of a section of printed patch

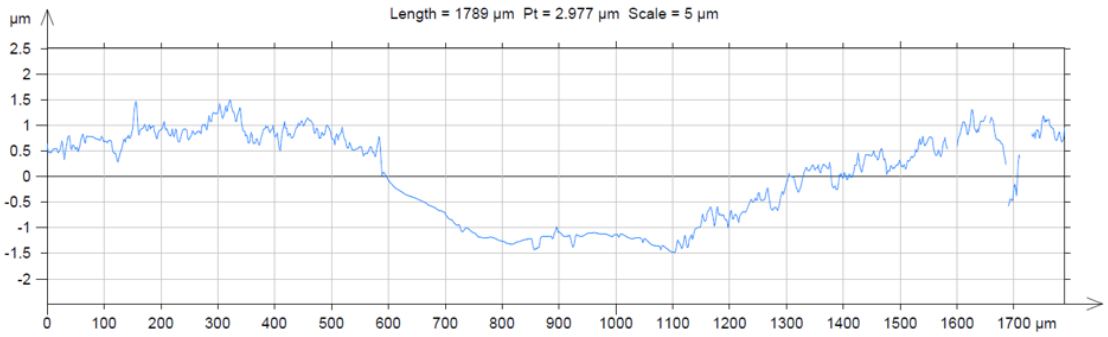

Fig. 4.10. Lateral surface roughness profile of the printed aperture

The measured reflection coefficient (S_{11}) response of the design is presented in Fig. 4.11. As it is evident from the results, OFF-state of the design resonated at 2.25 GHz with a bandwidth of 20% whereas ON-state resonated at 2.68 GHz with a bandwidth of 19%. Both the measured bandwidths were almost similar the bandwidths of simulations. The variation between the simulation and the measurement results was minimal and the design resonated at the desired frequency. Radiation patterns for the antenna are presented in Fig. 4.12 and Fig. 4.13 where Fig. 4.12 shows radiation patterns for the OFF-state while Fig. 4.13 shows the radiation patterns for the ON-state.

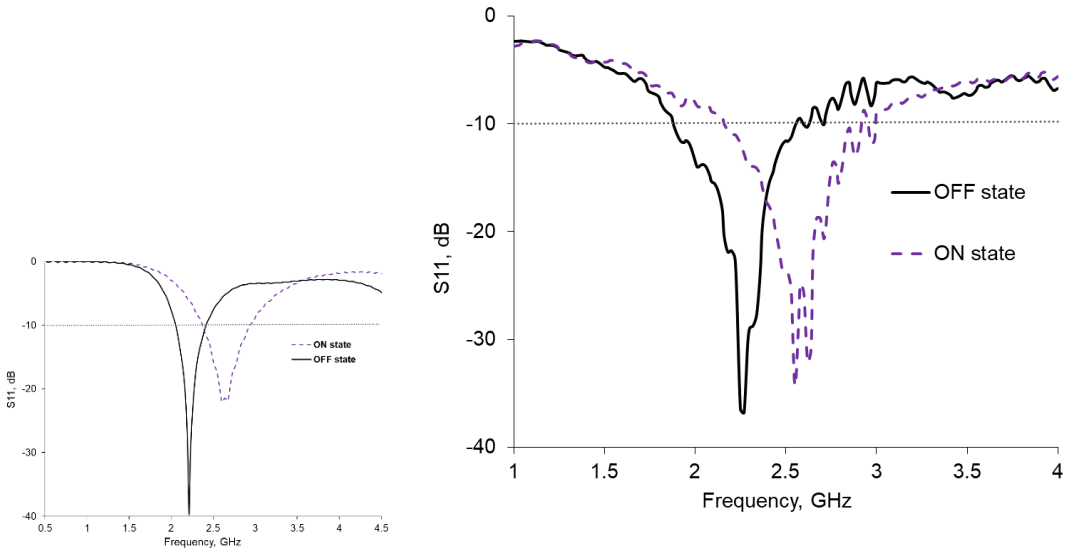

Figure 4.11 Measured reflection coefficient (S_{11}) of the antenna

As it can be determined from the plots, the simulated and the measured responses are in good correlation with one another. The radiation patterns are consistent with the typical slot antenna patterns. The simulated cross-polarisation magnitude for the XZ-plane was so low that it falls off the range of the polar plots. The measured directivity of the switching antenna was 4.1 dBi for the OFF state and 4.9 dBi for the ON state which were approximately 0.5 dBi lower than the simulated directivity for both the states. The resultant antenna efficiency was 0.79 for the OFF-state and 0.83 for the ON-state.

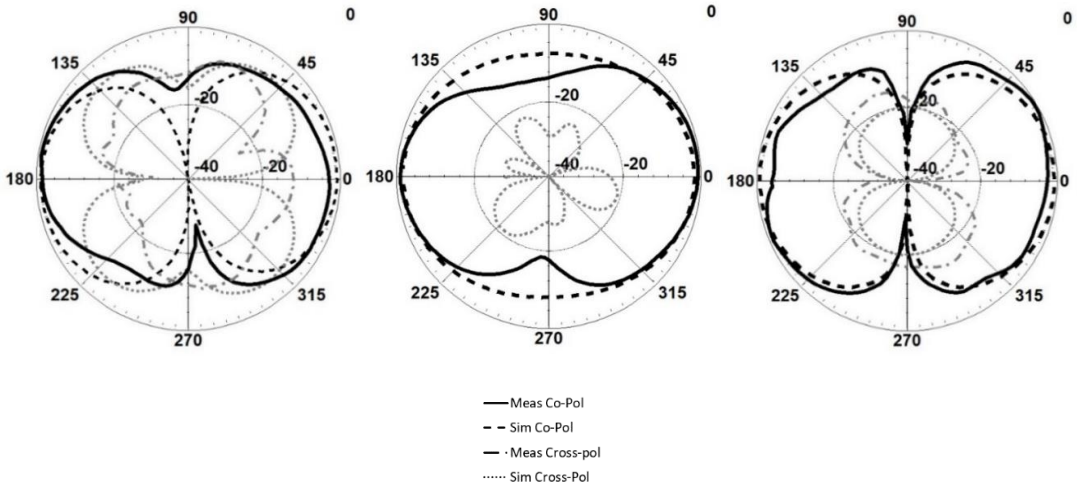

(a) (b) (c)

Fig. 4.12 Radiation pattern for the OFF state at 2.25 GHz in (a) XY-plane (b) XZ-plane and (c) YZ-plane

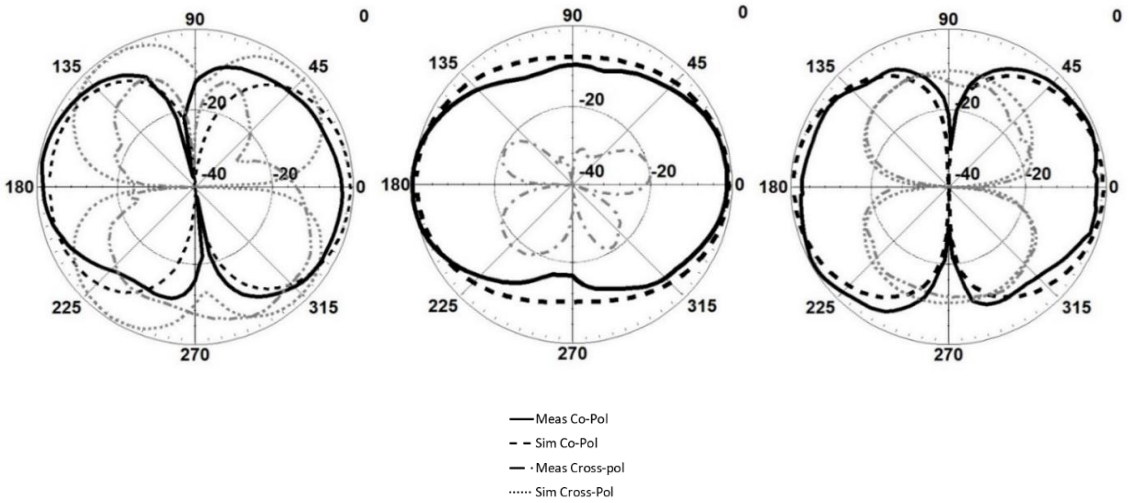

(a) (b) (c)

Fig. 4.13 Radiation pattern for the ON state at 2.68 GHz in (a) XY-plane (b) XZ-plane and (c) YZ-plane

4.4 Frequency tunable antenna

4.4.1 Antenna design

The design of the dual band tunable antenna solution was also realised using the same design aperture as the one that was presented in Fig. 4.1. Just by changing the positioning of the switching diode and replacing it with a varactor diode and also adjusting the dimensions of the slot, tunable antenna solution was obtained. In addition to that, the orientation and polarity of the DC voltage source was reversed in order for the antenna to operate in the variable capacitance region of the varactor. The new dimensions are given in Table 2 and Fig. 4.1 illustrate the tunable design whose basic layout remained the same. An inexpensive BB857 varactor diode [23] was connected between the two sides of the slot at L_d = 2.7 mm. The capacitors were affixed at the distance of 0.35 mm from both sides to create a slot which was set in size. 47 nH inductors are mounted on the side of the diode along with connecting wires for DC isolation as well as the wired connection necessary to tune the antenna by varying the DC supply voltage and a 1 kΩ resistor was also soldered at the end of the wire to control the current flowing into the diode. Fig. 4.14 denotes the simulated reflection coefficient (S_{11}). As the capacitance value was increased from 0.5 pF to 6.6 pF, the first resonant frequency varied and decreased from 2.55 GHz to 1.38 GHz.

TABLE II

Tunable antenna dimensions (in mm)

Length	L_d	L_p	L	W	W_s
Dimensions (mm)	2.7	14.6	61.9	44.7	0.7

The second resonant frequency band demonstrated a shift from 4.4 GHz to 2.9 GHz. Both the bands covered find significant importance in the 4G and 5G communications. The tuning design can work as a bridge between the two technologies. A relationship-plot between frequency bandwidth and capacitance can be seen in Fig. 4.15. The frequency value decreases gradually as the capacitance value is increased. A linear equation can be used which can be tracked using the following fitted equation:

$$f_o = -0.1897C + 2.5503$$

Where f_o represents frequency and C represents capacitance value. The fitting line curve has an R^2 estimate of 98%. The bandwidth gradually decreased as the value of capacitance was increased. The drop in the bandwidth, however, was non-linear in nature.

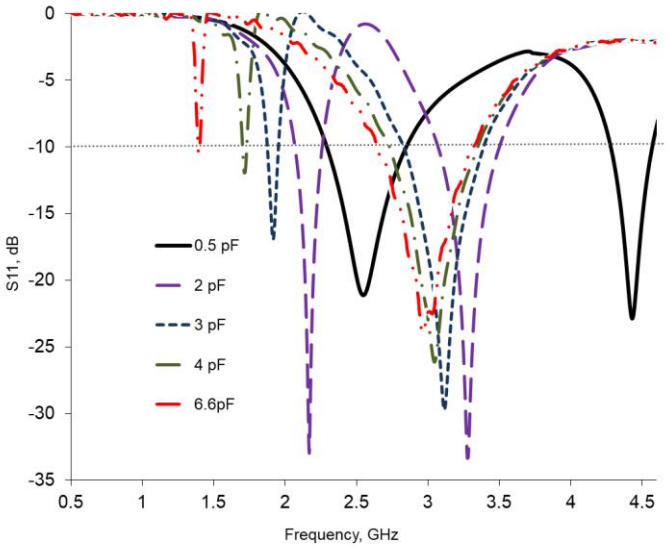

Figure. 4.14 Tunable antenna Simulated Reflection coefficient (S_{11})

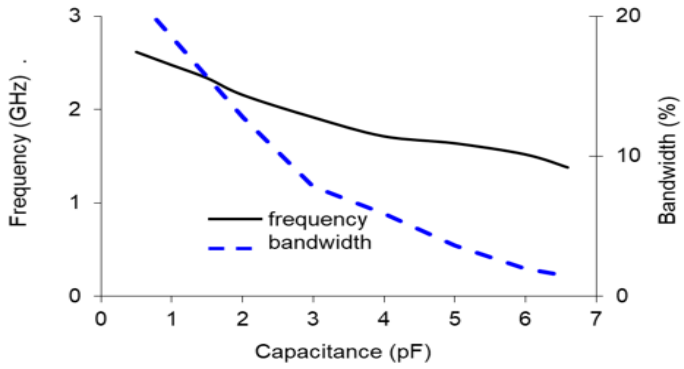

Figure 4.15 Frequency vs Capacitance vs Bandwidth relationship representation

Surface current density for the design for different capacitance values can be seen in Fig. 4.16. The surface currents depictions are represented at 0.5pF, 3pF and 6.6pF, in sub-section (a) (b) and (c), respectively. The surface currents demonstrate that the currents are primarily focused on and around the port and the side nearer to the diode. The surface current density was at the maximum for 0.45 pF and gradually decreased as the level of capacitance is increased.

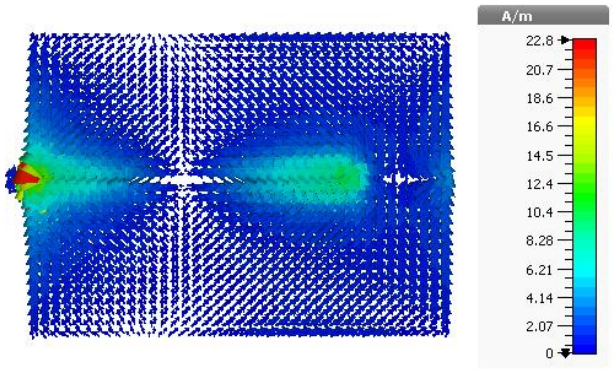

(a) 0.45 pF

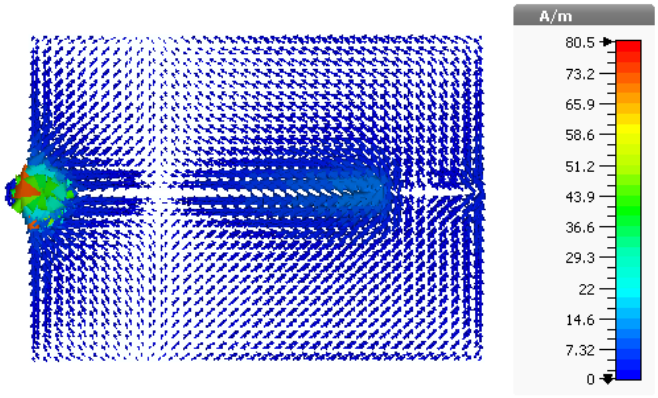

(b) 3 pF

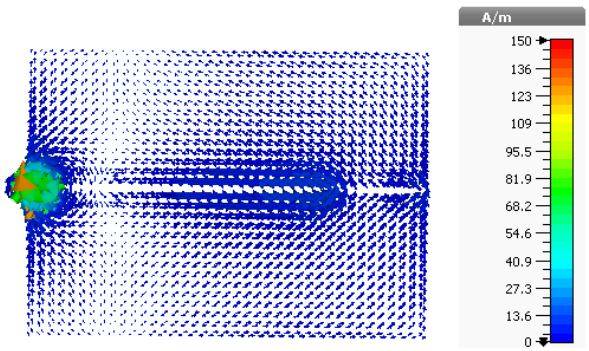

(c) 6.6 pF

Figure 4.16 Simulated surface currents at (a) 0.45 pF, (b) 3 pF and (c) 6.6 pF

4.4.2 Measurement results

As elaborated for the earlier switching antenna, the tunable antenna was also developed on the same printed aperture whose printing was discussed earlier. The components were mounted using the silver paint and conductive adhesive and the SMA was connected was added at the backside. The measured S_{11} can be seen in Fig. 4.17.

The main operational frequency was obtained when the supply voltage of 28 V was supplied. The antenna resonated at 2.4 GHz for the first resonant frequency band and at 4.3 GHz at the second resonant frequency band. A slight dip in the second resonant frequency is observed as the simulated result resonated a 4.4 GHz. The first resonant frequency band tuned from 2.4 GHz all the way down to 1.38 GHz. The second resonant frequency band tuned from 4.3 GHz all the way down to 2.2 GHz. As an interesting observation, at 1 V supply voltage, the measured reflection coefficient demonstrated a third resonant frequency band also. The three frequency bands at 1 V input supply voltage operated at a resonant frequency of 1.38 GHz, 2.2 GHz, and 3.3 GHz, respectively. The two resonant frequency bands tuned by varying the supply voltage provide a nexus between 4G and 5G spectrums with simulated and measured reflection coefficient showing excellent correlation and covering both the desired frequency bands. Fig. 4.18 represents the plot depicting the relationship between the DC input voltage and the corresponding resonant frequency as well as the bandwidth. The frequency value gradually increases as the DC input voltage is increased.

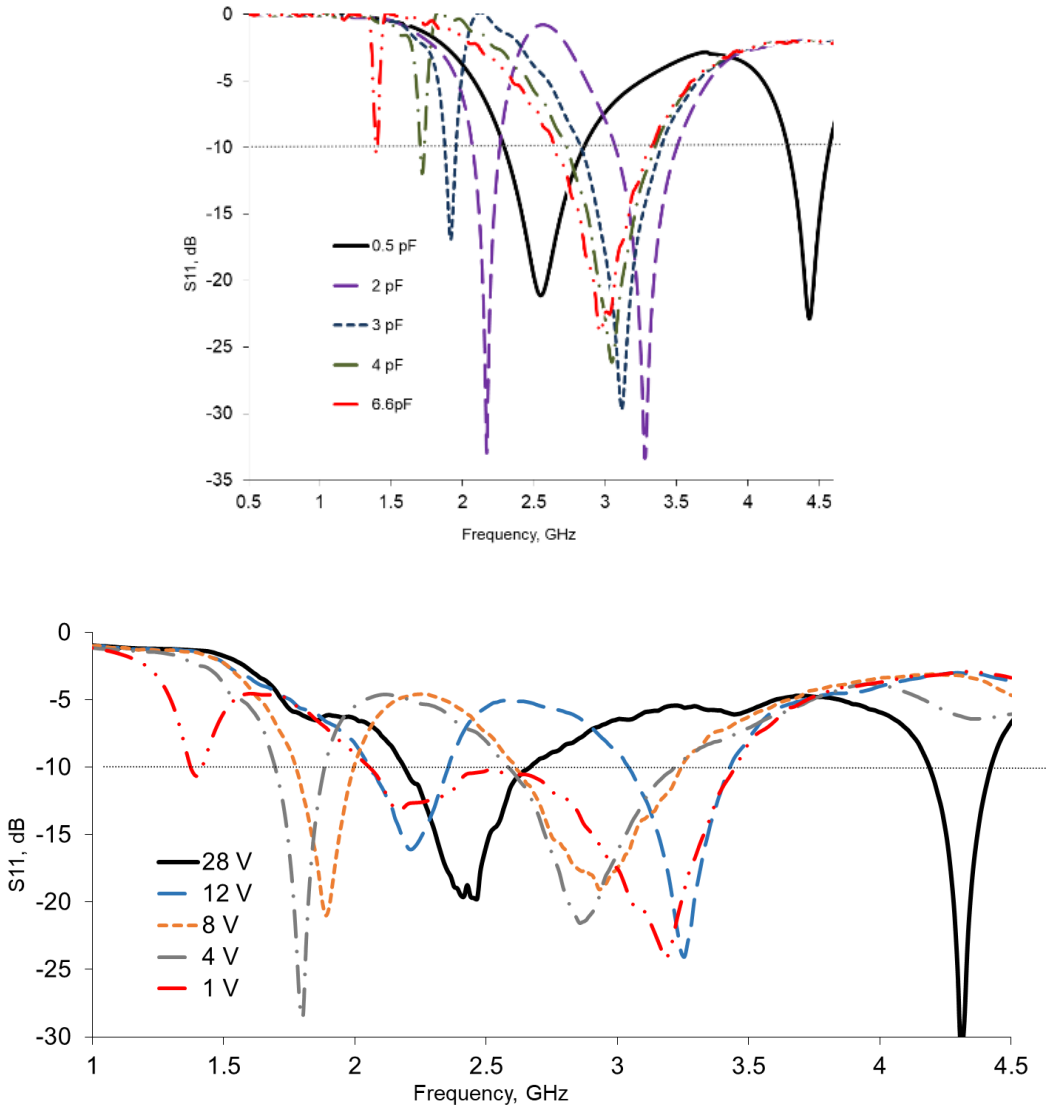

Figure 4.17. Tunable antenna measurement results

A linear curve-line equation can be implemented to determine the relationship that can be tracked using the following fitted equation:

$$f_o = 0.0311V + 1.6079$$

Where f_o represents frequency while V represents the DC input voltage. The fitting curve has an R^2 value of about 86%. The frequency bandwidth progressively dropped as the capacitance value increased. The fall in the bandwidth was nevertheless non-linear in nature.

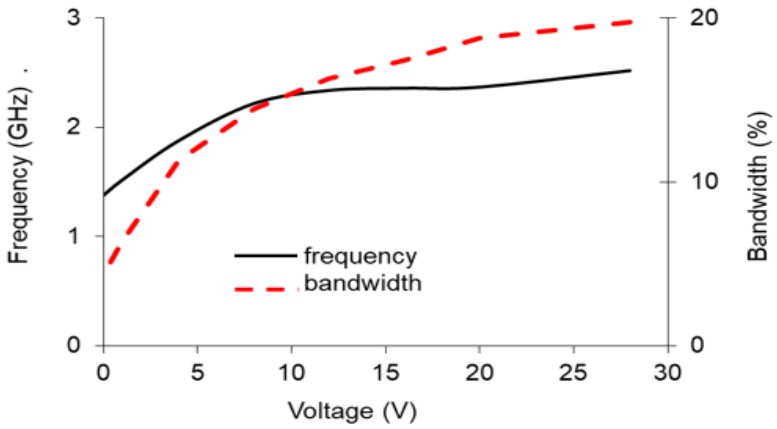

Figure 4.18. Frequency vs Voltage vs Bandwidth relationship representation

Figure 4.19, Fig. 4.20, and Fig. 4.21 represent the measured and simulated radiation pattern results at 28 V, 12 V and 1 V, respectively. Radiation patterns are in association and sync with those that are expected patterns for a complementary dipole that is fed using a coaxial cable from the backside. Patterns are predominantly omnidirectional in the XZ-plane. Calculated gain was 5.65 dBi for 0.5 pF and 1.86 dBi for 6.6 pF. Measured gain was 5.07 dBi at 28 V and 0.88 dBi at 1 V. The resultant efficiencies were 0.86 at 0.5 pF and 0.78 at 6.6 pF.

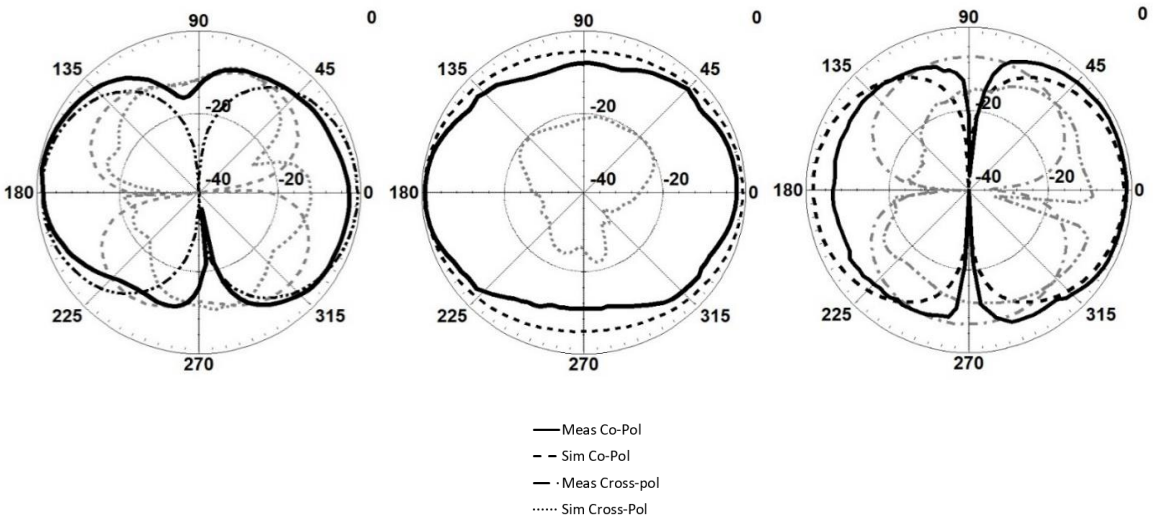

(a) (b) (c)

Fig. 4.19 Measured and simulated Radiation pattern results at 2.5 GHz for 28 V in (a) XY, (b) XZ and (c) YZ planes respectively

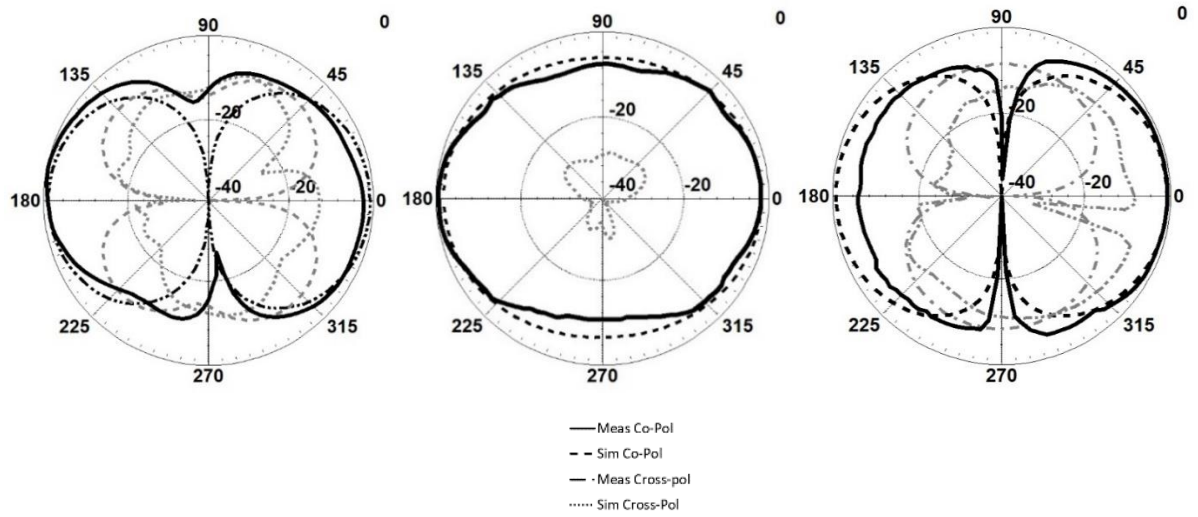

(a) (b) (c)

Fig. 4.20 Measured and simulated Radiation pattern results at 2.2 GHz for 12 V in (a) XY, (b) XZ and (c) YZ planes respectively

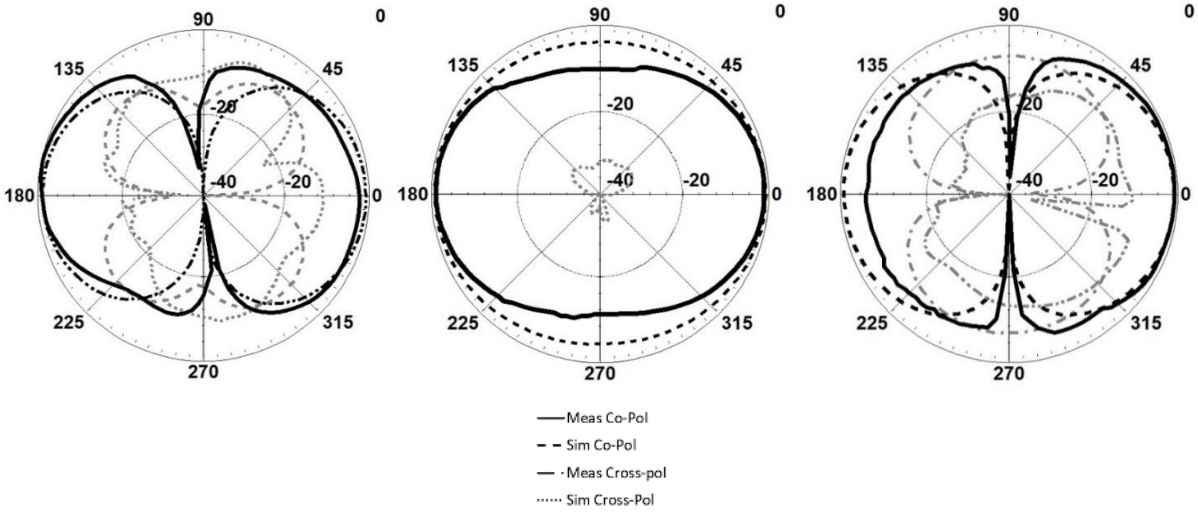

(a) (b) (c)

Fig. 4.21 Measured and simulated radiation patterns at for 1.38 GHz at 1 V in (a) XY, (b) XZ and (c) YZ planes respectively

At last, a comparison table between the two fabrication techniques in the development of frequency reconfigurable antenna is proposed in Table III. The table compares the key aspects of the development of antennas in the two methods and analyses the two techniques with one

another with etching being a method of subtractive manufacturing whereas inkjet printing being a method of additive manufacturing.

TABLE III

Comparison table among the presented Reconfigurable antenna fabrication techniques

Elements	**Etching**	**Inkjet Printing**
Substrate	Mylar	PET
Conductive layer	Copper	Nanoparticle silver ink
Thickness	0.05 mm	0.123 mm
Fabricable layers	Single and Double layer	Single layer only
Fabrication time	Approx. 1 hr	1-2 minutes
Components mounting	Soldering	Conductive adhesive
Substrate dimensions	Etching bed size	A4 sheet size only
Resistivity	$1.67\times10^{-8}\,\Omega$-m	$4.53\times10^{-7}\,\Omega$-m
Biasing tracks	Yes	No
Capacitive coupling	Yes	No
Direct reconfigurability	No	Yes
Flexibility	Yes	Yes
Bendability	Yes	No
Temperature tolerance	High	Low
Switching range	1.56 GHz – 2.5 GHz	1.7 GHz – 3 GHz
Tuning range	1.4 GHz – 2.6 GHz	1.38 GHz – 2.7 GHz
Bandwidth at f_c	21%	24%
Single aperture dual operations	Yes	No
Approximate cost per antenna	£ 10-15	£ 25-30

4.5 Conclusion

Considerations, manufacturing constraints in designing low-cost inkjet-printed frequency reconfigurable antennas are presented in this chapter. The efficiently designed cost dear solution comprises of using an off-the-shelf household inkjet printer with silver nanoparticle

conductive ink which was filled inside the refillable cartridges. This fabrication method posed certain shortcomings and constraints which were necessary to be considered in the planning and designing of the reconfigurable antenna solution. To prevail over these limitations, a design solution was proposed which consisted of two printed conductive rectangular patches which were connected with end capacitors and diodes to create smart complementary dipoles. The two patches were printed over a single-sided A4 size PET sheet with the help of the Brother printer. Active components were mounted over the top of the single-layer design with the help of conductive adhesives. The same double conductive patch aperture design solution was deployed to create two frequency reconfigurable antennas namely Switching and Tuning antennas. The placing of the active components and the kind of diode characterized the type of reconfigurable antenna. Magnified pictures of the surface profiles of the design exhibited the consistent deposition of the conductive ink across the printed area. A single band switching antenna was able to switch among two adjacent frequency bands while enhancing the total bandwidth by 23%. The radiation patterns were in excellent agreement with one another and omnidirectional radiation patterns in the XZ-plane were observed. The dual-band tunable antenna solution was also developed on the same inkjet-printed aperture by rearranging the active components. This antenna tuned between a wide range of frequencies in both operational bands. Measured and simulated values for the reflection coefficient results were in good rationality with one another and similar result patterns were obtained. Omnidirectional performance in the XZ-plane was also observed.

The low-priced inkjet-printing of frequency reconfigurable antennas demonstrated here extends an alternative to conventional production techniques while offering a cheaper alternative to the extra expensive solutions which have formerly been reported. Inkjet printing of frequency reconfigurable antenna could support developments within the defence and space communication sectors where lightweight and flexible designs are highly sought after. Inkjet-printed reconfigurable antennas could also be readily deployed to develop inexpensive, industry ready, environmentally friendly designs that demonstrate extremely reliable performances.

References

[1] S. D. Hoath, "Index," *Fundamentals of Inkjet Printing*, pp. 7–79, 2015.

[2] X. Song, J. Luo, L. Zhou, L. Zhang, W. Wu, and J. Peng, "A new poly-Si TFT compensation pixel circuit employing AC driving mode for AMOLED displays," *Journal of Semiconductors*, vol. 34, no. 12, p. 125011, 2013.

[3] D. Deng, A. Jain, N. Yodvanich, A. Araujo, and Y. Chen, "Three-dimensional circuit fabrication using four-dimensional printing and direct ink writing," *2016 International Symposium on Flexible Automation (ISFA)*, 2016.

[4] K. L. Yam, P. T. Takhistov, J. Miltz Intelligent Packaging: Concepts and Applications[M]. Springer Berlin Heidelberg, 2005: 34-36.

[5] P. Simon, Y. Gogotsi Materials for electrochemical capacitors J. Nature Materials. 2008, 7(11): 845-854.

[6] A. Mosaddek, H. K. R. Kommula, and F. Gonzalez, "Design and Testing of a Recycled 3D Printed and Foldable Unmanned Aerial Vehicle for Remote Sensing," *2018 International Conference on Unmanned Aircraft Systems (ICUAS)*, 2018.

[7] S. Y. Jun, A. Shastri, B. Sanz-Izquierdo, D. Bird and A. McClelland, "Investigation of Antennas Integrated Into Disposable Unmanned Aerial Vehicles," in *IEEE Transactions on Vehicular Technology*, vol. 68, no. 1, pp. 604-612, Jan. 2019, doi: 10.1109/TVT.2018.2882791.

[8] S. Chung, M. A. U. Karim, H.-J. Kwon, W. Scheideler, and V. Subramanian, "A highspeed inkjet-printed microelectromechanical relay with a mechanically enhanced double-clamped channel-beam," J. Microelectromech. Syst., vol. 26, no. 1, pp. 95– 101, 2017.

[9] S.-H. Kim, T. T. Nguyen, D.-J. Kim, and J.-H. Jang, "Printed dipole antenna with a 1-D EBG ground plane," *2010 IEEE Antennas and Propagation Society International Symposium*, 2010.

[10] J. Heirons, S. Jun, A. Shastri, B. Sanz-Izquierdo, D. Bird, L. Winchester, L. Evans, and A. McClelland, "Inkjet printed GPS antenna on a 3D printed substrate using low-cost machines," *2016 Loughborough Antennas & Propagation Conference (LAPC)*, 2016.

[11] A. Buerkle, K. F. Brakora, and K. Sarabandi, "Fabrication of a DRA Array Using Ceramic Stereolithography," *IEEE Antennas and Wireless Propagation Letters*, vol. 5, pp. 479–482, 2006.

[12] Z. Larimore, S. Jensen, A. Good, A. Lu, J. Suarez and M. Mirotznik, "Additive Manufacturing of Luneburg Lens Antennas Using Space-Filling Curves and Fused Filament Fabrication," in *IEEE Transactions on Antennas and Propagation*, vol. 66, no. 6, pp. 2818-2827, June 2018, doi: 10.1109/TAP.2018.2823819.

[13] B. T. Malik, V. Doychinov, S. A. R. Zaidi, I. D. Robertson and N. Somjit, "Antenna Gain Enhancement by Using Low-Infill 3D-Printed Dielectric Lens Antennas," in *IEEE Access*, vol. 7, pp. 102467-102476, 2019, doi: 10.1109/ACCESS.2019.2931772.

[14] B. Sanz-Izquierdo and E. A. Parker, "3-D Printing of Elements in Frequency Selective Arrays," IEEE Trans. Antennas Propagat., vol. 62, pp. 6060-6066, Dec 2014.

[15] A. Shastri, S. Jun, B. Sanz-Izquierdo, H. Aldawas, Q. Ahmed, and M. Sobhy, "Evaluation of a low-cost inkjet printed slot antenna for energy harvesting applications," *2016 Loughborough Antennas & Propagation Conference (LAPC)*, 2016.

[16] B. K. Tehrani, B. S. Cook and M. M. Tentzeris, "Inkjet Printing of Multilayer Millimeter-Wave Yagi-Uda Antennas on Flexible Substrates," in *IEEE Antennas and Wireless Propagation Letters*, vol. 15, pp. 143-146, 2016, doi: 10.1109/LAWP.2015.2434823.

[17] F. Molina-Lopez, A. V. Quintero, G. Mattana, D. Briand, and N. F. de Rooij, "Large area compatible fabrication and encapsulation of inkjet-printed humidity sensors on flexible foils with integrated thermal compensation," J. Micromechanics Microeng., vol. 23, no. 2, pp. 025012–025022, 2013

[18] M. D. Dankoco, G. Y. Tesfay, E. Benevent, and M. Bendahan, "Temperature sensor realized by inkjet printing process on flexible substrate," Mater. Sci. Eng. B., vol. 205, pp. 1–5, Mar. 2016.

[19] Y. Wang, H. Guo, J.-J. Chen, E. Sowade, Y. Wang, K. Liang, K. Marcus, R. R. Baumann, and Z.-S. Feng, "Paper-Based Inkjet-Printed Flexible Electronic Circuits," *ACS Applied Materials & Interfaces*, vol. 8, no. 39, pp. 26112–26118, 2016.

[20] G. Cummins and M. P. Y. Desmulliez, "Inkjet printing of conductive materials: A review," Circuit World, vol. 38, no. 4, pp. 193–213, 2012.

[21] Mitsubishi Silver Nanoparticle Ink, K-mpm.com, 2020. [Online]. Available: http://www.k-mpm.com/agnanoen/pdf/msds_nbsij-mu01.pdf . [Accessed: 21-Dec- 2019].

[22] A. W. Groenland, R. A. M. Wolters, A. Y. Kovalgin and J. Schmitz, "Four Point Probe Structures With Buried and Surface Electrodes for the Electrical Characterization of Ultrathin Conducting Films," in *IEEE Transactions on Semiconductor Manufacturing*, vol. 25, no. 2, pp. 178-184, May 2012, doi: 10.1109/TSM.2011.2181674.

[23] "Infineon BAR64-03W datasheet." [Online]. Available: https://www.infineon.com/dgdl/Infineon-BAR64-03W-DS-v01_01-EN.pdf?fileId=5546d462689a790c01690f0250e138fe . [Accessed: 20-Jun-2020].

[24] “Infineon BB857 Datasheet.” [Online]. Available: https://www.infineon.com/dgdl/Infineon-BB837_BB857SERIES-DS-v01_01-en.pdf?fileId=db3a304313d846880113d97339a9011a . [Accessed: 21-Jun-2020].

CHAPTER 5

LOW-COST FABRICATION OF FREQUENCY SELECTIVE SURFACES

5.1 Introduction

This chapter presents the fabrication of frequency selective surfaces (FSSs) using low-cost inkjet printing for microwave and sub millimetre wave applications. Two different approaches are presented for the low-cost fabrication. In the first section, two bandstop FSS structures are inkjet-printed using the household Inkjet printer discussed in the previous chapter. Two designs were printed to operate in the frequency bands of 2.4 GHz and 24 GHz, respectively. These two designs were printed on foldable, inexpensive paper substrates. They can be deployed within an indoor environment to enhance the signal strength of 4G and 5G networks and reduce the signal drop due to the absorption by walls ceilings and other building materials. The second section presents the development of a novel printer system that simultaneously deposits the substrate as well as the conductive ink. The printer system was developed by a team of researchers at University of Kent. The printer system was deployed to fabricate a fully 3D printed bandstop FSS made up of square loop elements. A standard Fused Filament Fabrication (FFF) printer was modified and calibrated and the extension components were 3D printed to mount the two extruders.

FSS designs are deployed as screens to obtain a filtering response from the incident EM signal [1]. A significant number of FSS designers are exploring the prospects of using the modern fabrication techniques such as 3D printing and additive manufacturing to fabricate their FSS structures [1], [2]. 3D printing or additive manufacturing of EM structures are developed by segmenting the models into numerous layers and depositing the manifold layers of the printing

material one by one. Throughout the preceding decade, 3D printing the FSS designs [3] – [14] and antennas [15] – [19] are frequently realized by using various 3D printing procedures.

Techniques such as screen printing, Inkjet printing, SLS, FFF, SLA, FDM, Aerosol Jet printing, combination of FDM and hand painting and various other combination of techniques have been widely reported. The 3D printed structures can be further classified alongside the line of fabricating using expensive industry grade equipment [5] – [13], [16] – [18] and low-cost fabrication equipment [3], [4], [14], [15] and [19].

This chapter is arranged as following. Section 5.2 discusses the low-cost inkjet printing of a microwave and a sub-millimetre wave bandstop FSS paper posters using the household inkjet printer discussed in the previous chapter. Section 5.3 discusses setting up a novel printer system to simultaneously print the filament based substate and conductive ink simultaneously and a bandstop microwave is presented as an example. Concluding remarks are presented in Section 5.4.

5.2 Low-cost Fabrication of Wallpaper Poster FSS

5.2.1 Wallpaper poster designs

This section elaborates two wallpaper posters based FSS solutions printed with the help of low-cost Inkjet-Printing for microwave and 5G applications. The two bandstop square loop FSS posters were printed by the Brother inkjet printer discussed in the previous chapter. Using of raisin coated photo paper for these proposed posters provided a cost-efficient solution for various applications.

The FSS designs comprised of arrays of square loops unit cell elements that were organized in a square lattice. Square loop FSS designs were selected to maximise the coverage of the design across the printed area while providing reliable shielding response. Square loop unit cell elements are trendy FSS unit structures that demonstrate dual-polarized responses alongside exhibiting outstanding angle of incidence performance. Square loop unit cell elements were also beneficial as they provide a uniform array structure that can be scaled without wasting material across the print area thereby reducing the overall cost of manufacturing. Initially, the microwave FSS design with square loop units was developed which was later redesigned for

mm-wave unit cell. The unit structure for the square loops can be seen from Fig. 5.1. Unit cell for the microwave design consisted of a unit cell of 45.6 mm by 45.6 mm dimensions. The loops had the square geometry with 32.16 mm sides and a thickness of 1.92 mm.

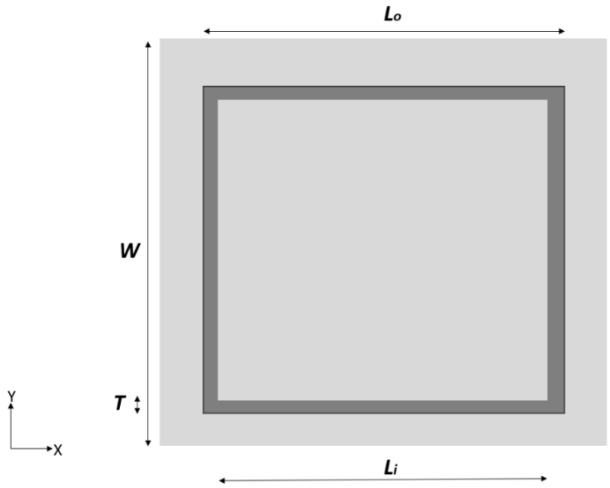

Fig. 5 1. Square loop unit cell layout

TABLE I.

DIMENSIONS IN MM

Perimeter	L_o	L_i	W	T
Microwave FSS	36	32.16	45.6	1.92
Sub mm-wave FSS	3	2.64	3.8	0.18

Unit cell for the sub mm-wave design had the width of 3.8 mm by 3.8 mm. Square loops of 3 mm by 3 mm lengths and thickness of 0.18 mm were designed using on a substrate that had the characteristics of a photo paper with a permittivity (ε_r), of 3 for both the poster structures. The designs were simulated using CST Microwave Studio™. Simulated transmission response of the microwave FSS poster can be seen in Fig. 5.2 where the response of the sub mm-wave poster is presented in Fig. 5.3.

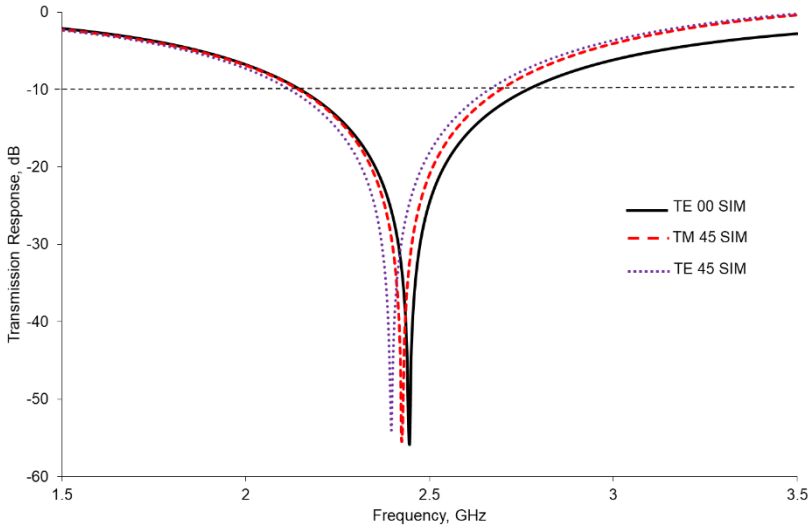

Fig. 5.2. Simulated transmission response for the microwave FSS poster design operating at 2.45 GHz central frequency.

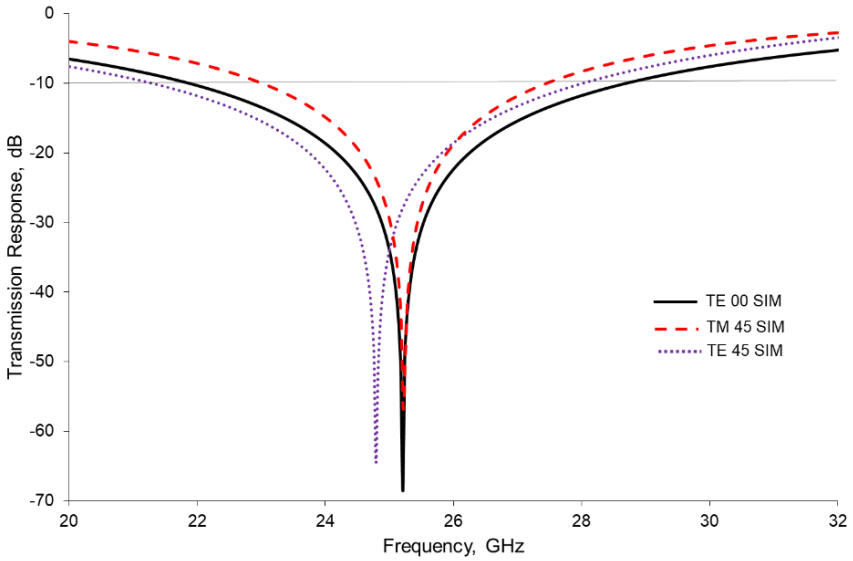

Fig. 5.3. Simulated transmission response for the mm-wave FSS poster design operating at 25.21 GHz central frequency

The microwave FSS design operated at 2.45 GHz. The response demonstrated nulls above the -50 dB levels for all the angle of responses. A shift of 2% or 0.05 GHz for the transverse electric (TE) and a shift of 1% for the transverse magnetic (TM) response were observed respectively at the counter-clockwise 45-degree angle from the normal angle of incidence response. TM-45 and TE-45 responses operated at 2.43 GHz and 2.4 GHz, respectively. All the three simulated

responses covered the 2.4 GHz band which made this design suitable for microwave applications.

The sub mm-wave design operated at 25.21 GHz and nulls of over -60 dB were observed for all the angles of response. A slight shift was observed in the TE and TM responses respectively for the 45-degree response. A shift of 2% or 0.42 GHz was observed for the TE-45 response. TM-45 response resonated at the same frequency as the normal response, but it presented a narrower bandwidth in comparison. All the three simulated responses contained the greatly coveted 24 GHz band which is generally utilized in 5G applications by -10 dB bandwidth available for all the three response cases.

The variation in the transmission responses for various angle of incidence can be observed in Fig. 5.3 and Fig. 5.4. The larger size of the wavelength compared to the substrate thickness results in the TM-45 response to resonate at the same frequency as the normal response with a narrower bandwidth. This effect is even more prominent for the fully 3D printed FSS presented in the next section and in the next chapter where higher frequency designs are presented.

5.2.2 Fabrication and Measurements

The two designs were printed using the same printer that was discussed in the previous chapter. Mitsubishi® raisin coated paper [20] was used as the substrate. The low-cost nature and the ability to provide reliable performances of printed electronics made this paper an attractive choice for the low-cost applications. PET could also have been used for these applications, but photo paper was chosen strictly due to the financial aspects of it.

The printed posters can be seen in Fig 5.4 and Fig. 5.5, respectively where microwave FSS poster is pictured in Fig. 5.4 and sub-mm wave FSS is shown in Fig. 5.5.

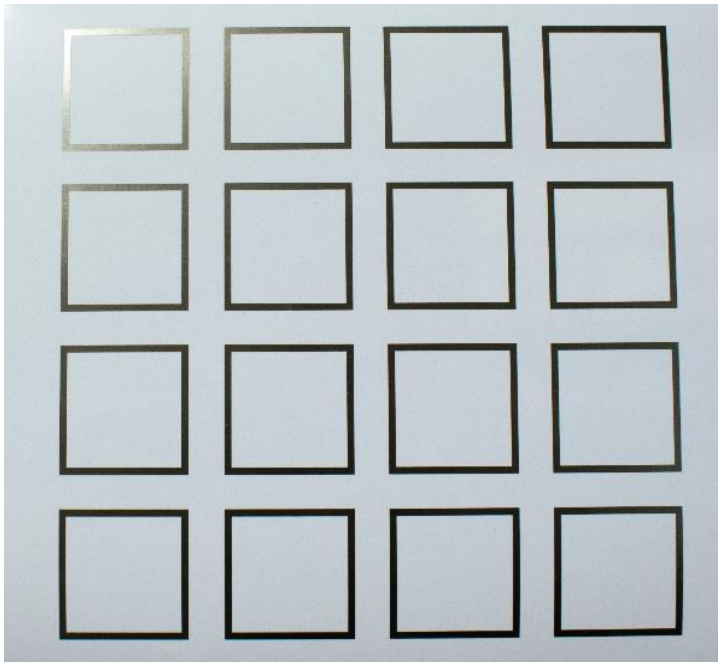

Fig. 5.4 Printed 4x4 sample area of the microwave FSS poster

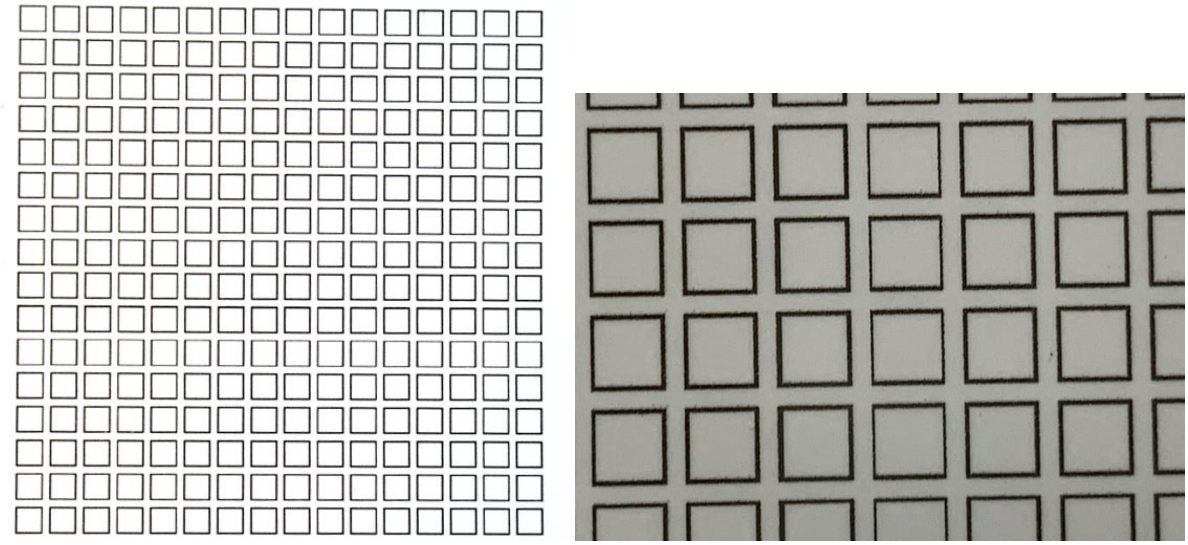

(a) (b)

Fig. 5.5 Printed sub mm-wave FSS poster with the full FSS in (a) and a magnified section of the poster in (b)

The measurements were performed making use of the standard transmission response measurement setup which can be seen in Fig. 5.6. The setup consisted of a bifurcated plain-

wave chamber that was fitted with absorber surfaces. The chamber was bifurcated by installing an absorber screen with a slot in its centre. The ability of the screen to rotate about its axis facilitated in observing the various angles of incidences. Two standard R&S helix antennas were used as the transmitter and the receiver antennas. The setup was normalised using the standard normalisation process. The measurement responses were observed using Anritsu® 37397C Vector Network Analyzer (VNA) and can be observed in Fig. 5.7 for the microwave poster and in Fig. 5.8 for the sub mm-wave poster.

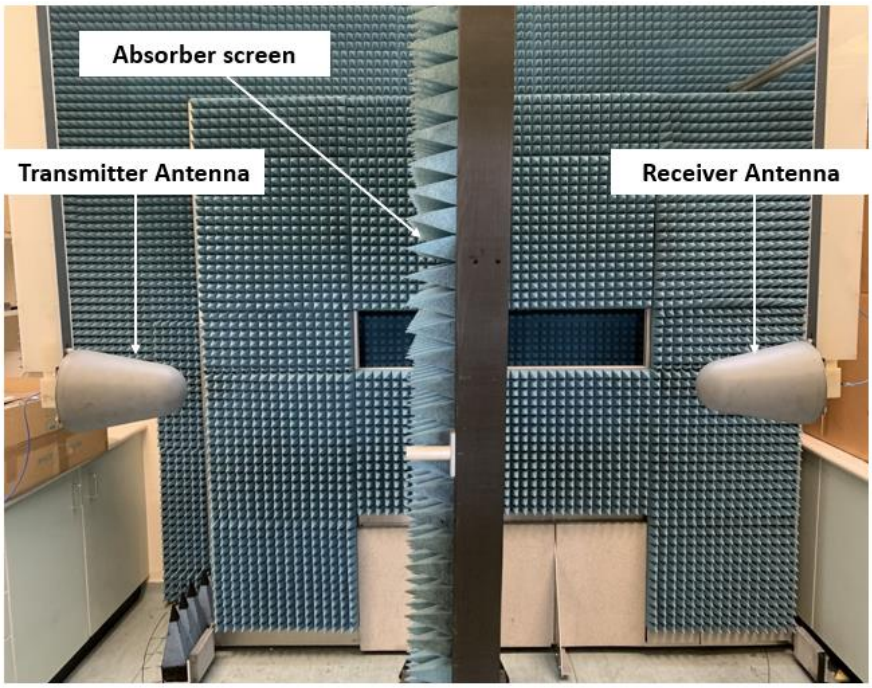

Fig. 5.6 Measurement Setup

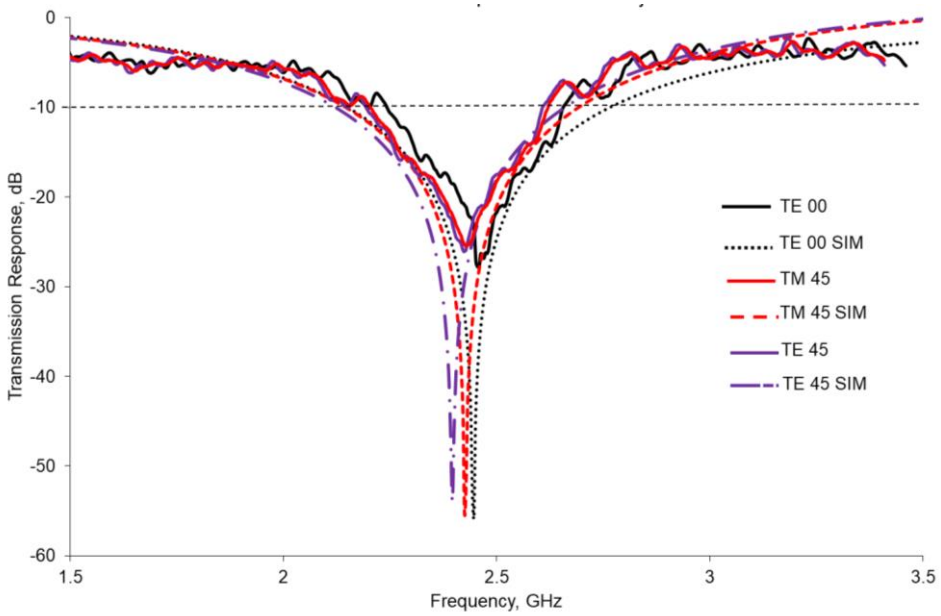

Fig. 5.7 Measured Transmission responses for the microwave poster FSS

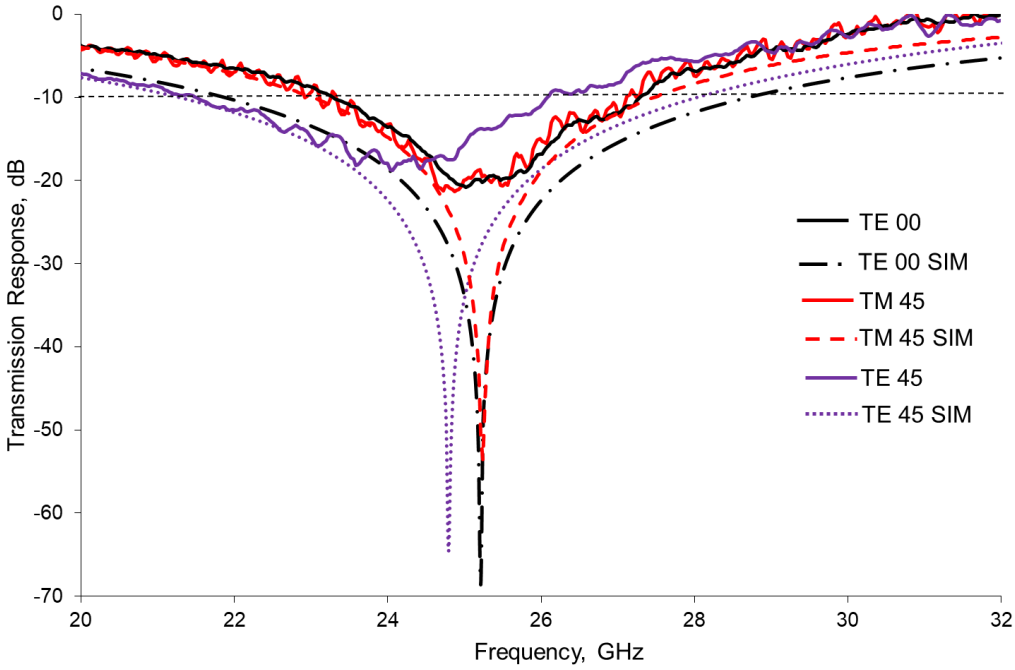

Fig. 5.8 Measured Transmission responses for the sub mm-wave poster FSS

The microwave FSS poster, presented in Fig. 5.7 operated at a central frequency of 2.46 GHz for the normal angle of incidence response. A shift of 2% and 1.8% was observed for the

TE-45 and TM-45 responses, respectively. A null of below -25 dB was observed for all the three angle of responses and the 2.4 GHz band was covered in all the three cases.

Normal transmission response for the sub mm-wave FSS, presented in Fig. 5.8, was consistent with the expected simulated transmission response and a null of approximately -20 dB was observed for the central frequency of 25.2 GHz. As it is evident from Fig. 5.9, the TM-45 response offered a response that was predominantly similar to the normal response but at the same time, offered a narrower bandwidth. The TE-45 resonated at a slightly lower frequency of operation at 24.7 GHz. All the presented transmission response measurements resonated below -12 dB for the desired and anticipated frequency band of 24 GHz which is particularly useful in 5G networks. Examining the bandwidths presented adequate exposure and reflection for the 24 GHz and its neighbouring bands.

5.3 Full 3D Printing of an FSS using a Low-Cost Open-Source Printer

5.3.1 Considerations for the Printer System

A thorough presentation of the development of a novel dual-extrusion setup for printing by deploying a low-cost open-source printer to fully 3D-print an FSS structure is presented in this section. The printer setup was developed by a team comprising of researchers and students who helped with certain specialised sections of development such as coding and calibration. The printing setup and calibration of the system was performed by me while a fellow researcher provided his inputs with coding. The printing setup utilized a low-cost open-source printer that could print a plastic reel-based filament as well as a conductive silver ink paste at the same time. As readily available printers did not exist in the marketplace for this sort of application, an open-source Fused Filament Fabrication (FFF) printer system was altered to accommodate two extruders mounted on the same extruder carriage which could deposit the filament and the conductive ink. A figurative model of the proposed printing system is presented in Fig. 5.9.

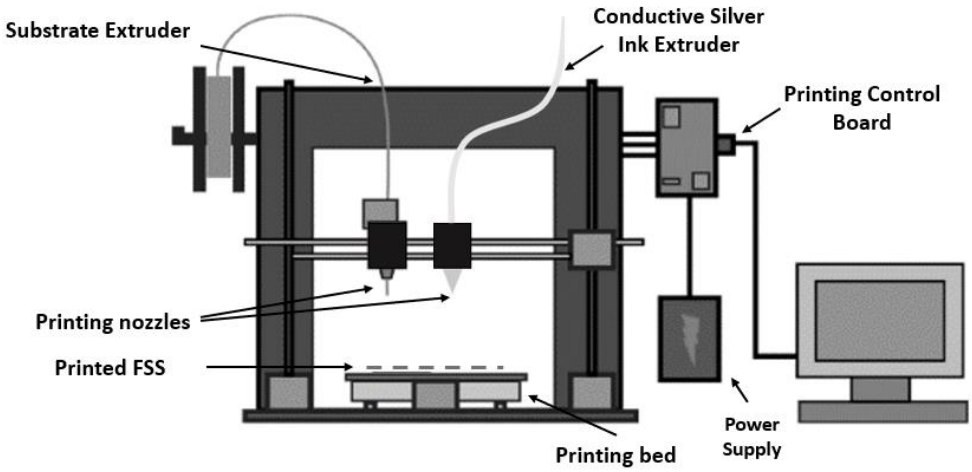

Fig. 5.9 Proposed 3D printer setup with dual extruders for simultaneous printing

A number of considerations were taken to accommodate the requirements for the proposed fabrication method employed within the proposed printer system. First and the foremost, one of the key objectives of this exercise was to keep the fabrication and system cost as low as possible. Keeping that in mind, a customized base frame of an open-source printer was chosen over any pre-existing multi-step printing bed which were available to buy in the market. Open-source 3D printers, as the name implies, are printer systems which have their hardware designs, their firmware and their software designs all made under an open-source license. Due to their open-source licenses, the open-source 3D printers are cost-efficient to obtain and construct. Second consideration dealt with the base frames which encompassed their own constraints in terms of the dimensions of the bed, resolution of the deposition and printing layer, speed of the motor and the printing speed. Aspects such as the printing resolution regulates the vital properties such as the material density and dielectric permittivity of the deposited filament based printed substrate. Thirdly, the majority of the accessible open-source low-cost printers available aided the fabrication of plastic wire-based PLA and ABS substrates only and therefore, the other printable substrates were not suitable for this type of setup. Furthermore, ABS substrates could only be supported with 3D printers which came with a built-in heating system in the printer bed. Fourthly, the conductive metal based had to be heated to a degree that it is in the liquid state and then deposited along with the filament substrate in structured and periodic arrangements. Since the mainstream conductive metals that are widely used in electronics such as silver need some extremely high temperatures to be liquefied and then, the molten silver ink is required to be cooled almost instantly in the close proximity of the substrate

therefore it does not disintegrate the printer and the substrate in particular as it is essential for the metal to be deposited in incorporation with additional materials such as plastic which possessed a significantly lower melting points. owing to this obvious and enormous discrepancy with the temperature constraints, this specific combination of melting the conductive metals was not sustainable.

Therefore, to surmount the manufacturing constraints, extensive studies that included market research, product comparison, studies of the machines as well as the study of materials and inks were conducted for various open-source printers and arrangements were made to find a solution named the Mbot Cube 3D printer [21], a cartesian frame structure which was a revamped duplicate of the Makerbot Replicator [22], an open-source printer. To address the issues pertaining with the printer beds and filament reel-based substrates, the designs were developed with a volumetric consideration of 200 x 200 x 170 mm^3 and reel-based PLA was carefully chosen as the substrate to eliminate the requirement for installing a heating bed. The larger size of the printing bed also enabled the production of bigger design structures and larger arrays.

Ultimately, to surmount the concerns pertaining with the conductive metallic silver, findings were performed, and studies were conducted to come up with an unconventional solution that deployed a liquified metallic silver paste which was dispensed through a pressurised system through a regulated duct such as a syringe. The silver paste, that came from the company named Voxel8 [23]. The company has produced a silver nanoparticle liquid ink paste which is supplemented for 3D printing applications. The conductive silver ink paste has an electrical resistivity of less than 3 x 10^{-7} Ω-m when it has fully cured and demonstrates a conductance of approximately 2 x 10^5 S/m. The ink is stored at a room temperature and as per the catalogue by the company, the ink cures at a room temperature in 15 minutes. The thermal resistivity of this paste meant that it can be used next to a heated FFF extruder without any complications.

5.3.2 Printer Assembly and Calibration

Since the arrangement and the operations of the original Mbot Cube printer were required to be changed and enlarged to accommodate the second extruder to deposit the conductive ink,

certain parts of the printer system were required to be add up at the extruder carriage point. The additional inclusion of a plastic filament-based extruder motor as well as an exchangeable pressure-based syringe extruder were added for a synchronized deposition of the PLA and the silver based conductive paste. Since the extruding unit grew to be larger in size with all the additions, the end stop features of the motor for the corners, edges and the far ends of the printing bed were lowered appropriately. To decrease the expenses of the designing, the parts needed to expand the extruder carriage to contain the dual-extrusion operations were printed using with the help of an industrial grade FDM printer. This industrial printer offered a layer resolution ranging between 0.02 and 0.35 mm, which implied that it could print certain extremely complex models with consistency and with high printing resolutions along with rapid printing speed with a maximum of 300 mm/s. The component models were constructed in CST Microwave Studio™ and the final blueprints were exported to the stl file and fed into the slicing software. The slicing software breaks a model design down into several layers. Some additional printing considerations remained necessary to print the parts. A 100 μm print resolution offered the smoothness of the printed parts. A range of 75-80% of infill facilitates the robustness of the printed constructions, but the stability is substantially elevated therefore, using an 80% maximum durability is cost-effective since it helps in saving the filament. A boundary coating threshold of two or greater guaranteed of good quality binding that contained significantly fewer possibilities of disintegration over a period of time. With the given considerations, the components were printed and built for the printer. The printer system was assembled, and the final printer system can be seen in Fig. 5.10.

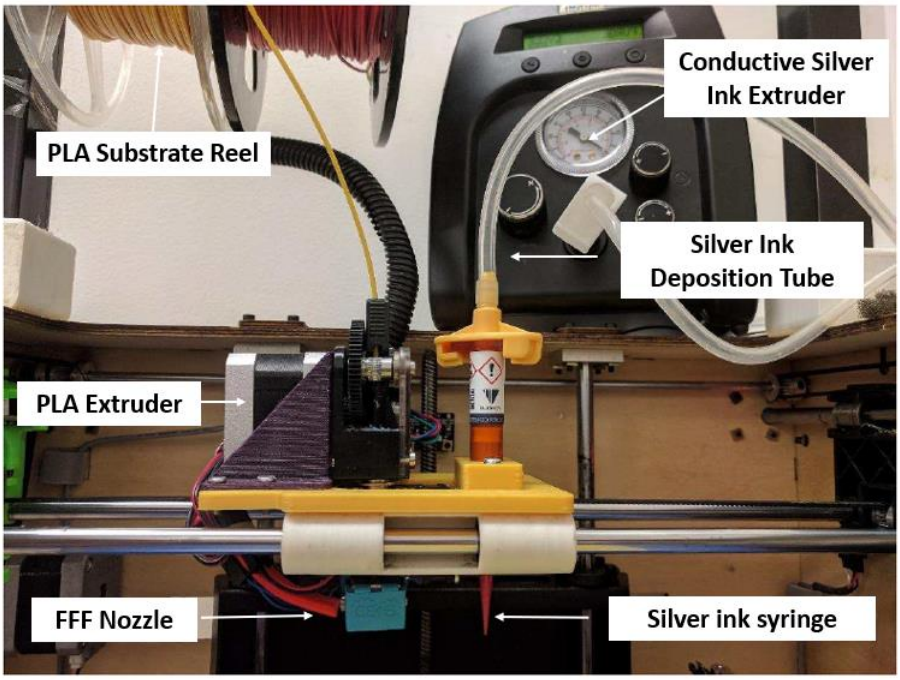

Fig. 5.10. Assembled 3D printer setup with dual-extruder deposition heads and the extension components.

The assembled printer setup had a layer resolution that ranged from 0.1 mm to 0.3 mm for smooth prints with reliable quality and a hoard 0.4 mm extruder hot end side. The printer motors had a travel rate of 50 to 120 mm/s and a printing speed which went up to 80 mm/s.

The dispenser that was used to deposit the silver paste was the Techcon TS250 [24], which was a digital fluid dispenser that dispensed fluids and pastes with low, medium, and high viscosities in accurate and repeatable manner. The dispenser consisted of a feature that enabled an adjustable vacuum-driven 'pull-back' option to regulate and minimise the wastage of the conductive ink, which was a vital condition for this whole exercise of developing the printer. The dispenser had a maximum input pressure of 100 psi with a wide 1-100 psi output pressure. The microcontroller that controlled the functioning of the printer and the extruders was the Arduino Mega 2560 which is a recognised and widely admired open-source board that consists of the ATMEL ATMEGA 2560 core microchip which ran on a 16 MHz crystal oscillator, 54 digital i/o (input/output) pins, 16 analogue inputs, 4 UARTs along with a USB connection. Majority of the FDM printers operated off the ATMEGA 2560 chips, which made them a dependable option to choose. The chips were mounted in RAMPS 1.4. The RAMPS 1.4 board is a shield used to contain the Arduino Mega 2560 chip. The board contained ports and headers

that offered connections for 6 stepper motors and their respective drivers, auxiliary header outputs to peripherals devices such as a Liquid Crystal Display (LCD) as well as an SD card reader that allowed the controller to print the designs without the obligation of a connection to a computer. This board simplified the design proposed in Fig. 5.10 even further by eradicating the requirement for a computer thereby reducing the costs related to the energy consumption.

Rest of the printer system comprised of Pololu A4988 motor drivers for the RAMPS 1.4 boards, four NEMA 17 motors which controlled the X, Y and Z axes as well as the extruder to push the filament out through the deposition head. These are standard issue motors for this type of printers and did not require any modification to their physical performance. RepRap Discount Full Graphic Smart Controller LCD screen was also deployed to examine the essential and critical details throughout the course of the printing process like the temperatures of the two extruders and the heated printer bed, the time passed through one print cycle and the status of the SD card. The whole system was powered by a 12 V, 20.8 A power supply. The high current output helped in generating the necessary heat to melt the filament and to power all the components such as the extruders and the cooling fan. Two crucial components of software which established the design's firmware were acquired and reworked as per the requirements, namely the Marlin firmware and the trigger script that controlled the second extruder. The Marlin firmware comprised of a collection of commands that characterized every one of the attributes that lied inside the printer's system and movements along with its focused functions for all the associated machines and modules. The codes were acquired through the readily available online resources and were modified with the help of a fellow researcher whose research specialised in dealing with the codes and trigger scripts. As the scripts and the code files were ready, the files were uploaded onto the RAMPS 1.4 PCB to execute the necessary G-codes. G-codes are any commands in a CNC based system that start with the letter G and they interact with the hardware system, instructing the machine tool perform the specific task such as swift motion, feeding of material within a straight stroke or curve, a combination of measured deposition movements, offsetting the tools and switching between co-ordinate systems to name a few. Both the printing extruders contained their own individual Arduino® microcontroller devices which controlled the deposition of the filament or the ink as well as their active and inactive states.

Calibration of the dual-extruder printer was an exceptionally crucial feature of this printer. The preliminary setup for the printer comprised of allocating the steps per millimetre along the axes for all the three axes as well as standardizing and realigning the bed-height for the modified printer. Looking from the software point of litigation, the printing temperature and print speed were needed to be in total harmony corresponding to the individual processes, to proceed with the extrusion multiplier and to go with the measurements of the boundaries of the modified setup. The steps per mm of motor that regulated the extruder regulated the quantity of filament which was fed to the hot end. 150 mm of PLA filament is measured and indicated from the top side of the extruder motor after the extruder has heated up to the required temperature. A set of instructions in the form of codes is subsequently transmitted through to the motor to extrude a further 100 mm of the filament.

The Techcon TS250 pressure dispenser machine that was installed for the conductive silver ink paste functioned via an alterable output of air-pressure that controlled and altered the stream of the paste and conductive ink. An analytical study to establish the optimum pressure flow was performed. The best and the most optimal width of the sample track was achieved when the pressure level was between 1-2 bar. Pressure was varied from 0.1 bar to 8 bar and the track widths for each one of the pressure levels were observed.

With all the calibration and system setup successfully completed with consistent and repeatable printing results achieved with the printer setup, the printer system was prepared for printing EM structures. A microwave FSS was designed and developed as a sample for printing to demonstrate the feasibility and accuracy using this low-cost printer setup.

5.3.3 Square Loop FSS Design

FSS arrays consisting of passive bandstop unit cell elements operate as filtering panels that provide safeguarding and shielding for electronic appliances from interferences triggered by the ambient RF signals. Square loop unit cell elements are preferred as they are popular unit structures for FSS that show dual-polarized responses while exhibiting excellent angle of incidence performance. The resonant frequency for the square loop is defined by the length of the arm of the loop that are typically $\frac{\lambda}{4}$ of the wavelength. The same design that was described for the microwave FSS design earlier in section 5.2 was used as a base which was redesigned

and modified. FSS square loop design is shown in Fig. 5.11 that was designed while concealing the manufacturing characteristics of the printer into consideration. The key dimensions for this FSS square loop can be seen from Table I. The element was designed for the PLA filament [25]. 3D FilaPrint based substrate model was deployed with a Voxel8 [22] silver ink paste model based on the datasheet for the ink provided by the manufacturer.

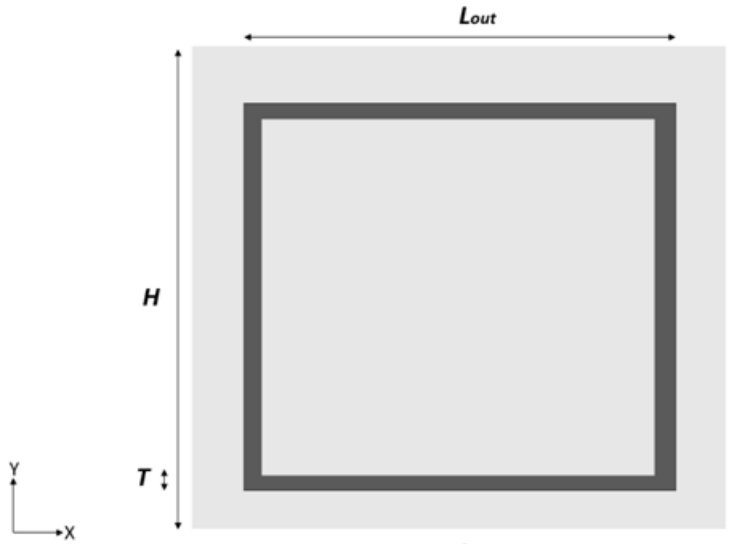

Fig. 5.11 Square-loop element FSS unit cell design

TABLE II
FSS UNIT CELL DIMENSIONS

Substrate	Length	L_{out}	H	T
PLA	**Dimensions (mm)**	26.4	28.95	1.25

The loops were designed to operate at a central frequency of 2.55 GHz. The length an arm of the arm of the square loop was 26.4 mm with a track width of 1.25 mm. The thickness of the design substrate was 0.8 mm which was exclusively developed in accordance with the printer to produce the PLA substrate as thin as feasible without spoiling the integrity of the printed substrate. The spacing between the two adjoining elements was 2.55 mm. A number of elements were designed where the distance between the adjoining elements was varied from 2 mm to 4.5 mm. A parametric study with the distance between the adjoining elements revealed that as the spacing among the unit cell elements was decreased, the equivalent capacitance increased, and the unit cell element resonated at a lower frequency. The simulated transmission response for the element can be seen in Fig. 5.12. The unit cell resonated at a central frequency

of 2.55 GHz. The TE and TM responses, namely TE-45 and TM-45 responses resonated at 2.61 GHz and 2.64 GHz, correspondingly. The extreme disparity with the larger size of the wavelength compared to the substrate thickness resulted in the variation of both TE-45 and TM-45 responses that resonated at a higher frequency than the normal response with a slightly narrower bandwidth. As there was a tolerance of ± 0.5 mm within the printer setup, certain parameters could also get altered during the fabrication and therefore, a parametric study for the variations was also conducted.

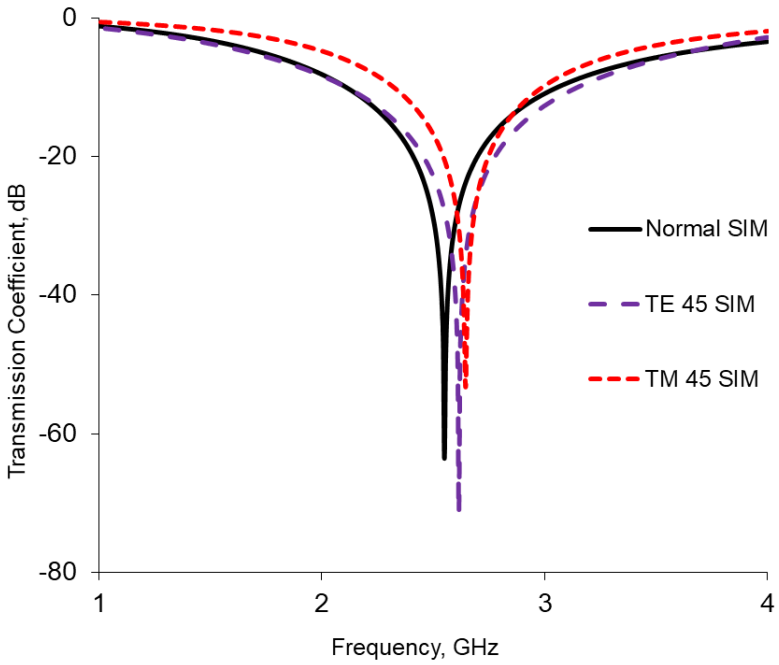

Fig. 5.12. Simulated transmission response and angle of incidence responses

A shift of nearly 3.5% was noticed among the transmission responses at 0 degrees and 45 degrees angle of incidence, respectively. The transmission response presented a considerably broad bandwidth of 38% at the normal angle response and 36% at the TE-45 and TM-45 responses. Collectively, the transmission response encompassed a wide range of operation from 2.1 GHz and going all the way up to roughly 3 GHz.

The relative permittivity (ε_r) of the substrate used in the simulation was 2.35 with a loss tangent of 0.01 which was consistent with the other implementations of the PLA substrate [26]. One of the advantages of PLA substrate is that the Relative permittivity, ε_r, is controllable based on

the way the filament is printed. The volume of the infill and the thickness of the printed structure are the contributing factors that can be altered to control the relative permittivity. Parametric studies pertaining to these two key elements can provide the guidelines for designing and fabrication considerations.

Fig. 5.13 denotes the parametric study that dealt with the effects of the substrate thickness on the resonant frequency. As the substrate thickness was increased by 0.1 mm, the resonant frequency decreased slightly. For every 0.1 mm variation in substrate thickness, the resonant frequency varied by approximately 0.025 GHz. The resonant frequency increased with a decrease in substrate thickness. The resonant frequency increased but the bandwidth decreased as the thickness of the substrate was decreased. The thickness of 0.8 mm provided the optimum balance between the frequency of operation, bandwidth, and the transmission null, which was highest at 0.8 mm.

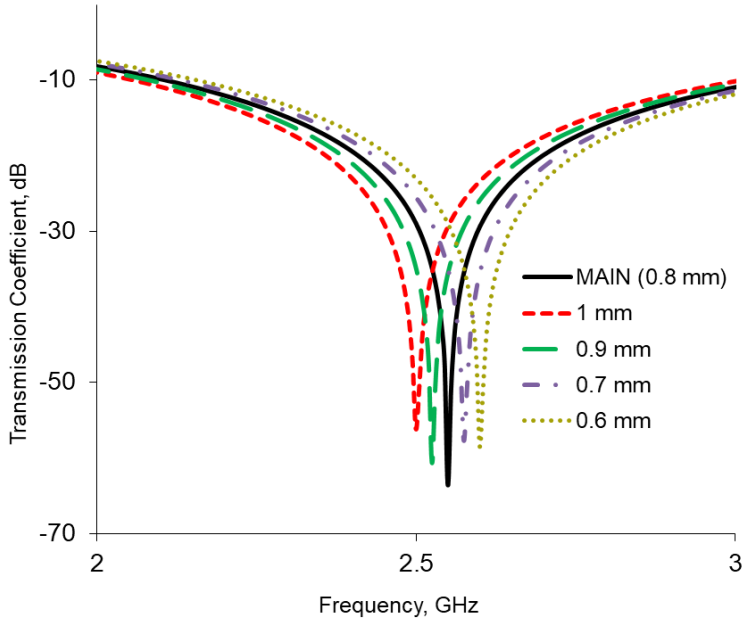

Fig. 5.13 Effects of the thickness of the substrate on the resonant frequency

Figure 5.14 (a) and Fig. 5.14 (b) present a parametric study on the effect of the relative permittivity on the transmission response for various angles of incidences. In comparison to Fig. 5.12, where the ε_r value was 2.35, two cases are presented with ε_r values as 2 and 2.7 in Fig. 5.14 (a) and 5.14 (b) respectively. The most significant variations that can be observed are in the resonant frequencies, the levels of the null and the TE-45 and TM-45 responses. In Fig.

5.12, the three responses presented a null of similar levels. In Fig. 5.14 (a), when the ε_r value is decreased to 2 from 2.35, the structure resonated at a central frequency of 2.63 GHz with the TE-45 and TM-45 responses resonating at 2.73 GHz and 2.74 GHz, respectively. The nulls for the three responses were asymmetric but showed a slightly better response than the proposed design as all three nulls below -70 dB were observed. When the ε_r value was increased to 2.7, as demonstrated in Fig. 5.14 (b), the resonant frequency at the normal angle of incidence decreased to 2.48 GHz with the TE-45 and TM-45 responses resonating at 2.57 GHz and 2.58 GHz, respectively. The nulls were about 10 dB lower in comparison to Fig. 5.14 (a). As it can be concluded from this parametric study and the results in Fig. 5.12, the shift in the angle of incidence responses reduces as the permittivity of the PLA substrate increases. The resonant frequency too increases with a decrease in permittivity. The bandwidth too gets narrower as the permittivity increases.

The biggest and the most significant finding of this parametric study is the noticeable and significant differences in the trends of the TE-45 and TM-45 responses in the three presented cases. When $\varepsilon_r = 2$, the TE-45 and TM-45 responses resonated almost adjacent to one another with a frequency shift of 0.01 GHz between the responses with a null which is well below the normal response. The maximum shift from the normal response is marginally over 4.2%. In the case of $\varepsilon_r = 2.7$, the disparity between the TE-45 and TM-45 responses was even more prominent with the TE-45 response resonating at significantly lower levels than the normal response whereas the TM-45 resonated had its null at a higher level of over 5 dB. The bandwidth too reduced significantly with a maximum frequency shift of 4% observed from the normal response. The maximum shift for the main proposed design, as presented in Fig. 5.12 earlier was 3.5% which was lowest among the three adjacent cases that are presented. As the ε_r value varied, the transmission response of the structure also changes as the property of the substrate material is altered. By varying the permittivity, the height of the tracks, and the deposition method of the conductive ink as well as the frequency of operation resulted in the varying transmission responses that were observed for the FSS designs fabricated on the raisin coated photo papers and PLA substrates. As this was a parametric study, experiments to characterise the process were not conducted. Further experiments can be carried out to validate the findings. The variable permittivity of PLA can be a lucrative property that can be used to develop designs that require the transmission response of any particular kind.

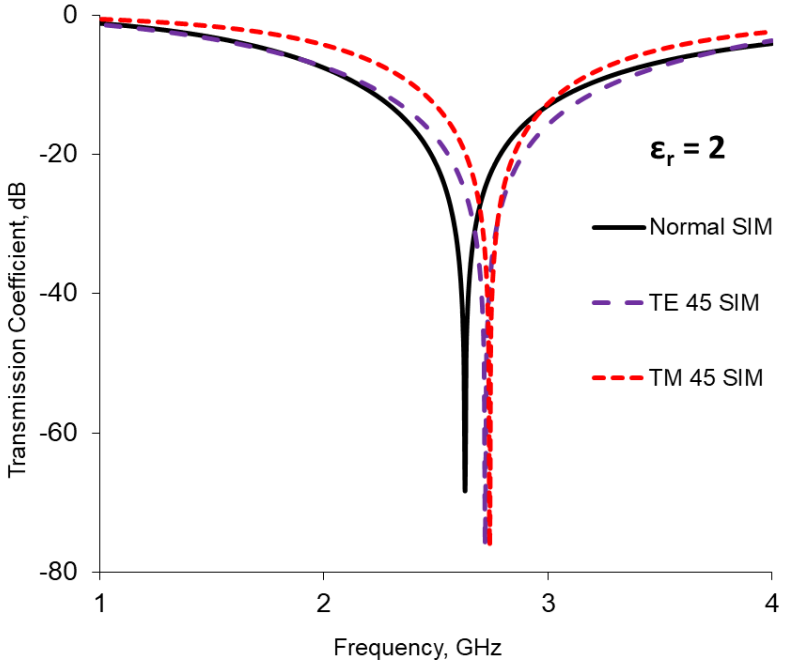

(a)

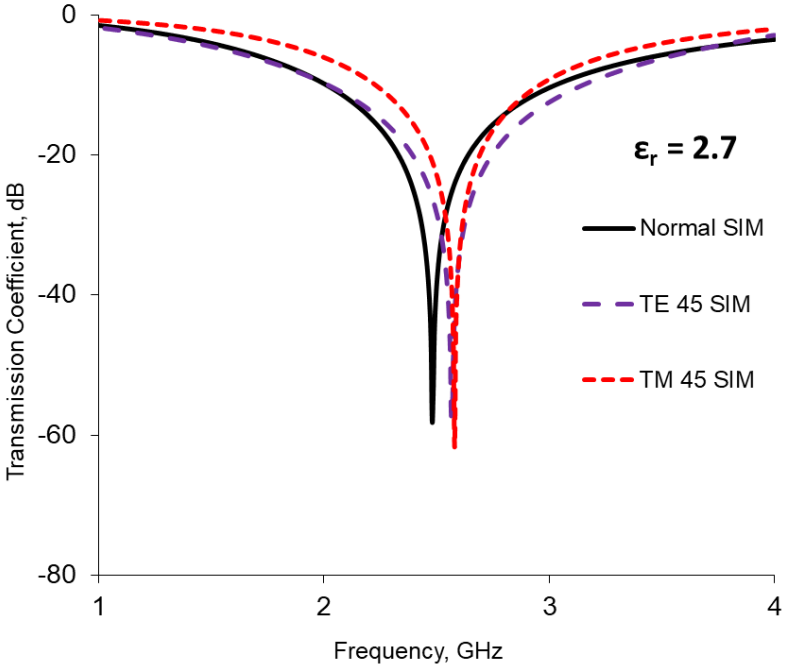

(b)

Fig. 5.14 Simulated transmission responses for (a) $\varepsilon_r = 2$ and (b) $\varepsilon_r = 2.7$

The permittivity of the printed PLA substrate can be varied by changing the density of plastic and the proportion of infill while designing and fabricating. Furthermore, the same design can be printed using filaments of different permittivity and the resultant frequency of operation and the angle of incidence responses can be deployed for the required applications.

5.3.4 Fabrication and Measurements

The entire FSS structure was printed as a whole array. An array consisting of 5 x 6 elements was printed as they fitted the bed size perfectly. The printed height of the fabricated PLA substrate was 0.8 mm. The substrate had an 100% infill for the durability of the design. A number of FSS samples were printed. The printing layer height of 200 microns was fed into the design that offered four layers of PLA deposition. The coating height was also set at 200 microns for the conductive silver ink paste. Just a single layer of deposition for the silver paste was adequate to safeguard the connection and reliable resistance levels for the printed loops with no requirements of any supplementary deposition of layers of ink.

A magnified photograph of one single loop of the 3D printed FSS design can be observed in Fig. 5.15. The pictures and profiles were acquired with the help of a Keynce® 4K Ultra HD microscope with 20x magnification and a Talysurf CCI optical interferometer. The resolution of the printed loop element is evidently visible in the photo. Uniformity of the printed substrate can also be observed. Fig. 5.15 (b) indicates the spacing between two square loop elements by enlarging the profile additionally. The measured gap among the two adjacent elements was 2481.14 µm or 2.48 mm which was sufficiently close to the anticipated 2.55 mm gap as per the design. Fig. 5.16 represents the surface profile roughness map for the PLA over a magnified segment of the substrate while Fig. 5.17 represents the side profile of the track and the 3D profile mapping of one of the printed FSS track and the substrate. The mean deviation within the printing of the PLA was 7.962 µm which displayed a reliable deposition. The cross-section silhouette exhibited the printing toolpath that fabricated the desired loop structure as a pattern of inner and outer loops, respectively. The close proximity of the ink then allowed the two loops to fuse together thus creating the single loop of the anticipated dimensions.

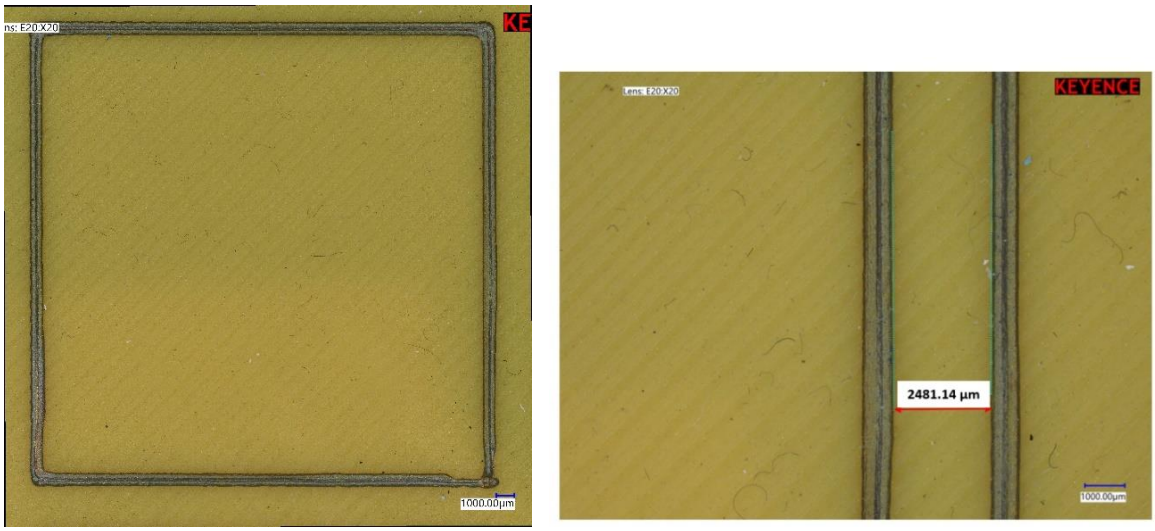

(a) (b)

Fig. 5.15 Printed square loop unit element in (a) and the gap between two adjacent square loops in (b)

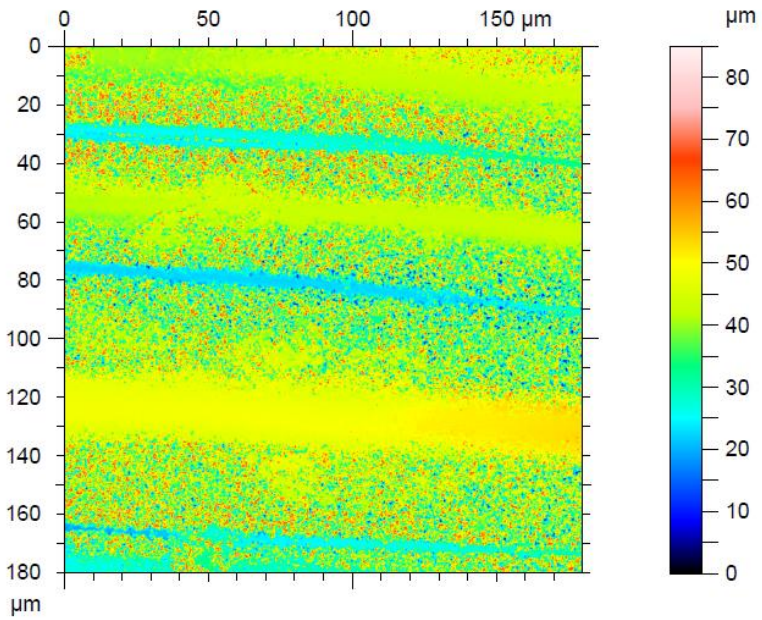

Fig. 5.16 Surface profile of the printed PLA substrate

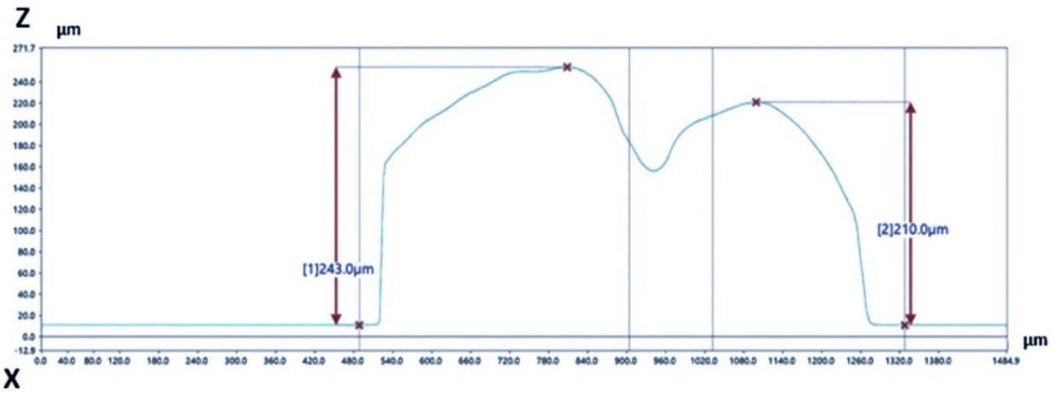

(a)

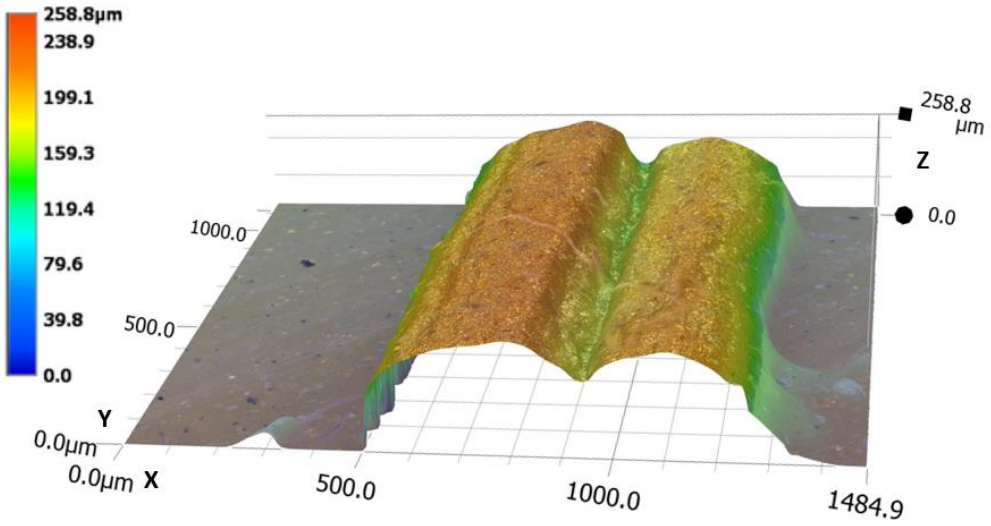

(b)

Fig. 5.17. Measured side profile of a printed track in (a) and 3D profile in (b)

These printed FSS designs were measured both separately and by joining a couple of printed sub-arrays to comprise a bigger array consisting of more elements. Framing two FSS adjoining to one another offered an effective array consisting of 10 x 6 elements. The transmission responses of the designs were evaluated in a plain-wave space. The measurement setup can be seen in Fig. 5.18. Same setup that was described earlier was deployed. The FSS structures were fitted inside the slot within an absorber screen that could rotate along its vertical axis to facilitate the angle of measurements. Placing of the joined printed FSS arrays within the slot inside the screen is depicted in Fig. 5.19. The 10 x 6 array was created by putting two FSS adjacent to one another that filled up the screen aperture. The measurements were performed

using an Anritsu® 37397C Vector Network Analyzer (VNA) using two standard R&S helix antennas.

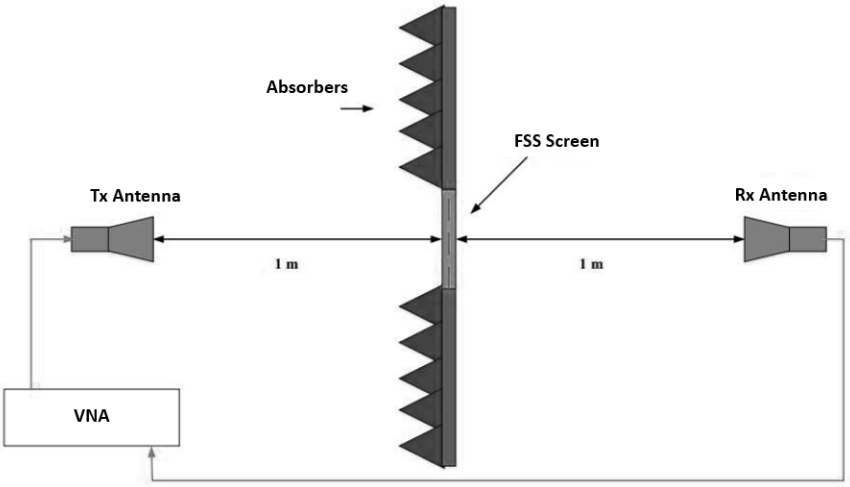

Fig. 5.18. Measurement Setup Layout

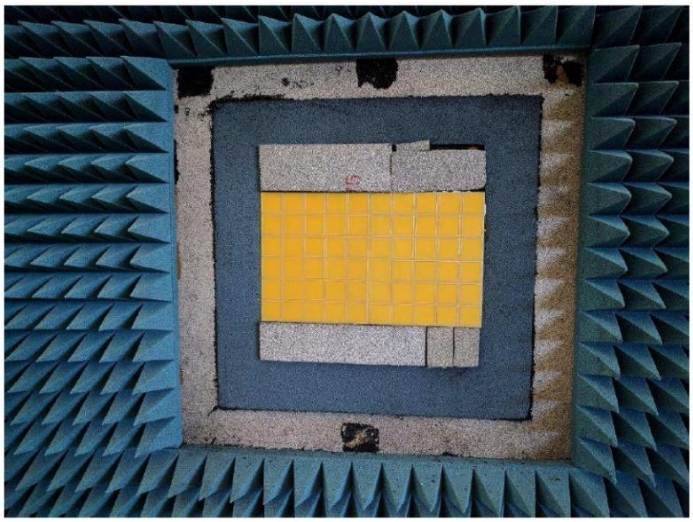

Fig. 5.19. FSS structure fitted inside the absorber screen

The FSS was measured for various transmission responses. The measured incident transmission responses at various angle of incidence are presented in Fig. 5.20. The FSS operated at a central frequency of 2.56 GHz which was roughly the equivalent of the simulated response. A 28% -10 dB bandwidth was monitored for the normal angle of incidence transmission response.

The TM-45 and TE-45 angle of incidence responses resonated at 2.65 GHz and 2.59 GHz, respectively. The TM-45 response suffered a shift of 3% although the TE-45 response exhibited a shift of 2%. All the three responses presented a significantly wide -10 dB bandwidth response that covered a band over 2.4 GHz by all the modes. Largely, the measured transmission responses were in good agreement with the simulated responses.

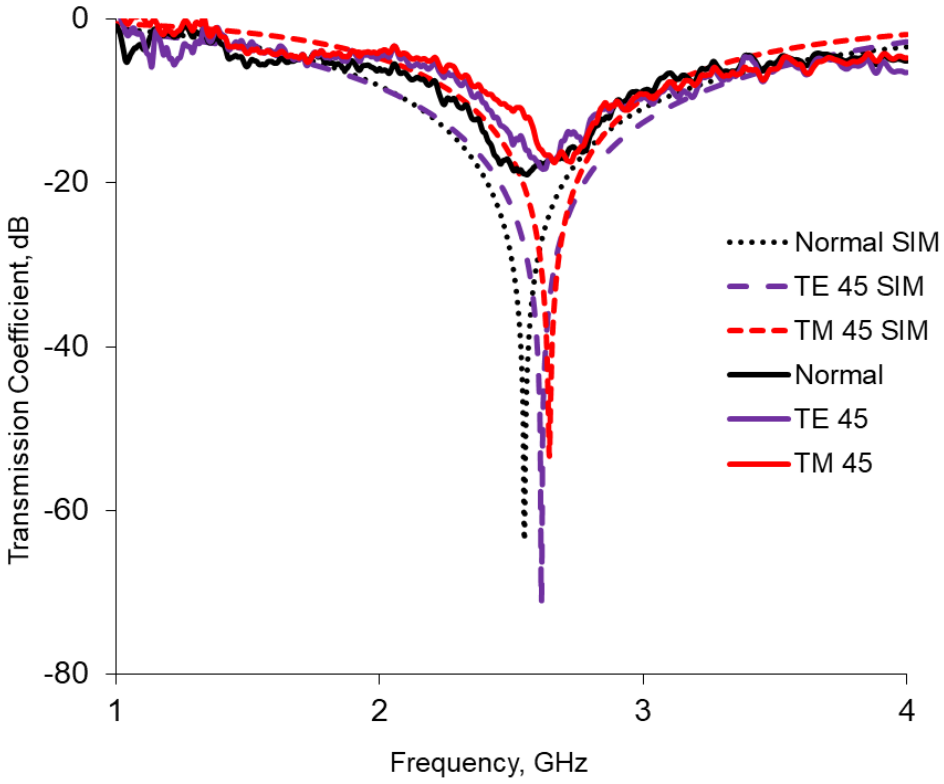

Fig. 5.20. Measured Transmission Response of the FSS structure

5.4 Conclusion

Inkjet printing of paper posters consisting of bandstop FSS have been presented in the first half of this chapter. The posters were developed for microwave and sub mm-wave applications, respectively. The two low-cost FSS poster solutions were inkjet-printed using the household Brother inkjet printer discussed earlier using silver nanoparticle ink filled in its refillable cassettes. Swift, low-priced and nature friendly printing made this printing method a suitable and sustainable alternative for FSS filtering posters. The precision and the consistency of the printed tracks made this a lucrative fabrication alternative. The measured responses for the two

posters offered coherence with the simulation transmission response at the frequency of operation of 2.49 GHz and 25.2 GHz while covering the 2.4 GHz band for microwave communications and 24 GHz band used in 5G communications, respectively.

The microwave FSS poster and the sub mm-wave FSS poster printed on a photo paper can be mounted on the walls of a room to reduce the drop in signal strength and enhance the reception for other futuristic 5G based applications. The performance of the design can be further enhanced by printing multiple layers of the FSS structure on top of one another. By adding active components, this FSS can also be developed as a smart FSS.

The development of an additive manufacturing open-source machine and the considerations for fully 3D printed Frequency Selective Surface structure has also been discussed. A low-cost printer system combining FFF with an air pressure dispenser was able to print plastic substrates and metallic conductive materials simultaneously. Several considerations and adjustments were required within the printer which included recalibrating the extruder limits and printing components for the printer built using an FDM printer.

A square loop FSS structure was designed and printed while taking the manufacturing constraints of the printing system into account. The printed profile of the FSS demonstrated the success of the fabrication technique. Each fabricated design was tested for conductivity and the designs demonstrated the conductivity in line with the expected values for the ink. The FSS operated at a central frequency of 2.55 GHz and provided a significantly stable angle of incidence response with all the modes of the angle of response covering the 2.4 GHz band while providing wide -10 dB bandwidths.

The scalable property of the printing setup makes it a lucrative option for the development of 3D structures which are printed in their entirety. The reliable performance of the ink could provide a potential solution of the development of fully 3D printed FSS designs and antennas fabricated on a variety of three-dimensional substrates while significantly reducing the cost of fabrication. The 3D printed designs can also be made flexible.

References

[1] B. A. Munk, Frequency selective surfaces: Theory and design, New York: Wiley, 2000, pp 636-659, doi: 10.1002/0471723770.

[2] E. A. Parker, “The Gentleman's Guide to Frequency Selective Surfaces,” 01-Jan-1991. [Online]. Available: https://kar.kent.ac.uk/59863/. [Accessed: 01-Aug-2020].

[3] A. A. Dewani, S. G. Okeefe, D. V. Thiel, and A. Galehdar, “Window RF Shielding Film Using Printed FSS,” *IEEE Transactions on Antennas and Propagation*, vol. 66, no. 2, pp. 790–796, 2018.

[4] B. M. Turki *et al*., "Significant Factors in the Inkjet Manufacture of Frequency-Selective Surfaces," in *IEEE Transactions on Components, Packaging and Manufacturing Technology*, vol. 6, no. 6, pp. 933-940, June 2016, doi: 10.1109/TCPMT.2016.2561972.

[5] D. Zhou, X. Huang and Z. Du, "Analysis and Design of Multilayered Broadband Radar Absorbing Metamaterial Using the 3-D Printing Technology-Based Method," in *IEEE Antennas and Wireless Propagation Letters*, vol. 16, pp. 133-136, 2017, doi: 10.1109/LAWP.2016.2560904.

[6] D. Lim, S. Yu and S. Lim, "Miniaturized Metamaterial Absorber Using Three-Dimensional Printed Stair-Like Jerusalem Cross," in *IEEE Access*, vol. 6, pp. 43654-43659, 2018, doi: 10.1109/ACCESS.2018.2862160.

[7] S. Cho, S. Yoon and I. Hong, "Design of Three-Dimensional Frequency Selective Structure With Replaceable Unit Structures Using a 3-D Printing Technique," in *IEEE Antennas and Wireless Propagation Letters*, vol. 17, no. 11, pp. 2041-2045, Nov. 2018, doi: 10.1109/LAWP.2018.2871175.

[8] R. Mirzavand, M. M. Honari, S. Aslanzadeh, H. Saghlatoon and P. Mousavi, "Evaluation of One-Staged 3-D Printed Frequency Selective Surface Using Carbon-Fiber-Reinforced Thermoplastic Composite," in *IEEE Transactions on Components, Packaging and Manufacturing Technology*, vol. 9, no. 11, pp. 2298-2304, Nov. 2019, doi: 10.1109/TCPMT.2019.2917197.

[9] A. Shastri *et al*., "Evaluation of Aerosol Jet Printing of Frequency Selective Surface on Glass for Building and RF Applications," *2020 14th European Conference on Antennas and Propagation (EuCAP)*, Copenhagen, Denmark, 2020, pp. 1-5, doi: 10.23919/EuCAP48036.2020.9135346.

[10] A. Shastri, B. Sanz-Izquierdo, E. A. Parker, S. Gao, P. Reynaert, Z. Chen and L. Winchester, "3D Printing of Millimetre Wave and Low-Terahertz Frequency Selective Surfaces Using Aerosol Jet Technology," in *IEEE Access*, vol. 8, pp. 177341-177350, 2020, doi: 10.1109/ACCESS.2020.3024584.

[11] B. Sanz-Izquierdo and E. A. Parker, "3D printing technique for fabrication of frequency selective structures for built environment," in *Electronics Letters*, vol. 49, no. 18, pp. 1117-1118, 29 August 2013, doi: 10.1049/el.2013.2256.

[12] B. Sanz-Izquierdo and E. A. Parker, "3-D Printing of Elements in Frequency Selective Arrays," in *IEEE Transactions on Antennas and Propagation*, vol. 62, no. 12, pp. 6060-6066, Dec. 2014, doi: 10.1109/TAP.2014.2359470.

[13] B. Sanz-Izquierdo and E. A. Parker, "Frequency selective surfaces formed by partially metalising 3D printed shapes," *2015 9th European Conference on Antennas and Propagation (EuCAP)*, Lisbon, 2015, pp. 1-4.

[14] J. Heirons, S. Jun, A. Shastri, B. Sanz-Izquierdo, D. Bird, L. Winchester, L. Evans and A. McClelland, "Inkjet Printed GPS antenna on a 3D printed substrate using low-cost machines," *2016 Loughborough Antennas & Propagation Conference (LAPC)*, Loughborough, 2016, pp. 1-4, doi: 10.1109/LAPC.2016.7807590.

[15] A. Shastri, S. Jun, B. Sanz-Izquierdo, H. Aldawas, Q. Ahmed and M. Sobhy, "Evaluation of a low-cost inkjet-printed slot antenna for energy harvesting applications," *2016 Loughborough Antennas & Propagation Conference (LAPC)*, Loughborough, 2016, pp. 1-5, doi: 10.1109/LAPC.2016.7807593.

[16] S. Y. Jun, B. Sanz-Izquierdo, E. A. Parker, D. Bird and A. McClelland, "Manufacturing Considerations in the 3-D Printing of Fractal Antennas," *IEEE Transactions on Components, Packaging and Manufacturing Technology*, vol. 7, no. 11, pp. 1891 - 1898, 2017.

[17] M. Liang, C. Shemelya, E. MacDonald, R. Wicker, and H. Xin, “3-D printed microwave patch antenna via fused deposition method and ultrasonic wire mesh embedding technique,” *IEEE Antennas Wireless Propag. Lett*., vol. 14, pp. 1346–1349, 2015.

[18] R. Xu *et al*., "140 GHz Additive Manufacturing Low-Cost and High-Gain Fabry-Perot Resonator Antenna," *2020 International Workshop on Antenna Technology (iWAT)*, Bucharest, Romania, 2020, pp. 1-4, doi: 10.1109/iWAT48004.2020.1570598322.

[19] S. Y. Jun, A. Elibiary, B. Sanz-Izquierdo, L. Winchester, D. Bird and A. McCleland, "3-D Printing of Conformal Antennas for Diversity Wrist Worn Applications," in *IEEE Transactions on Components, Packaging and Manufacturing Technology*, vol. 8, no. 12, pp. 2227-2235, Dec. 2018, doi: 10.1109/TCPMT.2018.2874424.

[20] "Mitsubishi Raisin Coated Paper | Special Media | Mitsubishi Paper Mills Limited", K-mpm.com, 2020. [Online]. Available: http://www.k-mpm.com/agnanoen/agnano_media.html. [Accessed: 19- Sep- 2020].

[21] [online] http://www.mbot3d.com [Accessed 24 Aug. 2020].

[22] [online] https://www.makerbot.com [Accessed 25 Aug. 2020].

[23] [online] www.voxel8.co [Accessed 25 Aug. 2020].

[24] "Digital Fluid Dispenser - TS250", *Techconsystems.com*, 2020. [Online]. Available: http://www.techconsystems.com/en/fluid-dispensers/digital-fluid-dispensers/basic-digital-dispensers/ts250-digital-fluid-dispenser/. [Accessed: 25- Aug- 2020].

[25] PLA", *Shop.3dfilaprint.com*, 2020. [Online]. Available: https://shop.3dfilaprint.com/pla-199-c.asp. [Accessed: 25- Aug- 2020].

[26] D. Sjöberg, A. J. Johansson and C. Larsson, "Electromagnetic properties of heterogeneous material structures produced in 3D-printers," *2014 International Conference on Electromagnetics in Advanced Applications (ICEAA)*, Palm Beach, 2014, pp. 605-607, doi: 10.1109/ICEAA.2014.6903930.

CHAPTER 6

AEROSOL JET PRINTING OF BANDSTOP AND BANDPASS FREQUENCY SELECTIVE SURFACES

6.1 Introduction

This chapter presents the development of Frequency Selective Surfaces (FSSs) using Aerosol Jet printing technology for filtering at microwave, millimetre, and low-THz waves, which find use in WLAN, Beyond 5G and eminent 6G applications. The aerosol jet printer is deployed to develop bandstop and bandpass FSS structures. Two solutions for microwave and sub millimetre wave bandstop FSS as well as two millimetre-wave and low-THz single-polarized bandpass FSS designs are presented. Aerosol Jet Printing technique using silver nano-particle ink is utilised in this chapter to develop the FSS reflectarrays. Aerosol Jet Printing is an AM technique which enables the fabrication of designs with millimetre to micrometre level precision delivered at a swift rate. With the accuracy and precision that aerosol jet provides, a number of AM design can be produced using this technique. Bandstop FSS solutions are developed here to create radio frequency (RF) shielding surfaces and frequency reflectors for indoor environments. Square loop unit cell elements are designed which are arranged in a square lattice for this solution. These FSS shields and reflectors are suitable for 4G as well as 5G applications. Two solutions are proposed, one for microwave applications and one for sub-millimetre wave applications. The design solutions when combined with Aerosol Jet printing are able to print extremely fine tracks that are required for the design solutions and the fabricated silver ink tracks provide adequate, uniform conductivity of the tracks which is essential for filtering performances. The microwave bandstop FSS structure operates at the resonant frequency of 2.5 GHz which is regularly used in 4G, WLAN and wireless communication systems across the world. Sub-millimetre wave bandstop FSS structures operate in the 26-28 GHz frequency band that is particularly sought after in 5G communication

networks. The aim is to demonstrate a potential solution for the development of FSS for buildings and RF shielding applications to reduce the signal drop within the indoor environments while also providing shielding from unwanted radio signals. Glass windows and walls can easily deploy these printed FSS solutions and enhance their RF signal capabilities while minimising the drop in signals. RF signals have frequently experienced drops in signal quality as well as signal strength inside a typical indoor environment owing to the surface absorption and transmission passing through various construction materials. With the arrival of 5G networks and the rolling out of the new high frequency signals within the surroundings, the issue of signal drop has significantly risen which affects multiple frequency bands and the proposed Bandstop FSS solutions can help minimise the drop in signals.

Two single-polarised Bandpass FSS designs were developed that operate in the millimetre wave and Low-THz regions of the frequency bands, respectively. The millimetre wave band design operated at 125 GHz and the Low-THz band design operated at 280 GHz. Simulated and measured results demonstrate a good coherence in the passing state as well in the blocking state. The fabrication strategies to develop the aerosol jet toolpath to create the slot FSS designs are also discussed. Surface profiles of the printed designs are also presented. Magnified images of the two designs reveal the precision of the slots at microscopic levels. The proposed bandpass FSS solutions can be deployed for Beyond 5G and 6G communications. The Kapton based design can also be used for satellite and galactic communications due to its high temperature tolerance.

FSSs are planar periodic structures which can provide a filtering response to the incident signal wave [1]. FSSs have been readily suggested to diminish and ideally eradicate the dropping of signals and to increase signal coverage and strength within building complexes [2] - [10]. Magnitude and levels of signal's dispersion losses are based upon the dielectric characteristics, conductivity, structural design, and the recurrent structures of the materials used in a building. These parameters all part of the EM architecture of the building. Figure 6.1 shows a typical window frequency reflector on glass substrate. FSS have been intended for installing on walls and false ceilings as well as in glass windows [2] – [17] inside a building. With the rapid growth of printable electronics and AM, a wide range of possibilities in the developed of FSS reflectors have appeared. Two such proposed solutions for bandstop FSS designs are proposed as some existing bandstop FSS designs are expensive and require some labour-intensive

implementation and development. The complex fabrications process mean that the design fabrications require specified skills. Simple, inexpensive and environment friendly AM method of developing designs is proposed here. The metallic layers of the 3D printed FSS arrays are fabricated with the help of silver-Nano particle ink deposited directly onto the two substrates by using aerosol jet printing.

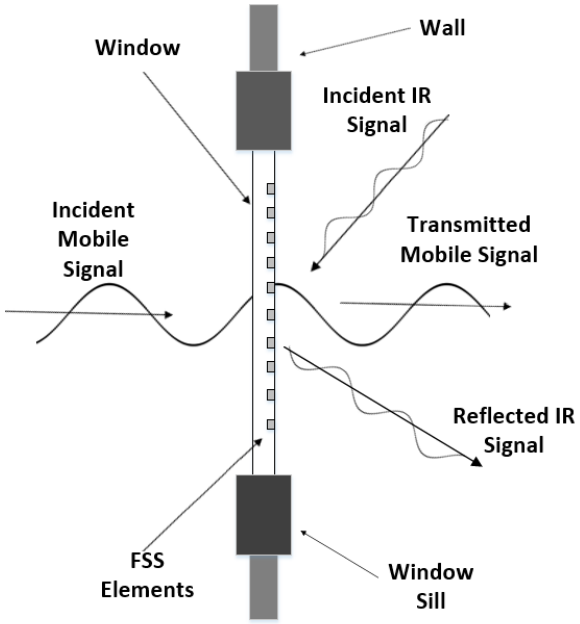

Fig. 6.1 A typical FSS reflector implemented on glass in windows [10]

Millimetre wave and THz bands, that are collectively referred to as low-THz bands nowadays, find wide range of applications [18] – [31]. To successfully develop communication and transmission technologies, it is essential to ensure that the loss and drop of the signals is ideally kept at the bare minimum. Absorption of signals in various indoor and outdoor materials as well as reflection of signals off some materials is the lead cause of loss of signals.

3D bandpass FSS are screens developed by the help of additive manufacturing to achieve wide-band filtering response. Slot FSS bandpass designs are particularly popular for filtering. A wide range of FSS designs developed using AM are presented in [32] – [42]. Aerosol jet printing of the design adds another dimension of AM of low-THz band designs.

This chapter is organized as following. Section 6.2 describes the microwave bandstop FSS design. Section 6.3 describes the millimetre wave bandstop FSS design. Section 6.4 presents the printing technique and surface profiles along with measurement results for the bandstop FSS designs. CST Microwave Studio^{TM} was used in simulation of the FSS designs.

6.2 Microwave bandstop FSS design

As was the case with the previous chapter, a square loop unit cell was the preferred choice for the FSS designs. The square loop array design provided an optimised cover across the space and offers reliable dual-polarized responses.

6.2.1 Design dimensions

The design for the microwave bandstop FSS consists of a unit cell that contains a loop element which is used for the array. The bandstop FSS design consists of an array of square loop elements arranged into a square lattice. Square loop design features a square track of uniform width. The unit cell of the structure can be seen in Fig. 6.2. The unit cell layout consists of the design square loop element of 27 mm by 27 mm dimensions with the printed loop that is of 23.2 mm by 23.2 mm sides and has a track with the width of 0.5 mm. For the Kapton design, the loops were of 25.2 mm by 25.2 mm. The thickness of the corning eagle glass substrate was 0.7mm and the predefined permittivity (ε_r), of 5.27 and a loss tangent of 0.001 for the glass [43], [44]. The thickness of Kapton substrate was 0.05 mm and the permittivity (ε_r) value 3.4 with a loss tangent of 0.002 [45].

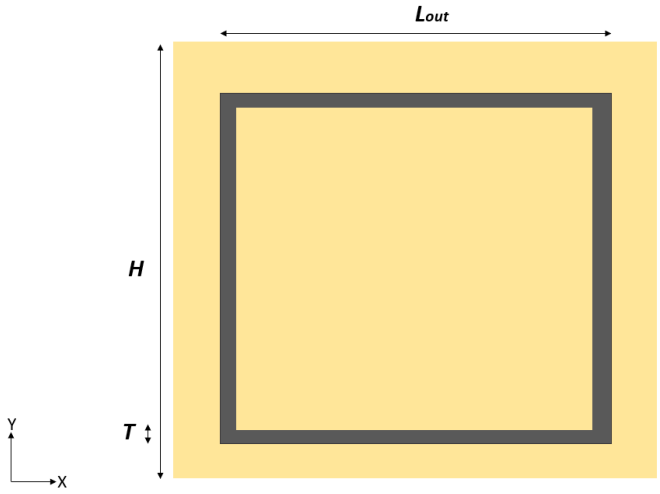

Fig. 6.2 Unit Cell of square loop element

TABLE II.

DIMENSIONS IN MM

Length	***Lout***	***H***	***T***
Dimensions (mm)	23.2	27	0.5

Equivalent circuit of the loop element with the equivalent values was calculated using [10] and [46]. The equivalent circuitry for the loop element can be seen in Fig. 6.3.

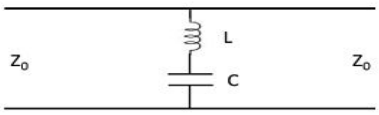

Fig. 6.3 Square loop element equivalent circuit

The equivalent values for the LC serial equivalent design can be calculated using [46] and follows the following equations:

$$L=3.937\frac{a^2}{8a+11c}\times K_g \quad (1)$$

Where, L is the inductance value and C is the capacitance values. Other variables can be defined as follows:

$$a = \frac{Lout + Lin}{4}$$

$$c = \frac{Lout - Lin}{2}$$

$$K_g = 0.57 - 0.145 ln \frac{T}{h}$$

Using the value of L obtained using (1), C can be calculated as:

$$C = \frac{1}{(2\pi f)^2 L} \quad (2)$$

Using equation (1) and equation (2), the equivalent calculated values of Inductance was 3.19 nH and the equivalent calculated value of the capacitance was1.32 pF.

6.2.2 Simulation responses

The simulated transmission response for the bandstop FSS design for glass is presented in Fig. 5.4 whereas the simulated response for Kapton is presented in fig. 5.5. The resonating frequency of 2.5 GHz with a null which is over -40 dB for all angles of response for the design can be observed. A slender shift from the conventional responses of a loop element FSS can be seen at the transverse electric (TE) as well as transverse magnetic (TM) responses respectively at 45^o angle. A below -10 dB transmission bandwidth of 18% is achieved after considering all the three transmission responses. This bandwidth is sufficient to cover the desired 2.4 GHz 4G, wireless band and surrounding WLAN bands.

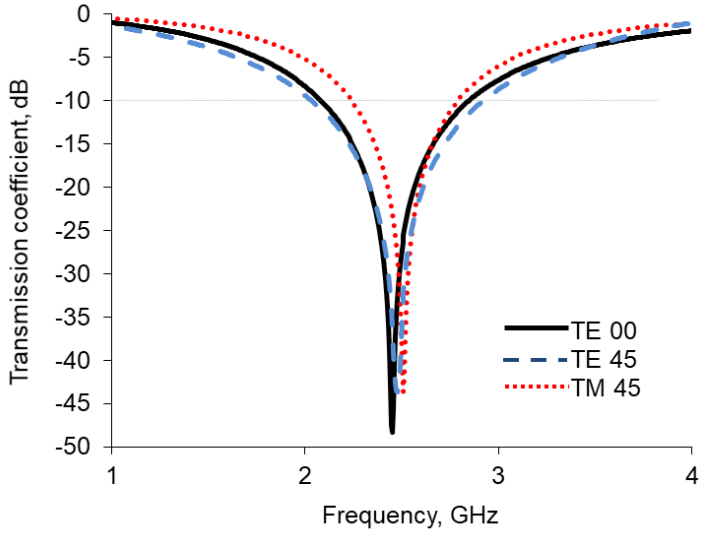

Fig. 6.4. Simulated transmission response of the microwave Bandstop FSS on glass

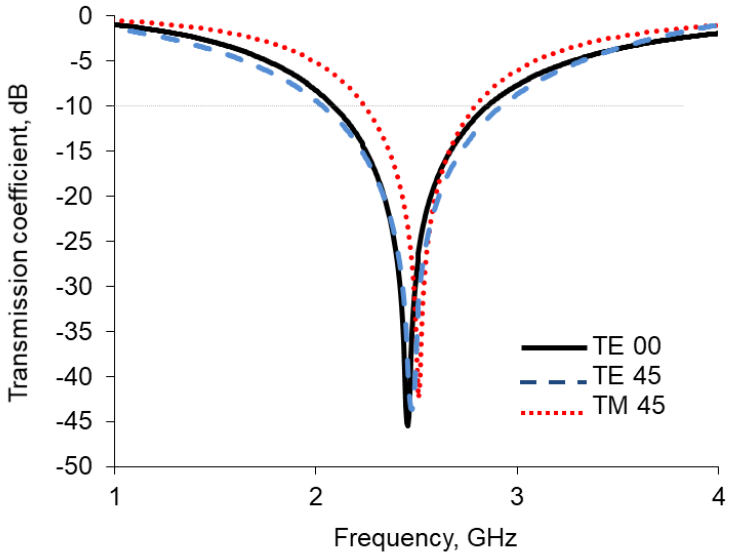

Fig. 6.5. Simulated transmission response of the microwave Bandstop FSS on Kapton

6.3 Millimetre wave bandstop FSS design

6.3.1 Design dimensions

Millimetre wave bandstop FSS with square loop element arrays work primarily as reflector screens to reduce the drop in signals in 5G communications and to protect wireless devices

from various signal interferences. The design for mm-wave bandstop FSS makes use of square loop elements array which is arranged in a square arrangement. The unit cell of square loop can be seen in Fig. 6.6. Table 6.2 represents dimensions of the design. The square unit cell layout consists of sides *H* of 3 mm width and height along with the square loop that have the outer dimensions as L_{out} which is 2.45 mm. The width of the track *T* for square loop was 0.42 mm. That makes the inner dimensions of the loop L_{in} as 2.03 mm. The designs were simulated with the help of CST Microwave Studio™ with both Kapton and corning eagle glass as substrates. The operational frequencies of the designs were 27.5 GHz for Kapton and 26.5 GHz for glass.

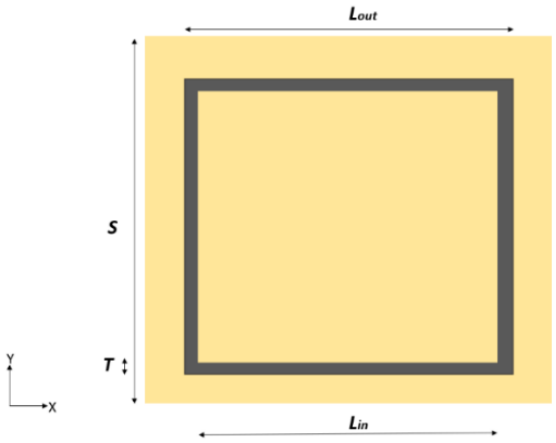

Fig. 6.6. Millimetre wave square-loop patch FSS unit cell design

TABLE III.

DIMENSIONS IN MM

Substrate	Length	L_{out}	*S*	*T*
Kapton	Dimensions (mm)	3.36	3.8	0.42
Glass	Dimensions (mm)	2.7	3.6	0.42

The thickness of the Kapton substrate was 50 microns or 0.05 mm and the thickness of glass was 0.7 mm. Relative permittivity (ε_r) for Kapton, and glass were 3.4 and 5.27, respectively. The loss tangents were 0.002 and 0.001, respectively. The equivalent circuit of the loop element was same as shown in Fig. 6.3. Using equation (1) and equation (2) from section 6.2, the calculated equivalent inductance value was 10.34 nH while the calculated equivalent capacitance value was 0.0032 pF.

6.3.2 Simulated transmission responses

The simulated transmission response for the millimetre wave bandstop FSS design on corning eagle glass is presented in Fig. 6.7. The resonating frequency for glass was 26.6 GHz with resonant frequency shifts of 2 GHz for all angles of response for the design can be observed. A shift from in the responses of a loop element FSS can be seen at the transverse electric (TE) as well as transverse magnetic (TM) responses respectively at 45-degree angle. TE 45 resonates at 25 GHz with 5% frequency shift while TM45 response resonates at 27 GHz with 1% shift. A below -10 dB transmission bandwidth of approximately 14% is achieved after considering all the three transmission responses.

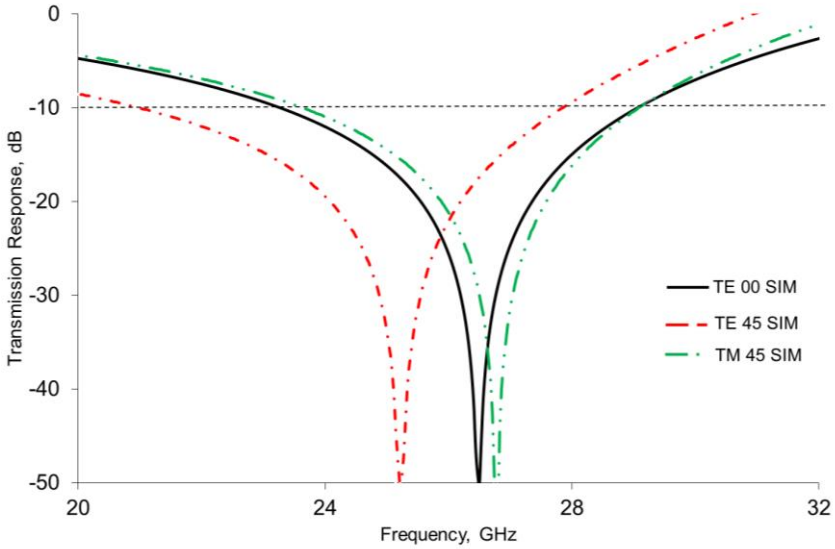

Fig. 6.7 Simulated transmission response for bandstop FSS design on glass

Simulated transmission response for bandstop FSS design on Kapton is presented in Fig. 6.8. The resonating frequency for Kapton was 30 GHz with frequency dip of 1.3 GHz for all angles of transmission response for the design was observed. A shift from in the responses of the Glass loop element FSS are observed at the transverse electric (TE) as well as transverse magnetic (TM) responses respectively at 45° angle. TE 45 resonated at 26.7 GHz with a resonant frequency shift of 8% while TM 45 response resonates at 28 GHz with a 7% shift. A below -10 dB transmission bandwidth of approximately 19% is achieved after considering all the three transmission responses.

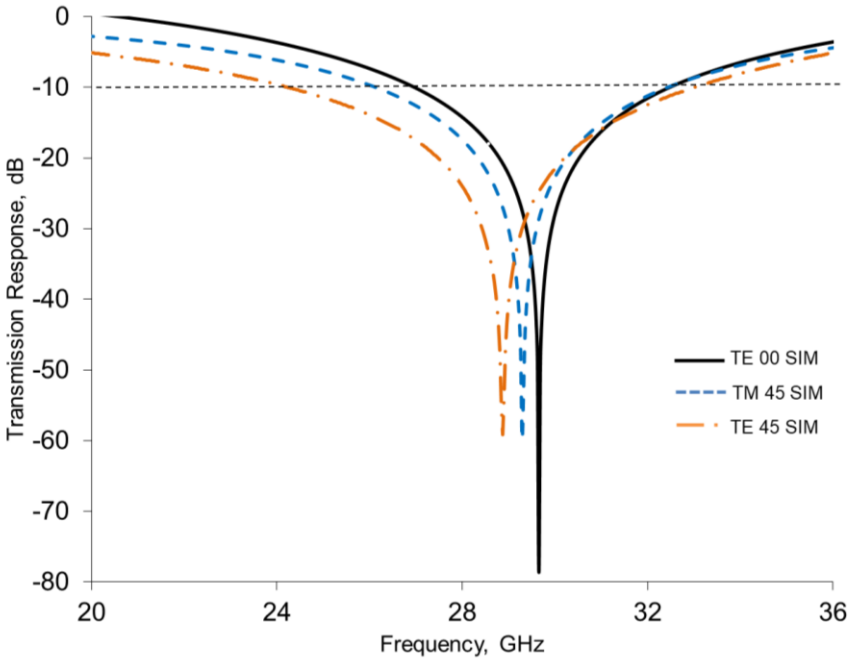

Fig. 6.8 Simulated transmission response for bandstop FSS design on Kapton

6.4 Aerosol Jet printing and measurement results

6.4.1 Aerosol Jet printing

The designs were fabricated at the Centre for Process Innovation, Sedgefield, Durham, United Kingdom using Aerosol Jet Printing technology. Aerosol Jet Printer are systems manufactured to facilitate, create, repair, enhance and fabricate intricate electronic designs with high precision [47] – [49]. A typical aerosol jet printing system was discussed in Chapter 2 and can also be seen in Fig. 6.9. The Aerosol Jet printing process makes use of aerodynamics to precisely concentrate and precisely deposit conductive inks onto substrates. The conductive ink is filled in the atomizer, that produces an extremely dense mist with incoming sheath gas and ink droplets with size ranging between 1 to 5 microns in diameter. The aerosol ink and sheath gas mist are then delivered through a tube into to the deposition head where it is concentrated by another addition of sheath gas, which encloses the aerosol as a ring.

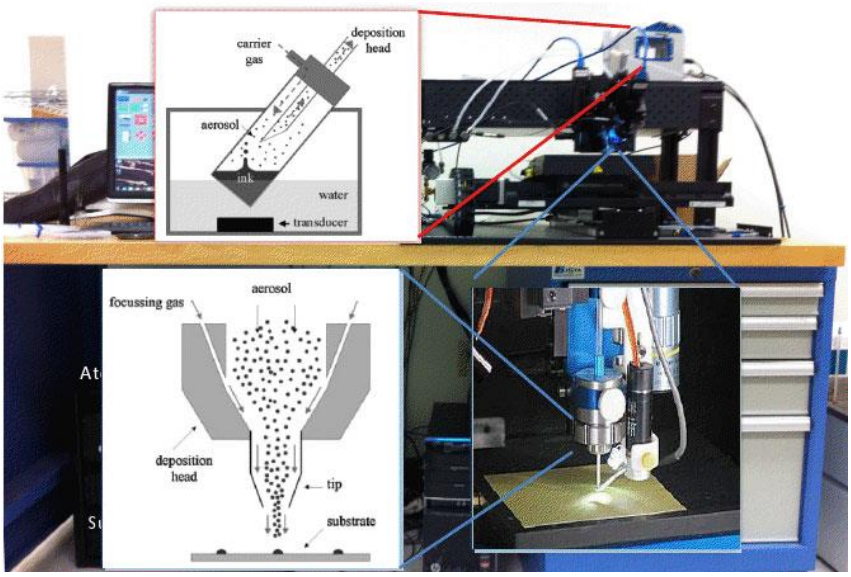

(a)

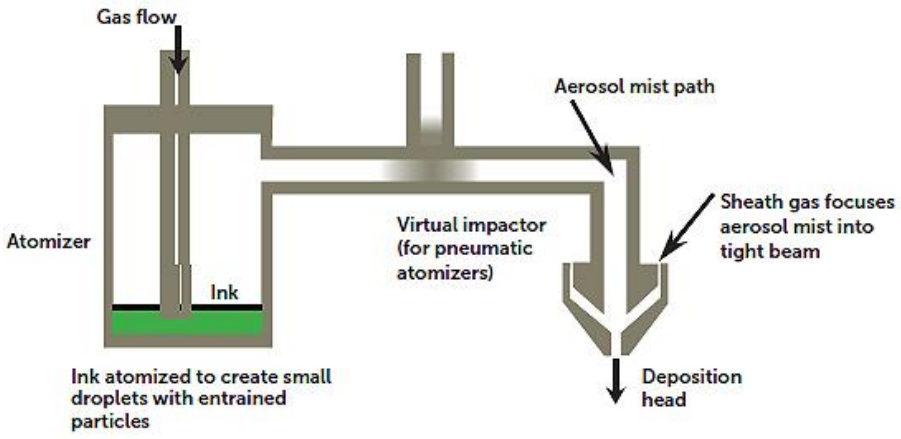

(b)

Fig. 6.9. A typical Aerosol Jet Printer in (a) with its functioning block in (b) [48]

When the added sheath gas as well as aerosol ink mist passes though the tiny nozzle, it is accelerated, and the aerosol is converted into a flow of droplets flowing in the sheath gas. The sheath gas, which is typically Nitrogen or pressurised air, also helps insulating the nozzle from clogging. The subsequent stream of high-speed ink is deposited on the substrate over a distance of 2 to 5 mm. The system is controlled and operated by standard CAD data that is used as a basis to create a vector-based tool path. The tool path allows the deposition of the ink in the desired patter by driving a 2D or 3D motion system. Printed features range from 10 microns to millimetres.

In order to achieve the desired conductive surface, a number of parameters within the aerosol jet systems are required to be adjusted. The parameters of the sheath gas flow, the speed of the deposition head, the flow rate and the size of the nozzle used define the quality and the thickness of the printed designs. Faster print speed results in finer tracks whereas a low sheath gas level results in more scattered prints across the printed area. Consistent clogging of the tube connecting virtual impactor and deposition head means the designs have to be broken into several parts and the tubes and the nozzles have to be repeated cleaned using IPA solutions. The diameter of the nozzle also helps in defining the resolution of the print. Smaller nozzles, however, get clogged more frequently and require consistent cleaning. All these critical designing and fabrication challenges were duly observed and overcome over the course of the 8 months of working at CPI.

TABLE IV.

AEROSOL JET PROPERTIES

Nozzle diameter	50 -300 μm
Drop volume	0.001 – 0.005 μl
Line width	10 – 50 μm
Ink viscosity	0.7 – 1000 cP
Stand-off distance	2 – 5 mm

Optomec M^{3}D® Aerosol jet system was used for fabrication of the designs. The machine was accessed at Centre for Process Innovation located in Durham, UK through the UK EPSRC High Value Manufacturing Fellowship grant that was awarded to my esteemed supervisor for research on high quality additive manufacturing designs. As the facility is a high-profile clean room facility, possibility of taking photos of the fabrication process of the designs were limited. The designs were converted originally into CAD designs by conversion into dxf files. The design layout was then mapped in CAD. A toolpath for the specific design was laid out in accordance with the design specific requirements. The designs had to be broken into several parts to allow a break in the printing process for cleaning of the tube and the deposition head. 100 μm nozzle was used for the fabrication of the two designs. The substrates were mounted on the printing vacuum bed. The FSS structures was fabricated using Cabot Nanoparticle silver ink [50]. FSS array of 7 x 7 unit cell was printed on Glass and 9 x 9 on Kapton for the

microwave design. For the mm-wave designs, an array of 40 x 40 unit-cell elements was printed on an A4 size Kapton sheet and on a 200 mm x 200 mm Corning Eagle glass. The completed designs were required to be cured for 60-90 mins on a hotplate at. The curing process helps the ink to dry out and bind with the substrate. The printing process can be seen in Fig. 6.10. The printed microwave FSS designs can be seen in Fig. 6.11. Fig. 6.11 (a) represents the design on glass substrate whereas Fig. 6.11 (b) represents the design on Kapton. Initial designs on Kapton were conducted on a thicker substrate with a rough profile. Due to the rough profile, the silver ink did not bind particularly well with the substrate despite repeated curing. The design was later fabricated on the mentioned thinner Kapton substrate.

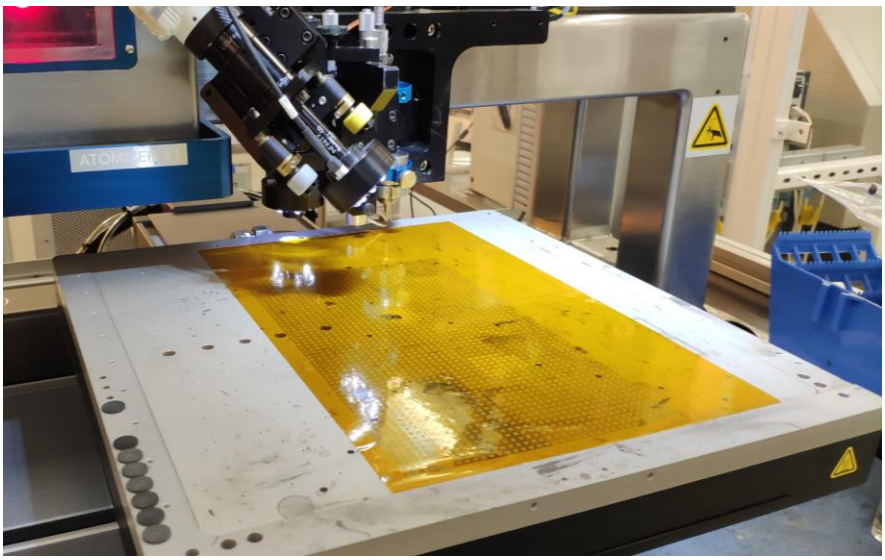

Fig. 6.10 Aerosol Jet printing bed with printed mm-wave Bandstop FSS on Kapton

The printed designs show the accuracy in developed FSS designs. The Some spattering is observed in the FSS design on glass in Fig. 6.11 (b) which is due to the tip that protects the nozzle spatters ink as it covers the nozzle everything the nozzle moves from one element to another. The spattering in the earlier designs was significantly high which was later reduced by regularly clearing the clogging and increasing the printing tool non-printing motion speed. Surface profiles for the designs were also measured and can be seen in Fig. 6.12 for the microwave Kapton design and Fig 6.13 for the microwave glass design. Figure 6.12 and Figure 6.13 clearly present the measured surface profiles for the microwave designs. The mean height for the Kapton design was approximately 1.25 µm. The widths of the printed tracks too were as per the simulation results. The mean height of the design on glass was roughly 0.9 µm.

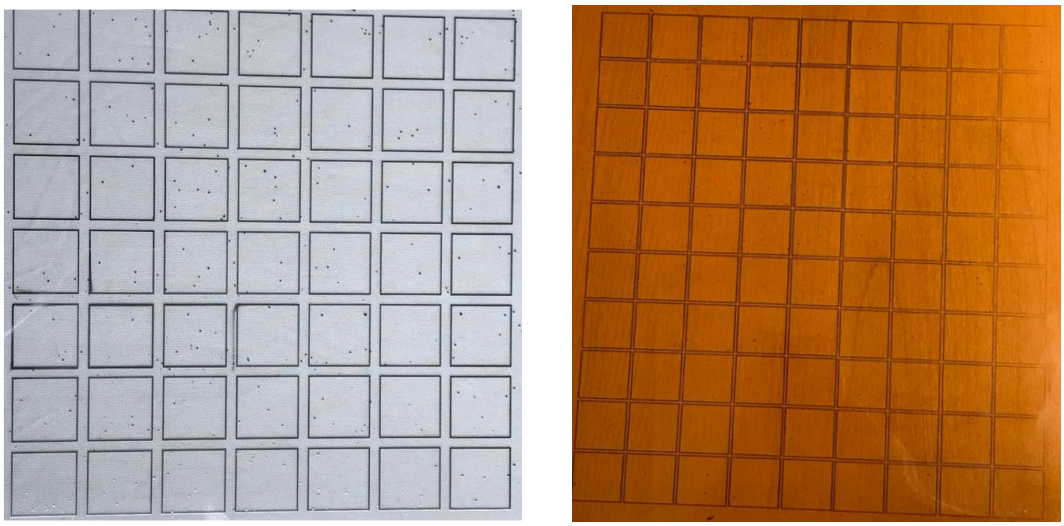

(a) (b)

Fig. 6.11 Microwave bandstop FSS design on (a) Corning eagle Glass and (b) Kapton

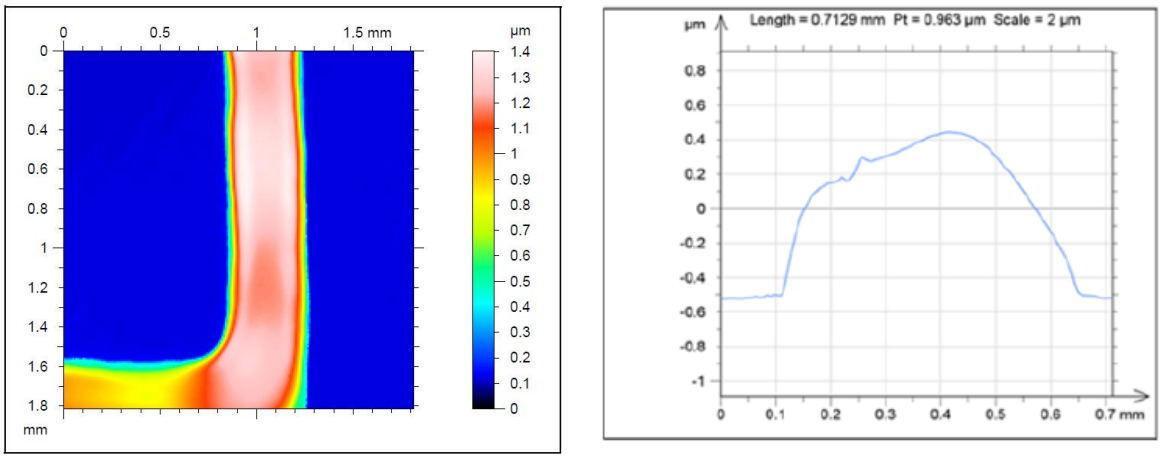

(a) (b)

Fig. 6.12 Measured surface profile of microwave Glass design

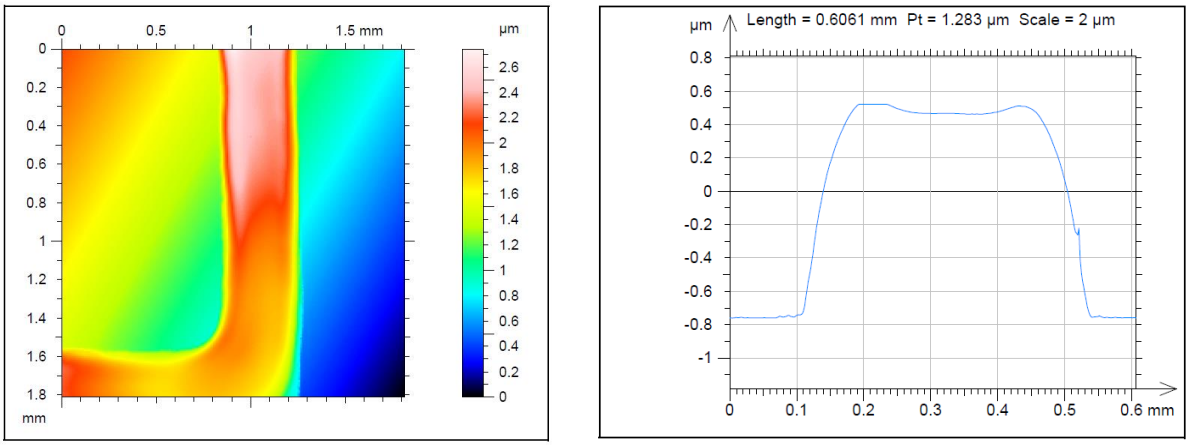

(a) (b)

Fig. 6.13 Measured surface profile of microwave Kapton design

6.4.2 Measurement results

The measurement setup can be seen in Fig. 6.14. The measurement setup consisted of a transmitter and a receiver pair of log periodic antennas across a screen which can be rotated around its axis and fitted with absorbers inside a plane wave chamber. The measurement results are presented in Fig. 6.15 for Glass and in Fig. 6.16 for Kapton, respectively. Measured transmission responses for the bandstop FSS design demonstrates a significantly coherent correlation of about -20 dB at a central frequency of 2.5 GHz for both designs. As it can be observed from Fig. 6.15 and Fig. 6.16, the TE 45 responses for the two designs suggest a considerably wider bandwidth of about 18% which is 6% higher in comparison to the simulation results. The TM 45 response also offered a wide bandwidth of about 17%. Both TE and TM responses resonated at well below -10 dB for the desired frequency bands. Considering the three bandwidths, the response was enough to cover the 2.4 GHz and its neighbouring bands.

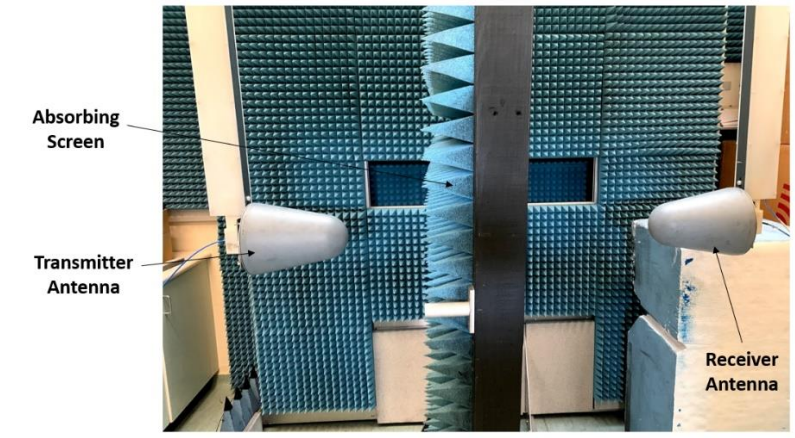

(a)

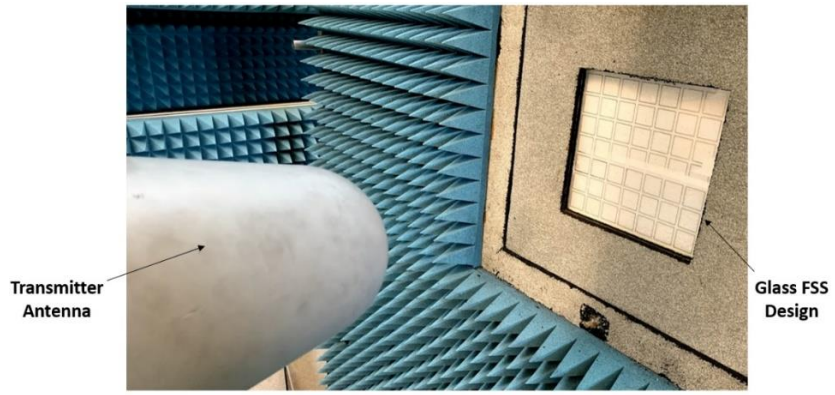

(b)

Fig. 6.14 Microwave design Measurement setup (a) Side view and (b) diagonal view

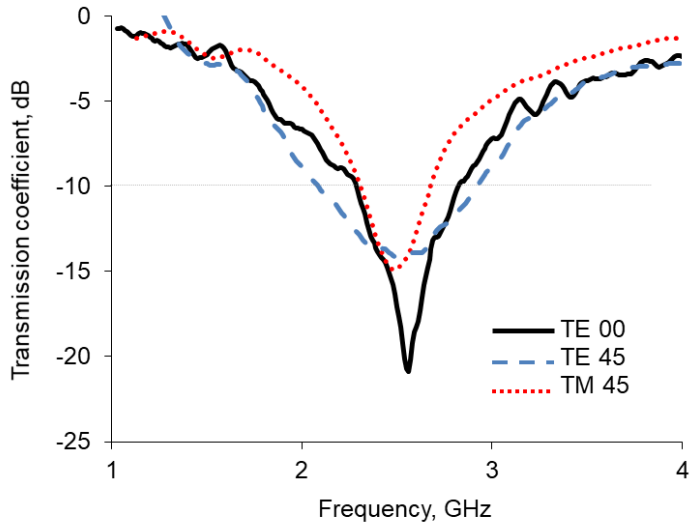

Fig. 6.15 Measured transmission coefficient for microwave FSS design on Glass

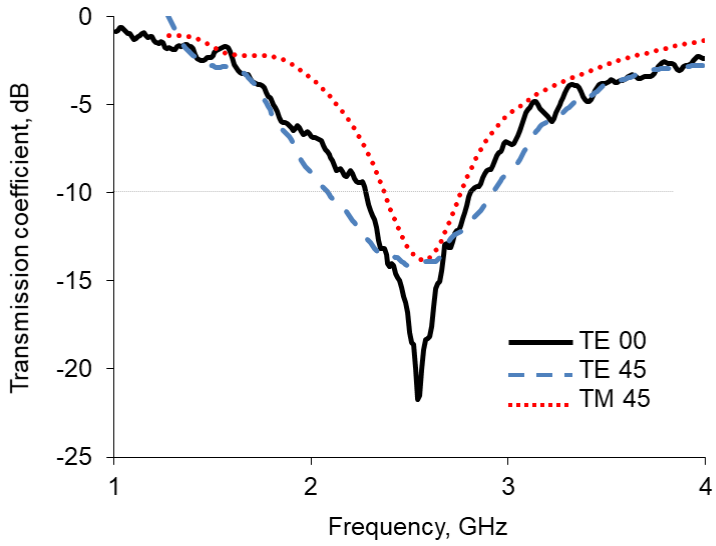

Fig. 6.16 Measured transmission coefficient for microwave FSS design on Kapton

Figure 6.17 shows the fabricated millimetre wave bandstop FSS designs on glass and Kapton, respectively. The fabricated FSSs were examined under a Keynce® 4K UHD microscope and Fig. 6.18 represents the magnified designs.

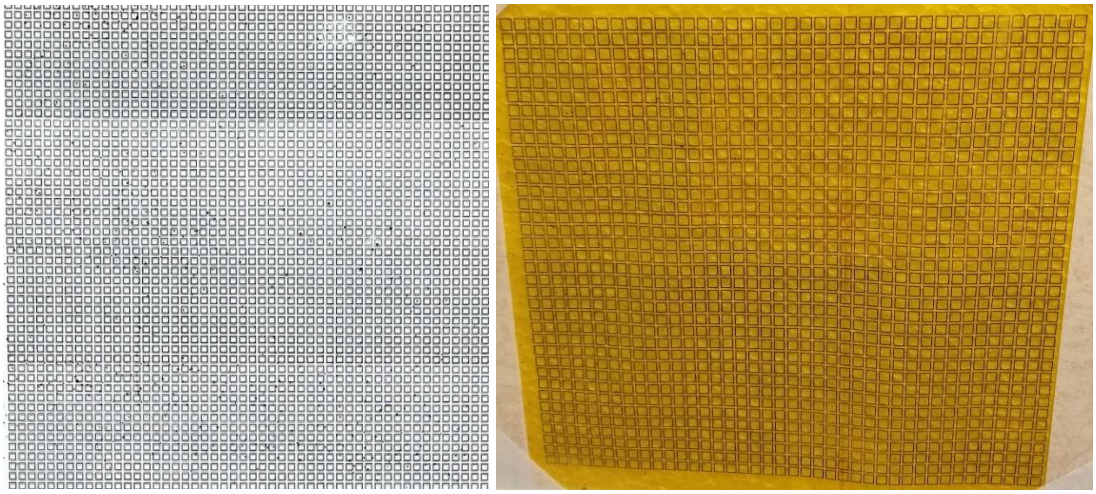

(a) (b)

Fig. 6.17 Fabricated millimetre wave FSS designs on (a) Corning eagle Glass and (b) Kapton

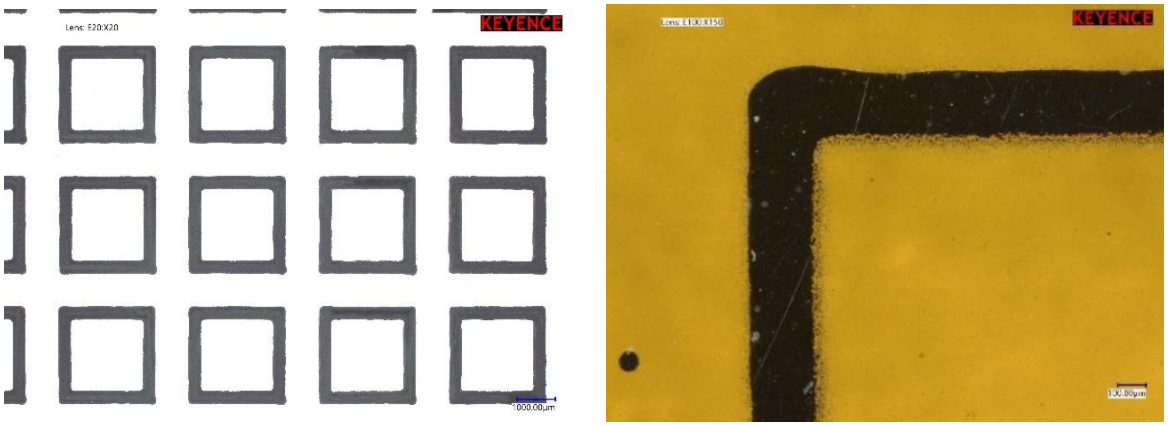

(a) (b)

Fig. 6.18 Magnified view of the printed tracks on (a) Glass and (b) Kapton

Figure 6.19 represents the measurement setup for millimetre wave FSS designs. The antennas were mounted on the screen that can be rotated around its axis and fitted with absorbers on the transmission side inside a plane-wave chamber. Transmitter and receiver antennas were placed on either side of the screen.

Fig. 6.19 Measurement setup for millimetre wave bandstop FSS designs

Figure 6.20 and 6.21 present the measured transmission responses for the millimetre wave FSS designs for Glass and Kapton, respectively. For FSS design on glass, the simulated and measured transmission responses at TE00 and TM 00 resonated at 26.7 GHz. TE 45 resonated at 24.5 GHz whereas TM 45 resonated at 27 GHz. The glass design offered a significantly wider bandstop response in comparison to Kapton. Transmission response was below -10 dB for a range from 22.9 GHz to 28.5 GHz with a bandwidth of 21%. TE45 response exhibited a shift of 8% whereas the TM45 response observed a shift of 1%.

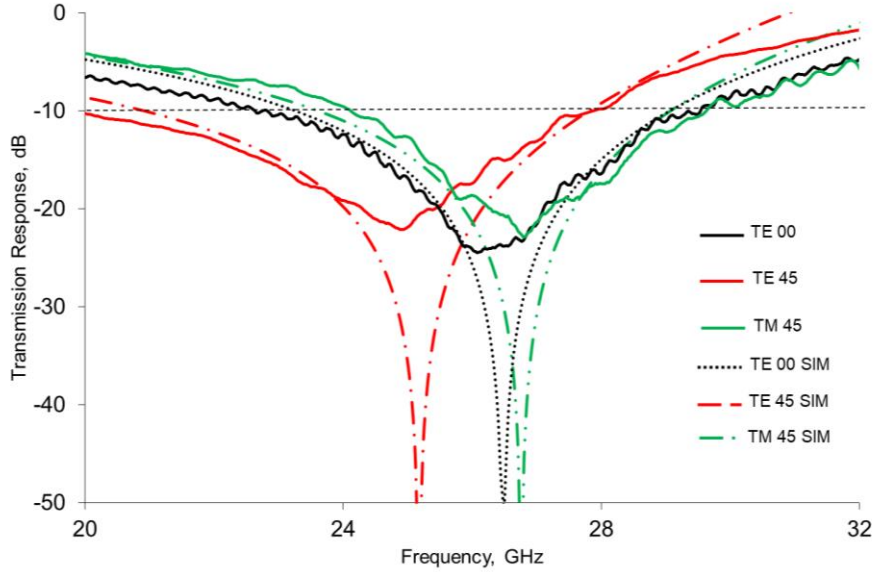

Fig. 6.20 Transmission responses for mm-wave FSS design on Glass

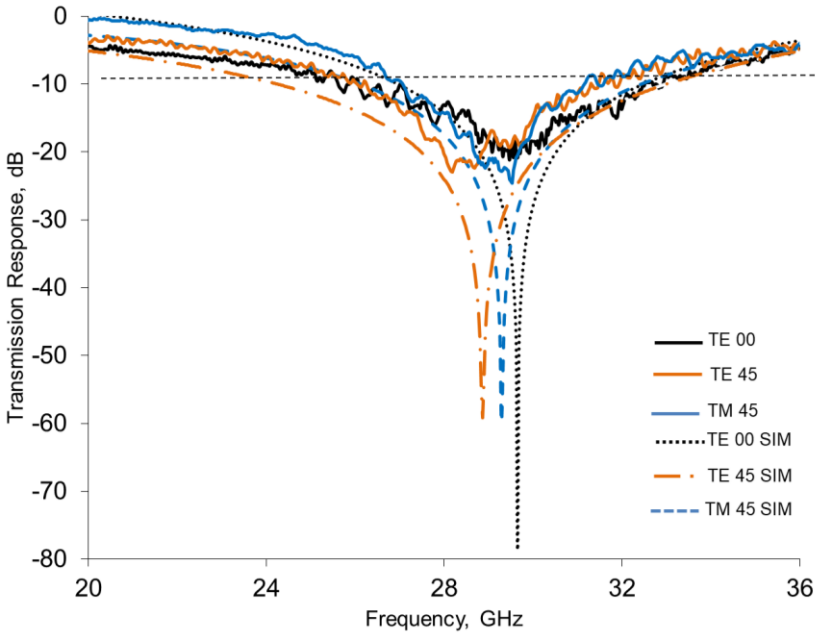

Fig. 6.21 Transmission responses for mm-wave FSS design on Kapton

Normal incident angle TE00 and TM00 response for Kapton resonated at the same frequency of 29.7 GHz. TE 45 response resonated at 28.4 GHz whereas TM45 resonated at 29.2 GHz. A Transmission response was below the -10 dB mark for frequencies ranging from below 25 GHz

to over 31 GHz with a bandwidth of 15%. A frequency shift of 4.2% was observed for the TE45 transmission response whereas 1.5% frequency shift was observed for TM45.

6.5 Millimetre wave low-THz bandpass FSS design

As a proof of concept for a challenging mm-wave low-THz bandpass FSS designs, a simple design was preferred. A single-polarised square slot was preferred as the main design. Single-polarised slot FSS provided passing and blocking state responses. As the manufacturing constraints of the machine required the development of a suitable toolpath, a dual-polarised design was not preferred.

6.5.1 Design dimensions

Keeping the wide range of frequencies of operations for slot FSS in mind, mm-wave bandpass FSS design with an array of slots was designed. The slot FSS design can be seen in Fig. 6.22. The square lattice of the unit cell of the slot consists of sides L and W respectively as 1mm. The slots dimensions are length L_s *as* 0.8mm and width W_s as 0.08 mm. The micrometre level precision required to create the slot width was novel with the development using aerosol jet printing. Just like the previous design, this design was simulated with the help of CST Microwave Studio™ with Kapton as substrate.

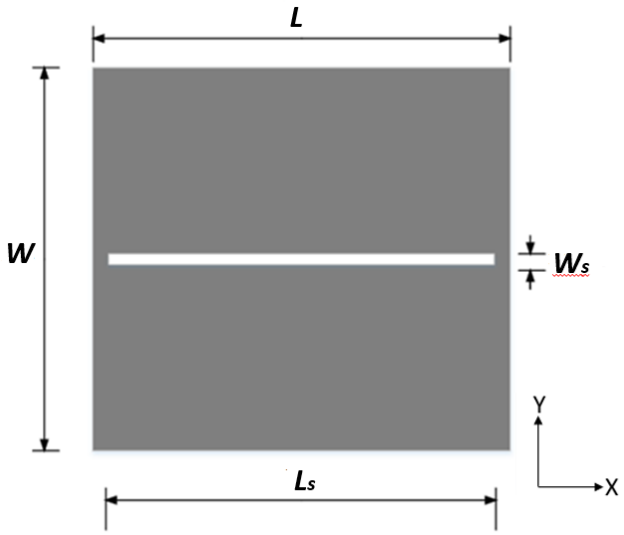

Fig. 6.22. Mm-wave Slot Bandpass FSS design unit cell layout with dimensions

TABLE V.

DIMENSIONS IN MM

Length	L_s	W_s	L	W
Dimensions (mm)	0.8	0.08	1	1

Low-THz bandpass slot FSS was also developed as an initial study to examine the absolute extremities of the aerosol jet printer's precision in printing. Low-THz designs are readily being considered for the increased data rate for the 6G communications and beyond. The design consisted of a slot FSS which is analogous to previous design. The parameters and the layout of the Low-THz FSS unit cell design were the same as seen in Fig. 6.22. Dimension of square slot unit cells got smaller with W and L both as 0.6 mm and slot size with L_s as 0.43 mm and W_s as 0.043 mm.

TABLE VI.

DIMENSIONS IN MM

Length	L_s	W_s	L	W
Dimensions (mm)	0.43	0.04	0.6	0.6

6.5.2 Simulation responses

The simulated transmission response for the 125 GHz bandpass FSS design is presented in Fig. 6.23 whereas the simulated transmission response for the 280 GHz design is presented in Fig. 6.24. As single polarized designs, both the designs transmit the signals in their respected passband TE state, which is lateral to the length of the slots while blocking the transmission of signals in their stopband state, which is orthogonal to the lengths of the slots. A gap in the passing (denoted in black) and blocking states (denoted in green) of over -20 dB is observed for the 125 GHz design in Fig. 6.23. The gap between the states is much more prominent at over -30 dB for the 280 GHz design as demonstrated in Fig. 6.24.

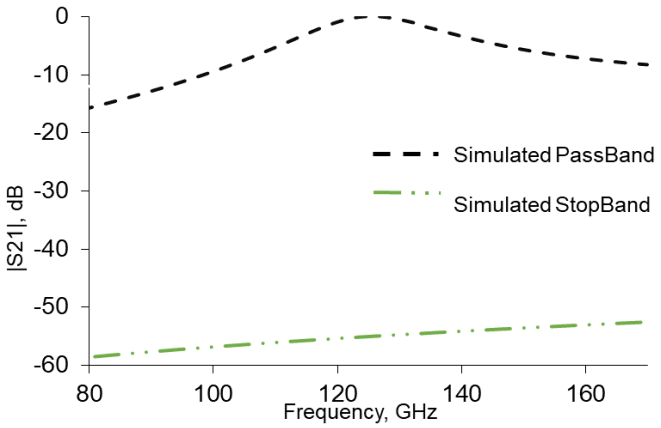

Fig. 6.23 Simulated transmission response of 125 GHz bandpass slot FSS design

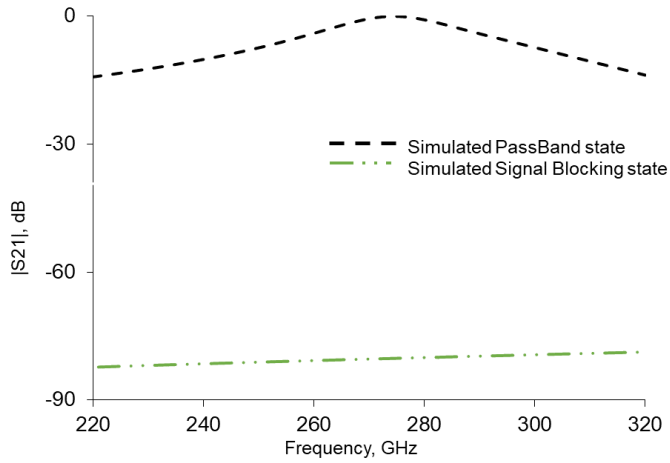

Fig. 6.24 Simulated transmission response of 280 GHz bandpass slot FSS design

6.6 Aerosol Jet printing of design

Aerosol Jet printing system was put to further extreme tests of its limits and constraints with this complex fabrication that required extremely minute micrometre precisions. Aerosol jet printing systems are now occasionally considered to be used for printing certain sub-parts of certain mm-wave and parts of THz designs which require 3D printing with millimetre and micrometre level precision. Fabrication of a collection of designs developed partially with the help of Aerosol Jet printing are widely reported in [42], [51] – [55].

Designs with extreme precision ranging from conformal, orthogonal antennas [51], transmission lines [52], to coplanar waveguides [53] to Yagi-Uda antenna [54] to FSS on

curved surfaces [55] demonstrates the diversity within the printing process. Majority of the proposed designs were elementary initial studies that were predominantly reported in conferences as introductory concepts. The indifferent reporting of the aerosol jet printed designs is due to the time consuming and complicated procedure it requires to complete the fabrication. The proposed bandpass FSS design made use of the aerosol jet printers and tested their limitations in terms of design fabrication and present some reliably accurate designs.

FSS designs was fabricated by translating the unit cell into a square array with dimensions which were 50 mm by 50 mm. Kapton [45] substrate of 50 micron or 0.05 mm thickness was used for fabricating designs. Extremely thin and smooth nature of this Kapton polymide sheet [45] made it particularly helpful in the designing of frequency filters and they also fit to be used as substrates to develop frequency shielding window taints and passband filters for desired frequencies. The tiny square FSS lattice contained an array of 50 × 50 unit-cells for the 125 GHz design. The square lattice for the 280 GHz design contained the array of approximately 83 × 83 elements. The array lattice was not fabricated in the conventional method like the square loop element designs which were discussed in Chapter 5. The designs were divided into four subparts and a strategic approach was taken to achieve the design quality. The designs were converted into the subdivided parts and as their toolpaths were being decided, the printing layout strategy was devised for the designs. The entire FSS structure was reimagined and designed as a combination of a mesh of horizontal and vertical lines. Horizontal line tracks were printed adjacent to one another and certain spaces of 0.1 mm was left after four adjacent tracks to make the gap for the slot layout and defined the slot heights. Vertical line tracks defined the smooth edges and widths of the slots. Margins were also left for the inks to disperse in an appropriate manner and spread within the design limits. The speed of the toolpath motion was also critically examined throughout the printing procedure. The optimum speed of the toolpaths was decided with a trial-and-error method as the margins were too extreme and the designs presented a novel approach in FSSs and thus have no predefined ways of toolpath motion. Critical details of the fabrication are reported in the table 6.6 below. The thickness of the Aerosol Jet printer's ink stream can be controlled by a number of ways. The size of the printing nozzle as well as increasing or reducing the flow rate of the sheath gas.

TABLE VII.

LOW-THZ FSS AEROSOL JET FABRICATION PARAMETERS

Nozzle size	150 µm
Sheath gas level	20 cm^3
Impact exhauster	600-700 cm^3
Atomizer	800 cm^3
Speed of toolpath for printing	4-6 mm/sec
Speed at corners	1 mm/sec
Speed at rapid tool motion	10 mm/sec

Smaller nozzle results in a concentrated stream but also increases the chances of the nozzle getting clogged during the printing process. Increasing the flow of sheath gas results in printing thinner tracks but thinner tracks can also result in incomplete or broken designs. The size of the nozzle used and the sheath gas flow has to be carefully set and the sheath gas flow and pressure should be regularly monitored in standard aerosol jet designs. Figure 6.25 denotes the three stages of dispersion of ink onto the substrate. Fig. 6.26 denotes a typical toolpath design showing vertical tracks with spaces for slots. Fig. 6.26 (a) denotes the initial stage where no tracks were printed, Fig. 6.26 (b) presents the instantaneous line tracks after printing with the gap clearly visible between them and Fig. 6.26 (c) denotes the ink after dispersion after getting deposited onto the substrate.

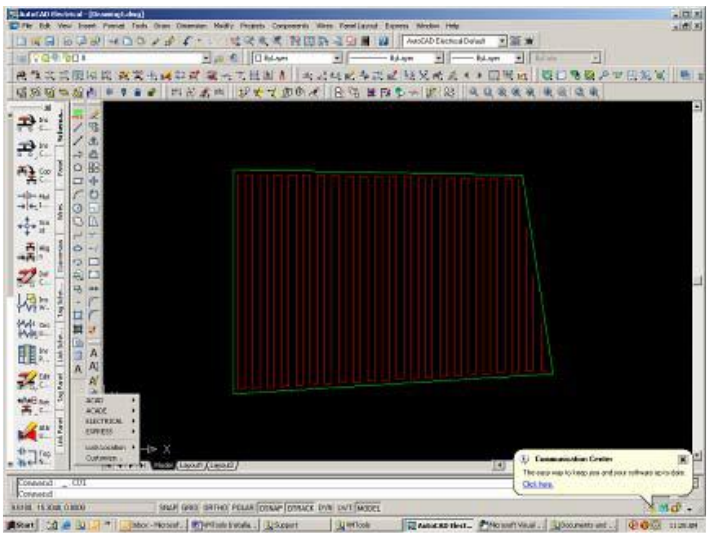

Fig. 6.25 A typical Aerosol jet printing toolpath designer with vertical zigzag track lines

The experimentation with the aerosol stream size and the ink dispersions were conducted and some initial designs resulted in the ink tracks not dispersing and fusing with one another. One such failed attempt is presented in Fig. 6.27. For this specific design, the impact exhauster volume was kept at 700 cm^3. The designs on corning eagle glass substrate too showed similar trends predominantly due to the difference in the surface properties of Kapton and glass. To overcome this issue, the impact exhauster volume was consistently monitored and varied between 620 cm^3 and 700 cm^3 depending upon the deposition of the ink and the track width. The speed of the toolpath.

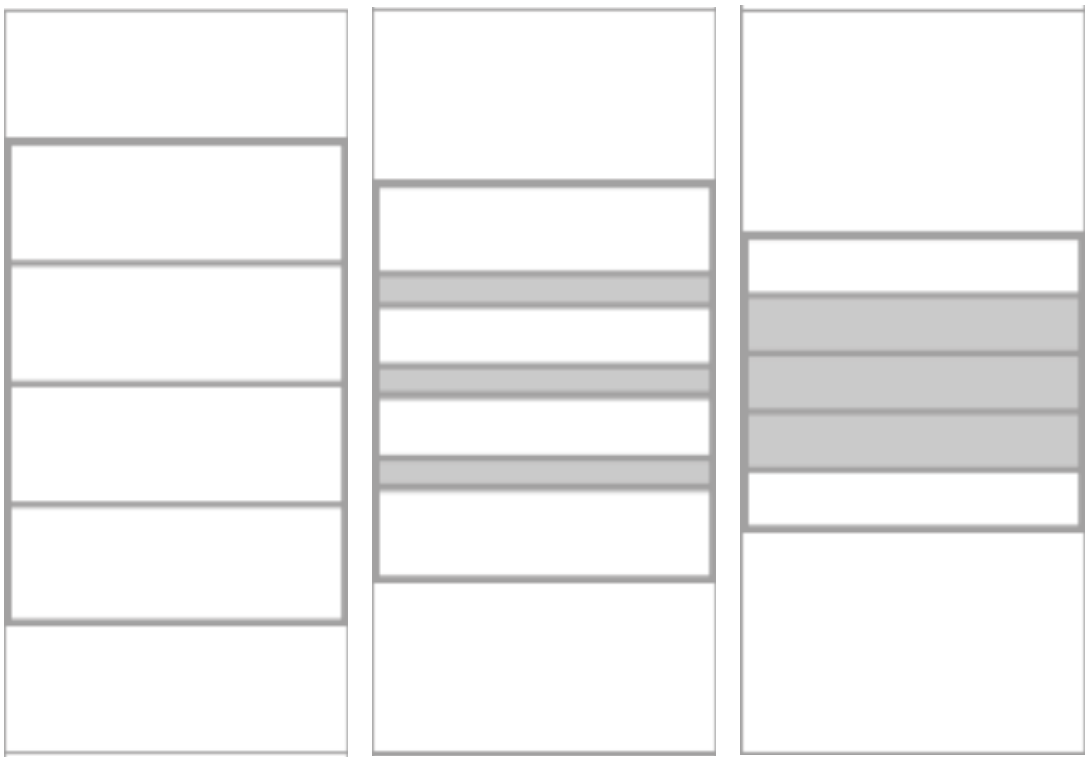

(a) (b) (c)

Fig. 6.26 The three stages of the ink dispersion onto the substrate in fabrication with (a) pre deposition, (b) post deposition and (c) after complete dispersion of ink

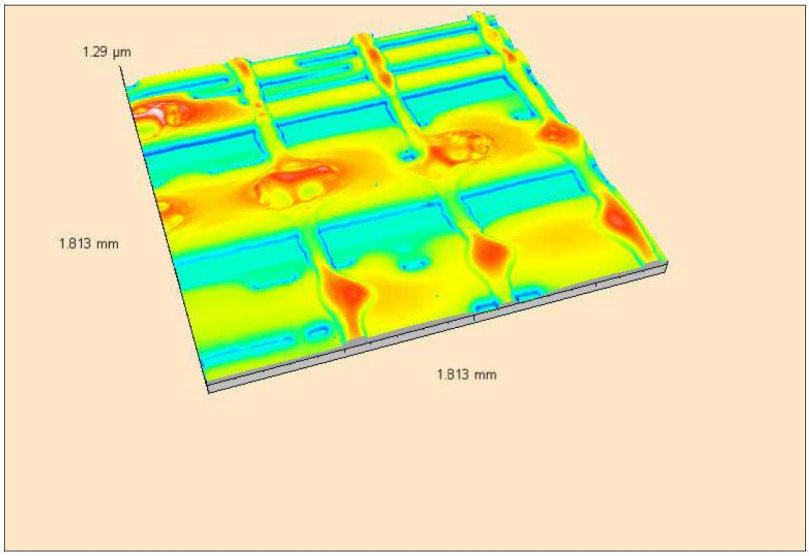

Fig. 6.27 Surface profile of a failed attempt for the fabrication of bandpass FSS on Glass

As Fig 6.27 demonstrates, the aerosol steam flow rate and thickness were essential in getting the deposition of ink correctly. With varied iterations in a couple of designs, and consistently watching and varying the sheath gas pressure values to get the deposition right. By carefully examining the sheath gas pressure throughout the printing process, the right shape for slots were achieved.

6.7 Surface profiles and measurement results

6.7.1 Surface profiles

The fabricated design of the slot FSS design for 125 GHz can be seen in Fig. 6.28. The real size picture shows the intricate nature of the fabricated design. At the bottom left corner of the photo, the extremely flexible nature of Kapton is also evident. Some tiny, scattered droplets can also be observed which were caused by spattering during the fabrication process. As the nozzle protector covering was cleaned more frequently than any other design, the spattering was significantly lower for this design.

(a)

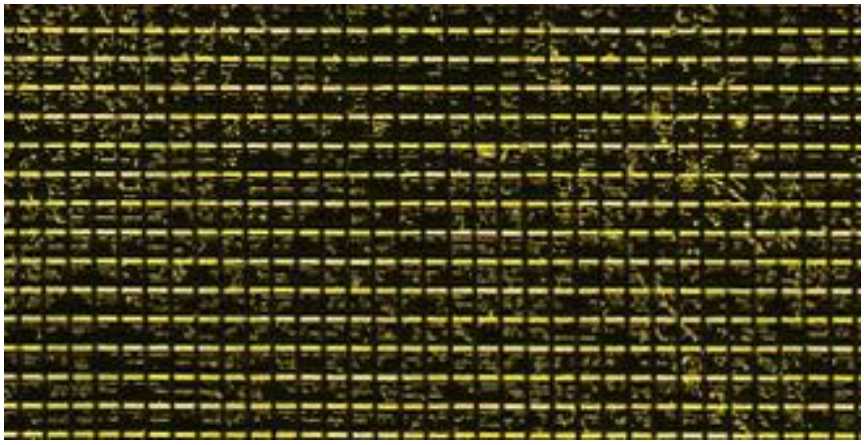

(b)

Fig. 6.28 Printed 125 GHz Slot FSS designs on Kapton (a) Full FSS design photograph and (b) Magnified photograph

Surface profiles for the designs were measured with the help of various microscopes. Keyence® 4K Ultra High-definition microscopes were accessed and highly magnified images of the printed slots were observed with the help of those microscopes. The printed profile for the 125 GHz is presented in Fig. 6.29 and Fig. 6.30, respectively.

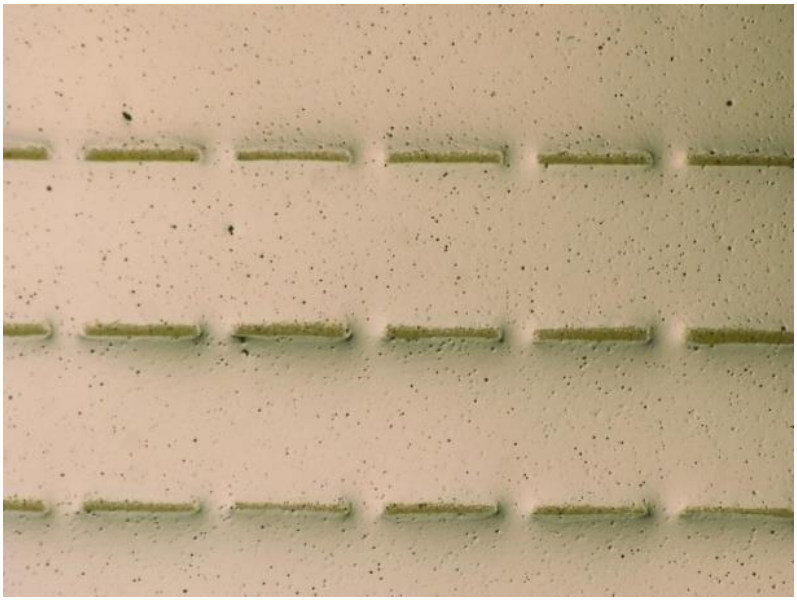

(a)

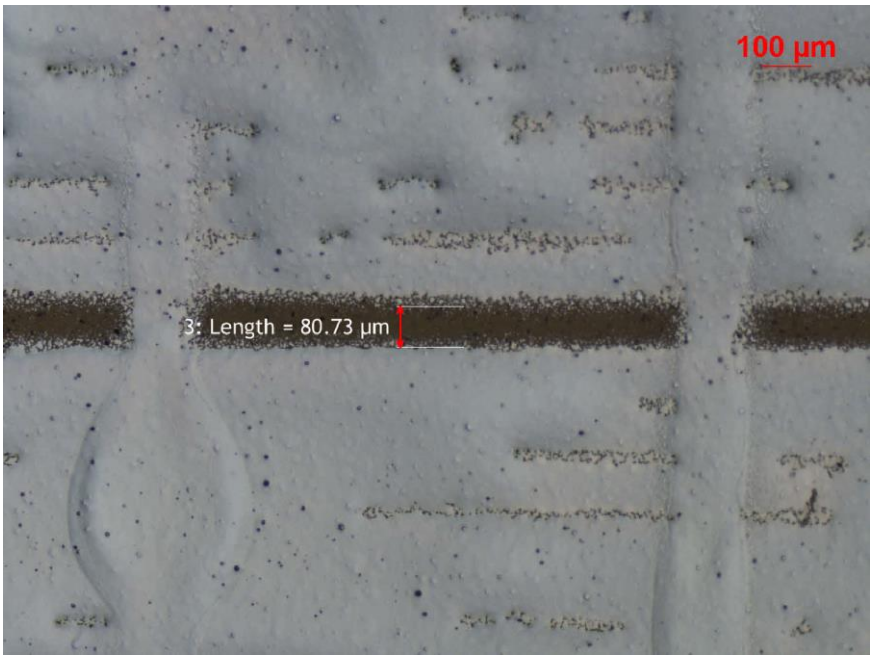

(b)

Fig. 6.29. Fabricated 125 GHz Slot FSS microscopic view (a) Printed slot array and (b) Individual Slot height

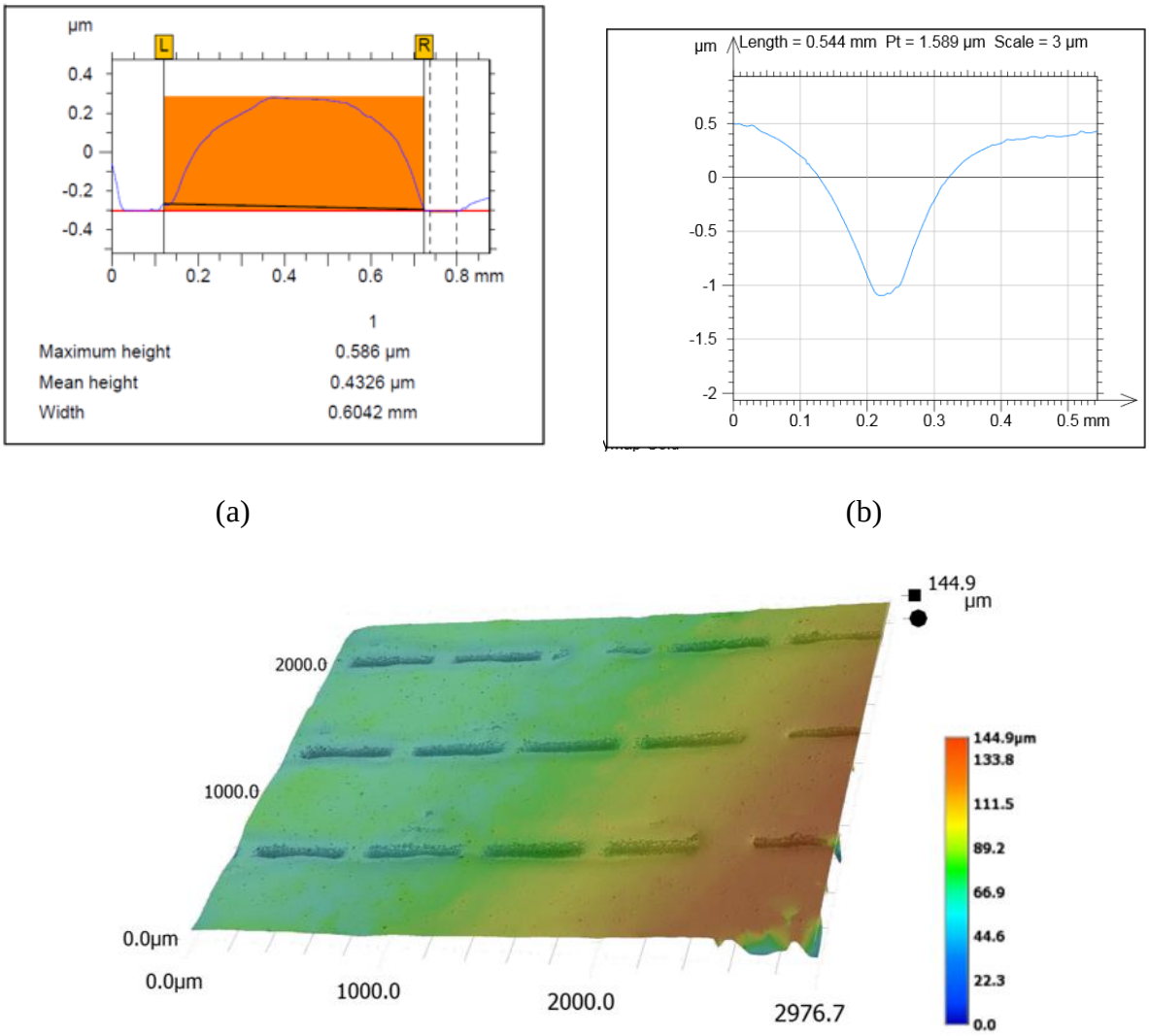

(a) (b)

(c)

Fig. 6.30. Fabricated 125 GHz Slot FSS microscopic view with (a) Profile measurement of printed height, (b) slot depth and (c) 3D profile of the printed area

A single-polarized FSS design was favoured over the efficient dual-polarized design as creating a toolpath and fabrication process was relatively reliable and straightforward with a small number of fabrication and quality assurance constraints. A series of sample prototype FSS fabrications were carried out by altering the flow of silver nanoparticle ink to produce the required dimensions. Some of the samples had issues of excessive ink dispersion that resulted in the slots being filled up. A constant monitoring and instant adjusting of the pressure levels was a must for this intricate design. The dimensions of the printed slots deviated marginally

around 0.08 mm and 0.8 mm. A width of 80.73 µm and a length of 0.79 mm were observed for one specific slot sample. Determined value for the resistivity of the printed FSS surface on Kapton was 2.6 x 10^{-7} Ω-m.

Measured surface profiles for the 280 GHz FSS design can be seen in Fig. 6.31. The details of the slots are so minute that it can be hard to spot the slots from naked eyes. Fig. 6.32 and Fig. 6.33 show the surface profile measurements for the design. Dimensions measured within the slots clearly indicate the accuracy of the fabrication process for the designs and can be observed in Fig. 6.32 and Fig. 6.33. The measured slot width was 0.43 mm, and the measured slot height was 0.043 mm which were similar to the designed width and height of 0.43 mm and 0.043 mm respectively.

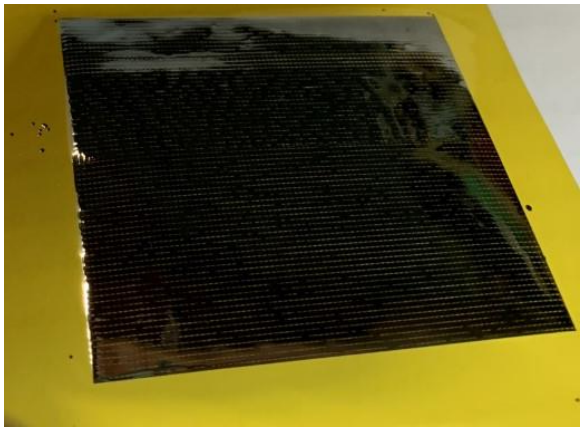

(a)

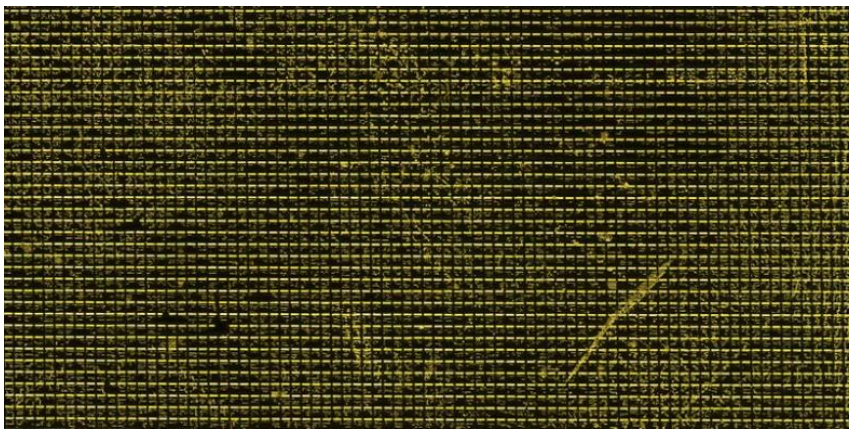

(b)

Fig. 6.31 Printed 280 GHz FSS design on Kapton (a) Full FSS photo and (b) Magnified view of the FSS

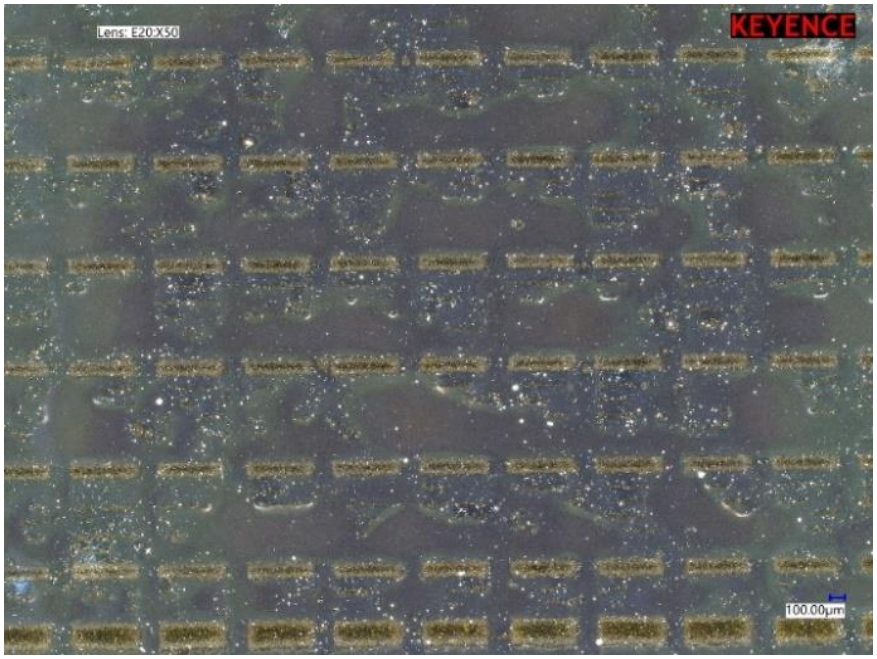

(a)

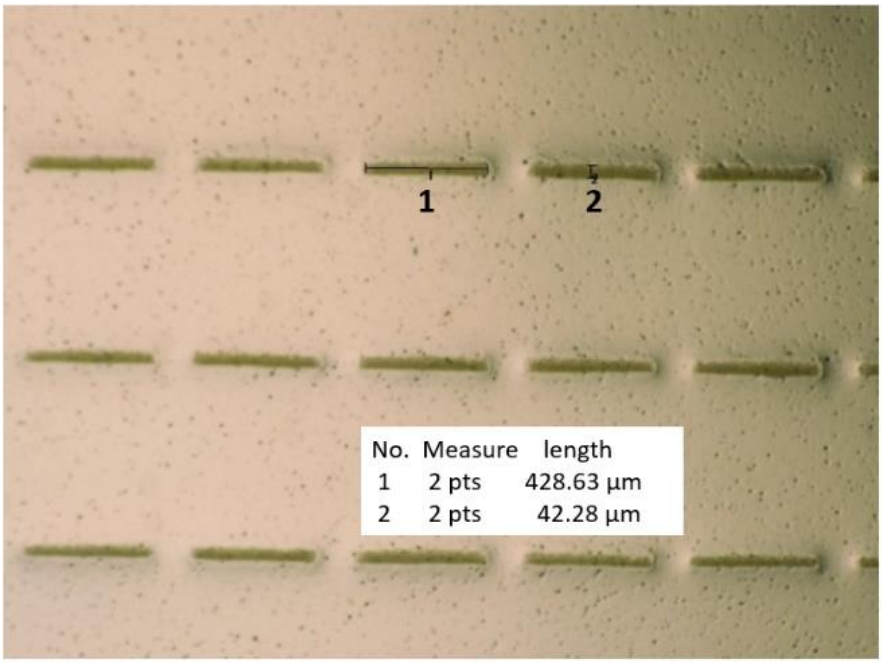

(b)

Fig. 6.32. Fabricated 280 GHz Slot FSS microscopic view (a) Printed slot array and (b) Individual Slot height

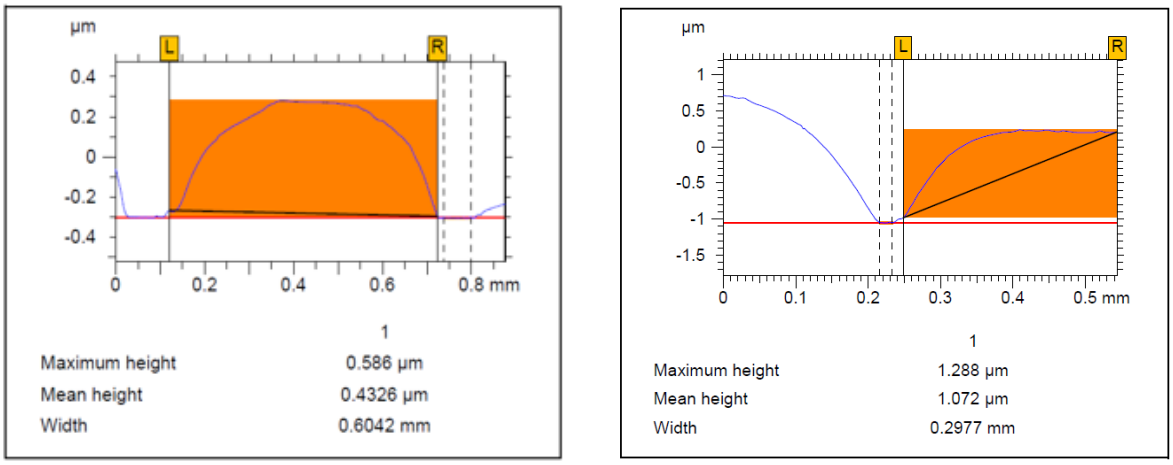

(a) (b)

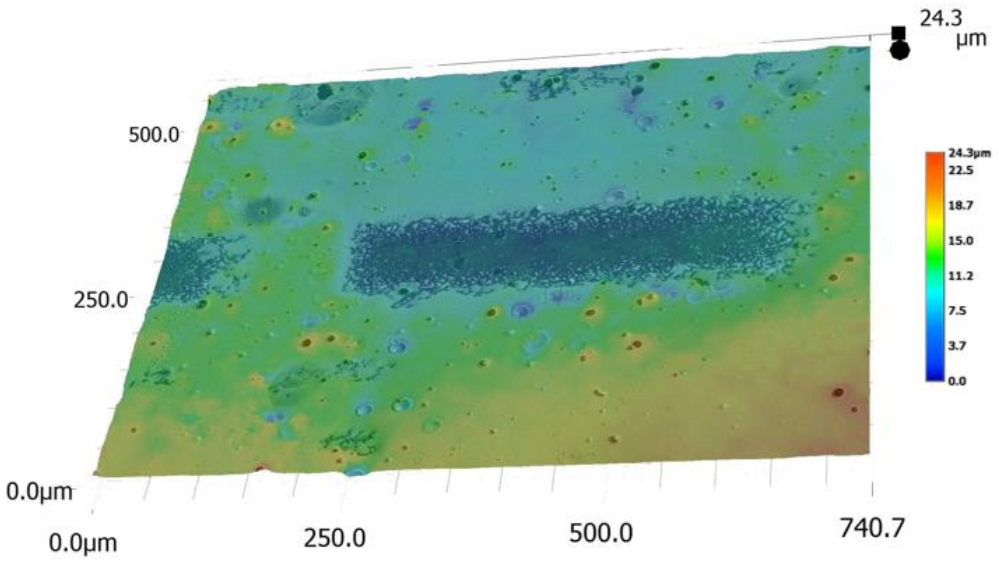

(c)

Fig. 6.33. Fabricated 280 GHz Slot FSS microscopic view (a) Profile measurement of printed height, (b) slot depth and (c) 3D profile of the printed area

6.7.2 Measurement results

Fabricated FSS designs were tested at the KU Leuven ESAT research facility which was accessed with the help of the University of Kent research collaboration with WISDOM research project. The designs were tested using the standard test setup for plain wave measurements.

Frequency extenders were added to the standard R&S horn antennas of the desired frequency bands. The test setup can be seen in Fig. 6.34. Absorbers around the FSS and the supporting rods were removed for clarity of pictures. Calibration of the setup was performed before every measurement. The FSS structure was mounted on a support structure and frequency extenders were used to achieve the desired frequency bands for both the measurements.

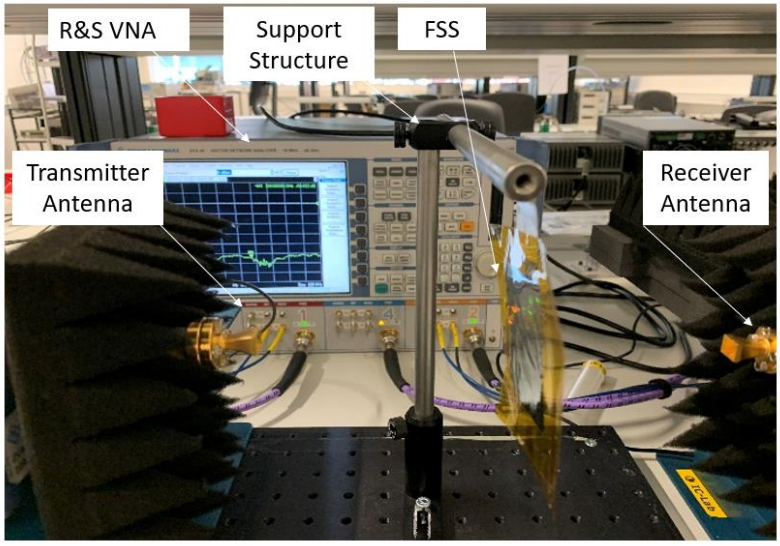

Fig. 6.34 Measurement test setup for transmission responses at 125 GHz and 280 GHz

The measurement results are presented in Fig. 6.35. The measurement results are coherent to those of a single-polarized bandpass FSS with passband and stopband orientations, respectively. Design operated at approximately 125 GHz with both measurement and simulation in good correlation with each other. Wide bandpass characteristics of the design can be observed with gap of more than 20 dB between the passband and stopband.

These FSS designs was designed and developed with the objective of proving the concept of fabrication using the expensive Aerosol Jet Printing as the technique to develop designs in a single step process that offers the transmission response at normal incidence angle and therefore, no additional studies were conducted for other angles of incidence due to the intricit nature of the FSS structures. The single-polarized FSS presented a passband response when H-plane incident wave was lateral and E-plane incident wave was orthogonal to the slot. A distinct signal blocking state with a gap of almost 20 dB was observed when the E-plane was lateral to the slot. Another gap between the measured and simulated blocking states was also observed.

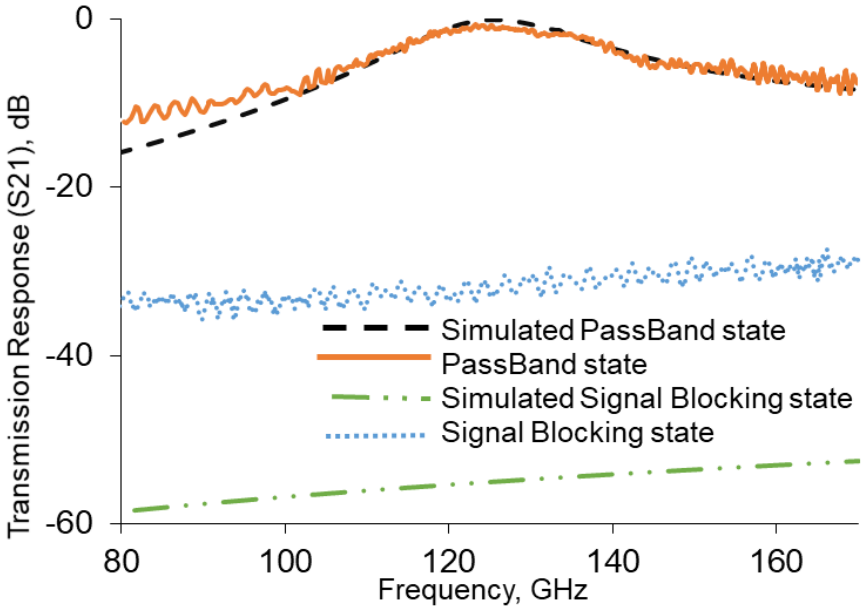

Fig. 6.35 Measured responses of 125 GHz Bandpass slot FSS design on Kapton

Transmission responses at normal angle of incidence were centered at the resonant frequency of 125 GHz. Wideband transmission response was obtained with a slow roll-off rate and a -10 dB passband that ranged from approximately 90 GHz all the way up to 170 GHz along with a bandwidth of 64%. Single-band features of FSS are emphasized further with a gap of more than 20 dB among passband and signal-blocking state. Insertion loss of 0.75 dB was also observed. Good overall agreement was observed between simulated and measured transmission responses when the simulations were conducted with ideal conditions without insertion losses.

Extremely high insertion loss was observed in the case of Corning Eagle Glass substrate during measurements at higher frequencies. Several simulations and measurements were conducted to ensure that the losses were not indeed reflections. That was not to be the case. It was concluded that the permittivity of the glass is not suitable for mm-wave and low-THz frequencies and therefore, not suitable beyond the mm-wave and low mm-wave applications. Kapton was thereby the preferred substrate as it demonstrates extremely high temperature tolerance and uniform permittivity at THz frequencies as shown in Fig. 6.36 that find applications in space, satellite and defence communications [56].

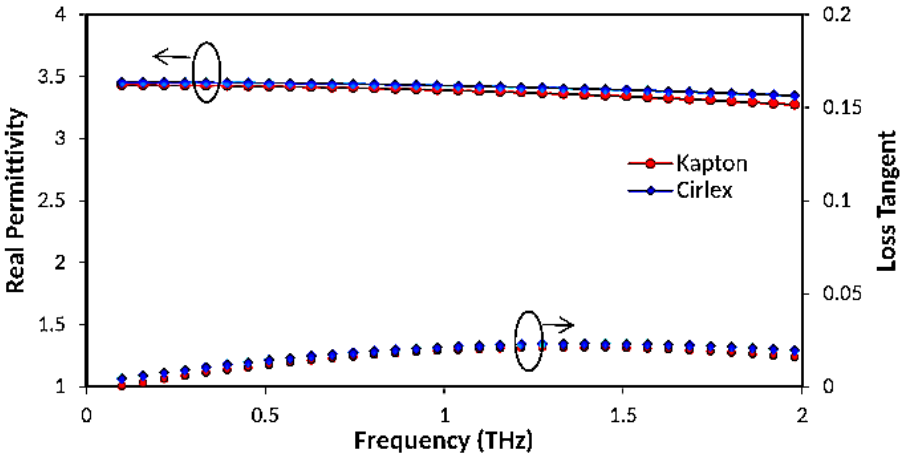

Fig. 6.36 Real Permittivity and loss tangents of Kapton Polymide and Cirlex Polymide for THz frequency [56]

Measured setup for the 280 GHz FSS design is same as seen in Fig. 6.34. Some absorbers were removed from the measurement setup for photographic clarity. The measured transmission response for the 280 GHz design can be seen in Fig. 6.37. The measurement transmission responses even at the Low-THz levels are in excellent coherence with those of a typical single-polarized bandpass FSS. Bandpass FSS design originally operated at a frequency of 280 GHz with the measured passband operating at a slightly lower frequency of nearly 278 GHz, a shift that was minimal. The understandable minute shift in resonant frequency can be due to certain slots having smaller sizes than expected due to the excess dispersion of ink. The passband for the Low-THz design was significantly narrower in comparison to the 125 GHz design discussed earlier with a bandwidth of 28%. Insertion loss of approximately 2.4 dB was observed. Stopband measurement and simulations also followed similar trends with an approximate gap of -20 dB observed between passband and stopband. Despite the slight shift, a predominantly similar measurement and simulation passband response is measured.

Blocking state response presented a null at around 260 GHz in the simulated responses when insertion losses were included within the simulation. The null corresponded well with the measured blocking state response. In the ideal case simulation with no insertion losses, as it was the case with the results presented in Fig. 6.15, a clear and linear blocking state response was observed.

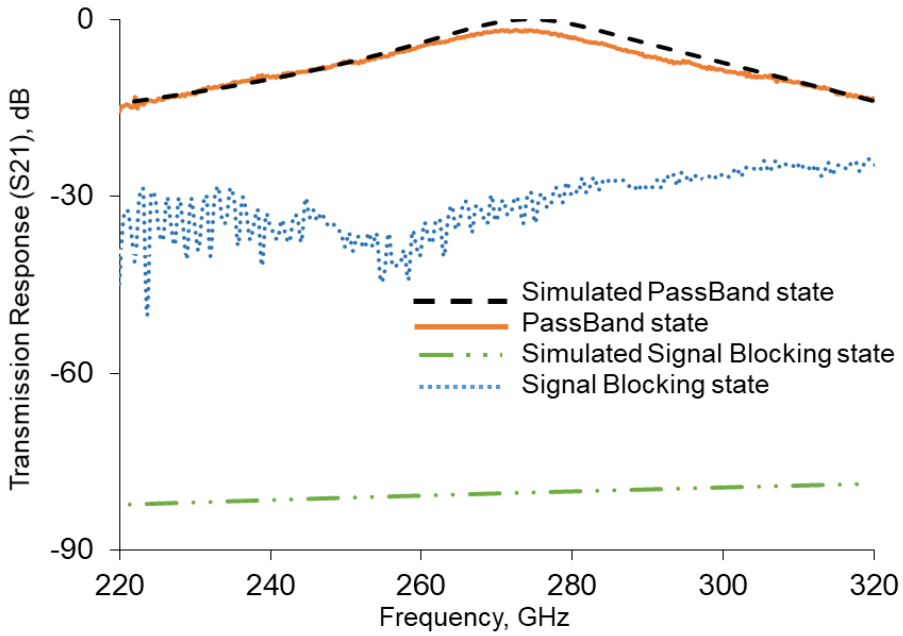

Fig. 6.37 Measured transmission responses of 280 GHz Bandpass slot FSS design

Finally, a comparison table depicting the advantages and disdavantages of various fabrication techniques namely traditional wet etching, screen printing, professional inkjet printing, inexpensive piezoelectric inkjet printing, and proposed industry-grade Aerosol Jet printing in the development of Frequency Selective Surfaces is presented in table 6.7. Various advantages and disadvantages of all the aforementioned fabrication techniques are presented for comparison. Aerosol Jet printing is the only existing technique that provides the option of direct 3D printing on curved or 3D surfaces albeit within the limits of the equipment. The small features and extreme precision of the techniques makes it a lucritive option for the development of high frequency futuristic FSS designs.

And finally, a comprehensive table comprising of a comparative analysis between the three methods proposed is presented in Table IX. The table illustrates the various salient features and drawbacks of the three techniques names low-cost inkjet printing, full 3D printing using FFF and conductive paste extrusion and Aerosol jet printing.

TABLE VIII.

COMPARISON TABLE BETWEEN PREVIOUSLY REPORTED FABRICATION TECHNIQUES FOR FSS

Fabrication Technique	Advantages	Disadvantages
Etching [57], [58]	• Least expensive • Scalable • Tiny details feasible (track size of 1 µm to 4 µm) • Printing on both sides supported. • Easily accessible • Consistent	• Multi-step fabrication • Constraints of stencils • Consumption of hazardous chemicals • Raw Material and chemical waste
Screen Printing [59]	• Scalable • Swift print speed • Tiny details feasible • Potential printing possible on various substrates • Multilayer and complex design fabrication viable	• Multi-step procedure • Constraints of stencils • Inadequate three-dimensional resolution
Low-Cost Piezoelectric Inkjet printing [60], [61]	• Low-cost apparatus • No stencil necessary • Reliable resolution • Single-step fabrication • Environment Friendly • Swift prototyping feasible	• Not suitable for bulk manufacturing • Track detail constraints (100 µm - 200 µm track size) • Cost-inefficient prices of conductive inks • Predominantly single-sided fabrication supported
Professional Inkjet printing [42], [61]	• No stencil necessary • High print resolution • Repeatability (5 µm - 25 µm) • Suitable with numerous substrates • Fabrication on 3D substrates viable • Swift prototyping feasible	• High apparatus cost • High fabrication cost • Incompatible for mass production • Cost-inefficient prices of ink to scale-up the production
Aerosol Jet Printing [62], [63], **Proposed method**	• Direct printing on 3D substrates within 2-5 mm heights feasible • No stencil necessary • Intricate details feasible (5 µm track width) • Extreme accuracy in fabrication • Appropriate for bulk manufacturing • Swift prototyping feasible	• High apparatus cost, highest amongst the techniques mentioned • High production costs (requirement of a trained machine operator) • Cost-inefficient prices of conductive ink for up-scaling of production

TABLE IX.

COMPARISON TABLE BETWEEN PROPOSED FABRICATION TECHNIQUES FOR FREQUENCY SELECTIVE SURFACES

Manufacturing Method	Saliant Features	Drawbacks
Low-Cost Inkjet printing	▪ Microwave and mm-wave designs presented ▪ Inexpensive manufacturing ▪ No stencil required ▪ Reliable print resolution of ~100 µm ▪ Single-step printing ▪ Printing time of a few seconds over A4 area ▪ Resistivity of 4.53×10^{-7} Ω-m with uniformity across tracks ▪ No curing requirements ▪ Eco Friendly	▪ Not suitable for bulk manufacturing ▪ Delicate nature of structures and substrates ▪ Resolution constraints with a limit on track size (100 µm - 200 µm) ▪ Costly conductive inks ▪ Only single-sided fabrication possible
Conductive Silver Ink extrusion	▪ Fully 3D printed microwave FSS presented ▪ Both substrate and FSS array are printed simultaneously with the same printer ▪ Permittivity of the substrate can be varied with different infill densities ▪ Varied permittivity offered variations in transmission responses ▪ Vacuum extrusion of conductive silver ink offered varied track thickness at different pressures ▪ Suitable with ABS and PLA ▪ Fabrication time of 1-2 hours for the proposed design ▪ Resistivity of $<3\times10^{-7}$ Ω-m ▪ Fabrication on 3D substrates within 4 mm range ▪ Room temperature curing	▪ Low-cost makeshift printer ▪ Not suitable for mass production ▪ Intricate tracks not feasible ▪ Limitations with the variation in track width due to the nozzle size ▪ Abrasive finish to the printed designs ▪ Challenging task to determine the suitable print speed at angles ▪ Method ideal for prototypes only ▪ Cost-inefficient prices of ink to scale-up the production
Aerosol Jet Printing	▪ Microwave, mm-wave, and low-THz designs presented ▪ FSSs operating at 2.4 GHz, 26-28 GHz, 140 GHz, and 280 GHz ▪ Direct printing on Kapton and glass ▪ Direct printing on 3D substrates possible ▪ 2-5 mm heights in 3D printing feasible ▪ Complex detailing of designs possible	▪ Highest cost among the techniques presented ▪ Higher production cost ▪ Requirement of skilled tool operations ▪ The conductive inks are in liquid form and spill after deposition ▪ Post deposition spillage of ink not ideals for details smaller than 5 µm ▪ Challenging post-processing on flexible and curved surfaces

	▪ 5 µm of track width achievable ▪ Resistivity of 2.6×10^{-7} Ω-m for Kapton and 2.5×10^{-7} Ω-m for glass ▪ Printing time of 3-4 hours for a single design ▪ Dry curing required for 60 minutes at 150° C ▪ Extreme accuracy with <1% deviation in fabrication	▪ Expensive conductive inks in view of up-scaling

6.8 Conclusion

Aerosol Jet printing of Bandstop and Bandpass Frequency Selective Surfaces for microwave, mm-wave, mm-wave and low-THz applications are presented in this chapter. The designs were printed using Optomec Aerosol Jet Printer at Centre for Process Innovation in UK. Rapid prototyping, significantly lower design costs and minimal wastage reduces the environmental impact and makes Aerosol Jet printing a lucrative direct printing alternative to traditional methods. Micrometre level precision and uniform conductivity helped depositing the precise FSS design onto glass and Kapton substrates. One design solution for microwave and one design solution for mm-wave bandstop FSS were proposed. Bandstop design consisted of an array of square-loop elements arranged in a square lattice. The novel FSSs using aerosol jet printing were printed on glass as well as on Kapton. High quality surface profiles and 3D design mapping for every design are also presented. Surface profiles in 4K Ultra HD quality signified the consistency of the designs.

Bandstop square loop element FSS design operated at 29.7 GHz for Kapton and a slightly lower transmission response at around 26.7 GHz for glass. Measured and simulated responses were in good correlation with one another. FSS design on Kapton produced a comparatively narrow band design whereas the design on glass produced a significantly wider frequency band of operation.

Glass FSSs are especially useful in buildings where glass bandstop FSS designs can be installed to reduce losses in transmission and reflect the interfering infrared waves from external sources. Installing FSS designs on Kapton can reduce signal absorption within the building

materials and can be used within an indoor environment to maintain the signal strengths. Deploying the glass FSS arrays on building windows can significantly reduce energy consumption too. The FSS designs could also be fabricated and prepared in a multilayer configuration to enhance their transmission responses. The presented FSS designs find particular applications in 4G and 5G applications for microwave and millimetre wave designs respectively. The glass designs can be readily installed on windows to work as RF frequency shields and can help in improving the signal strengths for 4G and 5G communications. Kapton designs can be installed on walls as signal reflectors to reduce the absorption of signals by materials used in construction of buildings.

Two bandpass design solutions for mm-wave and Low-THz bandpass FSS were also proposed in this chapter. Bandpass FSS designs consisted of arrays of slots arranged in square lattice. The novel fabrication of these bandpass FSS designs using aerosol jet printing was done on Kapton. Bandpass slot FSS designs that operate at 125 GHz and 280 GHz were presented. The two designs experimented with the extremity and precision of aerosol jet printers and 280 GHz Low-THz design tested the absolute extremities and limits of the printing machine. High quality surface profiles and 3D design mapping for every design are also presented. Surface profiles in Keyence® 4K Ultra HD quality demonstrated the consistency and precision of the fabricated designs at millimetre and Low-THz levels. Both the designs were fabricated on Kapton. Due to intricate and flexible nature of 50-micron Kapton substrate, only the responses at lateral angles were reported. Both the fabricated FSSs were in good correlation with their original design dimensions. Passband states as well as Stopband states for both the designs corresponded significantly well with one another. Passband state for the 125 GHz design offered a significantly wide passband range that started at the frequency of approximately 90 GHz and remained above -10 dB up until well beyond 170 GHz. For the 280 GHz design, the passband range was slightly lower and ranged from 240 GHz to almost 310 GHz.

Novel fabrication of the mm-wave and Low-THz designs provided an additional fabrication technique to produce complex designs with millimetre precision. Developing single-polarized bandpass FSS for mm-wave and low-THz applications provided economical and uncomplicated solutions as a validation for the development. The manufacturing challenges in the dispersion of ink and in the development of the most optimum toolpath for fabrication were addressed within the development of this study. These initial studies for the Low-THz design

could evolve further towards developing intricate and advance designs for ongoing 5G and imminent 6G communication networks. By fabricating with extremely thin substrates, the designs could also be manufactured to be 3D or foldable in nature.

References

[1] B. A. Munk, *Frequency selective surfaces: theory and design*. New York: John Wiley, 2000.

[2] G. Sung, K. Sowerby, M. Neve, and A. Williamson, "A Frequency-Selective Wall for Interference Reduction in Wireless Indoor Environments," *IEEE Antennas and Propagation Magazine*, vol. 48, no. 5, pp. 29–37, 2006.

[3] M. Raspopoulos and S. Stavrou, "Frequency Selective Buildings Through Frequency Selective Surfaces," in *IEEE Transactions on Antennas and Propagation*, vol. 59, no. 8, pp. 2998-3005, Aug. 2011, doi: 10.1109/TAP.2011.2158779.

[4] I. Ullah, D. Habibi, X. Zhao, and G. Kiani, "Design of RF/Microwave efficient buildings using frequency selective surface," *2011 IEEE 22nd International Symposium on Personal, Indoor and Mobile Radio Communications*, 2011.

[5] T. Parker, J. Batchelor, J.-B. Robertson, B. Sanz-Izquierdo, and I. Ekpo, "Frequency selective surfaces for long wavelength use in buildings," *IET Seminar Digests*, 2008.

[6] G.I. Kiani, A.R. Weily and K.P. Esselle, "A novel absorb/transmit FSS for secure indoor wireless networks with reduced multipath fading," IEEE Microw. Wireless Compon. Lett., vol. 16, no. 6, pp. 378-380, 2006.

[7] C. Mias, C. Tsokonas, and C. Oswald, An investigation into the feasibility of designing frequency selective windows employing periodic structures 2002, Nottingham Trent University, Nottingham, U.K., Tech. Rep. AY3922.

[8] M. Gustafsson, A. Karlsson, A. Rebelo, and B. Widenberg, "Design of Frequency Selective Windows for Improved Indoor Outdoor Communication," *IEEE Transactions on Antennas and Propagation*, vol. 54, no. 6, pp. 1897–1900, 2006.

[9] A. A. Dewani, S. G. Okeefe, D. V. Thiel, and A. Galehdar, "Window RF Shielding Film Using Printed FSS," *IEEE Transactions on Antennas and Propagation*, vol. 66, no. 2, pp. 790–796, 2018.

[10] A. Shastri *et al*., "Evaluation of Aerosol Jet Printing of Frequency Selective Surface on Glass for Building and RF Applications," *2020 14th European Conference on Antennas and Propagation (EuCAP)*, Copenhagen, Denmark, 2020, pp. 1-5, doi: 10.23919/EuCAP48036.2020.9135346.

[11] R. J. Langley and E. A. Parker, "Equivalent circuit model for arrays of square loops," in *Electronics Letters*, vol. 18, no. 7, pp. 294-296, 1 April 1982.

[12] B. Sanz-Izquierdo and E. A. Parker, "3-D Printing of Elements in Frequency Selective Arrays," in *IEEE Transactions on Antennas and Propagation*, vol. 62, no. 12, pp. 6060-6066, Dec. 2014, doi: 10.1109/TAP.2014.2359470.

[13] B. Sanz-Izquierdo and E. A. Parker, "Frequency selective surfaces formed by partially metalising 3D printed shapes," *2015 9th European Conference on Antennas and Propagation (EuCAP)*, Lisbon, 2015, pp. 1-4.

[14] M. Yan *et al*., "A Miniaturized Dual-Band FSS With Stable Resonance Frequencies of 2.4 GHz/5 GHz for WLAN Applications," in *IEEE Antennas and Wireless Propagation Letters*, vol. 13, pp. 895-898, 2014.

[15] A. A. Omar and Z. Shen, "Thin Bandstop Frequency-Selective Structures Based on Loop Resonator," in *IEEE Transactions on Microwave Theory and Techniques*, vol. 65, no. 7, pp. 2298-2309, July 2017.

[16] S. Khajevandi, H. Oraizi and M. Poordaraee, "Design of Planar Dual-Bandstop FSS Using Square-Loop-Enclosing Superformula Curves," in *IEEE Antennas and Wireless Propagation Letters*, vol. 17, no. 5, pp. 731-734, May 2018.

[17] W. Y. Yong *et al*., "Flexible Convoluted Ring Shaped FSS for X-Band Screening Application," in *IEEE Access*, vol. 6, pp. 11657-11665, 2018.

[18] Y.C.Sim, K.-M.Ahn, J.Y.Park, C.-S.Park,and J.-H.Son,‘‘Temperature dependent terahertz imaging of excised oral malignant melanoma,’’ IEEE Biomed. Health Infor., vol. 17, no. 4, pp. 779–784, Jul. 2013.

[19] A. Afsharinejad, A. Davy, B. Jennings, and C. Brennan, ‘‘Performance analysis of plant monitoring nanosensor networks at THz frequencies,’’ IEEE Internet of Things Journal., vol. 3, no. 1, pp. 59–69, Feb. 2016.

[20] S. Gui, J. Li, and Y. Pi, ‘‘Security imaging for multi-target screening based on adaptive scene segmentation with terahertz radar,’’IEEE Sensors J., vol. 19, no. 7, pp. 2675–2684, Apr. 2019.

[21] R. Appleby and R. N. Anderton, ‘‘Millimeter-wave and submillimeterwave imaging for security and surveillance,’’ Proc. IEEE, vol. 95, no. 8, pp. 1683–1690, Aug. 2007.

[22] R. Knipper, A. Brahm, E. Heinz, T. May, G. Notni, H.-G. Meyer, A. Tunnermann, and J. Popp, ‘‘THz absorption in fabric and its impact on body scanning for security application,’’ IEEE Trans. THz Sci. Technol., vol. 5, no. 6, pp. 999–1004, Nov. 2015.

[23] Z. Wang, M. Hu, E. E. Kuruoglu, W. Zhu, and G. Zhai, ‘‘How do detected objects affect the noise distribution of terahertz security images?’’ IEEE Access, vol. 6, pp. 41087–41092, 2018.

[24] M. Imbert, J. Romeu, M. Baquero-Escudero, M.-T. Martinez-Ingles, J.-M. Molina-Garcia-Pardo, and L. Jofre, ‘‘Assessment of LTCC-based dielectric flat lens antennas and switched-beam arrays for future 5G millimeter-wave communication systems,’’ IEEE Trans. Antennas Propag., vol. 65, no. 12, pp. 6453–6473, Dec. 2017.

[25] Q. Wu, J. Hirokawa, J. Yin, C. Yu, H. Wang, and W. Hong, ‘‘Millimeter wave multibeam end fire dual-circularly polarized antenna array for 5G wireless applications,’’ IEEE Trans. Antennas Propag., vol. 66, no. 9, pp. 4930–4935, Sep. 2018.

[26] R. Zhang, J. Zhou, J. Lan, B. Yang, and Z. Yu, ‘‘A high-precision hybrid analog and digital beamforming transceiver system for 5G millimeter-wave communication,’’IEEE Access,vol.7,pp. 83012–83023, 2019.

[27] M. Katz, M. Matinmikko-Blue, and M. Latva-Aho, ‘‘6Genesis flagship program: Building the bridges towards 6G-enabled wireless smart society and ecosystem,’’ in Proc. IEEE 10th Latin-Amer. Conf. Commun. (LATINCOM), Nov. 2018, pp. 1–9.

[28] M. Katz, P. Pirinen, and H. Posti, ‘‘Towards 6G: Getting ready for the next decade,’’ in Proc. 16th Int. Symp. Wireless Commun. Syst. (ISWCS), Aug. 2019, pp. 714–718.

[29] Gsma.com, 2020. [Online]. Available: https://www.gsma.com/spectrum/wp-content/uploads/2020/03/5G-Spectrum-Positions.pdf . [Accessed: 21- Jun- 2020].

[30] X.Yang, Y.Pi, T.Liu, and H.Wang,‘‘Three-dimensional imaging of space debris with space-based terahertz radar,’’ IEEE Sensors J., vol. 18, no. 3, pp. 1063–1072, Feb. 2018.

[31] M. C. Wiedner, I. Mehdi, A. Baryshev, V. Belitsky, V. Desmaris, A. M. DiGiorgio, J.-D. Gallego, M. Gerin, P. Goldsmith, F. Helmich, W. Jellema, A. Laurens, C. Risacher, A. Cooray, and M. Meixner, ‘‘A proposed heterodyne receiver for the origins space telescope,’’ IEEE Trans. THz Sci. Technol., vol. 8, no. 6, pp. 558–571, Oct. 2018.

[32] R. Dickie, R. Cahill, V. Fusco, H. S. Gamble and N. Mitchell, "THz Frequency Selective Surface Filters for Earth Observation Remote Sensing Instruments," in *IEEE*

Transactions on Terahertz Science and Technology, vol. 1, no. 2, pp. 450-461, Nov. 2011, doi: 10.1109/TTHZ.2011.2129470.

[33] B. Sanz-Izquierdo and E. A. Parker, "3D printing technique for fabrication of frequency selective structures for built environment," in *Electronics Letters*, vol. 49, no. 18, pp. 1117-1118, 29 August 2013, doi: 10.1049/el.2013.2256.

[34] B. Sanz-Izquierdo and E. A. Parker, "3-D Printing of Elements in Frequency Selective Arrays," in *IEEE Transactions on Antennas and Propagation*, vol. 62, no. 12, pp. 6060-6066, Dec. 2014, doi: 10.1109/TAP.2014.2359470.

[35] B. Sanz-Izquierdo and E. A. Parker, "Frequency selective surfaces formed by partially metalising 3D printed shapes," *2015 9th European Conference on Antennas and Propagation (EuCAP)*, Lisbon, 2015, pp. 1-4.

[36] R. Mirzavand, M. M. Honari, S. Aslanzadeh, H. Saghlatoon and P. Mousavi, "Evaluation of One-Staged 3-D Printed Frequency Selective Surface Using Carbon-Fiber-Reinforced Thermoplastic Composite," in *IEEE Transactions on Components, Packaging and Manufacturing Technology*, vol. 9, no. 11, pp. 2298-2304, Nov. 2019, doi: 10.1109/TCPMT.2019.2917197.

[37] S. Cho, S. Yoon and I. Hong, "Design of Three-Dimensional Frequency Selective Structure With Replaceable Unit Structures Using a 3-D Printing Technique," in *IEEE Antennas and Wireless Propagation Letters*, vol. 17, no. 11, pp. 2041-2045, Nov. 2018, doi: 10.1109/LAWP.2018.2871175.

[38] D. Zhou, X. Huang and Z. Du, "Analysis and Design of Multilayered Broadband Radar Absorbing Metamaterial Using the 3-D Printing Technology-Based Method," in *IEEE Antennas and Wireless Propagation Letters*, vol. 16, pp. 133-136, 2017, doi: 10.1109/LAWP.2016.2560904.

[39] D. Lim, S. Yu and S. Lim, "Miniaturized Metamaterial Absorber Using Three-Dimensional Printed Stair-Like Jerusalem Cross," in *IEEE Access*, vol. 6, pp. 43654-43659, 2018, doi: 10.1109/ACCESS.2018.2862160.

[40] W. G. Whittow, Y. Li, R. Torah, K. Yang, S. Beeby and J. Tudor, "Printed frequency selective surfaces on textiles," in *Electronics Letters*, vol. 50, no. 13, pp. 916-917, 19 June 2014, doi: 10.1049/el.2014.0955.

[41] O. Sushko, M. Pigeon, T. Kreouzis, C. Parini, R. Donnan and R. Dubrovka, "Low-cost inkjet-printed FSS band-pass filters for 100 and 300 GHz," *2016 10th European Conference on Antennas and Propagation (EuCAP)*, Davos, 2016, pp. 1-3, doi: 10.1109/EuCAP.2016.7481780.

[42] O. Sushko, M. Pigeon, R. S. Donnan, T. Kreouzis, C. G. Parini and R. Dubrovka, "Comparative Study of Low-THz FSS Filters Fabricated by Inkjet Printing, Microprecision Material Printing, and Photolithography," in *IEEE Transactions on Terahertz Science and Technology*, vol. 7, no. 2, pp. 184-190, March 2017, doi: 10.1109/TTHZ.2017.2662582.

[43] "Corning Eagle XG® Glass datasheet", https://www.corning.com/media/worldwide/cdt/documents/EAGLE%20XG%20®%20Slim%20Glass.pdf . [Accessed: 22-May-2020].

[44] S. Chen, K. N. Nguyen and M. N. Afsar, "Millimeter-Wave Dielectric Permittivity of Glasses," *2006 Joint 31st International Conference on Infrared Millimeter Waves and 14th International Conference on Teraherz Electronics*, Shanghai, 2006, pp. 406-406, doi: 10.1109/ICIMW.2006.368614

[45] "Dupont™ Kapton® HN datasheet", https://www.dupont.com/content/dam/dupont/amer/us/en/products/ei-transformation/documents/DEC-Kapton-HN-datasheet.pdf . [Accessed: 22-May-2020].

[46] S. N. Azemi, K. Ghorbani, and W. S. T. Rowe, "3D Frequency Selective Surfaces with close band spacing," *2012 Asia Pacific Microwave Conference Proceedings*, Vol. 29, 191-203, 2012.

[47] S. Y. Jun, A. Elibiary, B. Sanz-Izquierdo, L. Winchester, D. Bird and A. McCleland, "3-D Printing of Conformal Antennas for Diversity Wrist Worn Applications," in *IEEE Transactions on Components, Packaging and Manufacturing Technology*, vol. 8, no. 12, pp. 2227-2235, Dec. 2018, doi: 10.1109/TCPMT.2018.2874424.

[48] "3D Printed Electronics - Aerosol Jet Technology - Optomec", *Optomec*, 2020. [Online]. Available: https://optomec.com/printed-electronics/aerosol-jet-technology/ . [Accessed: 17- May- 2020].

[49] L. Teschler, "Your next circuit design could be fabricated on a 3D printer", *Electrical Engineering News and Products*, 2020. [Online]. Available:

https://www.eeworldonline.com/next-circuit-design-fabricated-printer/. [Accessed: 17-May- 2020].

[50] L. Mo et al., "Silver Nanoparticles Based Ink with Moderate Sintering in Flexible and Printed Electronics", *International Journal of Molecular Sciences*, vol. 20, no. 9, p. 2124, 2019. Available: 10.3390/ijms20092124.

[51] J. A. Paulsen, M. Renn, K. Christenson and R. Plourde, "Printing conformal electronics on 3D structures with Aerosol Jet technology," 2012 Future of Instrumentation International Workshop (FIIW) Proceedings, Gatlinburg, TN, 2012, pp. 1-4, doi: 10.1109/FIIW.2012.6378343.

[52] F. Cai, Y. Chang, K. Wang, W. T. Khan, S. Pavlidis and J. Papapolymerou, "High resolution aerosol jet printing of D-band printed transmission lines on flexible LCP substrate," 2014 IEEE MTT-S International Microwave Symposium (IMS2014), Tampa, FL, 2014, pp. 1-3, doi: 10.1109/MWSYM.2014.6848597.

[53] F. Cai et al., "Aerosol jet printing for 3-D multilayer passive microwave circuitry," 2014 44th European Microwave Conference, Rome, 2014, pp. 512-515, doi: 10.1109/EuMC.2014.6986483.

[54] Yuxiao He, C. Oakley, P. Chahal, J. Albrecht and J. Papapolymerou, "Aerosol Jet printed 24 GHz end-fire quasi-Yagi-Uda antenna on a 3-D printed cavity substrate," 2017 International Workshop on Antenna Technology: Small Antennas, Innovative Structures, and Applications (iWAT), Athens, 2017, pp. 179-182, doi: 10.1109/IWAT.2017.7915352.

[55] J. A. Byford, C. Oakley and P. Chahal, "Additively Manufactured Frequency Selective Structures on Curved Surfaces," 2018 48th European Microwave Conference (EuMC), Madrid, 2018, pp. 671-674, doi: 10.23919/EuMC.2018.8541568.

[56] S. Sahin, N. Nahar and K. Sertel, "Dielectric Properties of Low-Loss Polymers for mmW and THz Applications", *Journal of Infrared, Millimeter, and Terahertz Waves*, vol. 40, no. 5, pp. 557-573, 2019. Available: 10.1007/s10762-019-00584-2.

[57] M. Euler, V. Fusco, R. Dickie, R. Cahill and J. Verheggen, "Sub-mm Wet Etched Linear to Circular Polarization FSS Based Polarization Converters," in *IEEE Transactions on Antennas and Propagation*, vol. 59, no. 8, pp. 3103-3106, Aug. 2011, doi: 10.1109/TAP.2011.2158973.

[58] O. Çakır, "Review of Etchants for Copper and its Alloys in Wet Etching Processes", Key Engineering Materials, vol. 364-366, pp. 460-465, 2007. Available: 10.4028/www.scientific.net/kem.364-366.460.

[59] A. A. Dewani, S. G. O'Keefe, D. V. Thiel and A. Galehdar, "Window RF Shielding Film Using Printed FSS," in *IEEE Transactions on Antennas and Propagation*, vol. 66, no. 2, pp. 790-796, Feb. 2018, doi: 10.1109/TAP.2017.2780893.

[60] B. M. Turki *et al.*, "Significant Factors in the Inkjet Manufacture of Frequency-Selective Surfaces," in *IEEE Transactions on Components, Packaging and Manufacturing Technology*, vol. 6, no. 6, pp. 933-940, June 2016, doi: 10.1109/TCPMT.2016.2561972.

[61] F. J. Romano, *Inkjet! Everything You Need to Know About Inkjet History, Technology, Markets, and Applications*. Printing Industries Press, 2012, pp. 37-179.

[62] *3D Printed Electronics - Aerosol Jet Technology - Optomec*. [online] Available at: https://optomec.com/printed-electronics/aerosol-jet-technology/ [Accessed 7 July 2020].

[63] L. Teschler, "Your next circuit design could be fabricated on a printer", *Design World*, 2015. [Online]. Available: https://www.designworldonline.com/your-next-circuit-design-could-be-fabricated-on-a-printer/ . [Accessed: 22- June- 2020].

CHAPTER 7

CONCLUDING REMARKS

7.1 Conclusion

Manufacturing and development of frequency reconfigurable antennas and frequency selective surfaces have been presented in this thesis. Frequency reconfigurable antennas for smart sensing applications allow a single antenna to operate over a wide range of frequencies. The ability of antennas to tune between a wide range of frequency helps the antennas cover several adjacent frequency bands. Frequency reconfigurability can be achieved using numerous ways and the implementation using inexpensive diode was presented in chapter 3 and chapter 4. Frequency reconfigurable antennas are particularly useful in a number of applications such as smart voltage and current sensing, mobile and wireless communications, smart metering and satellite communications. With a wide range of possibilities with antennas and fabrication techniques, reconfigurable antennas provide low-cost, efficient and environment friendly designs with the option of being flexible and foldable when printed on flexible substrates.

Frequency selective surfaces are filtering screens that are used to filter the desired frequency band. There are two types of frequency selective surfaces (FSSs): Bandstop FSS and Bandpass FSS. Bandstop FSS designs work as frequency shields that allow only the resonant frequency band pass through and reflect all the other frequency bands and signals. Bandpass FSS designs work as frequency reflectors and filters that reflect and filter all the bands neighbouring from the resonant frequency bands. FSSs find applications in mobile communications, RF shielding, frequency reflectors in indoor environments, 5G communications and the imminent 5G beyond and 6G communications.

A variety of fabrication techniques are reported in the development of antennas and Frequency Selective Surfaces across the chapters in this thesis. Techniques such as etching, inkjet printing and aerosol jet printing are used to develop several designs. Various substrates such as Mylar, PET, resin coated photo paper, PLA, corning eagle glass, and Kapton are reported over the course of this thesis with various antennas and FSS designs. The designs cover some extremely distinct and wide frequency bands ranging from as low as 2.4 GHz and go as high as 280 GHz with an increase in bands by a factor of 120. Using different fabrication techniques provide a wide range of possibilities in the development of various designs in terms of the frequency of operation, overall cost of designs, design response, alteration in response by changing the property of the substrate etc to name a few. Advantages and disadvantages of additive manufacturing on different surfaces and substrates are studied and reported. Surface profiles and surface roughness of the printed substrates and designs are also explored and analysed. This chapter provides a summation of the conclusions arising from the research presented in this thesis along with the future direction with the upcoming work presented in Section 7.2.

The research work started with the literature review on the most frequently reported frequency reconfigurable smart antennas and designs over the years in Chapter 2. Advancements of bandpass and bandstop frequency selective surfaces over the years are also reported where the focus was primarily on the additive manufacturing of FSS structures. A number of traditional and modern fabrication techniques are also presented in the chapters.

Chapter 3 demonstrated the development of frequency reconfigurable antennas for smart sensing applications using close-coupled biasing technique. Inexpensive PIN diodes are deployed to realise the frequency reconfigurability with the help of slot antenna designs. Close-coupled biasing technique was presented in combination with slot antennas for the first time. The design solutions were able to switch and tune between several frequencies and covered a wide range of frequency bands of interest. The low-cost designing on flexible substrates provides a solution for the development of designs for wireless communications and sensor applications. A demonstration for the use of tunable slot antenna for a smart AC sensing system is also presented. The typical slot antenna is deployed with a novel current sensing system to sense the alternating current levels passing through the wires of a common household electric appliance. The dual-band antenna can perform the dual functions of sensing the current levels through the first mode and transmitting the data over Bluetooth network in the second mode

for smart metering. The thin and flexible nature of the substrate can help the antenna designs to be rolled around a wire or a curved surface for an efficient use of space.

Chapter 4 presented an industry ready solution and the manufacturing considerations that went into developing the frequency reconfigurable antenna aperture using low-cost inkjet printing technique. Two operations of frequency-switching and frequency tuning are described using the same antenna aperture. The solution presents a single-layer aperture of two rectangular patches that are a small distance apart from one another, effectively creating a slot of infinite length between them. Additional components are mounted on the antenna aperture to create a complimentary dipole. Inkjet printing of the patch aperture provides a low-cost, environment friendly commercially available solution that can print designs at a rapid rate with reliable performances and uniform characteristics. Inkjet printing finds particular interest for its simplicity and rapid prototyping and in developing electronics and antennas on foldable substrates such as photo-paper and PET.

Chapter 5 presented the low-cost additive manufacturing of FSS using inexpensive machines for microwave and sub millimetre wave applications. Two different approaches are presented for the low-cost fabrication. Two bandstop FSS wallpapers were printed using a household inkjet printer in which the ink cartridges were replaced with refillable cassettes filled with conductive nanoparticle silver ink. The designs were printed on the resin coated paper for their application as wallpapers for microwave and sub-millimetre wave reflectors for RF shielding of 4G and 5G networks. The designs provide a low-cost solution to help develop the wallpapers to enhance the signal strength from the comfort of homes and workplaces. The second part of the chapter presented the development of a fully 3D printed bandstop FSS design using an inexpensive open-source printer that was modified to accommodate dual-extrusion of the PLA filament substrate and the Voxel8 silver conductive ink. The manufacturing and developmental considerations that went into developing a low-cost printer system combining the FFF extrusion with an air pressure dispenser extruder to print the PLA and silver conductive materials simultaneously. The ability to develop custom made fully 3D printed FSS or antenna designs provides a lucrative alternative to develop intricate 3D EM structures with reliable performances. The controllable permittivity and the adjustable thickness of the PLA substrate can help in altering the physical properties of the design to provide a wide range of structural possibilities which can be explored further in the future.

Chapter 6 presented the aerosol jet printing of intricate Frequency Selective Surfaces. Various FSSs were designed and fabricated using Aerosol Jet printer accessed at Centre for Process Innovation, Durham, UK to develop bandstop FSS for microwave, sub mm-wave and mm-wave designs for WLAN, 4G and 5G frequency shielding applications as well as the novel 3D printing of bandpass FSS for mm wave and low-THz applications. Applications of RF shielding, 4G and 5G communications are presented with the help of microwave and sub-millimetre wave bandstop FSS designs. The designs covered the 2.4 GHz, 24 GHz, and 26-28 GHz bands, respectively. The designs were printing using aerosol jet printer with the help of conductive nanoparticle silver ink on Corning eagle glass as well as on Kapton substrates. The designs demonstrated exemplary performances and worked perfectly well for the orthogonal as well as for diagonal angles, the TE-00 and TM-45 angles. Measured surface profile shows the consistency of these Bandstop designs. Second part of the chapter presented the mm wave and low-THz Bandpass slot frequency selective surface designs using the same technology. These designs tested the accuracy and precision of the Aerosol Jet machines with the low-THz design testing the machine to its extreme limits. Several iterations were required to get the precise designs with reliable accuracy. The designs required the absolute micrometre level precision that an aerosol jets provide, and strategic toolpaths were created to get the desired designs to form into the shape of slot arrays. Two designs of bandpass slot FSS were presented which resonated at 125 GHz and 280 GHz, respectively. The bandpass designs operated in wideband mm-wave and low-THz regions and the measured transmission responses corresponded well with the simulated responses. These futuristic designs find applications in sensing systems, space communications, counter terrorism systems, and particularly with 5G and the imminent 6G communication systems. Using flexible Kapton substrates also leaves the options to make the designs flexible and foldable in nature. The measured surface profile and surface roughness designs show the precision in the fabrication process and demonstrate the acute accuracy with which an aerosol jet printer can print a design.

A comparison table comprising of the manufacturing trade-offs and comparisons between the two methods proposed for the development of frequency reconfigurable slot antennas is depicted in Table I. A similar table comparing the various AM techniques deployed in manufacturing FSS designs is presented as Table II. The two table, which were also presented in earlier sections as well, may provide key suggestions and considerations to future designers.

TABLE I.

COMPARISON TABLE AMONG THE PRESENTED RECONFIGURABLE ANTENNA FABRICATION TECHNIQUES

Elements	**Etching**	**Inkjet Printing**
Substrate	Mylar	PET
Conductive layer	Copper	Nanoparticle silver ink
Thickness	0.05 mm	0.123 mm
Fabricable layers	Single and Double layer	Single layer only
Fabrication time	Approx. 1 hr	2-3 minutes
Components mounting	Soldering	Conductive adhesive
Substrate dimensions	Etching bed size	A4 sheet size only
Resistivity	1.67×10^{-8} Ω-m	4.53×10^{-7} Ω-m
Biasing tracks	Yes	No
Capacitive coupling	Yes	No
Direct reconfigurability	No	Yes
Flexibility	Yes	Yes
Bendability	Yes	No
Temperature tolerance	High	Low
Switching range	1.56 GHz – 2.5 GHz	1.7 GHz – 3 GHz
Tuning range	1.4 GHz – 2.6 GHz	1.38 GHz – 2.7 GHz
Bandwidth at f_c	21%	24%
Single aperture dual operations	Yes	No
Approximate cost per antenna	£ 10-15	£ 25-30

TABLE II.

COMPARISON TABLE BETWEEN PROPOSED FABRICATION TECHNIQUES FOR FREQUENCY SELECTIVE SURFACES

Manufacturing Method	Saliant Features	Drawbacks
Low-Cost Inkjet printing	▪ Microwave and mm-wave designs presented ▪ Inexpensive manufacturing ▪ No stencil required ▪ Reliable print resolution of ~100 µm ▪ Single-step printing ▪ Printing time of a few seconds over A4 area ▪ Resistivity of 4.53×10^{-7} Ω-m with uniformity across tracks ▪ No curing requirements ▪ Eco Friendly	▪ Not suitable for bulk manufacturing ▪ Delicate nature of structures and substrates ▪ Resolution constraints with a limit on track size (100 µm - 200 µm) ▪ Costly conductive inks ▪ Only single-sided fabrication possible
Conductive Silver Ink extrusion	▪ Fully 3D printed microwave FSS presented ▪ Both substrate and FSS array are printed simultaneously with the same printer ▪ Permittivity of the substrate can be varied with different infill densities ▪ Varied permittivity offered variations in transmission responses ▪ Vacuum extrusion of conductive silver ink offered varied track thickness at different pressures ▪ Suitable with ABS and PLA ▪ Fabrication time of 1-2 hours for the proposed design ▪ Resistivity of $<3\times10^{-7}$ Ω-m ▪ Fabrication on 3D substrates within 4 mm range ▪ Room temperature curing	▪ Low-cost makeshift printer ▪ Not suitable for mass production ▪ Intricate tracks not feasible ▪ Limitations with the variation in track width due to the nozzle size ▪ Abrasive finish to the printed designs ▪ Challenging task to determine the suitable print speed at angles ▪ Method ideal for prototypes only ▪ Cost-inefficient prices of ink to scale-up the production
Aerosol Jet Printing	▪ Microwave, mm-wave, and low-THz designs presented ▪ FSSs operating at 2.4 GHz, 26-28 GHz, 140 GHz, and 280 GHz ▪ Direct printing on Kapton and glass ▪ Direct printing on 3D substrates possible ▪ 2-5 mm heights in 3D printing feasible ▪ Complex detailing of designs possible	▪ Highest cost among the techniques presented ▪ Higher production cost ▪ Requirement of skilled tool operations ▪ The conductive inks are in liquid form and spill after deposition ▪ Post deposition spillage of ink not ideals for details smaller than 5 µm ▪ Challenging post-processing on flexible and curved surfaces

	▪ 5 µm of track width achievable ▪ Resistivity of 2.6×10^{-7} Ω-m for Kapton and 2.5×10^{-7} Ω-m for glass ▪ Printing time of 3-4 hours for a single design ▪ Dry curing required for 60 minutes at 150° C ▪ Extreme accuracy with <1% deviation in fabrication	▪ Expensive conductive inks in view of up-scaling

7.2 Future work

The works that have been reported within this thesis have exhibited the successful additive manufacturing of reconfigurable antennas and frequency selective surfaces using low-cost and expensive printing equipment. Additive manufacturing using low-cost household inkjet printer using nanoparticle silver ink was presented to create an antenna solution as well as wallpaper reflector screens printed on paper-based substrates. A successful demonstration of low-cost inkjet printing on PET and raisin coated paper was demonstrated for WLAN, 4G and 5G applications across the smart antennas and FSS designs that encompassed the 2.4 GHz and 24 GHz bands, respectively. Some further investigations can therefore be conducted to develop the mm wave structures using the inkjet printers by developing some innovative and intricate designs that can overcome the limitations of the standard inkjet printers to be able to print the complex structures with repeatability and reliable accuracy and resolution of the printed intricate tracks.

Additionally, to take the developments of the passive FSS designs further, multiband FSS structures can also be developed that can accommodate two or more frequency bands depending on the specific designs. Multiband FSS designs can be particularly useful as frequency shields that can enhance the signal strength for both 4G and 5G signals simultaneously using the same wallpaper or printed FSS array. The flexible and foldable nature of the paper and PET based substrates can help mount the FSS in corners or uneven surfaces and still provide relatively good angle of incidence behaviours, which, in itself possesses scope for further investigations in the near future. Development of multiband FSS reflector screens that can provide reliable performances from on uneven surfaces provides an exciting challenge

for the researchers and works as something that can provide many manufacturing and designing possibilities.

In addition, additive manufacturing of active FSS structures is an area which remains largely unexplored as a large volume of the work conducted in this field of work is for the defence sector and therefore, the literature remains inaccessible and the real extent of the recent developments in this field of work remains beyond reach. Active FSS, as the name implies is the kind of smart FSS in which the frequency dependence of the transparency of the structure can be amended by using an external input signal of some kind. An FSS can be asserted as active or smart by one of these three means: when active components are mounted within the FSS structure, when alteration of the mode coupling that exists between the cascaded FSS designs can be achieved or when the electrical properties of the substrate can be altered [1]. The most reliable method for active and smart FSS designs has been using PIN or varactor diodes. There can be three potential ways in which the active elements can be incorporated within an FSS: as a part of the unit cell structures, between two adjacent unit cells and between the ground plane and the layers [1]. As the external input signal such as DC voltage is supplied, the FSS structure, with the help of its active components such as diodes, inverses its performance from being a reflective screen to a transmitting screen at the frequency of operation. In the transmitting state, the FSS acts as a transparent structure which switches its transparency levels when the mode is switched from transmitting state to reflective state.

With the rapid advancements in additive manufacturing, development of smart FSS structures using AM could be an attractive field of exploration. The manufacturing constrains, which were discussed in Chapter 4 about the development of smart antenna solution would help in establishing the manufacturing and designing considerations require for the desired smart FSS designs using low-cost machines. The substrates that are typically available for low-cost additive manufacturing typically have single-sided fabrication as well as low temperature tolerance which makes them unsuitable for multi-layered designs and mounting components using the conventional methods such as soldering. Additionally, due to the flexible nature of the suitable substrates, the printed FSS layout must be pre-mounted on a piece of foam or some similar thick substrate for durability and solidity. As the components cannot be soldered, conductive adhesives must be used to mount the components.

Keeping the aforementioned considerations and constraints in mind, an FSS will be designed, investigated, and developed as for the future course to take this research forward towards exploring the additive manufacturing of smart FSS. As the design was still in the developmental stage when this thesis was compiled, certain critical aspects of designs are not elaborated here in this section. Only the simulated transmission response is presented.

For the active FSS, a single-layer dipole FSS was designed while keeping the manufacturing considerations for the Brother inkjet printer in mind. Initially, a simple dipole was designed but the transmitting state response did not resonate as per expectations with even the best-case response of -4 dB observed for the resonant frequency of 2.4 GHz which was in accordance with the expected results illustrated in [2]. To overcome this issue, a new FSS unit cell design was proposed that consisted of two radiating elements to minimise the complexity that cannot be diminished even in an optimised design proposed in [2] and [3]. The design consisted of a single-polarised dipole FSS and a pair of periodic convoluted matching tracks. The FSS array created using this unit cell design can be called a dipole FSS with discontinuous H-shaped matching tracks. When the dipole strips are connected, the dipole acts as a discontinuous strip of conductive layer. The gaps were filled with switching diodes which were mounted using conductive adhesives. The intricate nature of the design required the diodes to be attached with extreme precision and accuracy. The whole process took a few weeks to complete due to the complex nature of the process. Initially, conductive inks were tried which turned out be ineffective in keeping diodes in place. The proposed design can be seen in Fig. 7.1 below. The design was printed on a raisin coated photo paper, the same one which was demonstrated for wallpaper reflector FSS designs earlier. The workmanship to mount the diodes which were attached using the conductive adhesive can be seen in the picture. H-shaped matching tracks can also be seen in the photograph.

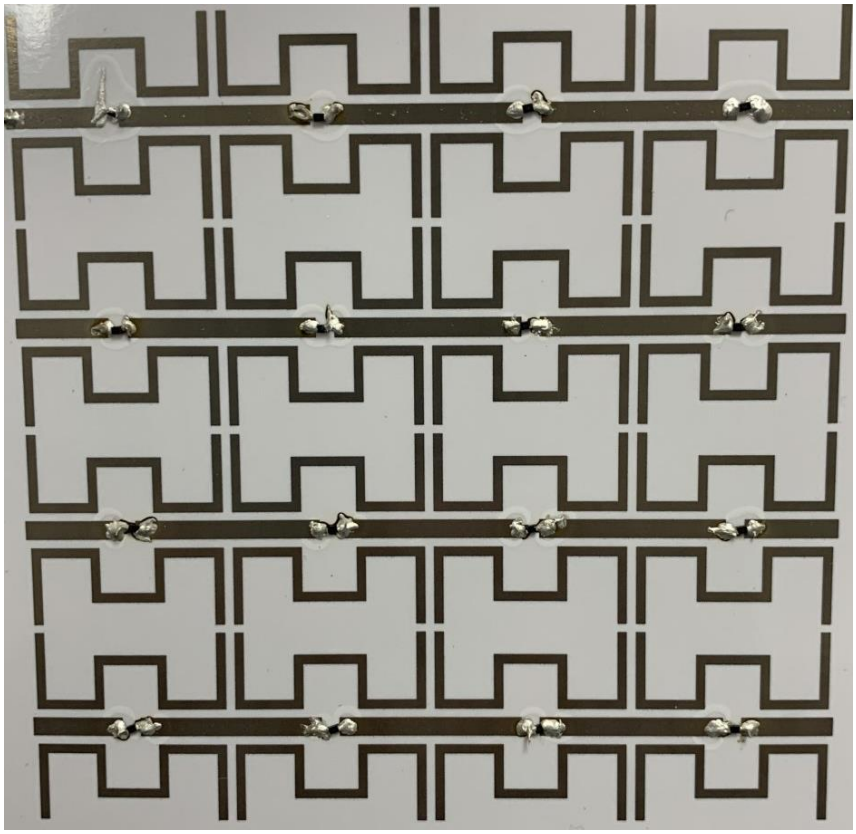

Fig. 7.1 Inkjet-printed active dipole FSS with H-shaped matching stubs

Depending upon the assessment of the design orientation to be horizontal or vertical, the matching stubs can be considered to be H-shaped or I-shaped. For clarity purposes, horizontal orientation was assumed for the array. The simulated CST transmission response can be seen in Fig. 7.2. Again, only the CST response was produced as the design was in the developmental stage.

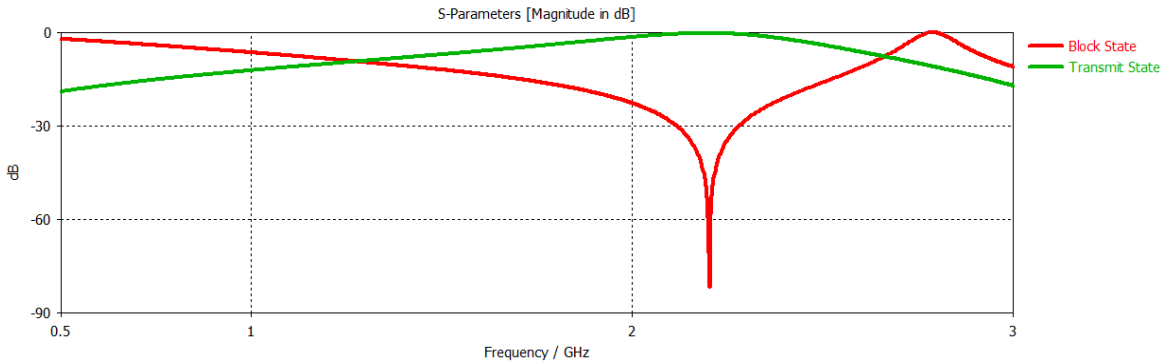

Fig. 7.2 Simulated CST Transmission Response of the proposed Active FSS design

With the potential success of this smart FSS, some future advancements along the lines of dual-polarised designs can be made using similar methods. The possibilities of deploying Varactor diodes for the inkjet-printed design to make the smart FSS tunable at various frequency with the variation in DC supply voltage also needs to be investigated in the coming future.

References

[1] E. Parker and S. Massey, *Ofcom.org.uk*, 2004. [Online]. Available: https://www.ofcom.org.uk/__data/assets/pdf_file/0021/27345/survey.pdf. [Accessed: 08-Aug- 2020].

[2] M. Bouslama, M. Traii, T. A. Denidni and A. Gharsallah, "Beam-Switching Antenna With a New Reconfigurable Frequency Selective Surface," in *IEEE Antennas and Wireless Propagation Letters*, vol. 15, pp. 1159-1162, 2016, doi: 10.1109/LAWP.2015.2497357.

[3] B. S. Izquierdo, E. A. Parker, and J. C. Batchelor, "Dual-band tunable screen using complementary split ring resonators," *IEEE Trans. Antennas Propag.*, vol. 58, no. 11, pp. 3761–3765, Nov. 2010.